Correction of Image Distortions in Magnetic Resonance Imaging

Intensity Inhomogeneities Correction and Evaluation

Siemens S.A. – Healthcare Sector

2009/2010

Rui Filipe David Lavrador

Physics Department,

Faculty of Sciences and Technology of University of Coimbra

September, 2010

Correction of Image Distortions in Magnetic Resonance Imaging

Intensity Inhomogeneities Correction and Evaluation

Siemens S.A. – Healthcare Sector

2009/2010

2004107454   Rui Filipe David Lavrador

Integrated Master in Biomedical Engineering

Physics Department,

Faculty of Sciences and Technology of University of Coimbra

September, 2010

Adviser from FCTUC: Doctor Nicolás Lori

Supervisor from Siemens: Engineer Filipe Janela

Aos meus pais

Acknowledgments

Abstract

With magnetic resonance imaging (MRI) technique it is possible to obtain a vast amount of both anatomical and functional information, allowing better diagnosis and patient treatments. Diagnosis can be improved when supported by automatic image analysis tools. That analysis may suffer the influence of some artifacts, being one of them the intensity inhomogeneity, caused by inhomogeneities in the radio-frequency pulse excitation and reception and electrodynamic interactions with the object, often described as RF penetration and standing wave effects. The desire of solving this problem led to the development of several algorithms having different theoretical underpinnings. Many evaluations and comparisons have been made between algorithms, but until now, none of them was considered unquestionably the best for all kind of data.

To solve this ambiguity one did not propose a new algorithm, in this work, four known algorithms were used to correct intensity inhomogeneities, in order to find an optimal method of correction for each MRI acquisition type. There were used simulated images with intensity inhomogeneities, generated with similar sequence parameters of real acquisitions with intention of obtaining intensities close to the clinical images and observe how this influences the correction methods. The image quality was measured by several image quality parameters.

It was found that the performance of each algorithm varies depending on the image that they correct. There was not found an algorithm that overcomes all the other for all situations. The evaluation of the algorithm was made taking into account the propose and the parameter that we wish to improve.

The choice of the most suitable algorithm for a specific type of image proved to be an important and useful step helping subsequent image analysis, in this case segmentation. These improvements may be used to support medical decisions and improving healthcare services.

Keywords: intensity inhomogeneity correction, MRI, segmentation, image quality, image processing

Rui Lavrador

Resumo

Usando a técnica de imagem por ressonância magnética (IRM) é possível adquirir uma vasta quantidade de informação tanto anatómica como funcional, obtendo-se assim melhores diagnósticos e ajuda no tratamento de pacientes. O diagnóstico pode ser melhorado utilizando ferramentas de análise automática das imagens. Essa análise poderá sofrer a influência de alguns artefactos, sendo um deles a distorção de intensidades, causado por não-uniformidades da excitação e recepção a quando do uso do pulso de rádio frequência (RF), assim com também é devido às interacções electrodinâmicas com o objecto. O desejo de resolver este problema levou ao desenvolvimento de vários algoritmos com diferentes bases teóricas. Realizaram-se ainda variadas avaliações e comparações entre eles, mas, até agora, não foi encontrado um algoritmo que possa ser considerado inquestionavelmente o melhor para todos os tipos de dados adquiridos com IRM.

Para resolver esta ambiguidade, neste trabalho não é proposto um novo algoritmo. Foram usados quatro conhecidos algoritmos para a correcção destas não-uniformidades, de maneira a tentar encontrar o melhor método de correcção para cada tipo de aquisição de IRM. Foram utilizadas imagens simuladas com não-uniformidades na intensidade, geradas com parâmetros de sequência idênticos às aquisições reais, de maneira a se puder obter imagens com intensidades próximas das imagens clínicas e observar como este factor influencia os algoritmos de correcção. As imagens corrigidas foram avaliadas com diversos parametros relacionados com a qualidade de imagem.

Verificou-se que a performance de cada algoritmo varia dependendo do tipo de imagem que está a corrigir. Não foi encontrado um algoritmo que fosse superior a todos os outros para todas a situações. A avaliação do melhor algoritmo foi realizada tendo em conta o propósito das imagens e o parâmetro que se pretende melhorar.

A escolha do método mais adequado para um tipo específico de imagens provou ser um passo importante quando se procura melhorar uma análise subsequente da imagem, neste caso segmentação. Estas melhorias poderão ser usadas para apoiar decisões médicas e melhorar assim os cuidados de saúde.

Palavras-chave: Correcção da não-homogeneidade, MRI, segmentação, qualidade de imagem, processamento de imagem

Rui Lavrador

Contents

Rui Lavrador

List of Figures

List of Tables

Rui Lavrador

Acronyms

CNR	Contrast-to-Noise Ratio
CSF	Cerebral Spinal Fluid
CT	Computer Tomography
CV	Coefficient of Variation
DICOM	Digital Imaging and Communications in Medicine
EM	Expectation Maximization
EPI	Echo Planar Imaging
FCM	Fuzzy-C-Means
FID	Free Induction Decay
FLASH	Fast Low Angle Shot
FM	Finite Mixture
FOV	Field of View
FSL	FMRIB Software Library
GM	Grey Matter
GRE	Gradient Echo
HMRF	Hidden Markov Random Field
IFT	Inverse Fourier Transform
IIH	Intensity Inhomogeneity
IR	Inversion Recovery
IT	Innovation and Technology
ITK	Insight Segmentation and Registration Toolkit
LM	Levenberg–Marquardt
MAP	Maximum-a-Posteriori
MATLAB	Matrix Laboratory

MR	Magnetic Resonance
MRI	Magnetic Resonance Imaging
N3	Nonuniform Intensity Normalization
NMR	Nuclear Magnetic Resonance
OS	Operative System
PABIC	Parametric Bias Field Correction
PET	Positron Emission Tomography Systems
RF	Radio Frequency
RMS	Root Mean Square
ROC	Receiver Operator Characteristic
ROI	Region of Interest
SAR	Specific Abortion Rate
SE	Spin Echo
SNR	Signal-to-Noise Ratio
SPECT	Single-Photon Emission Tomography Systems
SPM	Statistical Parametric Mapping
T	Tesla
TE	Echo Time
TR	Repetition Time
WM	White Matter

Chapter 1

Introdution

1.1 Scope

In modern healthcare services, imaging has become one of the essential cornerstones in the daily routine of physicians and other professionals. Diagnostic and procedures rely on innovative imaging technologies for disease detection, treatment, and follow-up, that are as safe, patient-friendly and effective as possible [1, 2].

Magnetic resonance imaging (MRI) is a powerful non invasive technique that allows great contrast in soft tissues, high spatial resolution and has both anatomical and functional information. The automatic extraction of clinical relevant information has became mandatory to efficiently deal with the large amount of data generated using imaging techniques. However, several artifacts can degrade the quality of acquired data [3, 4, 5, 6].

The intensity inhomogeneity is one of those artifacts and are caused by static field inhomogeneities, gradient field nonlinearities or by perturbations due to the sample presence. These artifacts results in a smooth variation of the intensity of a tissue across the image, thus the same tissue has different intensity according to its location. This distortion, in many cases, is usually hardly noticeable to the human observer, but can influence many medical image analysis methods, such as segmentation and registration, that are highly sensitive to variations in image intensities [7, 8].

Numerous methods with different theoretical underpinnings were proposed to solve this distortion, but none of them proved to be clearly superior to the others, for all kind of images and needs. In the majority of the studies the corrected images are simulated or acquired by 1.5T scanners, and there are few specific MRI sequences analysed. The images are generally considered simply T1, T2 or PD-weighted to simplify and to easily match with simulated images. Another trend is to combine the intensity inhomogeneity correction (IIH) with other frameworks incorporating knowledge such as segmentation or registration [3, 7, 8, 9].

1.2 Presentation of the project

This project emerges in order to find an optimal method to correct the intensity distortion. This correction will improve the physicians analysis or the analysis made by a computer, bringing obvious advantages to the clinical practice, providing more reliable diagnosis.

Regarding the intensity distortion issue, it was performed an evaluation of the state-of-the-art algorithms, and the study focused on methods based on a retrospective image analysis, which means that one uses exclusively information of the acquired image and in some cases *a priori* knowledge. Four algorithms with different underpinnings, with available source codes and already implemented in other software widely used in image processing were chosen.

The first step of the project was the familiarization with different programming languages and use different operative systems (OS). The next step was to correct simulated images, generated on *BrainWeb*[1]. Parameters for evaluation were then calculated in the corrected images in order to assess several features of the images such as homogeneity within the tissues, contrast and signal-to-noise ratio, segmentation performance, among others. An evaluation of the correcting algorithms was made in order to find the best correction for which image and also taking into account the purpose of the image.

In Table 1.1 is shown the plan that was followed during this project.

Table 1.1: Description of the work plan.

Month	Work Plan	1st W	2nd W	3rd W	4th W
October	Understand the Siemens world and in particular the Healthcare Sector				
	Familiarization with Siemens products and solutions				
	Basic formation on anatomy and physiology				
	Learn the magnetic resonance imaging basics				
November	Learn the magnetic resonance imaging basics				
	Research international and national data related to MRI artefacts and image corretion				
	Choose the algorithms and software to correct the intensity distortion				
December	Detailed analysis of the chosen algorithms to intensity distortion				
January	Familiarization with development software				
	Compare and evaluate the algorithms related to intensity distortion correction				
February	Compare and evaluate the algorithms related to intensity distortion correction				
	Propose paper to a conference				
March	Compare and evaluate the algorithms related to IIH correction using more data sets				
April	Compare and evaluate the algorithms related to IIH correction using more data sets				
	Evaluate the effect of the corrections in subsequent image processing methods				
May	Evaluate the effect of the corrections in subsequent image processing methods				
	Propose abstract to a conference				
June	Consolidation of the results				
	Thesis Writing				
July	Write paper to a conference				
	Thesis Writing				
August	Thesis Writing				

---

[1] http://mouldy.bic.mni.mcgill.ca/brainweb/

1.3 Contribution of the work

The approach used in this work regarding the IIH correction will allow to adapt a specific correction method to a specific MRI acquisition type and take into account the purpose of the image.

The results achieved in this work could be used in order to support the decision about the algorithms that should be incorporated in magnetic resonance (MR) scanners or incorporated in Syngo®. This meets the objectives of the Siemens S. A. Healthcare Sector in order to have always the best solution for its costumers, in this case regarding image quality, helping physicians and technicians to provide the best health care possible.

1.4 Siemens S.A. presentation

With 500 production centers in 50 countries and representation in 190 countries, Siemens is spread all over the world. In Portugal, Siemens S.A. encloses two factories, software research & development centers (Lisbon and Porto) and has a significant representation all over the country through its partners and company headquarters. Since 2008, the company is organized in three major sectors: Industry, Energy and Healthcare.

The Industry Sector and its solutions address Industry customers regarding production, transportation and building systems. This Sector is organized in five divisions: Industry Automation and Drive Technologies, Building Technologies, Industry Solutions, Mobility and OSRAM. The Energy Sector offers products and solutions for generation, transmission and distribution of electrical energy. This Sector is organized in six divisions: Fossil Power Generation, Renewable Energy, Oil & Gas, Energy Service, Power Transmission and Power Distribution. The Healthcare Sector stands for innovative products and complete solutions, as well as service and consulting in healthcare industry. This Sector is organized in three divisions: Imaging & IT, Workflow & Solutions and Diagnostics.

The Imaging & IT Division provides imaging systems for early diagnosis and intervention, as well as for a more effective prevention, namely Magnetic Resonance Imaging Systems (MR), Computer Tomography Systems (CT), Radiography and Angiography Systems, Positron Emission Tomography Systems (PET/CT), Single-Photon Emission Tomography Systems (SPECT and SPECT/CT), Ultrasound Units, among others. These systems are networked with high-performance healthcare IT to optimize processes (such as hospital data systems like Soarian®, image processing systems like Syngo®, and knowledge-based technologies for diagnoses support).

The Workflow & Solutions Division provides complete solutions for fields such as cardiology and oncology and neurology. This Division offers solutions for, e.g. women's health (mammography), urology, surgery and audiology. It also provides turnkey solutions (including national health IT systems, complete solutions for healthcare providers), and consulting. In

addition, Workflow & Solutions is responsible for the Sector's service business and for managing customer relations. The Diagnostics Division covers business with in-vitro diagnostics, including immune diagnostics and molecular analysis. The Division's solutions range from point-of-care applications to automation of large laboratories.

Thus, Siemens Healthcare Sector is the first fully integrated diagnosis company, providing a complete technological portfolio for the entire supply chain in healthcare Siemens IT Solutions and Services, leader in Information Technologies services, works as a transverse business unit.

In Portugal, Siemens SA Healthcare Sector is a market leader in the healthcare area, known for its competence and innovation skills in diagnostic and therapy systems, as well as information technologies and systems' integration. In recent years, Siemens SA Healthcare Sector has promoted the contact and cooperation with key partners in the areas of science and biomedical technology, namely Universities and Research Institutes, establishing a knowledge network and strategic partnerships and thus promoting innovation, research and development in healthcare.

Today, the Healthcare Sector's R & D Group in Portugal is comprised by over 15 elements, working in strategic areas, such as Information Systems, Computational Imaging, Automatic Medical Imaging Analysis, Modeling and Decision Support Tools and Strategic Technology Evaluation. This work has already been demonstrated by one approved patent application, two filed invention disclosures and over ten scientific publications.

Recent Milestones in Portugal

- Breast Pathology Service in Hospital de São João in Porto, Hospital da Luz in Lisbon and Clínica Dr. João Carlos Costa in Viana do Castelo – first total patient focus units, including all necessary technologies for the complete clinical process;

- Hospital da Luz in Lisbon – first hospital in Portugal with SOARIAN®clinical information system, becoming one of the most modern health care installations in Europe;

- Clínica Quadrantes, in Lisbon – in-vitro diagnostics and information technology systems, which together with a PET/CT system, complemented the existing Siemens in-vivo diagnostic systems at the clinic;

- Universidade de Coimbra – 3 Tesla Magnetic Resonance Imaging System exclusively for neuroscience research. This unit is part of the Brain Imaging Network Grid, a scientific cooperation network which integrates the Universities of Coimbra, Aveiro, Porto and Minho.

- R & D Highlights:

    - Patent number DE 10 2007 053 393, System zur automatisierten Erstellung medizinischer Reports;

– F. Soares, P. Andruszkiewicz, M. Freire, P. Cruz e M. Pereira, Self-Similarity Analysis Applied to 2D Breast Cancer Imaging, HPC-Bio 07 - First International Workshop on High Performance Computing Applied to Medical Data and Bioinformatics, Riviera, France (2007);

– J. Martins, C. Granja, A. Mendes e P. Cruz, Gestão do fluxo de trabalho em diagnóstico por imagem: escalonamento baseado em simulação, Informática de Saúde – Boas práticas e novas perspectivas, edições Universidade Fernando Pessoa, Porto (2007);

– F. Soares, M. Freire, M. Pereira, F. Janela, J. Seabra, Towards the Detection of Microcalcifications on Mammograms Through Multifractal Detrended Fluctuation Analysis, 2009 IEEE Pacific Rim Conference on Communications, Computers and Signal Processing, Victoria, B.C., Canada (2009).

Chapter 2

Magnetic Resonance Imaging

2.1 Nuclear magnetic resonance

Physically, MRI is based on the nuclear magnetic resonance (NMR) phenomenon, described first by Felix Bloch and Edward Purcell in 1946, and primarily it was used to study molecular structure and dynamics within the fields of physics and chemistry. Only 30 years ago, Lauterbur and Mansfield, introduced the MRI to obtain clinical images [5].

A rigorous description of the physics of NMR requires some quantum mechanics knowledge, however a classical approach of nuclear system is sufficient to describe most of the relevant phenomena [1, 6].

2.1.1 Nuclear Spins

The spin or intrinsic spin angular momentum is a quantum number and it is one of the properties of elementary particles. Only a determinate number of spins can be found in nature and its physical quantity depends on atomic number and weight of the particles. Nucleus have a spin number, I, if the nucleus has an even number of both protons and neutrons, then both I and S are zero and have a spin angular moment, S, given by Equation 2.1.

$$S = \hbar I \tag{2.1}$$

Where $\hbar$ is the Planck's constant divided by 2π. The magnetic dipole moment for spin, μ, is given by Equation 2.2.

$$\mu = \gamma S \tag{2.2}$$

The constant γ is the gyromagnetic ratio and its value depends on the element.

The hydrogen nucleus is a natural choice for probing the body because it is abundant all over it and, besides that, has an odd atomic weight resulting in a spin equal to 1/2 [6].

For simplicity lets consider the nucleus/protons as a tiny magnet that spins along its axis in a constant velocity, creating a microscopic magnetic moment along that axis. The interactions of the protons spin with the magnetic field produces the torque, causing it to precess about $\vec{B}_0$ as the fixed axis, giving them an unique characteristic that allows for magnetic resonance [5].

2.1.2 B$_0$, the main magnetic field

Considering an arbitrary volume of tissue containing hydrogen atoms (protons) and each with spin vectors with equal magnitude, the spins are normally oriented randomly when there is no magnetic field applied to them, as shown on Figure 2.1a, being the sum of the individual magnetic moments, magnetization M, null (Equation 2.3).

$$M = \sum \mu = 0 \tag{2.3}$$

However, as said before, when a magnetic field is present, and in case of the H^1 protons, there are two possible spin states, corresponding to two energy levels, Equation 2.4, this energy difference is proportional to B$_0$ and the spins precess along/parallel (lower energy) or against/anti-parallel (higher energy) to the field direction, Figure 2.1b [5].

$$\Delta E = \gamma \hbar B_0 \tag{2.4}$$

The ratio between parallel n_+ and anti-parallel n_- oriented spins is not exactly 50:50, the distribution of the two populations is given by the Boltzmann distribution, Equation 2.5.

$$\frac{n_+}{n_-} = e^{-\frac{\Delta E}{kT}} \tag{2.5}$$

Where the k is the Boltzmann's constant and T is the absolute temperature. The excess spin magnets in one direction add up to a macroscopic effect, creating a significant and easily detectable polarization in a preferred orientation, conventionally z, Figure 2.2 [6].

The proton precession frequency ω depends on its gyromagnetic ratio and the strength of the static magnetic field B$_0$. This relationship is described by the Larmor equation, Equation 2.6. The Larmor frequency increases proportionally with the magnetic field B$_0$ [6].

$$\omega_0 = \gamma B_0 \tag{2.6}$$

(a) Spins oriented randomly, $M = 0$.

(b) Spins oriented with the magnetic field, $M \uparrow$.

(c) Magnetization vector.
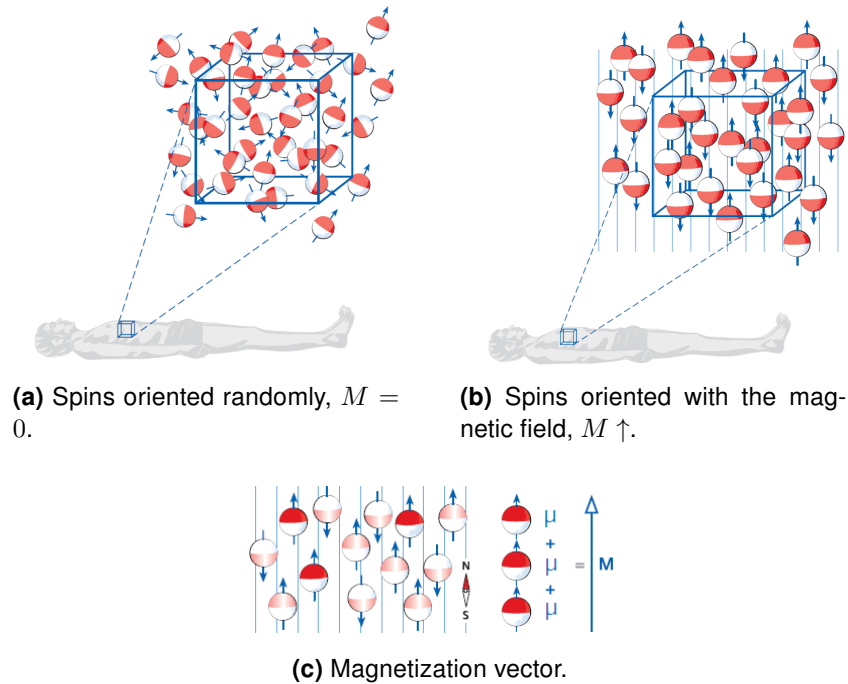
Figure 2.1: Magnetization with and without B_0. [10]

2.1.3 B_1, the excitation radio frequency field

The creation of the magnetic resonance (MR) signal is based on bringing the M vector to the transverse plane (xy-plane), away from the longitudinal plane (z-plane), as shown in Figure 2.3a. This is done by applying a magnetic field B_1, also known as radio frequency (RF) field, that is applied by a short period of time (1-5 ms) and for that reason it is considered a pulse. B_1 rotating on the transverse plane (xy-plane) at frequency ω_0 and in phase with the magnetization M, will resonate with the ensemble of spins in the polarising field B_0.

By the Faraday's law of induction, the precessing magnetization changes the flux Φ in the coil whose axis are on the transverse plane, inducing an electromotive force ϵ, given by Equation 2.7 and illustrated in Figure 2.3b. The course of the voltage over time is the MR signal. The stronger the transverse magnetization, the stronger the MR signal.

$$\epsilon = \frac{\partial \Phi}{\partial t} \tag{2.7}$$

After the end of the RF pulse, this MR signal is called free induction decay (FID). The most simple experiment consists of applying a RF pulse that turns the magnetization to the transverse plan, named 90° RF pulse, for a short time and then obtain the MR signal. Transverse magnetization M_{xy} and the MR signal are shown in Figure 2.3c
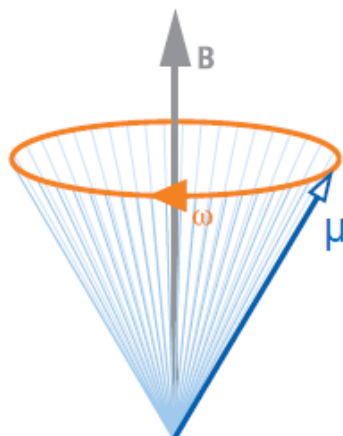
Figure 2.2: Precession. [10]

| (a) | (b) | (c) |
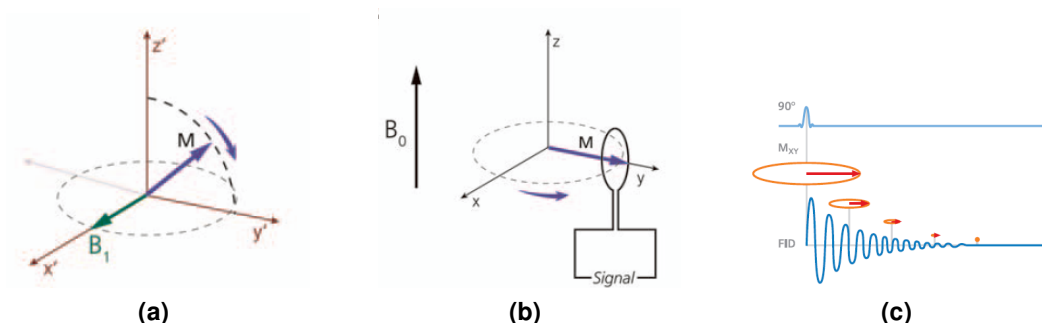
Figure 2.3: Application of B_1 field. (a) Influence of B_1 in the magnetization vector.[11], (b) Reception of the NMR signal.[11], (c) Free induction decay[10].

2.1.4 Relaxation times (T1 and T2)

After being influenced by a RF pulse the spins system return to a state of thermal equilibrium, minimum energy, through a process of relaxation. The restoration of the magnetization on the z-plane (longitudinal), "spin-lattice" decay, is due to the interaction between the spins with their surroundings and it will tend to grow up along the direction of the main magnetic field B_0. T1 is the time constant that characterizes the rate of regrowth along the main magnetic field axis being the magnetization time evolution encountered by solving the Bloch equations, which incorporate both relaxation and precession effects [1, 5]. Considering an state where $M_z(0) = 0$ the subsequent regrowth of M_z is given by Equation 2.8,

$$M_z(t) = M_0(1 - e^{\frac{-t}{T_1}})$$
(2.8)

where M_0 is the initial magnetization.

The recovery of longitudinal magnetization follows an exponential curve. After time T1, longitudinal magnetization has returned to 63% of M_0, Figure 2.4a.

Another type of relaxation is caused by a loss of synchrony of precession among the protons spin. With the application of a RF pulse for a determined time interval the spins synchronize

and stay in phase. When the pulse is turned off the spins desynchronise by the interaction with their neighbours and in random collisions lose energy. This process is named transverse or spin-spin relaxation characterized by the time constant T2. The decay of the magnetizations on the plane perpendicular to main field, xy-plane, can be described by Equation 2.9.

$$M_{xy}(t) = M_{xy}(0)e^{\frac{-t}{T_2}} \tag{2.9}$$

Such as T1, the transverse relaxation is described by an exponential curve. After time T2 the transverse magnetization has lost 63% of its original value, Figure 2.4b. T2 is always faster than T1, that is, the spins dephase occurs faster than the alignment to the magnetic field.

Actually, we could expect that the MR signal (FID) decays with the constant T2. However, the FID decays much more quickly, that is, with a shorter effective time constant $T2^*$, shown in Figure 2.4c. $T2^*$ refers to the effects of additional field inhomogeneities contributing to dephase of the spins. These are mainly local field variations caused by the patient's body as well as technical inhomogeneities of the magnet. It is these static magnetic field differences that add to the fanning of the spins: they dephase more quickly than the T2 relaxation [10, 12].
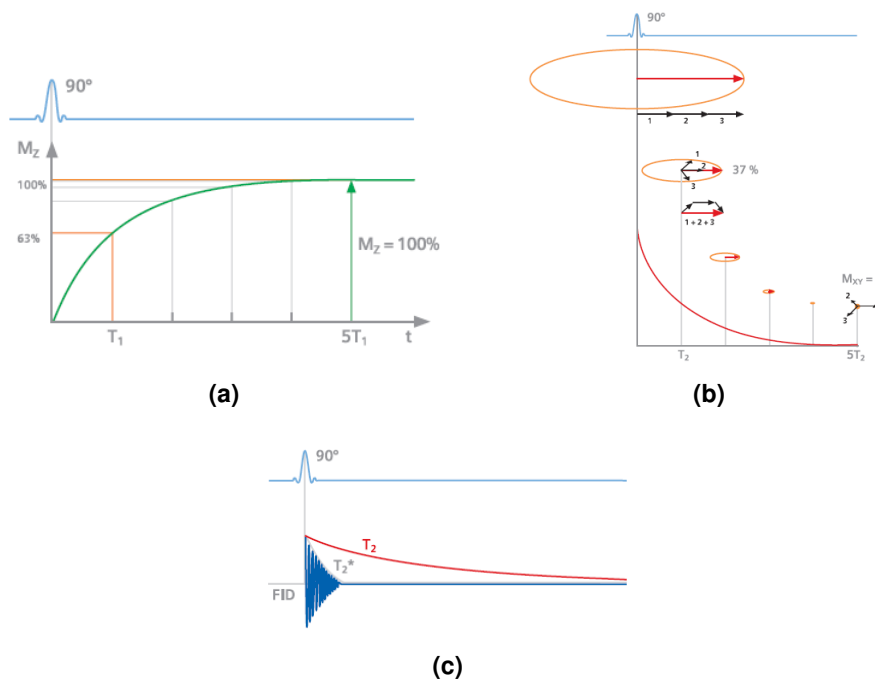
Figure 2.4: Longitudinal (a), transverse (b)and $T2^*$ decay (c). [10]

2.2 Magnetic resonance imaging

Clinically MRI is based on imaging mostly water, abundant in our body, which has hydrogen, whose nucleus is composed by one proton. The MRI signal is generated from this nucleus, hence the use of the word nuclear in NMR [5, 11]. MRI image modality is so powerful because,

beside its resolution, it gives flexibility and sensibility to a broad range of tissue properties such as proton densities, relaxation times, temperature, proton motion, the chemical shifts in the Larmor frequencies and tissues heterogeneities. MRI has also the advantage of being relatively safe, non-invasive and it does not use ionizing radiation, making this technology able to be used in individuals of almost any age. MRI has the capacity to offer anatomical and functional images, that help us understanding much more about the human body [5].

2.2.1 Image contrast

Proton density, T1 and T2 times are intrinsic features of biological tissues and vary from one tissue to the other. Depending on which of these parameters is emphasized/weighted in a MR sequence the resulting image differs in their tissue-tissue contrast [12].

Repetition time (TR) and T1 weighed images

The times of relaxation are different from one tissue to another and that is the key for image contrast. The longitudinal relaxation is intimately related with the repetition time (TR). Repetition time is the length of the relaxation period between two excitation pulses and is therefore crucial for T1 contrast. If the TR is long, more spins have the same direction of the static magnetic field, z-plane, resulting in a large longitudinal magnetization. If a short repetition time, TR A (in Figure 2.5) is used the image contrast is strongly affected by T1. In tissues with short T1 the relaxation is more quick, giving a stronger signal after the next RF pulse. On the other hand, in tissues with a longer T1 the spins' relaxation is slower, the longitudinal relaxation is smaller between excitatory RF pulses. This causes these tissues to emit less signal than the tissues with short T1, appearing dark in the image [5, 12].

If we choose a long TR, typically over 1500ms, TR B in Figure 2.5, all tissues, with long and short T1, have time to completely recover the longitudinal magnetization, for that reason the T1 contrast effect in the image is small, then the image is less T1-weighted.
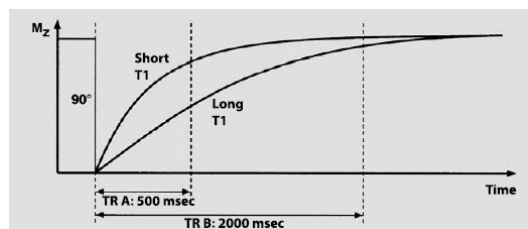
Figure 2.5: Relationship between TR and T1 contrast. [12]

Echo Time (TE) and T2 weighed images

The dephasing of the spins due to the interaction with their neighbours and random collisions led the FID signal to disappear. To put the spins back in phase and make the MR signal

reappear, techniques involving the application of a specific RF pulse sequences or pairs of field gradient pulses must be used. The most common spin echo sequence uses a 90° radio frequency pulse which flips the longitudinal magnetization M_z into the xy-plane, then the transverse magnetization M_{xy} starts to precess with the Larmor frequency. This preparation phase is then followed by an acquisition phase where a 180° radio frequency pulse is applied to refocus the spins, as shown in Figure 2.6a. Echo time (TE) is the interval between application of the excitation pulse (90 ° pulse) and collection of the MR signal. When several 180 degree pulses are following each other in sequence, several spin echoes are generated by a *multi-echo sequence*, Figure 2.6b. The amplitude of the echoes is smaller than that for the FID [10, 11, 12].
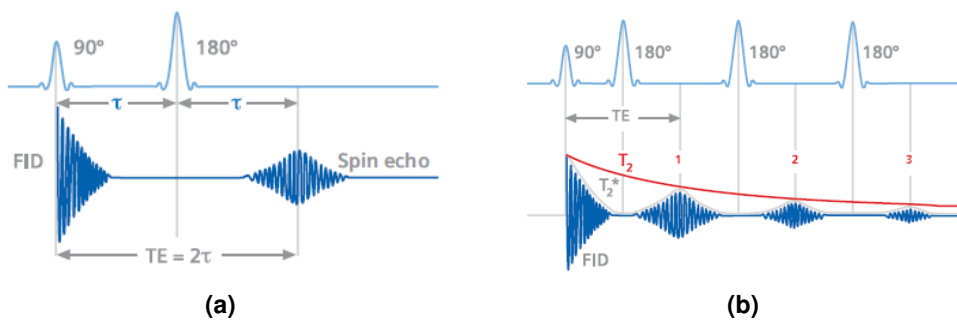
Figure 2.6: Spin echo. Application of a single 180° RF pulse (a), multi-echo sequence (b). [10]

T2 influence on the contrast is determined by the TE. As can be seen in Figure 2.7, if a short TE (TE A) is used the difference between the signal of the two tissues is small, because T2 relaxation has only just started and there has only been little signal decay at the time of echo collection. The resulting image is less T2-weighted. If the TE was longer (TE B) the difference between signals will be bigger, allowing a better contrast between the two tissues, making the resulting image more T2-weighted. A tissue with a short T2 will appear darker in the images while a tissue with a long T2 will appear brighter [10, 12].
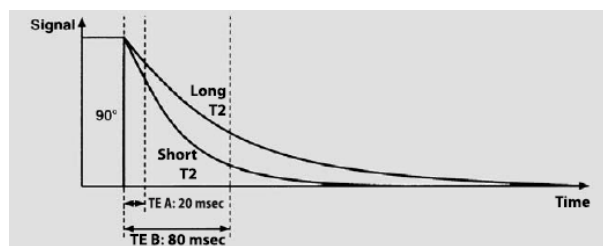
Figure 2.7: Relationship between TE and T2 contrast. [12]

PD weighting

Proton density contrast is a quantitative summary of the number of protons per unit tissue. This is done by adjusting the parameters of the scan, namely TE and TR, in order to minimize the effects of T1 and T2. A higher number of protons, in a given volume, results in a greater

transverse magnetization component and appears brighter on image. PD images have also a higher signal-to-noise ratio due to a long TR that allows the recovery of the longitudinal magnetization while the short TE minimizes the signal decrease due to the decay of transverse magnetization. PD images are useful to evaluated structures with low intensity such as bones, ligaments and tendons [5, 10, 12].

2.2.2 Slice selection and spatial encoding

Linear gradients

In order to produce an image from the NMR signal we must be able to decompose the received signal into components arising from different positions within the sample. This is achieved using magnetic field gradients G to encode different spatial positions r, such that magnetic field becomes a function of position, Equation 2.10,

$$B_i = B_0 + G.r_i \qquad (2.10)$$

where B_i is the magnetic field at location r_i [6, 10, 12].

In the MR scanner the magnetic field gradients have a linear variation and only in one direction. There are used three physical gradients, one in each of the x, y, and z directions. These gradients are required to obtain an image and are used for slice selection, readout/frequency encoding, and phase encoding. The combination of these gradients, RF pulses, data sampling periods, used to acquire an image, is known as a pulse sequence [6, 12].

Considering the magnetic field gradients, the Larmor equation given in Equation 2.6 requires a expanded version, Equation 2.11, where ω_i is the frequency of the proton at position r_i and G is a vector representing the total gradient amplitude and direction.

$$\omega_i = \gamma(B_0 + G.r_i) \qquad (2.11)$$

This means that each proton will resonate at an unique frequency that is related with its exact position within the gradient field.

Slice selection

The first step in encoding the signal in space is the slice selection and its aim is to excite with a RF pulse the spins of a specific plane of imaging, the remaining of the spins in the body should remain along the z-axis, not yielding a signal. For slice selection, a gradient is switched in the z-direction simultaneously to the RF pulse, this gradient is called the slice selection gradient (G_z). The central frequency of the pulse, Equation 2.12, determines the particular location excited by the pulse when the G_z is present, being the different slice position achieved by

changing the central frequency of the pulse [6, 10].

The stimulating RF pulse has a certain bandwidth neighbouring frequency, Equation 2.13, about is center frequency ω_0. In this manner it can stimulate the desired spatial area of the slice thickness (Δz_0, in Figure 2.8a). A steeper gradient produces a thinner slice (Δz_a, Figure 2.8b), whereas, a shallower gradient produces a thicker slice Δz_b, Figure 2.8b [6, 10].

$$\omega_0 = \frac{\omega_1 + \omega_2}{2} \tag{2.12}$$

$$\Delta\omega = |\omega_2 - \omega_1| \tag{2.13}$$
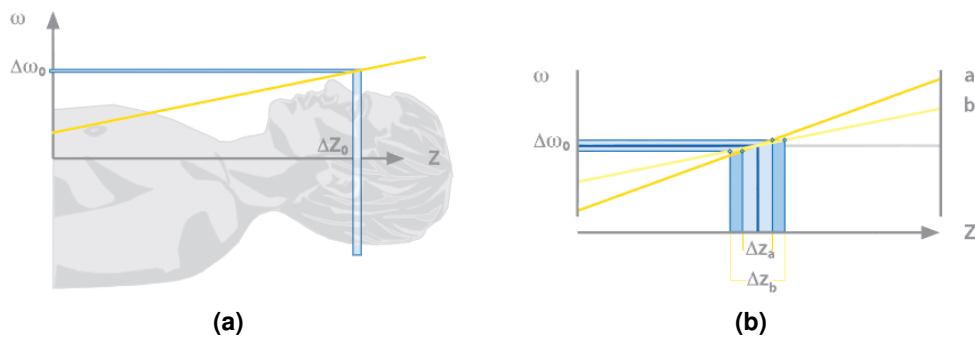
Figure 2.8: Selection of the slice thickness. Relationship of frequency bandwidth (a) and gradient (b) on slice thickness. [10]

Spatial encoding

Once we have chosen the slice position and its thickness, we can proceed to the *spatial encoding* of the MR signal. This is the most difficult task in the generation of the MR image. For this task two more gradients are necessary, the one along the x-axis and the other along y-axis. The spatial encoding comprehends two steps, *frequency encoding* and *phase encoding*.

- **Phase encoding**

For the phase encoding, the gradient is commonly applied in the y-direction and is switched on after the RF pulse that excite the spins along the xy-plane. The phase encoding gradient G_y change the Larmor frequency of the spins depending on its location along the gradient. The spins that experiment a higher magnetic field precess more quickly that the ones that are exposed to a lower magnetic field [12].

After the gradient is turned off, all the spins return to their initial precession rate, however, they are now ahead or behind in phase relative to their previous state. The degree of the phase shifts is dependent of the duration and amplitude of the G_y and the location of the nuclei along the gradient. The phase now varies linearly along the y-axis, so each column within a slice can be identified univocally by its unique phase [12].

- **Frequency encoding**

The next step in spatial encoding is to encode the rows along the x-direction. To accomplish that, a frequency-encoding gradient G_x has to be applied. This gradient varies linearly along the x-axis and where the magnetic field is higher the spins precess faster than the other ones with a lower field applied to them, as result of the variation of the Larmor frequency.

During the reception of the MR signal the G_x is switched on, allowing to receive not only a single frequency, but a whole frequency spectrum comprising several frequencies depending on the magnetic field applied. Each row in a slice is thus characterized by a specific frequency.

2.2.3   Image reconstruction

The fundamental equation when considering the MR signal from an elemental volume of a sample of spin density $\rho(x, y, z)$ is shown in Equation 2.14.

$$\delta S(t) = \rho(x, y, z)e^{-i\phi(x,y,z)} \tag{2.14}$$

Where $\phi(x, y, z)$ is the phase of the elemental volume of sample and the spin term, $\rho(x, y, z)$, is simply the density of mobile water molecules [13].

The phase of the elemental signal, from Equation 2.14, is dictated by the time history of the local magnetic field at position (x, y, z). The phase term is given by Equation 2.15,

$$\phi(x, y, z) = \gamma \int B_z(x, y, z) \, dt \tag{2.15}$$

where $B_z(x, y, z)$ is the net static magnetic field at position (x, y, z).

As we have seen before in the previous section, to generate an image it is necessary to perform a spatial encoding of the net magnetic field. This is accomplished by generating gradients in coil that are able to generate the terms $G_x = dB_z/dx$, $G_y = dB_z/dy$ and $G_z = dB_z/dz$ to modulate the magnetic field [13, 14].

In Equation 2.11, and considering the gradients in x and y directions, the Larmor frequency will vary according to $\omega_x = \gamma B_0 + \gamma G_x x$ and $\omega_y = \gamma B_0 + \gamma G_y y$, respectively. Writing the Larmor equation for an elemental volume of sample at the position (x, y), $\rho(x, y)$, assuming that the a slice in z direction has already been chosen, Equation 2.16.

$$\omega = \gamma B_o + \gamma G_x x + \gamma G_y y \tag{2.16}$$

After the initial RF pulse, t time after the excitation, the signal contribution that is induced in the receiver coil by the precessing elemental volume is a vector whose magnitude is equal to the number density of spins at position (x, y) multiplied by the size of the elemental pixel $dxdy$,

and whose phase is equal to $\phi(x, y, t)$. The contribution to the signal from position (x, y) can therefore be written as shown in Equation 2.17.

$$S(t) = \iint \rho(x, y) e^{-\gamma i (\int G_x(x,y) x \, dt + \int G_y(x,y) y \, dt)} \, dx dy \qquad (2.17)$$

It is convenient to represent the terms $\int G_x(x, y) x \, dt$ and $\int G_y(x, y) y \, dt$ by k_x and k_y, respectively, which represent the Fourier space of the image (as well representing the field gradient history), thus one can rewrite the Equation 2.17 as shown in Equation 2.18.

$$S(k_x, k_y) = \iint \rho(x, y) e^{-\gamma i (k_x x + k_y y)} \, dx dy \qquad (2.18)$$

Using the modern MRI pulse sequences the raw signal is generated by sampling the (k_x, k_y) space line-by-line or in a spiral, by adjusting the gradient parameters when sampling the k-space. The image is then reconstructed applying the inverse Fourier transform (IFT), yielding a map of spin density $\rho(x, y)$ [13, 14]. The steps since the image acquisition to the image reconstruction are shown in Figure 2.9.
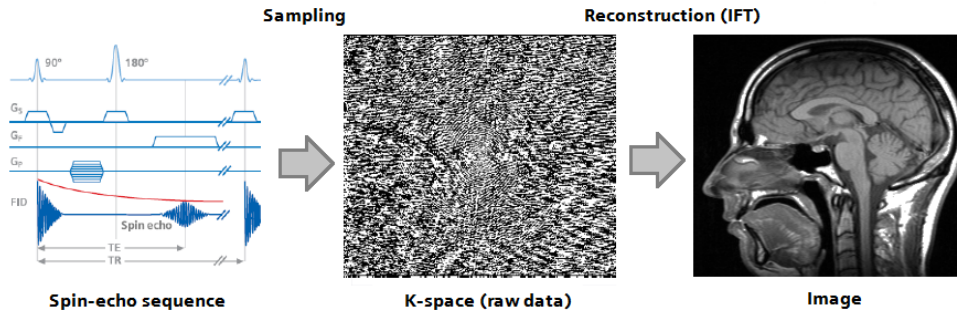
Figure 2.9: From signal to image. [10]

Note that the proton precession is continuous making the MR signal continuous or analog in nature. However, postprocessing techniques such as Fourier transformation require a digital representation of the signal. To produce a digital version, the FID signal is measured or sampled using an analog-to-digital converter (ADC) [6, 10].

Magnetic field strength

The use of high magnetic field stems to the fact that the SNR increases with the field strength, mainly because the signal presents a quadratic growth with B_o strength, as demonstrated by Haacke *et al.* [5], but this is partially offset by the fact that the noise linearly depends on the B_0 at high fields. Other concerns relate to RF heating and RF inhomogeneities. Some advantages and drawbacks of the use of high field are summarized in Table 2.1.

Table 2.1: Advantages and disadvantages of the use of high magnetic fields in MRI.

Advantages	Disadvantages
Higher SNR (linear with field)	Increased specific absorption rate (SAR)
Higher resolution and/or faster imaging	Reduced contrast and/or anatomical coverage
Better T2* contrast, excellent functional MRI	Magnetic fields inhomogeneities
Increase chemical shitf, better spectroscopy	Increased susceptibility artifacts
Excelent time-of-flight angiography	Longer T1 leads to protocol adaptation
	Increase sensitivity to motion

2.3 MR systems and their components

MR device consists of only three main hardware components: the main magnet, the magnetic field gradient system and the radio frequency system. The whole system is represented in Figure 2.10
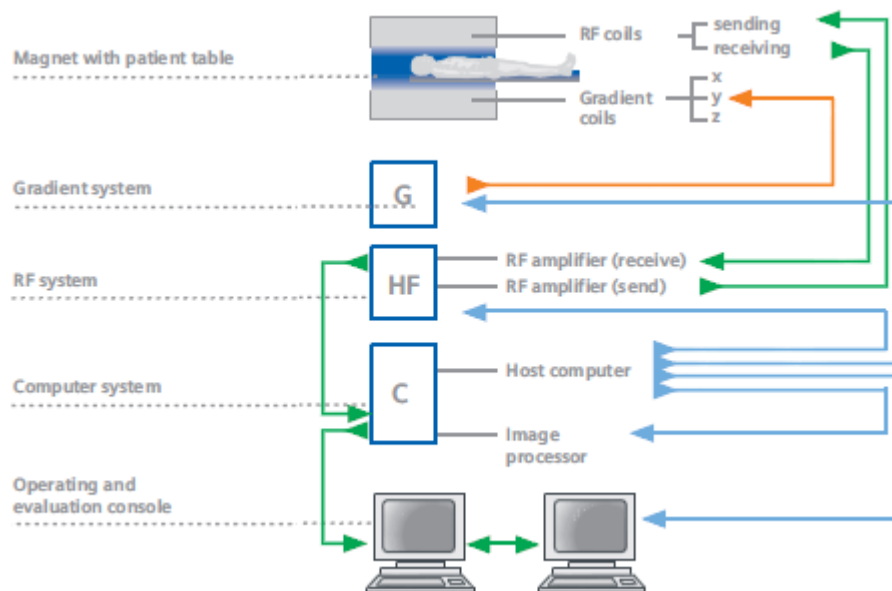
Figure 2.10: MRI system components. [10]

2.3.1 The main magnet

The main magnet is the most important and the most expensive component of the MR system. It aims to create a strong and homogeneous magnetic field. Currently, there are used two types of magnets:

Permanent magnets with a magnetic induction between 0.01 and 0.35 Tesla (T). They are composed by large blocks made from ferromagnetic alloys and these pole pieces are located above and below the patient. This configuration is frequently used with open systems, e.g., the Siemens MAGNETOM C! 0.35T [10].

Super-conducting magnets generally with field strengths between 0.5 and 3.0 Tesla, but it can be higher reaching 7, 9.4 Tesla or even more. Basically, it is an electromagnet, where a strong magnetic field is generated by the electric current flowing in large coils. The conducting wires of the coils are made from a niobium/titanium alloy that is embedded in copper. Liquid helium is used as the coolant, while liquid nitrogen may be used for precooling. This configuration is used in most of the MR systems, e.g,. the Siemens MAGNETOM Symphony 1.5T and Siemens MAGNETOM Trio 3T [10].

2.3.2 The magnetic field gradient system

The MR systems are constituted by three gradient coils, one for each spatial direction (x, y and z). They do not generate a permanent magnetic field, instead they switch on and off several times during the exam.

The gradients generated by these coils are needed for the spatial encoding of the signal, allowing the posterior reconstruction of the image, as explained in the subsections 2.2.2 and 2.2.3. The gradient coils are operated via special power supplies, known as gradient amplifiers, having to switch currents up to 500 ampere at great accuracy and stability. A good gradient coil design aims to produce a linear variation along each principal direction, minimise current requirements and heat deposition by possessing high efficiency, low inductance and low resistance. In order to improve scanning time it is required that the coils obtain the maximum amplitude in the minimum of time. The gradients generally have a maximum amplitude of 20 to 40 milliTesla/meter, this determines the maximal spatial resolution. Their slew rate, corresponding to their switching speed, are 50 to 200 Tesla/meter/seconds for high field and 200 to 400 Tesla/meter/seconds for ultra high fields [10].

2.3.3 The radio frequency system

The radio frequency system goal is to transmit and receive the radio frequency waves and is constituted by the RF antennas (coils), the RF transmission amplifier and the RF receiving amplifier. This system is involved in exciting the nuclei, selecting slices, applying gradients and in signal acquisition.

The main issues to take into account are the SNR, power transmission and field homogeneity. For a transmission coil, the homogeneity of the RF field in the stimulated volume is an important quality criterion.

There are many shapes and sizes for the RF antennas coils. They can be divided in two principal groups: volume coils and surface coils.

Volume coils are located in the cylinder of the machine, homogeneously covering the entire scan volume, possessing a large region of relatively uniform sensitivity. However, in some situations, the noise arising from the whole volume can be significantly greater

than the signal arising from a restricted region of interest (ROI). To overcome this issue we can use the surface coils [10].

Surface coils can be used to improve SNR, since they are placed in direct contact with the zone of interest, therefore possessing a small noise volume, they also have less depth and are more heterogeneous. These coils can improve imaging capacity with higher spatial resolution.

The most common design for volume coils are capable of generating a B_1 field, perpendicular to the static field B_0, is the so called birdcage coil.

Depending on the manufacturers and the type of coil, certain coils can be transmitters, receivers or both [10].

The inhomogeneities related to the transmitting and receiving the RF pulses and the inhomogeneities in the main magnetic field, are the main causes of the distortion addressed in this work. This matter will be developed in the next Chapter.

2.4 Image artifacts

Once we have grasped the concept of spatial encoding and know the MR systems and their components, it will be easy to understand the different kinds of artifacts that degrade the MR images. In this section the most important are enumerated.

The artifacts are structures in the images that do not correspond to the spatial distribution of tissue in the image plane. According to Hendrix [15], the artifacts can be sorted in three types: motion artifacts, physically-caused artifacts and technically-caused artifacts.

2.4.1 Motion artifacts

The most pronounced artifacts in the image acquisition are related to the motion, since the objects movements can produce a blurry and noisy image, mainly in the phase-encode direction. This happens because it occurs an incorrect encoding due to phase mismapping of protons.

Motion artifacts can be divided in two groups: ghosting and smearing.

Ghosting is a result of a quasi periodic motion, for example, breathing movement.

Smearing results from structures with an aperiodic motion, e.g., eye movements.

2.4.2 Physically-caused artifacts

As a result of physically-caused artifacts the images shows relief and contour formations as well as distortions. The main sources for this artifact are the chemical shift[1] and magnetizability[2] (susceptibility).

Relief artifacts in the frequency direction are caused by chemical shift signals from fat and water allocated to different voxels. These incorrect encoding lead to a higher signal or to a invalid signal in the respective frequency encoding direction. In Echo planar images (EPI) this artifact is due to the use of low bandwidth in the phase encoding direction.

Contour artifacts are due to chemical shifts signal from fat and water that may have a phase shift when using gradient echoes (GRE) sequences, causing "phase nulling".

Distortion artifacts are caused by local magnetic fields variations and the intensity of the artifact depends on local conditions, showing an increase or decrease in the signal. The transition areas are more susceptible, such as between tissue and bones or between tissue and air. It can be caused also by ferromagnetic objects on the patient's body or clothing.

The susceptibility of the tissues also play a role in this distortions. The sequences where this artifact is more noticeable are the GRE and EPI sequences and for higher fields.

2.4.3 Technically-caused artifacts

Technically-caused artifacts are related to the technology used for MR, and can be explained by using technical limits, such as the size of the system or the limitation of data volume generated.

Truncation artifacts consists in striped rings caused by abrupt signal transitions in tissue, generated by edge oscillation while sampling the signal.

Warp-around artifacts due to aliasing are caused by the use of a field of view (FOV) smaller than the object to be measured and occur in the phase encoding direction.

Deformation or distortion artifacts are due to loss of linearity of gradient system and occurs when using large FOVs.

RF interferences can be caused by external RF fields due to radios, mobile phones, electronic controls, electrical motors or by Faraday cage deficient isolation.

---

[1]Chemical shift occurs due to differences in resonate frequencies in protons under different chemical environment.

[2]Magnetizability is the ability of the tissue to become magnetic.

Many types of image artifacts can be prevented by carefully instructing the patient and by selecting suitable sequences and parameters. Besides that in some cases it is possible to somehow enhance and correct the images by using post-processing image techniques [15].

Chapter 3

Intensity distortion

3.1 Intensity inhomogeneity

In a healthcare system increasingly dependent on imaging, the automatic extraction of clinical relevant information has become mandatory to efficiently deal with the large amount of data generated by medical imaging techniques. This information is essential for diagnosis, therapy planning and execution, and monitoring the evolution of a disease. The extraction of this information frequently requires a preprocessing step in order to deal with several artifacts that may degrade the results of a subsequent image analysis. One of these artifacts is the intensity inhomogeneity (IIH) [1, 2, 7].

The intensity inhomogeneity, also known as intensity non-uniformity, shading or bias field, is present in several image modalities, but above all in MRI. The IIH is considered to be a slow and smooth intensity variation across the image, resulting in different intensities for the same tissue according to its location. This distortion, in many cases, is hardly noticeable to a human observer but can influence many medical image analysis methods such as segmentation and registration, because most of the automated quantitative methods rely on the assumption that a given tissue has a similar voxel intensities throughout the data, so these methods are highly sensitive to variations on image intensities [3, 7, 16, 17, 18, 19, 20, 21]

In Figure 3.1 are shown simulated images from BrainWeb with and without IIH. In Figure 3.1b it can be observed that the intensity varies for the pixels of the same tissue.

The first publications related to this problem dates back to 1986 [22, 23], since then it was extensively studied. The IIH is mainly caused by unwanted local flip angle variations but the triggers for this variations can be multiple and can be divided into two groups depending on its sources: due to the MRI device and pulse sequences, and due to the imaged object.

Inhomogeneities of the static magnetic field, B_0, bandwidth filtering of the data, eddy currents and specially the RF transmission and reception inhomogeneities are the causes related to the first group. RF coils homogeneity is related to their geometric and physical properties,

(a)   **(b)**
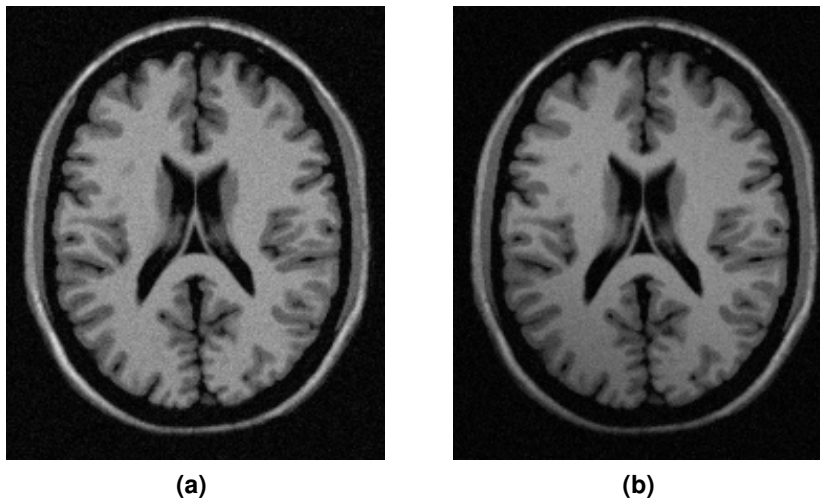
Figure 3.1: Simulated image with (b) and without (a) intensity inhomogeneity.

this may result from sensitivity problems associated with the use of surface coils [24, 25]. However, this artifact is not limited to these type of coils [26, 27].

Both spin echo (SE) or gradient (GRE) pulse sequences can cause this artifact [28, 29]. For SE it appear that some parameters, such as slices interleave, TR or number of echos, have influence in the quality of the image. Eddy currents can be triggered inside the imaged object, when gradients are switched too rapidly and after a large number of echos the refocusing can be altered.

The causes related to the second group are the shape, position and orientation of the object inside the magnet, its specific magnetic permeability and dielectric properties, this last group is more difficult to deal with [30].

The impact of IIH distortion is minor in lower magnetic fields than in higher fields. This is due to the linear increase of the frequency necessary to stimulate the nuclei under higher magnetic field, which enhances the effect of RF standing waves and penetration [31].

3.1.1 Mathematical approach for IIH

For lower magnetic fields, IIHs are assumed as a smooth spatially varying function that alters image intensities. The most simple models assume that IIH is multiplicative or additive. The multiplicative model is considered consistent with inhomogeneous sensitivity of the reception coil, however is less compliant with inhomogeneities due to induced currents and nonuniform excitation [3, 7, 32].

Two sources of noise are described in the signal form, the biological noise, which corresponds to the within tissue inhomogeneity and the scanner noise, that arises from MR devices imperfections. Generally only one of these sources is modelled, and consider that the noise is approximated by a Gaussian distribution, that arises from the scanner and is therefore inde-

pendent from the IIH field [7, 33, 34].

The most common model used to describe the corrupted images is the multiplicative model with additive noise:

$$v(x) = u(x)b(x) + n(x) \tag{3.1}$$

where $v(x)$ is the acquired image, $u(x)$ inhomogeneity-free image (ideal image), $b(x)$ the intensity inhomogeneity field (bias field), and $n(x)$ the noise.

Another model, Equation 3.2, that is used considers only biological noise, which is scaled by the bias field so that the SNR is preserved.

$$v(x) = (u(x) + n(x))b(x) \tag{3.2}$$

A third model for MR image formation is based on log-transformed intensities, where the multiplicative model becomes additive.

$$\log v(x) = \log u(x) + \log b(x) + n(x) \tag{3.3}$$

Other authors used more complex algorithms [7], but the majority of the correction methods are based on simple and more reliable correction models 3.1 3.2 and 3.3. However it should be pointed out that these models may not always yield satisfying corrections, for example if the properties of the tissues also vary smoothly across the anatomy, it is not trivial to differentiate these variations from the IIH artifact. If a higher magnetic field is used, the models are found unreliable, because bias field could act not as a smooth function, but as a wave [7, 35].

3.1.2 IIH correction

Now that we have studied the bias behaviour, we must find a method to remove it from our image.

A IIH correction aims to find u knowing v. This results in a undetermined problem, since only $v(x)$ is known, while both $b(x)$ and $u(x)$ have to be computed [3, 7, 32].

IIH corrections have been widely studied and depending on the specific needs numerous methods were developed. The correction could be performed using better acquisition protocols, or correction algorithms to retrospectively correct the MR images, both with the aim of improving subsequent quantitative analysis. The methods of correction can therefore be divided into two groups: prospective and retrospective [3, 7, 8].

Prospective methods

Prospective methods are based on prior knowledge about acquisition parameters and treat intensity inhomogeneity as systematic error of the MRI acquisition process and can be minimized by acquiring additional images of a uniform phantom, by acquiring additional images with different coils, or by devising special imaging sequences.

Phantom Based: The estimation of IIH is obtained by acquiring images of a uniform phantom whose physical properties and geometry are known by scaling and smoothing of the acquired image from the phantom. The coil and sequence properties are the remaining unknown factors. Another strategy consists in acquiring several datasets from the same object with different sequence protocols, so the influence of sequence or coil components is then separately evaluated [3, 7].

The major disadvantage of this technique is the fact of not allowing the correction of patient-induced inhomogeneity. Another disadvantage is related to the temporal and spatial variation of the coil profile that requires frequent acquisitions of the phantom images. The usefulness of this method is limited by the specific imaging conditions and sensitive to input parameters [3, 7].

Multicoil: In MR there are used different coils depending on the imaged object, the surface coils and the volume coils. These coils differ in geometry, which gives them different properties. Surface coils give a good SNR ratio, but bad spatial uniformity, while the volume coils have a worse SNR but better spatial uniformity. These methods require an acquisition and combination of these two coils in order to get free IIH images and better SNR. More detailed description of the methods can be found in [36, 37, 38].

Special sequences: This group of techniques is mainly related with specific acquisitions designs, and therefore, briefly described [7]. As an example, for certain pulse sequences, the spatial distribution of the flip angle can be estimated and used to find the IIH [39].

Retrospective methods

Retrospective methods rely exclusively on the information of the acquired image and sometimes also on some *a priori* knowledge. These methods have the advantage of being relatively general and usually make few assumption about the acquisition process. They also remove patient dependent inhomogeneity, in contrast with the prospective methods that only correct inhomogeneities induced by a MR scanner.

Numerous retrospective methods were developed to solve the IIH problem. To simplify, they can be classified into three main groups.

Filtering methods: Assumes that the IIH is a low-frequency artifact and can be separated from the high-frequency signal of the imaged object by a low-pass filtering. The main difference between filtering methods is the filter type used on the extraction step.

There are two main approaches that have been proposed: homomorphic filtering [40] and homomorphic unsharp masking (HUM) [24]. This last one is considered the most simple and one of the most commonly used methods for IIH correction.

For most of the anatomical structures these methods may result in an overlaping of the anatomy and IIH frequencies. These methods are also affected by other image features, such as edge effects, most present in high contrast images. Some methods have been proposed to minimize these effects [3, 7, 8].

Surface fitting models: Since it is considered that the bias field is slowly varying, it seems reasonable to approximate the IIH by a parametric smooth function. Then, the correction is performed dividing voxel-by-voxel the original image by the computed surfaces. There are two families of basis functions that are considered: the spline and polynomial functions.

The different algorithms using spline basis functions vary in the way the fitting is performed. This fitting can require a single pass or multiple pass [3].

Polynomial basis functions also consider a simple pass fitting [41] or a multiple pass fitting [42](Section 4.2.2) to determine the surface's parameters.

These methods are often linked to image segmentation, which leads to frameworks that simultaneously correct the IIH and perform the segmentation [8].

Statistical models: The statistical methods assume that IIH follows a distribution or model the IIH as a random process. They are frequently integrated in segmentation frameworks, because it is taken into account that IIH is a important factor that can distort segmentation results.

Segmentation can be achieved by means of Maximum-Likelihood (ML), Maximum-a-Posteriori Methods (MAP)-based methods or by Fuzzy-C-Means-based (FCM) methods [7, 43].

ML and MAP-based methods label pixels according to probabilities based on intensity distribution of the image. The ML or the MAP criterion may be used to estimate the image intensity probability distribution by parametric models. Finite mixture and more frequently finite Gaussian mixture models are used and modified to incorporate IIH.

Because the Gaussian model is only an approximation of a single tissue probability density, several Gaussians can be used for each main tissue, for example, 3 for white matter and 2 for grey matter in the brain, and much more for minor, less significant tissues. Instead of using image segmentation only to estimate the initial model parameters, the authors in [16, 44] proposed an iterative framework, interleaving segmentation, registration and intensity inhomogeneity correction to improve tissue segmentation, further description can be found in Section 4.2.4.

A hidden Markov random field in frequently incorporated in some correction methods in order to exploit the information about spatial connectedness of neighbouring pixels

belonging to the same class [17, 20]. The method presented by Zhang *et al.* [17] is described in Section 4.2.3.

The FCM segmentation methods cluster data by computing a measure membership, called the fuzzy membership, at each voxel for specified number of classes. Since FCM based methods have difficulties to deal with data corrupted by IIH, there were developed some extensions to these methods, in order to compensate the IIH [33, 45].

The N3 method [32] is different from the other correction algorithms that involves a classification step, but it is also a statistical method. This method will be described in more extensively in Section 4.2.1.

3.2 Comparative studies

Numerous methods with different theoretical underpinnings were proposed to solve the intensity distortion, but few studies have been performed in order to compare these methods.

The evaluation of IIH on real images is not a straightforward matter, because the bias field is unknown. In the majority of the studies, the evaluations are made on simulated brain images with known biases or on brain images acquired only on 1.5T scanners and there are few specific sequences analysed [7, 9].

Sled *et al.* [46] compared three IIH correction algorithms, the expectation maximization (EM) [47], the white matter (WM) method [48] and the N3 algorithm, using simulated T1, T2 and PD weighed data. The WM method performed better than the other two, for T1-weighted volumes, probably due to the high contrast between WM and the other tissues, characteristic in T1 images . The EM method made excessively large correction, for voxels that fall outside classifier's tissue model, being consistent with that pointed out by Guillemaud and Brady [49]. The N3 method is the most stable for all simulated images in this comparison. Also there was not taken into account the relation between the corrections and the purpose of the images.

In the article written by Velthuizen *et al.* [50] there were evaluated four IIH correction in brain tumor segmentation. A phantom method [51], two low-pass filtering methods [52, 40], and a surface fitting method with reference points selected from white matter [48]. No improvements were found in segmentation after IIH correction and the surface fitting method was considered to be inferior to the others.

A more extensive study is presented by Arnold *et al.* [9], where six algorithms are compared, the N3 [32], HUM [53], eq [54], bfc [34], SPM99 [44], and cma[1] algorithms, using simulated images from BrainWeb. The article evaluated real images using the same subjects and that were scanned with 3D FLASH and 3D Grass sequences, under 1.5T and 3T magnetic fields, also using different scanners. The N3 and the bfc are shown to be superior to the other four. The bfc is better than the N3 for lower bias levels, however none of the methods performs

---

[1]Available in the Nautilos Library from the Center for Morphometric Analysis at the Massachusetts General Hospital.

ideally under all circumstances. The filtering methods, HUM, bfc and cma, were found to exhibit higher frequency structures of brain anatomy. The SPM99 was considered unstable mainly when operating on relatively uniform images.

Other comparisons were made, comparing the fuzzy segmentation method and its adaptive version [33]. In [52, 53] the HUM is compared with variations of this method.

From all the comparisons none of the algorithms proved to be clearly superior to the others, for all kind of images and needs. Their performance varies greatly depending on the image and the very notion of performance is itself questioned [3, 7, 9, 55].

Most of the methods have been comparatively evaluated only once and many evaluation were found to be incomplete. In some comparisons only a few parameters are evaluated and it is not established a relation between them and the real improvements in subsequent image analysis [7].

Chapter 4

Methods

As mentioned before, the IIH is a well studied issue and there were proposed numerous methods to its correction. Taking into account the comparisons already made, it can be stated that it was not found an algorithm that overrides all the others in all situations.

Therefore, it may be useful to evaluate the correction regarding the purpose of the images, in other words, the question is to find which is the parameter of the image that is to be improved and what is the algorithm that produces the better improvement.

In this work we proceed by simulating brain images with different features, correct them with four IIH correction algorithms and evaluate the corrected images, searching for the parameters that have been improved, Figure 4.1.
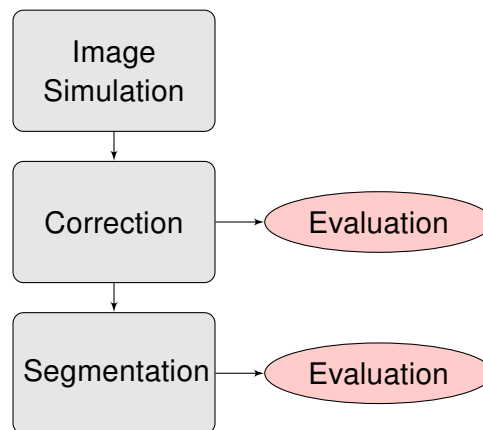
Figure 4.1: Methodology.

4.1   Simulated brain images

Since the analysis of the IIH correction is not a straightforward matter, because the bias field is unknown, it was chosen to use simulated images. The advantage of using a simulated image
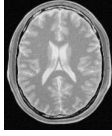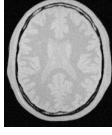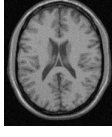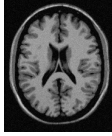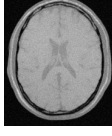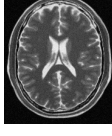
is that the ground truth is known *a priori* in the experiment, in this case, the applied bias field. The other parameters can be independently controlled.

In this work the simulated brain images were obtained using BrainWeb [56], a popular and widely known image simulator that is used for many authors for IIH evaluation [9, 16, 32, 57, 58].

The images were simulated with pulse sequence parameters identical to the parameters usually used to perform scans on patients, with the intrinsic limitation of the options available in BrainWeb.

Six different images were simulated, three T2, two T1 and one PD-weighted. Besides the SE protocol, there were used a fast low angle shot (FLASH) and an inversion recovery (IR) protocol, that are scan techniques less studied in relation to IIH artifact. The simulated images and parameters are shown on Table 4.1.

Table 4.1: Simulated images, noise 3% and inhomogeneity 20%.

Custom designation	Sequence parameters	Simulated images
T2_EPI	Spin echo TR: 2000ms TE: 70ms Flip angle: 90°	
PD_SE	Spin echo TR: 3000ms TE: 17ms Flip angle: 90°	
T1_fl	FLASH TR: 250ms TE: 2.46ms Flip angle: 70°	
T1_IR	Inversion recovery TR: 2300ms TE: 2.28ms Flip angle: 90° IR: 900ms	
T2_fl	Spin echo TR: 27ms TE: 20ms Flip angle: 15°	
T2_SE	Spin echo TR: 6000ms TE: 93ms Flip angle: 90°	

The referred images were simulated several times, varying the noise, the shape of the bias field and level of bias field in order to assess the performance of the correction algorithms when the noise and the bias shape are changed. The volumes have the dimensions 181 x

217 x 60 and 3mm thickness. For rf of 20% (rf will be used to refer the inhomogeneity level) it means that the multiplicative nonuniform field has a range of values of 0.90-1.10 over the brain area. For other rf levels, the field is linearly scaled accordingly (for example, to a range of 0.80-1.20 for a 40% level). The noise in the simulated images has Rayleigh statistics in the background and Rician statistics in the signal regions. The "percent noise" number represents the percent ratio of the standard deviation of the white Gaussian noise versus the signal for a reference tissue. Twelve groups of images were simulated as shown in Table 4.2.

Table 4.2: All simulated images

Noise	Bias field	Inhomogeneity(rf)	Custom designation
3%	A	20%	no3_rf20_A
		40%	no3_rf40_A
		100%	no3_rf2_100_A
	B	20%	no3_rf20_B
		40%	no3_rf40_B
		100%	no3_rf2_100_B
	C	20%	no3_rf20_C
		40%	no3_rf40_C
		100%	no3_rf2_100_C
9%	A	20%	no9_rf20_A
		40%	no9_rf40_A
		100%	no9_rf2_100_A

4.2 Correction algorithms

As mentioned before, there were proposed many algorithms for IIH correction, so it became necessary to select some criteria in order to choose the algorithms to use in this work. The choice was made taking into account, their theoretical backgrounds, some evaluations already done, popularity and their code availability.

4.2.1 N3

The nonuniform intensity normalization algorithm (N3) is a well-known algorithm for IIH correction, is often taken as the gold standard algorithm used to compare other algorithms [59, 60].

The N3 algorithm achieves high performance without requiring a model of tissue classes, is independent of the pulse sequence and insensitive to pathological data and does not require extended scan time nor expertise supervision.

It follows a multiplicative model, Equation 3.1, and in a noise-free case, in which the true intensity u at each voxel location x is independent and identically distributed random variables.

Making a log transformation $\hat{u} = \log u(x)$ the image formation model becomes additive, Equation 4.1.

$$\hat{v}(x) = \hat{u}(x) + \hat{b}(x) \tag{4.1}$$

Considering the distribution of values that $\hat{b}$ takes over a region of interest (ROI) to be a probability distribution of a random variable.

Let U, V, B be the probability densities of $\hat{u}$, $\hat{v}$ and $\hat{b}$ and making the approximation that $\hat{u}$ and $\hat{b}$ are independent or uncorrelated variables, the distribution of their sum is found by convolution as follows, Equation 4.2.

$$V(\hat{v}) = B(\hat{v}) + U(\hat{v}) = \int B(\hat{v} - \hat{b})U(\hat{b}) \, d\hat{b} \tag{4.2}$$

The nonuniformity distribution B can be viewed as blurring the intensity distribution U.

Correction strategy

The IIH can be seen as a blurring that reduces the high frequency components of U, so the task to correct this artifact consists in restoring the frequency content of U.

Since B it is unknown is not clear what frequency components U need to be restored to get from V to the true distribution U.

The bias field $\hat{b}$ is considered to be smooth and slowly varying, the space of possible distributions U corresponding to a given distribution V is small enough that the problem becomes tractable.

In N3, the correction of the IIH is achieved by finding the smooth, slowly varying , multiplicative field that maximizes the frequency content of U. Empirical results show that B is typically unimodal or at least was approximated by a unimodal distribution. These results also suggest that full width at half maximum (FWHM) of the distribution lies between 0.1 and 0.4, for typical brain scans.

However there are two problems when we try to search through all possible fields $\hat{b}$ to find the one that maximizes the frequency content of U. The first is related to the extremely vast search of all 3-D fields $\hat{b}$ and the second is that spectral estimates and related measures, such as entropy, are difficult to compute with sufficient accuracy to detect subtle changes in U.

In this approach is proposed a distribution for U by sharpening the distribution V, and then, an estimation of the smooth field which produces the corresponding distribution for U is made. While searching through the space of all distributions U may seem more tractable than search through the space of all fields $\hat{b}$.

Taking into account the simple form of B distribution and assuming that its distribution is

Gaussian, we need only to search the space of all distribution U corresponding to a Gaussian distributed B having zero means and a given variance. The space of all distribution U is collapsed down to a single dimension, the width (FWHM) of B distribution.

The bias field B is only approximately Gaussian and some of the considered assumptions, as zero noise are violated. To overcome these difficulties there was adopted an iterative approach to estimate U and corresponding $\hat{b}$.

Knowing that any Gaussian distribution can be decomposed into a convolution of narrow Gaussian distributions, the space of all U distributions corresponding to Gaussian distribution B can be searched incrementally by deconvolving narrow Gaussian distributions from subsequent estimates of U. A smooth field $\hat{b}$ is estimated between subsequent estimates of U.

This iteration proceeds until no further changes in $\hat{b}$ or U result from deconvolving narrow Gaussian distributions from V.

Field Estimates

For a measurement $\hat{v}$ at some location x, $\hat{u}$ is estimated using the distribution U and B. Since the choice of x is arbitrary the measurement $\hat{v}$ can be treated as a random sample from the distribution V.

The expected value of $\hat{u}$ given a measure of $\hat{v}$ and after some developments, that can be checked in Sled J. *et al.* [32], a Gaussian kernel is used in place of the actual distribution of B, Equation 4.3.

$$E[\hat{u}|\hat{v}] = \frac{\int_{-\infty}^{+\infty} \hat{u}B(\hat{v}-\hat{u})U(\hat{u})\,\mathrm{d}\hat{u}}{\int_{-\infty}^{+\infty} B(\hat{v}-\hat{u})U(\hat{u})\,\mathrm{d}\hat{v}} \tag{4.3}$$

When the Gaussian kernel is used in place of the actual distribution B.

An estimate of $\hat{b}$ can be obtained using the estimation of $\hat{u}$ from Equation 4.3 as follow, Equation 4.4.

$$\hat{b}_e = E[\hat{b}|\hat{v}] = \hat{v} - B(\hat{v}-\hat{u})U(\hat{u}) \tag{4.4}$$

The distribution U and Gaussian kernel are used to compute, from Equation 4.4, the mapping which maps measured intensities $\hat{v}$ to estimate $\hat{b}_e$. Where $\hat{b}_e$ is an estimate on $\hat{b}$ at location x based on the single measurement of $\hat{v}$ at x. This estimation should be smoothed by the operator S to produce the estimate $\hat{f}_s$ based on all of the measurements in a neighbourhood of x.

Finally given the distribution B and the measured distribution of intensities V, the distribution U can be estimated using a deconvolution filter as follows:

$$\tilde{G} = \frac{\tilde{B}^*}{|\tilde{B}| + Z^2} \qquad (4.5)$$

$$\tilde{U} \approx \tilde{G}\tilde{V} \qquad (4.6)$$

where $*$ denotes complex conjugate, $\tilde{B}$ is the Fourier transform of B, and Z is a constant term to limit the magnitude of $\tilde{G}$. This estimate of U is then used to estimate a corresponding field $\hat{b}$.

Implementation details

The N3 algorithm was implemented for the ITK C++ library by Nicholas J. and James C. [61].

They tried to maintain the minimal difference between this implementation and the original algorithm. The only intended variation was the substitution in the way that the bias is fitted. They used the class "itk::BSplineControlPointImageFilter" instead of the proposed least-square approach for B-spline fitting used to model the bias field in the original algorithm. A much detail description of the implementation can be found in [61].

The parameter that was chosen to vary was the FWHM, since the key contribute of N3 is the usage of a simple Gaussian to model the bias field. There were used the 0.1, 0.15 and 0.3 FWHM.

It was also altered the subsample factor from 2 to 4, this change will in principle increase the algorithm speed and since the bias bias field is considerate to be smooth it should not affect the correction.

The last parameter that was varied was the fitting levels. The used values were 2, 4 and 6. Each successive level doubles the B-spline mesh resolution.

For convenience in this manuscript the methods were named as following:

N3_(FWHM)_(subsample)_(fitting levels)

So it results in the following corrections:

N3_01_2_4 FWHM 0.1, subsample 2 and fitting level 4

N3_03_2_4 FWHM 0.3, subsample 2 and fitting level 4

N3_015_2_2 FWHM 0.15, subsample 2 and fitting level 2

N3_015_2_4 FWHM 0.15, subsample 2 and fitting level 4

N3_015_2_6 FWHM 0.15, subsample 2 and fitting level 6

N3_015_4_4 FWHM 0.15, subsample 4 and fitting level 4

In this work it was not used any mask, with the intention of maintaining the algorithm as automatic as possible. And according to Sled J. *et al.* [32], the mask generation is not crucial and good results can be achieved using a simple Otsu thresholding.

4.2.2 PABIC

The correction method called parametric bias field correction (PABIC) is based on a simplified model of the imaging process, a parametric model of tissue class statistic and polynomial model of the IIH. It assumes that each pixel of the image is associated to a small number of categories with *a prior* known statistics and that the bias field can be modelled by smooth functions, which in this case are Legendre polynomials.

This method intends to determinate the correct class k for each pixel in the data set, i.e., the segmentation of the image data. In the case of a human brain, those classes are usually taken as three: white matter, grey matter and cerebral spinal fluid (CSF).

It considers that the image acquisition techniques such as MRI, the bias IIH is a multiplicative effect, Equation 3.1. In this method the image is logarithmic transformed taking the form, Equation 4.7.

$$\log v(x) - \log b(x) = \log \left(u(x) + \frac{n(x)}{b(x)} \right) \tag{4.7}$$

The method also assumes that $b(x)$ can be brought to a linear combination of m smooth basis functions. The basic functions selected in this case are Legendre polynomials. Therefore the bias field is modelled by $\hat{b}(x,p)$, where p are the coefficients of the Legendre polynomials. The number of coefficients of $p(m)$, depends on l, the maximum degree chosen for Legendre polynomials. The parameter vector p for 3-D case is given by $m = (l+1)((l+2)/2)((l+3/3)$. So, for example, for a Legendre polynomials up to third degree would be required 20 coefficients for p. The choice of the degree of Legendre polynomials largely depends on prior knowledge of the coil and expected type of smoothness of the field. The bias field is determined as follows, Equation 4.8.

$$\hat{b}(x,p) = \sum_{i=0}^{l} \sum_{j=0}^{l-i} \sum_{k=0}^{l-i-j} p_{ijk} P_i(x) P_j(y) P_k(z) \tag{4.8}$$

With P_i denoting a Legendre polynomial of degree i.

The p parameters are estimated directly from data by the iteratively search of the global minimum of an energy function, stepping-out from non-optimal minimum. The energy function is given by the Equation 4.9,

$$e(p) = \sum_i (a_i - c_i(p))^2 \tag{4.9}$$

where a_i is the data and $c_i(p)$ is a model used to parametrise single-class model and is found between Valley functions which is a robust family of M-estimators, Equation 4.10,

$$valley(d) = \frac{d^2}{d^2 + 3\sigma^2} \tag{4.10}$$

showing inflection points at $d \pm \sigma$. The valley functions of each class are multiplied so the total energy function remains and takes the form shown in Equation 4.11.

$$e_{tot\_img}(p) = \sum_{x \in img} \prod_k valley(v(x) - \hat{b}(x, p) - \mu_k) \tag{4.11}$$

Finding the parameter vector p with minimum energy $e(p)$ is a nonlinear optimization problem, independent of the type of bias field and energy function. The method used in PABIC for this minimization is the 1+1 Evolution Strategy algorithm, where each $p(x)$ represents an individual.

Implementation details

It was used the application "MRI Bias Correction" [1], developed by Martin Styner, from the ITK C++ library, more precisely the utility "BiasCorrector"

In order to maintain the algorithm as automatic as possible, it was not provided a mask. The program will calculate a mask by itself, setting zero values on those pixels which have a grey value below 10% of the histogram.

The order of Legendre polynomials determines the accuracy and stability of the calculated bias field, for this case, 3-D images of the human brain, there was used a 3rd degree polynomial.

To calculate the intensity means and standard deviation of the different tissue classes it was used a k-means classifier available in the MATLAB software. The number of classes should be chosen depending on the number of dominant tissues in the image. There were calculated the means and standard deviations with the k-means in order to use PABIC with 2 or 3 classes. Resulting in the following methods:

PABIC_2cl when considering 2 classes (ideally GM and WM)

PABIC_3cl when considering 3 classes (ideally GM, WM and CSF)

The remaining parameters of the algorithm were left as default. For a detailed description of the algorithm and evaluation of the settings of the parameters, please refer to [42, 62].

---

[1]http://www.itk.org/ITK/applications/MRIBiasCorrection.html

4.2.3 HMRF-EM (FSL algorithm)

It was proposed by Zhang *et al.* [17] a novel hidden Markov random field (HMRF) for image segmentation, since the finite mixture (FM) is an histogram based model and does not take into account any spatial information, producing unreliable results, mainly when artifacts such as partial volume effects and IIH are present.

The advantage of the HMRF derives from the way that spatial information is encoded through the mutual influences of neighbouring sites. Unlike other authors, to fit the HMRF model an expectation-maximization is used.

This algorithm assumes that the images are piecewise constant. However the images are often corrupted by IIH, as mentioned before. Therefore there was incorporated the IIH correction algorithm of Guillemaud and Brady [49] in this segmentation method.

The algorithm proposed by Guillemaud and Brady is a modification of Wells *et al.* algorithm for IIH correction [47], introducing a new class "others" with a non-Gaussian probability distribution.

In Wells *et al.*, the bias field $B(b_1, \ldots, b_N)$ is modelled as a multiplicative field of N-dimensional random vector with zero mean Gaussian prior probability density $p(B) = G_{\psi_B}(B)$, where ψ_B is the $N \times N$ covariate matrix. Let the $I = (I_1, \ldots, I_N)$ and $I^* = (I_1^*, \ldots, I_N^*)$ be the observed and the ideal intensities of a given image, respectively.

After a logarithmic transformation, the bias field effect can be treated as an additive artifact. Let y and y^* be the observed and the ideal log-transformed intensities: then $y = y^* + B$. Given the class labels x of the ideal intensity values at pixel i, that follow a Gaussian distribution with parameter $\theta(x_i) = (\mu_{x_i}, \sigma_{x_i})$ and incorporate an outlier class, which is called "other" with uniform distribution, as proposed by Guillemaud and Brady.

With the bias field b_i taken into account and letting $\mathcal{L}_G$ denote the set of labels for Gaussian classes and l_0 the class label for the "other" class. The intensity distribution of the image is still a finite mixture except for an additional non-Gaussian class, Equation 4.12.

$$p(y_i|b_i) = \sum_{j \in \mathcal{L}_G} \{g(y_i - b_i; \theta(j))P(j)\} + \lambda P(l_0) \tag{4.12}$$

where λ is the density of the uniform distribution. Due to the large variance of the uniform distribution, the bias field is only estimated with respect to the Gaussian classes.

The MAP principle is then employed to obtain the optimal estimate of the bias field, given the observed intensity values, Equation 4.13.

$$\hat{B} = \arg max_B p(y|B)p(B) \tag{4.13}$$

A zero-gradient condition is then used to assess this maximum, which leads to Equation 4.14

and 4.15.

$$W_{ij} = \frac{p(y_i|x_i, \beta)p(x_i)}{p(y_i|\beta)} \qquad (4.14)$$

$$b_i = \frac{[FR]_i}{[F\psi^{-1}1]_i}, \text{ with } 1 = (1, 1, ..., 1)^T \qquad (4.15)$$

Where R is the *mean residual* for pixel i

$$R_i = \sum_{j \in \mathcal{L}_G} \frac{W_{ij}(y_i - \mu_j)}{\sigma_j^2} \qquad (4.16)$$

ψ is the mean inverse covariance and F is a low-pass filter. W_{ij} is the posterior probability that pixel i belongs to class j given the bias field estimate.

$$\psi_{ik}^{-1} = \begin{cases} \sum_{j \in \mathcal{L}_G} W_{ij}\sigma_j^{-2} & \text{if } i = k \\ 0 & \text{otherwise} \end{cases} \qquad (4.17)$$

The EM algorithm is applied to Equation 4.15 and 4.16. The E step assumes that the bias field is known and calculates the posterior tissue class probability W_{ij}. In the M step, the bias field B is estimated given the estimated W_{ij} in the E step. Once the bias field is obtained, the original intensity I^* is restored by dividing I by the inverse log of B. Initially, the bias field is assumed to be zero everywhere.

In [47, 49] can be found a more detailed explanation of the IIH correction and the integration of the IIH correction in the HMRF-EM framework [17].

Implementation details

The HMRF-EM method is implemented in the FMRIB Software Library (FSL)[2] in the FAST4 library, used to segment brain images.

Before running the FAST4, the BET, also available on FSL, is used to perform a brain extraction. For simplicity, it was used the default values and the T1_IR image, with 3% noise and 20% inhomogeneity to obtain a mask that was used for brain extraction in the rest of the images.

The parameters that were chosen to change in this correction algorithm were the bias field smoothing (FWHM) and the number of classes used to segment the brain images.

Generally we choose 3 classes (GM, WM and CSF), however it is recommended to use 2 classes in images with poor grey/white contrast. In T2-weighted images it is recommended the use of 4 classes so that non-brain matter is processed correctly. For images with strong

---

[2]http://www.fmrib.ox.ac.uk/fsl/

lesions 4 classes is also recommended, but in this work this is not the case.

The choice of the FWHM is related with the severity of the bias field applied to the image for smoother bias field a higher FWHM is recommended and for a more pronounced bias a lower FWHM.

The other parameters were left as default. For further information about the parameters involved, interested readers must refer to [63].

The variations used were:

FSL_2_20 2 classes and a FWHM of 20mm

FSL_3_10 3 classes and a FWHM of 10mm

FSL_3_20 3 classes and a FWHM of 20mm

FSL_3_30 3 classes and a FWHM of 30mm

FSL_4_20 4 classes and a FWHM of 20mm

For simplicity, this IIH correction algorithm will be referred as "FSL algorithm".

4.2.4 SPM8

In the algorithm proposed by Ashburner and Friston [16] it is used a probabilistic framework that interleaves segmentation, registration and IIH correction. The model is based in a finite Gaussians mixture and is extended to incorporate a smooth intensity variation and non-linear registration with tissue probability maps. After registration, these maps represent the prior probability of different tissue classes being found at each location in an image. Bayes rule is then used to combine these priors with tissues type probabilities derived from voxel intensities to provide the posterior probabilities.

The authors propose a multiplicative model of bias and optimising a function that minimises the entropy of the histogram of the bias corrected intensities. When the bias field is uniformly zero, the entropy is minimised, resulting in a single bin containing all the counts. This problem was pointed out by Arnold *et al.* [9] for the bias field correction using the SPM99 [44], where there was a tendency for the correction to reduce the mean intensity of brain tissue in the corrected image. The constraint that the multiplicative bias should average to unity resulted in a bowl shaped dip in the estimated bias field.

The objective function

In this model it is defined an objective function that accommodates the mixture of Gaussians model (μ and σ), the IIH (β), spatial priors (γ) and deformable spatial priors (α).

The IIH is modelled as a multiplicative effect and the noise is assumed to be due to variations in tissues properties, Equation 4.18.

$$v = (u + n)/b \tag{4.18}$$

The IIH correction is included in the mixture of Gaussians by extra parameters that account smooth variations. The field modelling the variation at element i is denoted by $b_i(\beta)$, where β is a vector of unknown parameters. Intensities from the kth cluster are assumed to be normally distributed with mean $\mu_k/b_i(\beta)$ and variance $(\sigma_k/b_i(\beta))^2$.

A more detailed description of the model parameters and the construction of the objective function can be found in [16].

Optimization

For optimization of the objective function it is used an iterated conditional modes approach. It begins by assigning starting estimates for the parameters and then iterating until a locally optimal solution is found. Each iteration involves alternating between estimating different groups of parameters, while holding the others fixed at their current "best" solution (conditional modes).

The EM is used to update the mixture-classification parameters while holding the bias and deformations fixed at their conditional modes. The bias is estimated while holding the mixture parameters and deformation constant. Since the IIH is assumed to be smooth it can be described by a small number of parameters, making the Levenberg–Marquardt (LM) scheme ideal for this optimization. The deformations of the tissue probability maps are re-estimated while fixing the mixture parameters and bias field. A low-dimensional parametrisation is used for the deformations, so the LM strategy is also applicable here.

Starting estimates for the cluster parameters are randomly assigned. Coefficients for the bias and nonlinear deformations are initially set to zero, but an affine registration using the objective function of D'Agostino *et al.* [64] is used to approximately align with the tissue probability maps.

The model is only specified for brain, as there are no tissue probability maps for non-brain tissue. A exclusion of non-brain pixels is done by fitting a mixture of two Gaussians to the image intensity histogram. In most cases, one Gaussian fits air, and the other fits everything else. A suitable threshold is then determined, based on a 50% probability.

Implementation details

This framework is implemented in the SPM8[3] software, and is used to segment MRI brain images.

---

[3]http://www.fil.ion.ucl.ac.uk/spm/

The default tissue probability maps used were the modified versions of the ICBM Tissue Probabilistic Atlases [4].

The only parameter that was chosen to be changed in the IIH correction algorithm was the FWHM of Gaussian smoothness of bias. If the IIH is very smooth, is recommended to choose a large FWHM. This will prevent the algorithm from trying to model out intensity variation due to different tissue types. Note also that smoother bias fields need fewer parameters to describe them. This means that the algorithm is faster for smoother IIH. It is expected that for rf20 a higher FWHM will work better and for rf100 a lower FWHM.

The remaining parameters were left as default.

The corrections performed were:

SPM_30 FWHM of 30mm

SPM_60 FWHM of 60mm

SPM_90 FWHM of 90mm

For simplicity this IIH corretion algorithm will be referred in this work by "SPM8 algorithm".

4.3 Correction evaluation

The question that we might ask is how to assess the performance of a IIH correction algorithm. Many different evaluation methods have been proposed for IIH correction. The evaluation methods can be divided in two major categories, qualitative and quantitative evaluation. The qualitative evaluation is considered less scientific and is based on subjective visual inspection of the correction results. The quantitative evaluations relies on certain measures that are considered relevant for a given application [7].

4.3.1 Qualitative evaluation

The scatter plots were used in [9] and they intend to compare the values obtained for the bias field against the true bias field. Ideally, the values obtained for the bias field and the true bias field should be the same, forming a linear relationship (a straight line in the graph).

Additionally, the Pearson correlation, Equation 4.19, was calculated in order to measure the strength of the association between the obtained and true bias field. The correlation is a number between -1 (indirect) and +1 (direct), a value near of +1 or -1 have higher strength of the association.

---

[4]http://www.loni.ucla.edu/ICBM/

$$r = \frac{\sum_{x \in \Omega}(B(x) - \mu_B)(B_0(x) - \mu_{B0})}{(N-1)\sigma_B \sigma_{B0}} \tag{4.19}$$

Where B and B_0 the obtained and true bias fields, μ_B and μ_{B0} the means values of the latter variables, σ_B e σ_{B0} the standard deviation, and Ω is the region of interest of size N.

The time taken by each algorithm to correct an image was also evaluated.

4.3.2 Quantitative evaluation

For a more complete and precise evaluation, there were evaluated some parameters on the corrected images. There were used parameters based on intensities variation and based on the bias field inhomogeneity.

In the first group were included the signal-to-noise ratio (SNR), contrast-to-noise ratio (CNR) and coefficient of variation (CV) parameters. Whereas, in the second group was included the root mean square (RMS).

The SNR (4.20) and CNR (4.21) are typical measures of image quality. CNR was performed between the grey matter (GM) and the white matter (GM). If this parameter increases it could mean that the GM and WM are more differentiated and more easily discriminated. The following formulas show how the calculation is done:

$$SNR = \frac{\mu(C)}{\sigma(n)} \tag{4.20}$$

$$CNR(C_1, C_2) = \frac{\mu(C_1) - \mu(C_2)}{\sigma(n)} \tag{4.21}$$

where C (or C_i) is a tissue class, σ is the standard deviation, μ the mean and n the noise. The standard deviation of the noise was calculated using the background values according to the discrete anatomical model available on BrainWeb.

CV is a parameter widely used in IIH analysis [32, 48, 58, 59, 65, 66]. It is assumed that the spatial distribution of a tissue of interest is piecewise constant, therefore, its variance or standard deviation should be reduced if IIH is removed, smaller CV correspond to a more uniform intensity within a tissue class. The CV is an indirect measure of the performance of the correction and is defined as a quotient between standard deviation and the mean of a selected tissue class, in our case GM or WM.

$$CV(C) = \frac{\sigma(C)}{\mu(C)} \tag{4.22}$$

The RMS was used to measure the difference between the bias field obtained with the correction and the true bias field applied to the image.

$$RMS(B_0(x), B(x)) = \sqrt{\frac{1}{N} \sum_{x \in \Omega} (B_0(x) - B(x))^2} \tag{4.23}$$

Where B_0 and B are the true bias field applied artificially and the bias field found by the algorithms, respectively, and Ω is the region of interest of size N.

4.4 Segmentation

As said before, the IIH influences subsequent automatic image analysis. One of the procedures that is affected by this artifact is the segmentation. Actually, it is considered the major difficulty in the segmentation of MR images [21], particularly, in methods that assume that the intensity value of a class is a constant over the image.

It is common to find methods for image segmentation that interleaves segmentation and IIH correction. It is the case of the method for segmentation used in this work. As mentioned before, the HMRF-EM method include the IIH correction algorithm proposed by [49].

In HMRF-EM method, the segmentation is treated as a statistical model-based problem with 3 steps: model selection, model fitting and classification. The HMRF-EM enables an adaptive and reliable automatic segmentation [17]. The HMRF-EM is implemented in the FAST4 software that comes with the FSL.

Before the segmentation, there was applied the same mask that was used before in the FSL IIH correction step using the HMRF-EM framework, in the corrected images from N3, PABIC and SMP8.

All images are segmented using 3 classes, with the default parameters and no additional IIH correction.

4.4.1 Segmentation evaluation

The segmentation accuracy indirectly reflects the effects of IIH correction. Since IIH correction aims to improve the segmentation, some parameters related to the segmentation should be also improved.

The resulting images from the segmentation, performed by the FAST4, were visually evaluated to confirm if the segmentation fail to segment the images, verifying if the WM and GM were clearly visible and discriminated.

A more scientific analysis was performed, calculating the Dice coefficient, sensitivity and specificity.

Dice coefficient, Equation 4.24, is used by some authors [16, 40] in IIH correction analysis and is used to compare the similarity between sample sets, in this case, between the obtained

segmentation and the gold standard segmentation.

$$Dice(S_1, S_2) = \frac{2|S_1 \cap S_2|}{|S_1| + |S_2|} \tag{4.24}$$

Where the S_1 and S_2 sets are, respectively, the obtained and the gold standard segmentations of a given tissue.

In this work it has been used a discrete anatomical model, available in BrainWeb as gold standard segmentation.

Sensitivity, Equation 4.25, is intended to evaluate the ability of the segmentation to correctly classify the tissues, and it gives the probability of deciding if a tissue was well classified, when it belongs to that class.

$$sensitivity = \frac{TP}{TP + FN} \tag{4.25}$$

Where TP is true positives and FN is false negatives.

The sensitivity, by itself, does not give us if the other tissues were well classified, for that it is necessary to calculate the specificity. The specificity, Equation 4.26, intends to evaluate the ability of the segmentation to correctly exclude the tissues that do not belong to a given class. So it gives the probability of deciding if the tissue in question was excluded of a class, when it actually does not belong to it.

$$specificity = \frac{TN}{TN + FP} \tag{4.26}$$

Where TN is true negatives and FP is false positives.

After obtaining the specificity and the sensitivity, a receiver operator characteristic (ROC) space was built for each image with the four correcting algorithms. All evaluation parameters were calculated for grey matter and white matter.

In order to evaluate the significance of changes in the Dice coefficients, in relation to the IIH correction method, an ANOVA of repeated measures was performed. The multiple comparisons were made using contrasts and having the uncorrected image as reference. All analysis were performed on SPSS software.

Chapter 5

Results

5.1 Correction algorithms

It was observed when looking at the images with 3% noise that the performance of the algorithms is somehow constant for the images that only vary the morphology of the bias field, keeping the other features, noise and inhomogeneity level. As an example it can be observed in Figure 5.1 the dependence of the CNR parameter with the correction methods. This happens for all parameters, with few exceptions that will be pointed out when convenient. For 9% noise, Figure 5.1d, it was found a different behaviour in the correction, so it was treated separately from 3% noise images.

Some graphics of evaluation parameters of image quality are shown here. The respective tables and additional tables must be consulted in Appendix A and B.
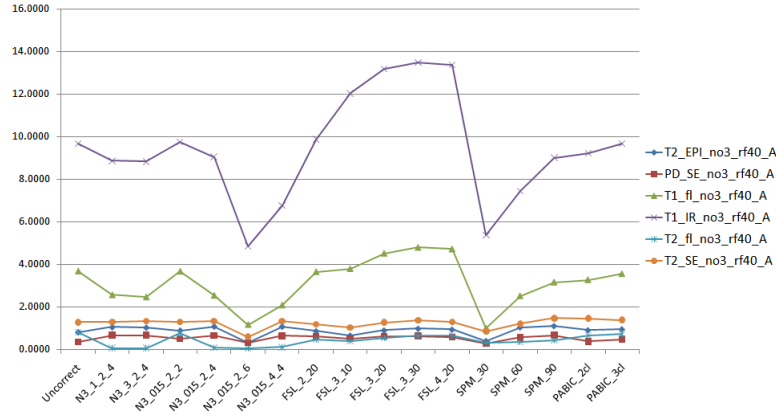
(a) Noise 3%, field A
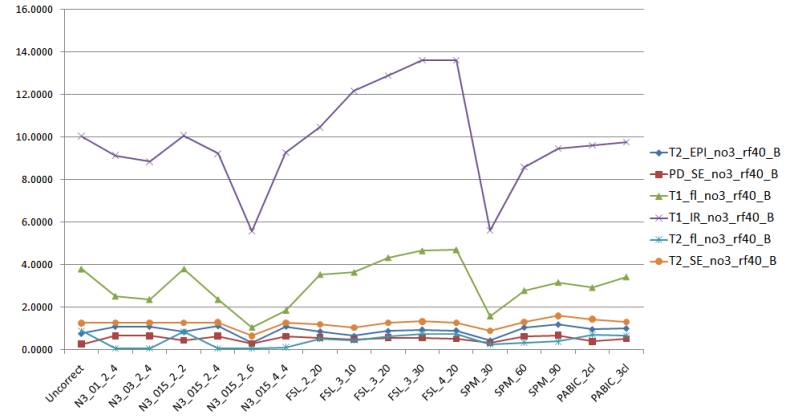
(b) Noise 3%, field B
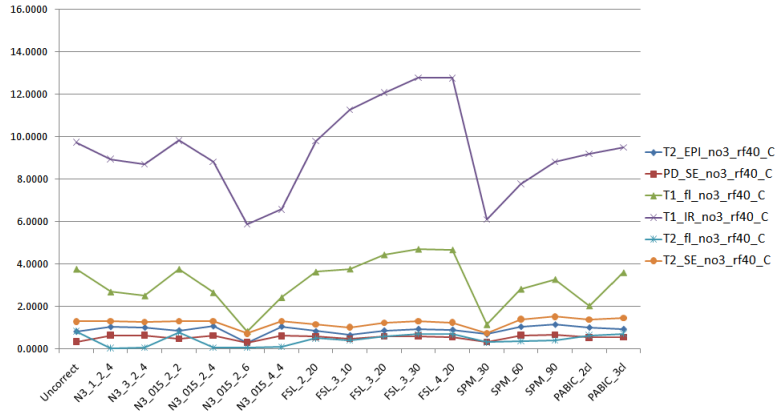
(c) Noise 3%, field C
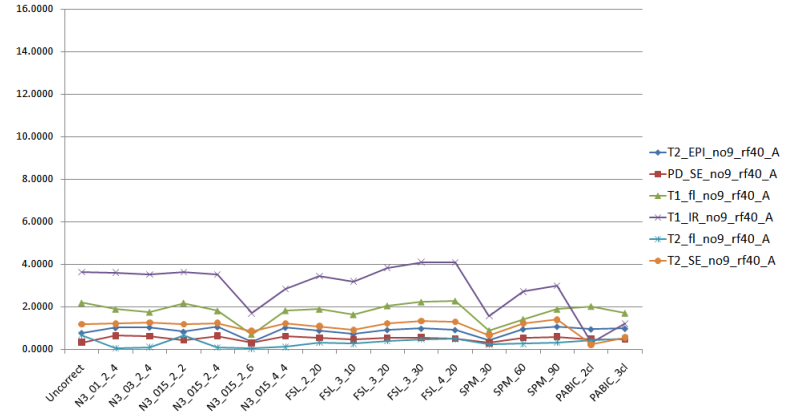
(d) Noise 9%, field A

Figure 5.1: Comparison between CNR values for diferent bias fields with 40% inhomogeneity and 3% noise.

5.1.1   Signal-to-noise ratio

3% Noise

Observing the Figure 5.2 and 5.4, that in some cases the SNR is improved, particularly for higher rf levels, Figure 5.2c and 5.4c.

For N3 algorithm it can be said that the N3_015_2_2 is the correction that improves more the SNR for all images, for both GM and WM. The one that performs worse in N3 algorithm is the N3_015_2_6. The N3 and the PABIC are the algorithms that perform better when correcting T2_SE images, specially for lower bias levels.

It can be observed in Figure 5.2 that the results for SNR using the PABIC are generally better using 2 classes, however the values for the two tests of PABIC vary much depending on the number of classes chosen. The use of 3 classes appears to substantially degrade the SNR.

On SPM8, better results are achieved when using higher FWHM.

In the FSL algorithm the more noticeable improvements are observed in T2-weighted images. The values encountered in FSL are in general greater than the ones found in the rest of the methods and for the same image the results do not vary much, making the algorithm less dependent on the parameters, therefore, considered the most stable.

9% Noise

Observing the Figures 5.3 and 5.5, it can be said that for the N3 algorithm the best results for SNR are encountered when using N3_3_2_4 and N3_015_2_2 methods.

The PABIC fails to increase the SNR for GM and WM, whereas the FSL increase the SNR in almost every images, using any of its parameters.

As it happens in 3% noise image the SPM8 usually performs better with higher FWHM, and for higher rf's.
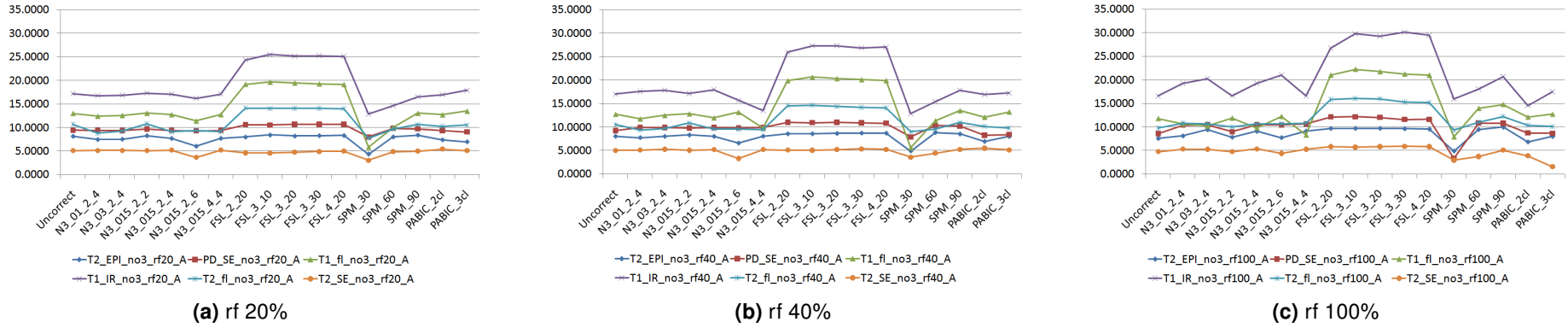
Figure 5.2: SNR for GM in images with 3% noise and the bias field A with various bias levels.
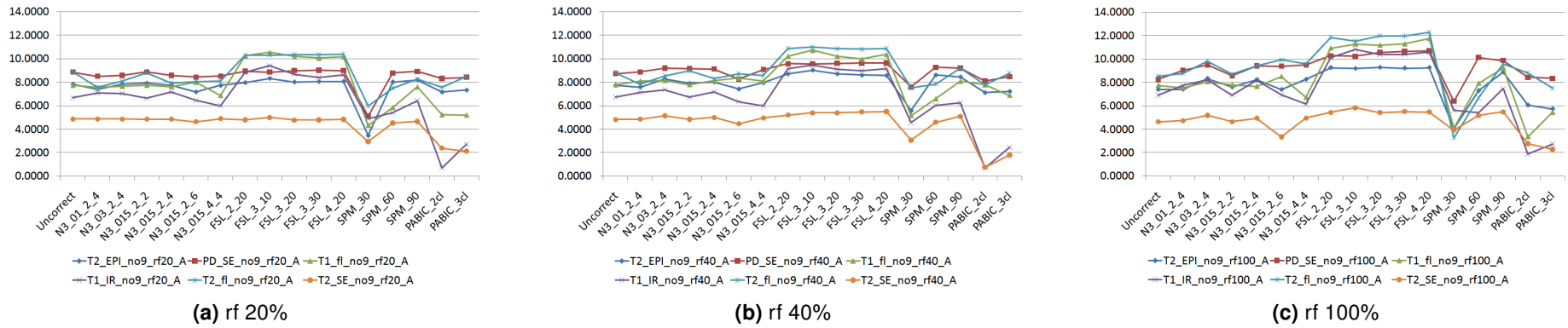
Figure 5.3: SNR for GM in images with 9% noise and the bias field A with various bias levels.
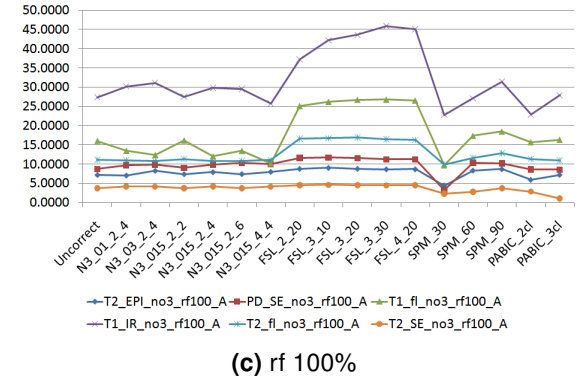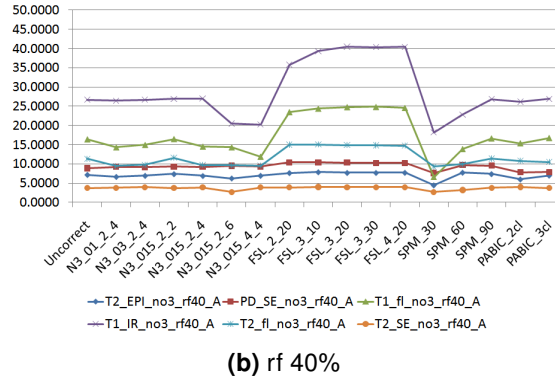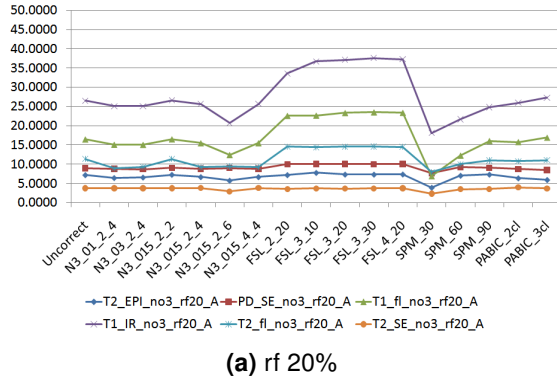
Figure 5.4: SNR for WM in images with 3% noise and the bias field A with various bias levels.
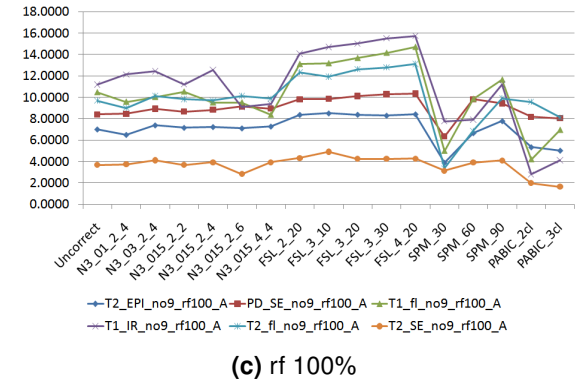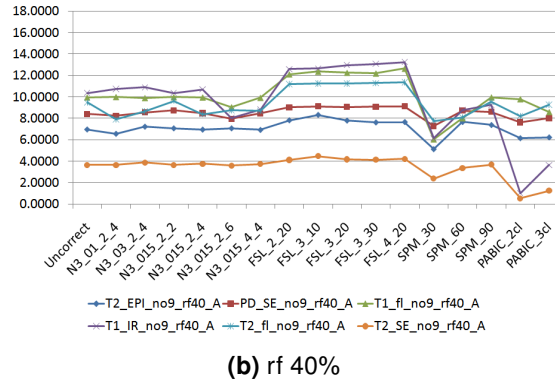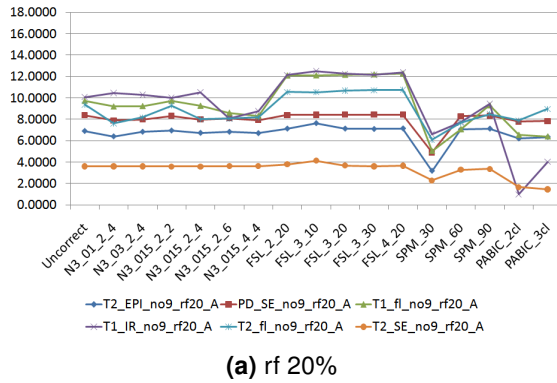
Figure 5.5: SNR for WM in images with 9% noise and the bias field A with various bias levels.

5.1.2 Contrast-to-noise ratio

3% noise

Looking at the graph shown in Figure 5.6, the best CNR for T1-weighted images is achieved using the FSL_3_30 and FSL_4_20. Higher FWHM in FSL seems to work as well as the use of 3 or 4 classes. For all the other algorithms lower values for CNR are obtained, and for some cases even lower that the uncorrected image.

For the T2_fl images none of the algorithms succeed to increase the CNR, in SPM8 algorithm the decrease is specially bigger.

In general all algorithms increase the CNR values for images simulated with a SE sequence (T2_EPI, PD_SE and T2_SE images). The SPM_90 correction gives the best results in these images.

Except for N3_015_2_2, the N3 reduces the CNR in the T1-weighed images. The choice of higher fitting levels, reduce the CNR in N3 algorithm.

In PABIC the use of 2 or 3 classes, does not influence much the CNR.

9% noise

As in the 3% noise images, and looking at Figure 5.7 the CNR of T2_fl images decrease with the IIH correction.

The FSL_3_30 and FSL_4_20 continue to be the best algorithms to correct the T1-weighted images. The first is better in images with rf of 20% and 40%. The second for rf of 100%.

The SPM_90 also continues to give the best results for images simulated with a SE sequence.

In PABIC the choice of the number of classes has more influence in the values obtained than in 3% noise images. The choice of the number for the PABIC is crucial when increasing CNR. The choice of the best number of classes to use is not clear.

(a) rf 20% **(b)** rf 40% **(c)** rf 100%
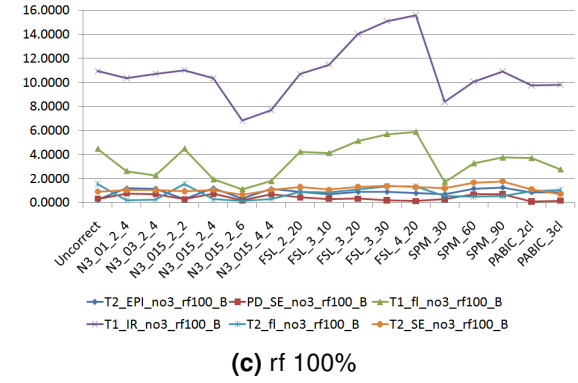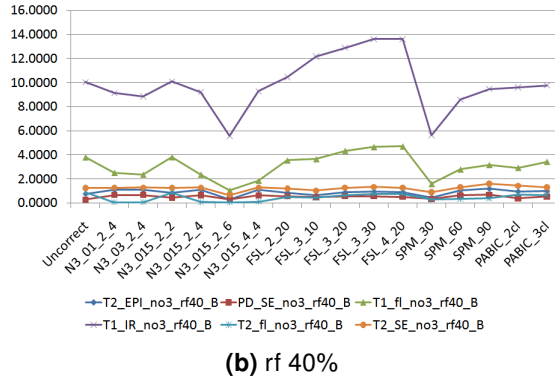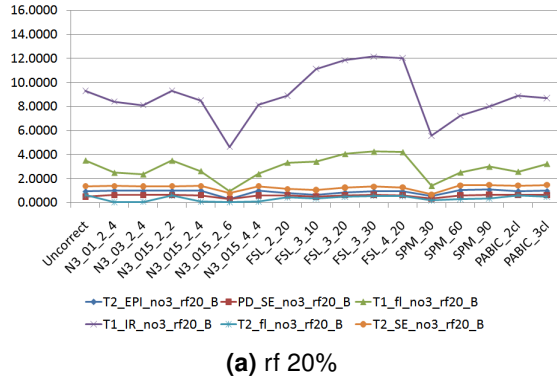
Figure 5.6: CNR between WM and GM in images with 3% noise and the bias field B with various bias levels.

(a) rf 20% **(b)** rf 40% **(c)** rf 100%
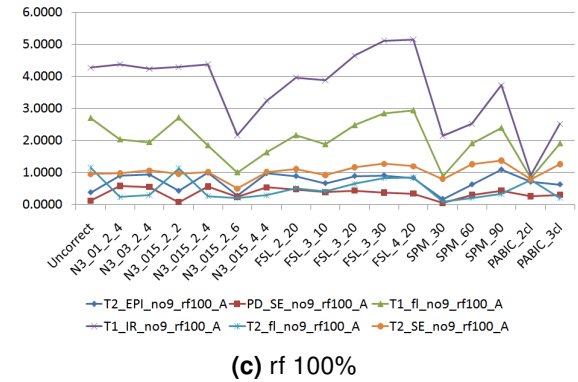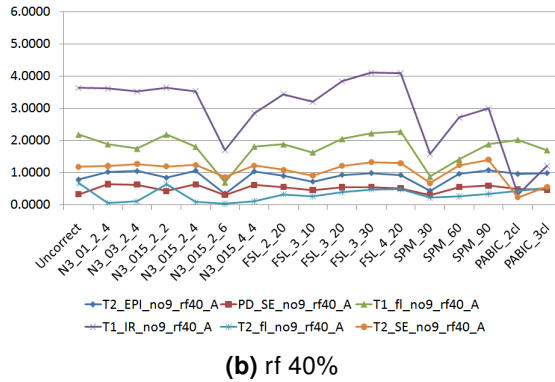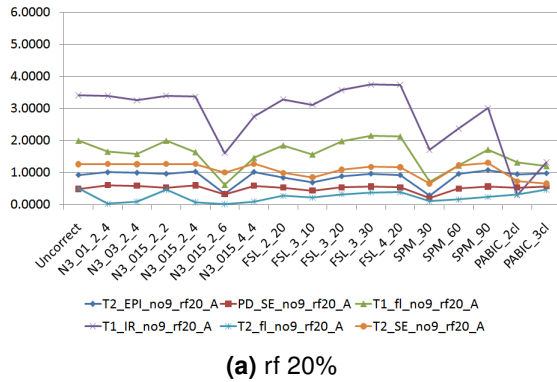
Figure 5.7: CNR between WM and GM in images with 9% noise and the bias field B with various bias levels.

5.1.3 Coefficient of variation

3% noise

As a global view it can be said that all corrections generally improve the CV, for both GM and WM, Figures 5.8 and 5.10.

The FSL_3_10 is clearly the correction that gives better results for almost all images. It is not the best only in T2_fl images with rf40 and rf100.

For SPM8 the best results are usually achieved using a FWHM of 90mm, and both SPM8 and PABIC have some difficulties improving CV in GM in T2_SE, specially for rf20.

PABIC does not show consistency that allow us to choose the ideal parameters, but it globally improves the CV.

In N3 the best CV's are achieved using N3_3_2_4 and N3_015_2_6. The N3_3_2_4 performs better when the image has bigger CNR and SNR (T1-weighted) and the N3_015_2_6 for lower CNR and SNR (T2 and PD-weighted).

For higher rf's the improvements are more noticeable, i.e., the differences between the uncorrected and the corrected images are bigger.

9% noise

For most of the images and corrections it can be observed (Figures 5.9 and 5.11) some improvements in the CV, and such as the 3% noise the improvements are more noticeable for higher rf's.

FSL_3_10 continues to be the algorithm that performs better reducing the CV, for both GM and WM.

In GM images the SPM8 gives better results using higher FWHM.

N3, PABIC and SPM8 have difficulty in lowering the CV in T2_SE images. The FSL and SPM in all cases (except, SPM8 with T2_SE images) improve the CV, so are good choices for lowering the CV without having to pick some special parameters to do it.

(a) rf 20% **(b)** rf 40% **(c)** rf 100%
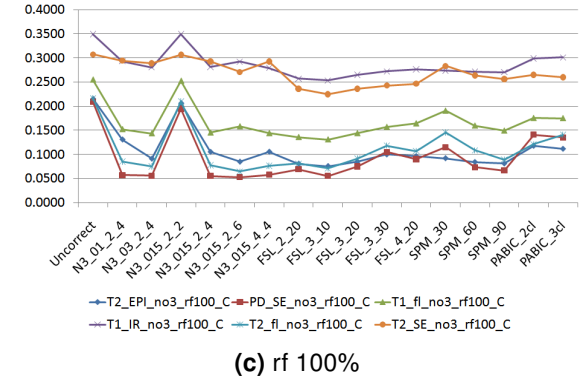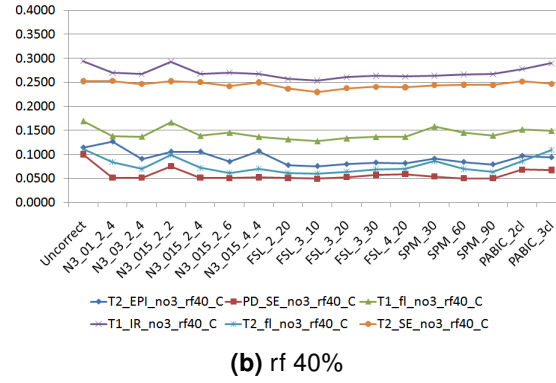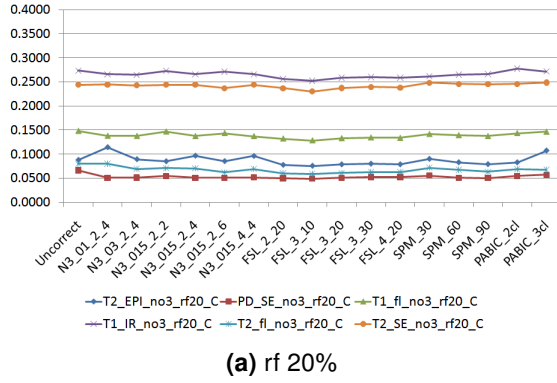
Figure 5.8: CV for GM in images with 3% noise and the bias field C with various bias levels.

(a) rf 20% **(b)** rf 40% **(c)** rf 100%
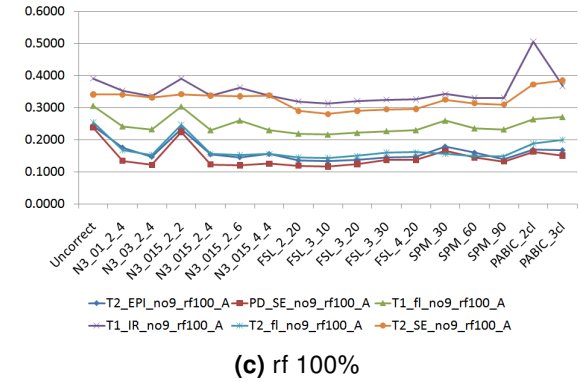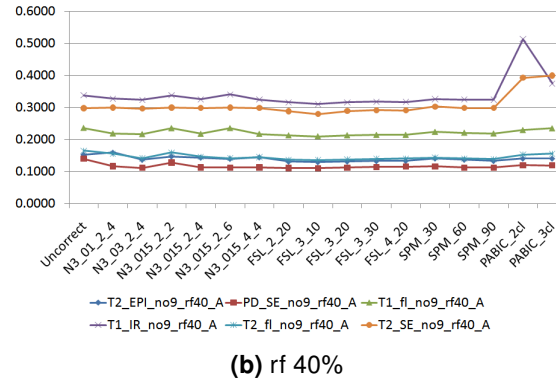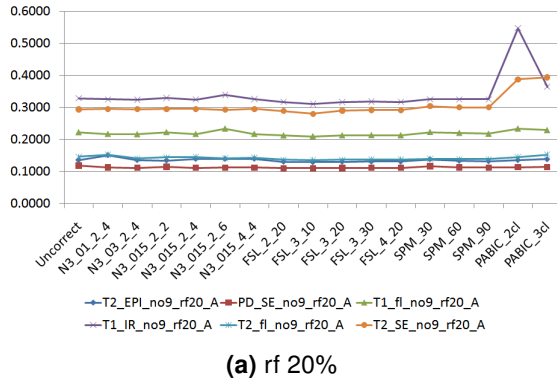
Figure 5.9: CV for GM in images with 9% noise and the bias field A with various bias levels.

(a) rf 20% (b) rf 40% (c) rf 100%
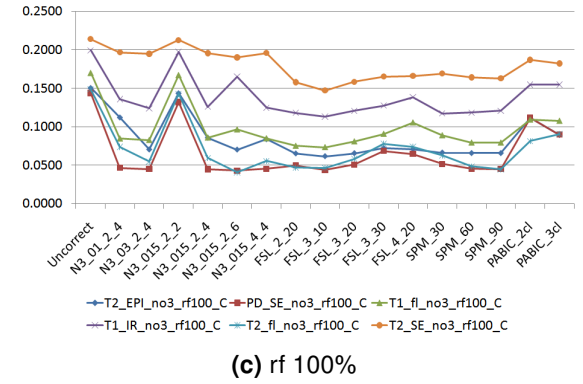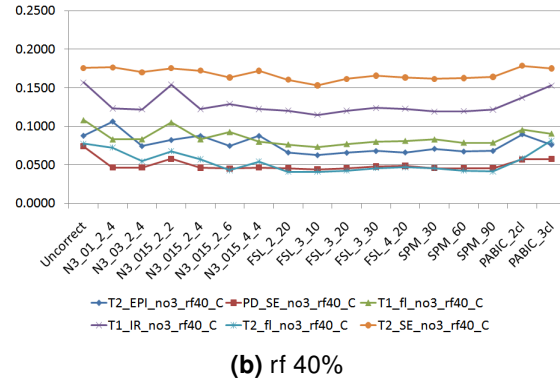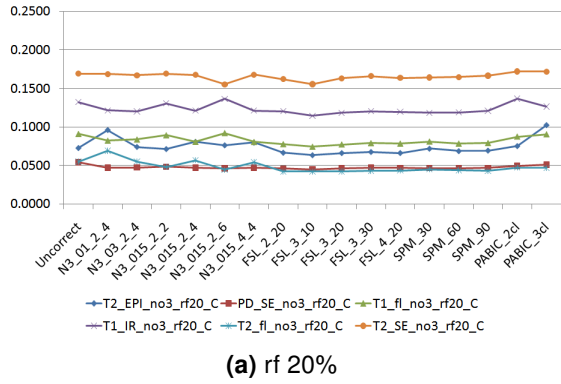
Figure 5.10: CV for WM in images with 3% noise and the bias field C with various bias levels.

(a) rf 20% (b) rf 40% (c) rf 100%
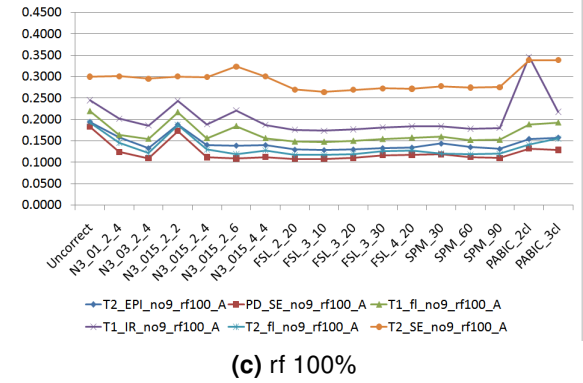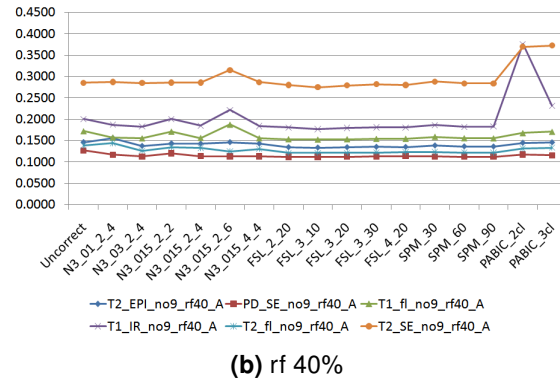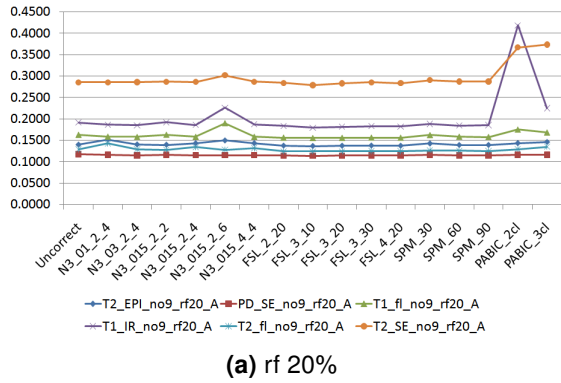
Figure 5.11: CV for WM in images with 9% noise and the bias field A with various bias levels.

5.1.4   Root square mean error

3% noise

For rf20 the best method for PD_SE, T1_fl and T1_IR images is the N3_1_2_4, and for T2_SE, in all rf's, the best method is the N3_3_2_4.

Inside the N3 algorithm there was not observed a set of parameters that gives globally better results. Looking into the Table 5.1 it can be seen the parameters that give better RMS for each case. The use of higher sub-sample parameter (N3_015_2_4), gives for the majority of the images better approximation with the true bias field.

In the SPM8 it can be observed that SPM_90 fits better for rf20, FWHM of 60mm for rf40 and FWHM of 30mm for rf100.

In FSL it is possible to see the same behaviour regarding the FWHM, but it is less noticeable. Inside FSL the values of RMS do not vary much, therefore is considered stable, but in some cases the best RMS found in FSL is much worse than the best RMS possible, obtained in other algorithm.

In PABIC it is not clear the number of classes that should be chosen to obtain a good approximation of the true bias, the values of RMS are very dependent on the choice of the number of classes.

9% noise

For rf20 the N3_015_2_4 performs better for T1_fl, T1_IR and T2_SE, but it does not maintain for other rf's (Table 5.2). The use of sub-sample 4 gives even better results that the ones observed in 3% noise images.

In FSL the FSL_3_30 demonstrate some stability and is a good choice for images with rf20 and most of the rf40. For rf100 the FSL_2_20 appears to be the elected. However, the best results achieved in FSL, in some cases are far from the best RMS achieved specially in N3.

The performance of the SPM8 is quite dependent on the FWHM, the choice of the most adequate FWHM is not a straightforward matter and its dependence with the levels of rf is less evident.

In PABIC the choice of 3 classes generally gives a better approximation to the true bias.

Table 5.1: RMS for images with 3% noise, A bias field and the three rf levels.

	N3_01_2_4	N3_03_2_4	N3_015_2_2	N3_015_2_4	N3_015_2_6	N3_015_4_4	FSL_2_20	FSL_3_10	FSL_3_20	FSL_3_30	FSL_4_20	SPM_30	SPM_60	SPM_90	PABIC_2cl	PABIC_3cl
rf20																
T2_EPI_no3_rf20_A	0.0971	0.045	0.0453	0.0569	0.0898	0.053	0.0512	0.063	0.046	0.0414	0.0407	0.8524	0.0305	0.0591	0.092	0.1974
PD_SE_no3_rf20_A	0.0238	0.0487	0.049	0.038	0.0504	0.0331	0.0484	0.0397	0.0362	0.0358	0.0363	0.1476	0.0691	0.0582	0.0287	0.0297
T1_fl_no3_rf20_A	0.0437	0.1013	0.0428	0.0444	0.1217	0.0436	0.0689	0.0689	0.0487	0.0411	0.0381	1.2809	0.2871	0.0332	0.0217	0.0711
T1_IR_no3_rf20_A	0.026	0.1762	0.0434	0.0472	0.1639	0.0494	0.1025	0.0563	0.0424	0.0379	0.0395	0.3855	0.1843	0.067	0.0438	0.0719
T2_fl_no3_rf20_A	0.0899	0.0646	0.0578	0.0544	0.055	0.0477	0.0467	0.0362	0.0341	0.0338	0.034	0.3673	0.0879	0.021	0.0304	0.0245
T2_SE_no3_rf20_A	0.0418	0.0776	0.038	0.0346	0.0984	0.0381	0.0785	0.1033	0.0717	0.0618	0.0531	0.6497	0.0446	0.0287	0.094	0.0425
rf40																
T2_EPI_no3_rf40_A	0.1082	0.0468	0.0853	0.0705	0.0939	0.0677	0.0737	0.0832	0.0726	0.0714	0.0718	0.5918	0.1506	0.1132	0.1264	0.0624
PD_SE_no3_rf40_A	0.0441	0.0823	0.0989	0.0689	0.0905	0.065	0.0673	0.0686	0.0672	0.0682	0.0692	0.1164	0.163	0.1507	0.093	0.066
T1_fl_no3_rf40_A	0.0535	0.1075	0.0869	0.0643	0.1335	0.0587	0.0819	0.0774	0.0684	0.0667	0.067	1.3121	0.0927	0.1091	0.0819	0.109
T1_IR_no3_rf40_A	0.0533	0.1858	0.0882	0.0926	0.1702	0.0776	0.1109	0.0797	0.0701	0.0674	0.0677	0.3573	0.1025	0.1063	0.0734	0.101
T2_fl_no3_rf40_A	0.0914	0.1034	0.0945	0.0709	0.0839	0.062	0.0664	0.0669	0.066	0.0669	0.0676	0.1284	0.0555	0.0962	0.0549	0.0818
T2_SE_no3_rf40_A	0.0852	0.1292	0.084	0.0642	0.1401	0.0636	0.0883	0.1023	0.0811	0.0784	0.0819	0.3575	0.0965	0.0982	0.152	0.0838
rf100																
T2_EPI_no3_rf100_A	0.2119	0.1566	0.148	0.295	0.1397	0.2383	0.1586	0.1634	0.1588	0.1618	0.1644	0.4635	0.3447	0.383	0.1449	0.2166
PD_SE_no3_rf100_A	0.1121	0.1087	0.1091	0.1434	0.0979	0.2567	0.1562	0.1553	0.1581	0.167	0.1657	1.4684	0.3589	0.349	0.2024	0.192
T1_fl_no3_rf100_A	0.1937	0.1833	0.1648	0.3709	0.1689	0.1689	0.1569	0.1589	0.1557	0.1597	0.1649	0.4317	0.2982	0.3457	0.1974	0.2359
T1_IR_no3_rf100_A	0.1844	0.2161	0.1973	0.3786	0.2577	0.1908	0.1698	0.1618	0.1554	0.1574	0.1624	0.1355	0.2232	0.3426	0.1498	0.2557
T2_fl_no3_rf100_A	0.1599	0.1545	0.1539	0.1908	0.1398	0.2322	0.1549	0.1548	0.1591	0.1679	0.1689	0.1329	0.2589	0.3459	0.2256	0.2041
T2_SE_no3_rf100_A	0.4834	0.4928	0.5018	0.4781	0.535	0.2106	0.1678	0.1799	0.1668	0.1678	0.1727	0.4817	0.1686	0.2135	0.1637	2.7269

Background = best parameters for the algorithm, darker background = best RMS for the image.

Table 5.2: RMS for images with 9% noise, A bias field and the three rf levels.

	N3_01_2_4	N3_03_2_4	N3_015_2_2	N3_015_2_4	N3_015_2_6	N3_015_4_4	FSL_2_20	FSL_3_10	FSL_3_20	FSL_3_30	FSL_4_20	SPM_30	SPM_60	SPM_90	PABIC_2cl	PABIC_3cl
rf20																
T2_EPI_no9_rf20_A	0.0531	0.0307	0.0387	0.0489	0.0373	0.0342	0.0477	0.0612	0.0438	0.039	0.041	1.2255	0.0611	0.0737	0.0835	0.0708
PD_SE_no9_rf20_A	0.019	0.0125	0.0138	0.0255	0.0165	0.024	0.0356	0.0379	0.0356	0.0358	0.0368	0.6937	0.0299	0.0374	0.0423	0.0342
T1_fl_no9_rf20_A	0.031	0.0346	0.0403	0.0612	0.0246	0.0177	0.056	0.0701	0.0474	0.0395	0.0398	0.8269	0.3216	0.0317	0.4648	0.482
T1_IR_no9_rf20_A	0.0234	0.032	0.0233	0.0696	0.035	0.023	0.0851	0.0971	0.0614	0.0484	0.0495	0.4263	0.2445	0.0563	11.4805	1.5349
T2_fl_no9_rf20_A	0.0365	0.0281	0.025	0.0343	0.025	0.0169	0.0358	0.0383	0.0344	0.0338	0.0343	0.4728	0.1688	0.0583	0.1486	0.0572
T2_SE_no9_rf20_A	0.0972	0.0942	0.0966	0.0715	0.0963	0.0284	0.0936	0.1239	0.0682	0.0531	0.0547	0.6566	0.0777	0.0459	1.2719	1.5579
rf40																
T2_EPI_no9_rf40_A	0.0905	0.0391	0.0584	0.1001	0.0562	0.0745	0.0741	0.0839	0.0722	0.0702	0.0722	0.3433	0.1636	0.1394	0.0788	0.0767
PD_SE_no9_rf40_A	0.0351	0.0158	0.0203	0.0343	0.0204	0.0634	0.0669	0.0682	0.0674	0.0688	0.0701	0.0939	0.1159	0.1072	0.0388	0.0409
T1_fl_no9_rf40_A	0.0368	0.0332	0.0315	0.1202	0.0307	0.0343	0.078	0.0887	0.072	0.0676	0.0686	0.5116	0.1533	0.0949	0.0823	0.1083
T1_IR_no9_rf40_A	0.0538	0.075	0.0616	0.1392	0.0509	0.0497	0.0995	0.1086	0.0796	0.0707	0.0718	0.5329	0.1088	0.0636	10.8578	1.8365
T2_fl_no9_rf40_A	0.0741	0.0402	0.0598	0.0499	0.0575	0.0511	0.0666	0.0679	0.0662	0.0669	0.0679	0.1304	0.0807	0.0956	0.0874	0.0784
T2_SE_no9_rf40_A	0.1766	0.1874	0.1927	0.1616	0.2299	0.0745	0.1032	0.1368	0.0898	0.0805	0.0833	0.5614	0.0533	0.1055	6.0615	1.9887
rf100																
T2_EPI_no9_rf100_A	0.2091	0.1972	0.1684	0.3104	0.1684	0.2387	0.1588	0.1637	0.1595	0.163	0.166	0.7016	0.1493	0.3085	0.1651	0.2466
PD_SE_no9_rf100_A	0.1449	0.147	0.1321	0.1607	0.1325	0.2461	0.1563	0.1563	0.1593	0.1663	0.1671	0.171	0.3436	0.3152	0.1895	0.1725
T1_fl_no9_rf100_A	0.18	0.2018	0.1809	0.35	0.1766	0.154	0.1568	0.1624	0.1576	0.1612	0.1654	0.8421	0.1708	0.3136	1.2973	0.3299
T1_IR_no9_rf100_A	0.1592	0.1002	0.1743	0.3781	0.1984	0.1774	0.1645	0.171	0.1586	0.16	0.164	0.2311	0.1956	0.2197	3.3084	1.5266
T2_fl_no9_rf100_A	0.2197	0.1875	0.198	0.217	0.1954	0.215	0.1548	0.1552	0.1582	0.1651	0.1666	1.5825	0.1804	0.2484	0.2032	0.1124
T2_SE_no9_rf100_A	0.4624	0.483	0.5015	0.4473	0.457	0.2058	0.1812	0.204	0.1727	0.1717	0.1779	0.1522	0.2622	0.3091	0.7706	1.1412

Background = best parameters for the algorithm, darker background = best RMS for the image.

5.1.5   Scatter plots and Pearson correlation

To illustrate that the performance of the correction algorithms depends on the image features, in Figure 5.12 there are shown six scatters plots of the true bias *vs.* extracted bias considering the best results for RMS parameter of FSL algorithm for each image with noise of 3% and the bias field A. More scatter plots can be observed in Appendix A.2.

The results of each algorithm applied to a given image are different, as we can see in Figure 5.13, for each algorithm is obtained a different distribution and Pearson correlation values. It is also possible to see that the algorithm performs differently depending on the rf level present in the images.

The PABIC is usually the one that obtains a worse Pearson correlation and an analysis of Figure 5.13, confirms that a less linear and more disperse distribution is presented.

The FSL shows to be in general the one that gives the best relations between the extracted and true bias, although for same cases this relation is placed a bit lower than the perfect correlation (blue line). The obtained Pearson correlation was usually greater than 0.9.

With the SPM8 correction, a good relation between the extracted and bias field is also obtained.

For the images with lower SNR and CNR (PD_SE and T2_SE)the relation between the two fields is usually more linear and less disperse, leading to a higher Pearson correlation.

The obtained bias are, globally, in the range of the applied bias.

5.2   Segmentation evaluation

5.2.1   Dice coefficient

3% noise

The T2_fl images are not considered in this analysis, because the FAST4 segmentation algorithm fails to segment them.

It can be observed that the IIH correction improves the dice coefficient, specially for rf40 and rf100, Table 5.3 and 5.4.

The correction that shows to be more coherent along all the images is the SPM_90.

In the N3 the best parameters were the FWHM of 0.15, with shrink factor of 2 and fitting levels of 6, for the majority of the image types.

Within the FSL algorithm the values of Dice coefficient do not vary much and best results are achieved with the use of FSL_3_30 and FSL_4_20.

In the PABIC is not clear the ideal number of classes to improve the Dice coefficients. However
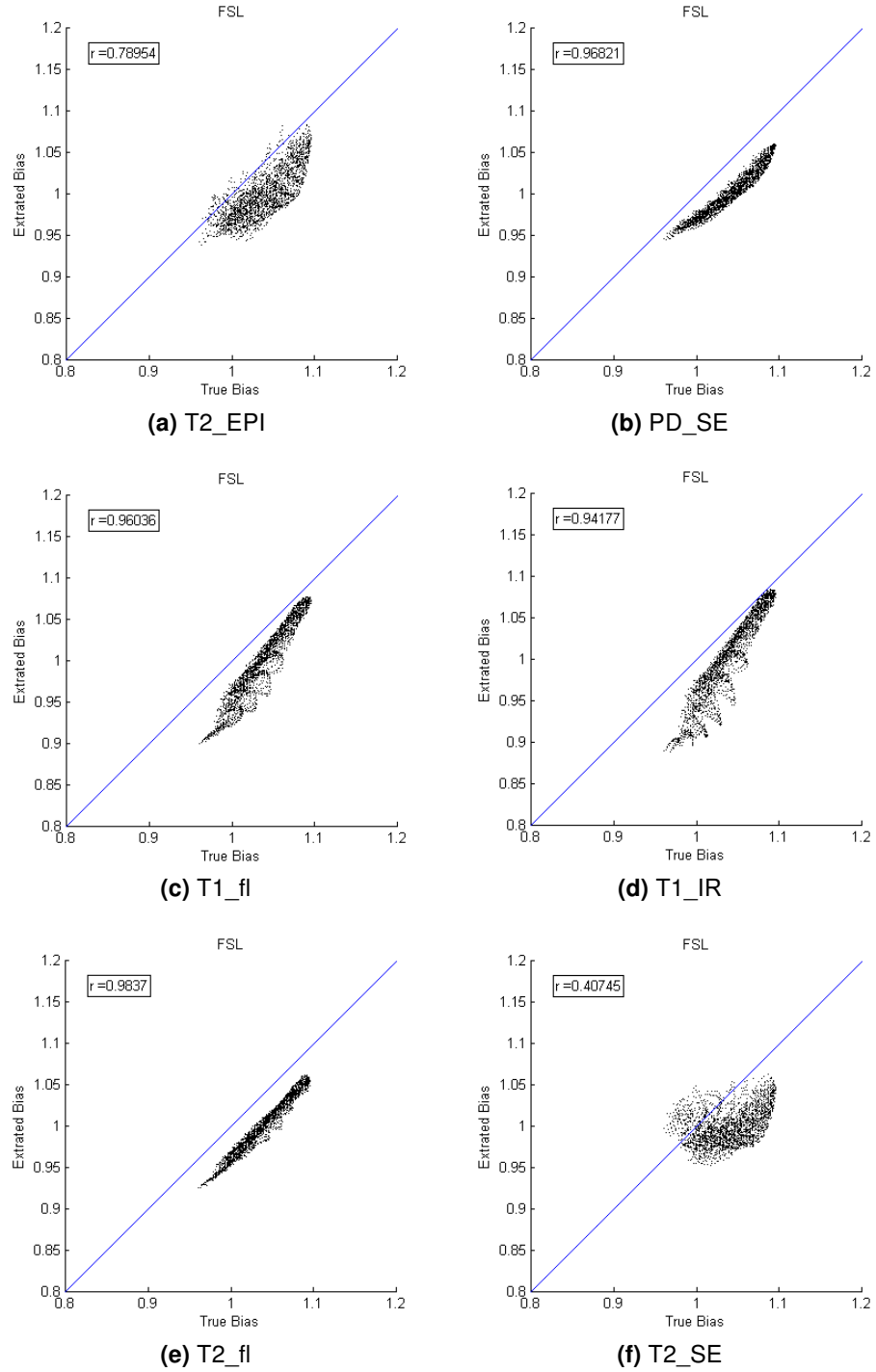
Figure 5.12: Scatter plots relating the extracted bias and the true bias, for the better results of RMS, obtained in FSL for images with 3% noise, rf 20 and B bias field.
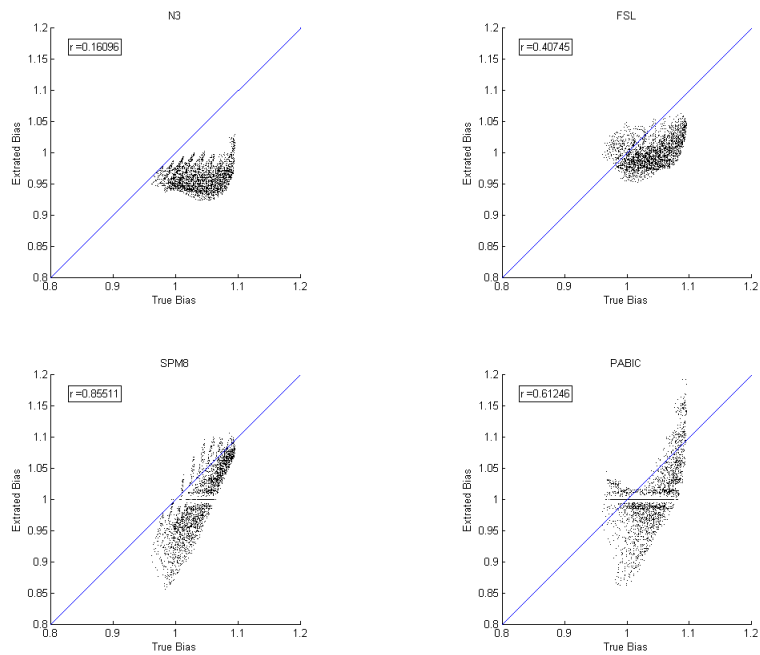
(a) rf20
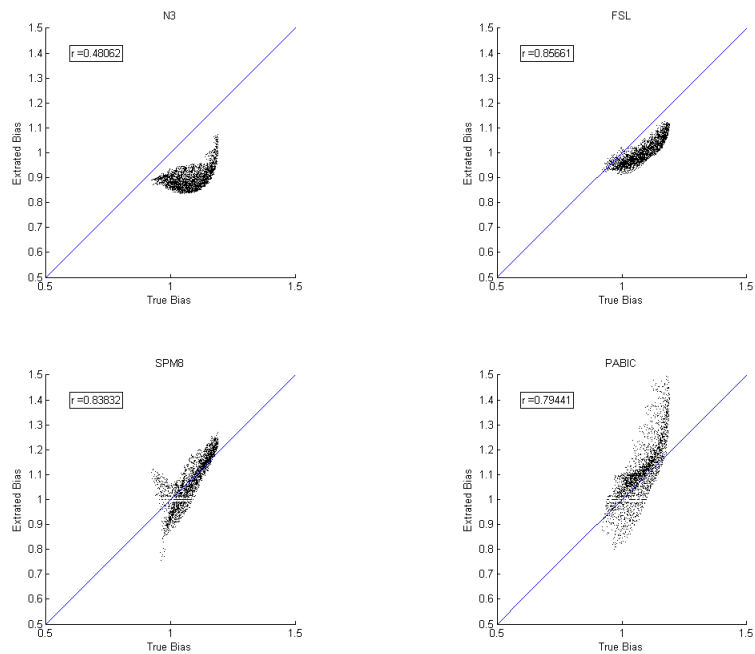
(b) rf40

Figure 5.13: Scatter plots relating the extracted bias and the true bias, for the better results obtained with the four IIH correction algorithms, for T2_SE images, with 3% noise and B bias field.
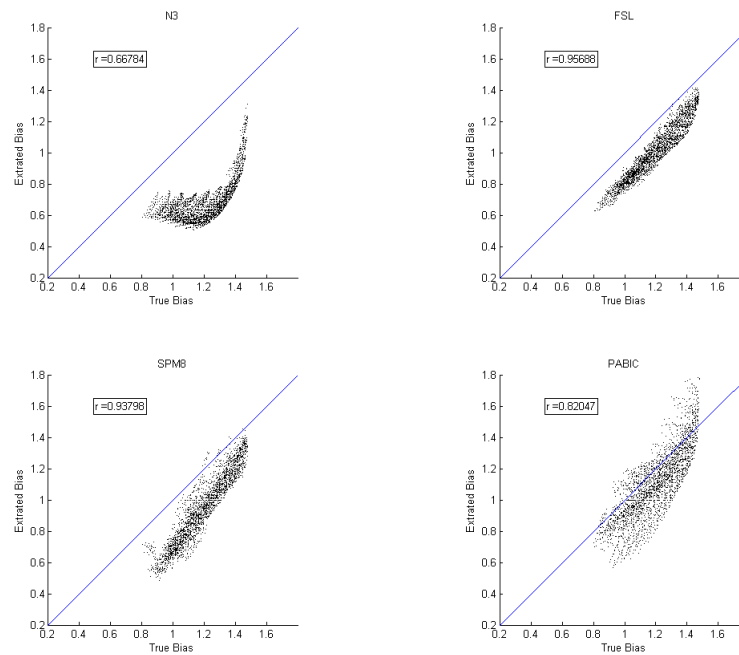
(c) rf100

Figure 5.13: Scatter plots relating the extracted bias and the true bias, for the better results obtained with the four IIH correction algorithms, for T2_SE images, with 3% noise and B bias field.

for PD_SE the used of 3 classes generally gives best results.

T1-weighted images are commonly used for segmentation, because they have good contrast between white matter and gray matter and high resolution in the usual neuroimaging protocols. Therefore they were analysed with more detail.

T1-weighed images   For T1 images it can be observed that the IIH corrections improve the Dice coefficient for most of the cases.

In the N3 algorithm, it is unclear which parameters allow higher Dice coefficients, and it works well for higher rf's. N3 is the algorithm that appears to deal better with images that have high noise levels and/or high rf. For the T1_IR image the best parameters seem to be a FWHM of 0.3, with shrink factor of 2 and fitting levels of 4. For the T1_fl image the parameters are not so clear. A higher fitting level gives a worse segmentation and it was also observed that using a greater shrink factor, e.g. 4, the results do not vary much and the time necessary for correction decreases.

In FSL the parameters that allow a greater Dice coefficient are number of classes equal to 3; and for a rf20 and rf40 a FWHM of 30mm, whereas for a rf100 a 20mm FWHM is better. This occurs because the variation is more abrupt for higher rf values and a smaller FWHM fits those cases better.

The IIH correction algorithm present on SPM is considered to be the most regular of the

algorithms. The best parameter for T1_fl images is to use a FWHM of 90mm, and for the T1_IR images is to use a FWHM of 60mm. A FWHM of 30mm was also used, but the results of the segmentations show it is worse than for the uncorrected image.

In PABIC algorithm, it can be observed that for rf20 the use of 2 classes is adequate for T1_fl images, while the use of 3 classes is adequate for T1_IR images. For higher rf's, the opposite happens.

9% noise

For 9% noise there were only considered the T1-weighed images, because the FAST4 segmentation algorithm fails to segment the other images.

It can be seen that the algorithm used for the segmentation does not perform as well in 9% noise images. The Dice coefficients are generally lower when compared to the segmentation of 3% noise images, Table 5.5 and 5.6

The correction that is more coherent is the N3_015_2_2, since it always improves the dice coefficient, independently of the rf level applied.

For rf lower than 100 the SPM8, FSL and PABIC do not improve the dice coefficient.

Table 5.3: Dice values for GM, 3% noise and A field images.

	Uncorrected	N3_01_2_4	N3_03_2_4	N3_015_2_2	N3_015_2_4	N3_015_2_6	N3_015_4_4	FSL_2_20	FSL_3_10	FSL_3_20	FSL_3_30	FSL_4_20	SPM_30	SPM_60	SPM_90	PABIC_2cl	PABIC_3cl
rf20																	
T2_EPI_no3_rf20_A	0,7206	0,6704	0,7151	**0,7369**	0,7027	0,5168	0,7046	0,6362	0,5839	0,6494	0,6675	0,6718	0,6513	0,7398	**0,7621**	**0,7506**	0,7375
PD_SE_no3_rf20_A	0,6378	**0,7391**	0,7362	0,7191	0,7373	0,6255	0,7325	0,7420	0,7251	**0,7494**	0,7475	0,7390	0,6782	0,7417	**0,7507**	0,7214	0,7208
T1_fl_no3_rf20_A	0,7641	0,7561	0,7349	**0,7686**	0,7579	0,5474	0,7635	0,6980	0,6883	0,7632	0,7884	**0,8009**	0,6996	0,7577	**0,7771**	0,7811	0,7709
T1_IR_no3_rf20_A	0,8003	0,8046	0,8039	0,8018	**0,8055**	0,6695	0,8053	0,7655	0,8002	0,8033	**0,8048**	0,8040	0,7818	0,8031	0,8047	0,8013	0,7998
T2_SE_no3_rf20_A	0,7142	**0,7145**	0,7098	0,7138	0,7128	0,6257	0,7100	0,4732	0,4533	0,4852	0,5010	0,4888	0,6617	0,7178	**0,7229**	0,7184	**0,7206**
rf40																	
T2_EPI_no3_rf40_A	0,6308	0,6484	**0,7137**	0,6649	0,6857	0,5123	0,6856	0,7035	0,6220	0,6997	0,7138	**0,7195**	0,6254	0,7235	**0,7569**	0,6995	**0,7216**
PD_SE_no3_rf40_A	0,5352	**0,7318**	0,7304	0,6248	0,7312	0,6225	0,7234	**0,7099**	0,6956	0,7097	0,6901	0,6670	0,6469	0,7094	**0,7345**	0,5108	**0,5895**
T1_fl_no3_rf40_A	0,7086	**0,7564**	0,7365	0,7192	0,7505	0,5505	0,7528	0,7368	0,7491	0,7753	**0,7801**	0,7745	0,7060	0,7615	**0,8061**	0,7247	**0,7492**
T1_IR_no3_rf40_A	0,7891	0,8048	0,8041	0,7916	**0,8056**	0,7064	0,8048	0,7679	0,8001	0,8037	**0,8051**	0,8043	0,7835	**0,8033**	0,7784	**0,8010**	0,7934
T2_SE_no3_rf40_A	0,6731	0,6756	**0,6813**	0,6769	0,6782	0,5611	0,6770	0,6716	0,6404	0,6908	**0,6997**	0,6873	0,6571	0,6989	**0,7166**	0,6925	**0,7063**
rf100																	
T2_EPI_no3_rf100_A	0,4355	0,6119	**0,6992**	0,4485	0,6811	0,5114	0,6740	**0,6895**	0,5811	0,6418	0,6301	0,6487	0,6829	0,7489	**0,7621**	**0,6436**	0,6043
PD_SE_no3_rf100_A	0,4075	0,6878	0,7057	0,4028	**0,7059**	0,5850	0,6834	0,6610	**0,6614**	0,6372	0,5714	0,5460	0,6289	0,6874	**0,7137**	0,5012	**0,5032**
T1_fl_no3_rf100_A	0,5742	0,7297	0,7414	0,5786	**0,7451**	0,5624	0,7450	0,7451	0,7343	**0,7629**	0,7524	0,7188	0,6923	0,7441	**0,7651**	0,6797	0,6878
T1_IR_no3_rf100_A	0,7004	0,7769	**0,7948**	0,7046	0,7925	0,7177	0,7913	0,7728	0,7905	**0,8009**	0,8004	0,7897	0,7752	0,8033	**0,8061**	**0,7806**	0,7637
T2_SE_no3_rf100_A	0,3585	0,3704	0,3700	0,3572	**0,3716**	0,3706	0,3670	0,6668	0,6107	0,6717	**0,6779**	0,6596	0,5852	0,6759	**0,6896**	0,6453	0,5678

No background = worse than the uncorrected, background = better than the uncorrected, bold = best parameters for the algorithm, underline = best correction for the image.

Table 5.4: Dice values for WM, 3% noise and A field images.

	Uncorrected	N3_01_2_4	N3_03_2_4	N3_015_2_2	N3_015_2_4	N3_015_2_6	N3_015_4_4	FSL_2_20	FSL_3_10	FSL_3_20	FSL_3_30	FSL_4_20	SPM_30	SPM_60	SPM_90	PABIC_2cl	PABIC_3cl
rf20																	
T2_EPI_no3_rf20_A	0,7505	0,6890	0,7532	**0,7684**	0,7361	0,5370	0,7400	0,7404	0,7028	0,7510	0,7642	**0,7673**	0,6987	0,7786	<u>0,7978</u>	**0,7860**	0,7701
PD_SE_no3_rf20_A	0,6093	**0,7000**	0,6993	0,6793	0,6971	0,5555	0,6904	0,6968	0,6618	0,7127	<u>0,7196</u>	0,7080	0,6130	0,6874	**0,7061**	0,6681	**0,6862**
T1_fl_no3_rf20_A	0,8321	0,8218	0,8015	**0,8359**	0,8235	0,6081	0,8292	0,7690	0,7553	0,8090	0,8294	**0,8377**	0,7671	0,8280	**0,8425**	<u>0,8455</u>	0,8365
T1_IR_no3_rf20_A	0,8527	0,8572	0,8576	0,8540	<u>0,8579</u>	0,7355	0,8577	0,8305	0,8544	0,8565	**0,8577**	0,8564	0,8346	0,8567	**0,8578**	0,8534	0,8556
T2_SE_no3_rf20_A	0,8177	**0,8181**	0,8147	0,8177	0,8177	0,7189	0,8142	0,6830	0,6697	0,6879	0,6959	0,6925	0,7629	0,8242	<u>0,8295</u>	0,8204	**0,8253**
rf40																	
T2_EPI_no3_rf40_A	0,6639	0,6576	**0,7510**	0,6920	0,7120	0,5323	0,7138	0,7410	0,6773	0,7417	0,7502	**0,7512**	0,6680	0,7608	<u>0,7923</u>	0,7278	**0,7501**
PD_SE_no3_rf40_A	0,5033	0,6949	**0,6959**	0,5882	0,6938	0,5562	0,6850	0,6596	0,6317	**0,6692**	0,6591	0,6346	0,6038	0,6689	<u>0,6968</u>	0,1001	**0,5589**
T1_fl_no3_rf40_A	0,7937	**0,8220**	0,8038	0,8014	0,8159	0,6083	0,8190	0,8051	0,8134	0,8395	**0,8447**	0,8398	0,7720	0,8322	<u>0,8574</u>	0,7990	0,8174
T1_IR_no3_rf40_A	0,8413	<u>0,8579</u>	0,8571	0,8438	0,8576	0,7671	0,8571	0,8323	0,8535	0,8564	**0,8574**	0,8545	0,8350	**0,8561**	0,8435	**0,8514**	0,8414
T2_SE_no3_rf40_A	0,7752	0,7783	**0,7855**	0,7793	0,7817	0,6384	0,7807	0,7771	0,7403	0,7946	**0,8028**	0,7925	0,7596	0,8041	<u>0,8226</u>	0,7957	0,8103
rf100																	
T2_EPI_no3_rf100_A	0,5209	0,6221	**0,7517**	0,5365	0,7122	0,5480	0,7028	**0,7269**	0,6511	0,7052	0,6946	0,6879	0,7284	0,7860	<u>0,7947</u>	0,6375	**0,6616**
PD_SE_no3_rf100_A	0,3764	0,6627	**0,6820**	0,3704	0,6805	0,5707	0,6587	**0,6331**	0,6103	0,6201	0,5672	0,5048	0,6089	0,6751	<u>0,7035</u>	0,4373	**0,4422**
T1_fl_no3_rf100_A	0,6996	**0,8228**	0,8155	0,7035	0,8135	**0,6331**	0,8151	0,8156	0,7980	**0,8306**	0,8286	0,7995	0,7860	0,8351	<u>0,8438</u>	0,7775	0,7831
T1_IR_no3_rf100_A	0,7808	0,8366	**0,8501**	0,7840	0,8485	0,7643	0,8477	0,8358	0,8431	0,8537	**0,8541**	0,8323	0,8318	0,8553	<u>0,8555</u>	0,8330	0,8184
T2_SE_no3_rf100_A	0,4440	0,4874	0,4852	0,4393	0,4870	**0,5135**	0,4780	0,7718	0,7170	0,7869	**0,7891**	0,7632	0,5718	0,7766	<u>0,7918</u>	**0,7547**	0,6828

No background = worse than the uncorrected, background = better than the uncorrected, bold = best parameters for the algorithm, underline = best correction for the image.

Table 5.5: Dice values for GM, 9% noise and A field images.

	Uncorrected	N3_01_2_4	N3_03_2_4	N3_015_2_2	N3_015_2_4	N3_015_2_6	N3_015_4_4	FSL_2_20	FSL_3_10	FSL_3_20	FSL_3_30	FSL_4_20	SPM_30	SPM_60	SPM_90	PABIC_2cl	PABIC_3cl
rf20																	
T1_fl_no9_rf20_A	0,6275	0,6102	0,6016	**_0,6280_**	0,6077	0,4890	0,6062	0,5825	0,5543	0,5949	0,6106	0,6059	0,5635	0,5976	0,6165	0,6162	0,6051
T1_IR_no9_rf20_A	0,7038	0,6980	0,6931	**_0,7040_**	0,6948	0,5615	0,6895	0,6523	0,6313	0,6733	0,6881	0,6839	0,6351	0,6794	0,6941	0,4891	0,6621
rf40																	
T1_fl_no9_rf40_A	0,6180	0,6170	0,6063	**0,6199**	0,6119	0,4910	0,6132	0,5862	0,5560	0,5991	0,6164	0,6110	0,5629	0,6021	**0,6200**	_0,6253_	0,6065
T1_IR_no9_rf40_A	0,6983	**_0,7044_**	0,7002	0,6993	0,7029	0,5720	0,6989	0,6580	0,6385	0,6808	0,6952	0,6909	0,6368	0,6879	**0,7003**	0,5103	0,6519
rf100																	
T1_fl_no9_rf100_A	0,5539	0,6074	0,6023	0,5570	0,6092	0,4912	**0,6102**	0,5942	0,5636	0,6061	**0,6190**	0,6089	0,5595	0,6038	_0,6199_	**0,5918**	0,5814
T1_IR_no9_rf100_A	0,6486	0,6875	0,6977	0,6512	0,6999	0,5763	**0,7003**	0,6684	0,6506	0,6906	**0,7018**	0,6944	0,6372	0,6888	_0,7026_	0,5771	**0,6572**

No background = worse than the uncorrected, background = better than the uncorrected, bold = best parameters for the algorithm, underline = best correction for the image.

Table 5.6: Dice values for WM, 9% noise and A field images.

						Correction methods											
	Uncorrected	N3_01_2_4	N3_03_2_4	N3_015_2_2	N3_015_2_4	N3_015_2_6	N3_015_4_4	FSL_2_20	FSL_3_10	FSL_3_20	FSL_3_30	FSL_4_20	SPM_30	SPM_60	SPM_90	PABIC_2cl	PABIC_3cl
rf20																	
T1_fl_no9_rf20_A	0,7125	0,6903	0,6804	_0,7126_	0,6877	0,5078	0,6857	0,6577	0,6229	0,6728	0,6914	0,6862	0,6341	0,6792	0,6979	0,6922	0,6847
T1_IR_no9_rf20_A	0,7928	0,7875	0,7825	_0,7930_	0,7842	0,6262	0,7787	0,7447	0,7240	0,7645	0,7780	0,7741	0,7253	0,7716	0,7842	0,5605	0,7480
rf40																	
T1_fl_no9_rf40_A	0,7107	0,7015	0,6892	_0,7121_	0,6949	0,5142	0,6974	0,6651	0,6300	0,6815	0,7009	0,6958	0,6396	0,6874	0,7058	0,7082	0,6912
T1_IR_no9_rf40_A	0,7884	_**0,7935**_	0,7895	0,7893	0,7919	0,6418	0,7880	0,7498	0,7304	0,7707	0,7840	0,7801	0,7268	0,7784	**0,7893**	0,5899	0,7385
rf100																	
T1_fl_no9_rf100_A	0,6751	**0,7104**	0,7042	0,6777	0,7048	0,5437	0,7062	0,6844	0,6518	0,7005	**0,7168**	0,7077	0,6708	0,7073	_**0,7227**_	**0,6773**	0,6755
T1_IR_no9_rf100_A	0,7541	0,7881	0,7934	0,7562	_0,7965_	0,6654	_0,7965_	0,7615	0,7439	0,7815	**0,7928**	0,7871	0,7413	0,7852	**0,7955**	0,6548	0,7499

No background = worse than the uncorrected, background = better than the uncorrected, bold = best parameters for the algorithm, underline = best correction for the image.

Significance of Dice coefficient

The Table 5.7 has the significance values for the Dice coefficients for each correction algorithm. The values lower that 0.05 are considered significant.

For the T2_SE images the changes in Dice coefficient are generally non-significant. Only for the SPM_60 and SPM_90 method significant results were obtained. This method was pointed out before, in this work, to be the one that improved the most the Dice coefficient in these images.

The method N3_015_2_6 significantly decrease the Dice coefficient in all considered images, except for T2_SE.

Almost all methods significantly improved the Dice of the PD_SE images. The PABIC is the one that gives worse results.

The SPM_90 is pointed as the method that improves most the Dice coefficient in almost all image types except for T1_IR images, where the SPM_60 performs better. For the T1_IR the method that improves significantly the Dice coefficient is the N3_015_2_2. N3_015_2_2 also works well in T2_EPI images.

The FSL_3_20, FSL_3_30 and FSL_4_20 significantly improves the Dice in T1_fl, but the one that gives a minor p is the SPM_90, being the most significant.

Table 5.7: Significance of the Dice coefficient (ANOVA results).

	T2_EPI		**PD_SE**		**T2_SE**		**T1_IR**		**T1_fl**	
	GM	WM	GM	WM	GM	WM	GM	WM	GM	WM
N3_01_2_4	.183	.600	2.94E-05	1.24E-04	.401	.387	.012	.008	.024	.048
N3_03_2_4	.020	.012	4.80E-05	1.63E-04	.534	.430	.021	.018	.095	.229
N3_015_2_2	.005	3.33E-04	.004	.009	.305	.842	7.50E-05	1.52E-04	.007	.030
N3_015_2_4	.046	.049	4.65E-05	1.84E-04	.400	.445	.016	.341	.027	.633
N3_015_2_6	.092	.030	.011	.090	.012	.056	.003	4.32E-04	.001	4.34E-05
N3_015_4_4	.047	.047	3.97E-05	1.96E-04	.595	.592	.021	.020	.020	.039
FSL_2_20	.044	.017	2.25E-05	2.57E-04	.322	.198	.883	.960	.180	.453
FSL_3_10	.758	.341	2.47E-04	.002	.592	.416	.386	.558	.227	.746
FSL_3_20	.035	.011	3.23E-05	2.03E-04	.225	.131	.055	.066	.018	.048
FSL_3_30	.012	.004	2.75E-05	1.55E-04	.179	.106	.023	.023	.005	.012
FSL_4_20	.010	.002	6.85E-05	1.99E-04	.235	.135	.029	.036	.004	.012
SPM_30	.168	.121	6.57E-04	.011	.246	.709	.994	.629	.998	.523
SPM_60	.007	.004	3.37E-05	3.47E-04	.048	.043	.044	.044	.038	.048
SPM_90	.003	.002	2.54E-05	1.81E-04	.037	.032	.656	.887	4.15E-04	2.65E-04
PABIC_2cl	.005	.287	.126	.806	.076	.049	.556	.340	.012	.043
PABIC_3cl	.022	.976	.076	2.55E-04	.072	.039	.326	.683	.019	.060

Bold: $p < 0.05$

(Column group header: **Segmented images**; row group label: **Correction methods**)

5.2.2 Sensitivity, specificity and ROC space

A typical problem of segmentation methods was observed: a higher sensitivity corresponds normally to a lower specificity and vice versa. However, observing the ROC space it is possible to find the best relationship.

In Figure 5.14 it can be observed an example of a ROC space. The relationship between sensitivity and specificity is better for almost all the corrected images. In this case best result is found using the SPM8 algorithm. The FSL also produce good results.

The other ROC spaces were made and was found that they show a similar behaviour to the Dice coefficient. It was observed that the best relationship between sensitivity and specificity for each image, correspond in 81% of the cases to the best Dice coefficient for that image.

The tables relative to the sensitivity and specificity, used to build the ROC spaces, can be found in Appendix B.1.3, B.1.4, B.1.5 and B.1.6.
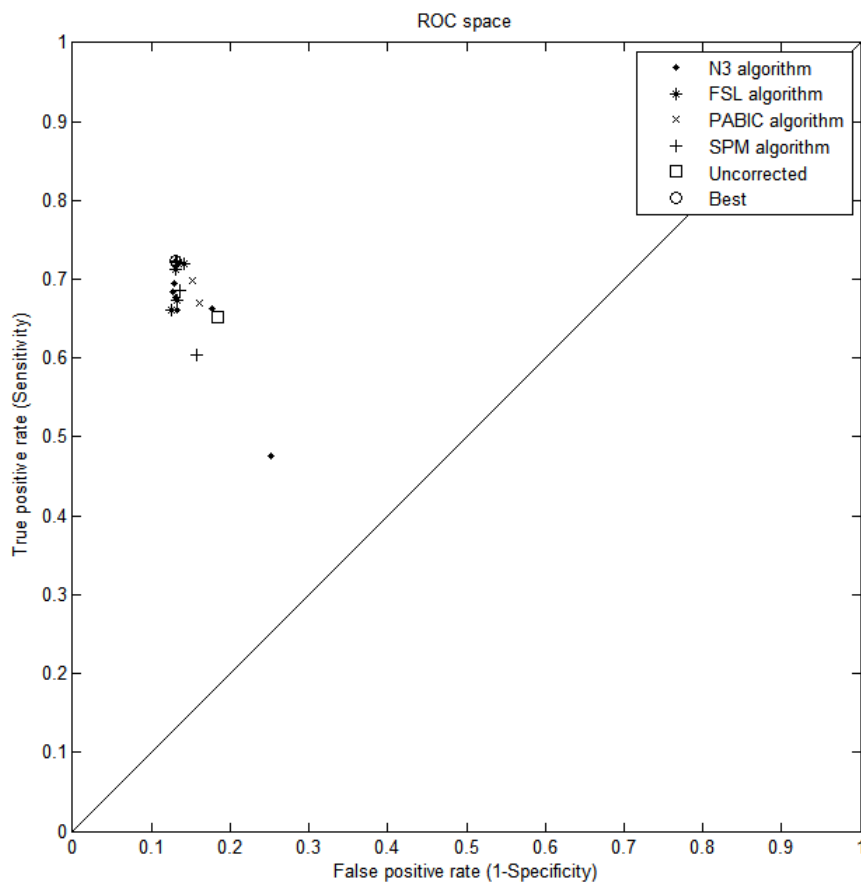
Figure 5.14: ROC space of the T1_fl image,with 3% noise and rf40% and bias field B.

Chapter 6

Discussion

FSL reveals to be the algorithm that is less dependent on the choice of the parameters used. It is true that some parameters give better results for determinate images, but in general the behaviour of the algorithm is highly stable for any of the evaluation parameter used, making it to be a good choice when having to correct an image that you have little information and for general use.

The FSL continues to perform well in improving CNR as in some cases the SPM_90.

The results do not evidence a clearly optimal algorithm or parameters for IIH correction. However the algorithm implemented in FSL can be considered globally the one that gives the most satisfactory results, except in CNR for T2 images.

The effects in SNR and CNR have never been evaluated before. It was expected that the SNR and CNR remain the same or slightly vary. For many cases that does happen. In the FSL algorithm it is observed that the SNR is considerably enhanced for some parameters and, particularly, for T1-weighted images.

In SPM_30 the SNR is lowered in all images, thus this parameter is to be avoid when the improvement of SNR is aimed.

Another correction that should be avoid, regarding CNR, is the choice of a small number of fitting points in N3 algorithm (N3_015_2_2).

It was chosen to use the N3 algorithm in this work, because of its popularity and good results demonstrated in previous comparisons performed by several authors. The results obtained in this work do not demonstrate that N3 algorithm is somehow superior in relation to the other algorithms in analysis.

The use of a bigger sub-sampling factor in N3 algorithm does not appear to have much influence in the performance of the algorithm, moreover the use of a higher sub-sampling factor speeds the algorithm, which is, when compared to the remaining algorithms, the slowest.

The analysis of the PABIC performance is quite limited since there are made only two variations in its parameters. However it can be said that the choice of 2 or 3 classes has much

influence in all evaluation parameters, except for CV, where there is observed some consistency.

It appear that the performance of the PABIC could be intimately related with the choice of the mean and standard deviation values for the classes used in the correction. Maybe the k-means is not the ideal classification method for the tissues. The used fitting Gaussians to histograms, used by Styner M. *et al.* [42], may give better results to compute the class parameters. The fact that there was not provided any mask in the classification and correction steps, in order to maintain the correction algorithm as automatic as possible, could be in part responsible for these results.

It was assumed that the lowering of the CV will help the segmentation, because the tissue becomes more piecewise constant facilitating the segmentation. It is a fact that the Dice coefficient is actually improved, but it is not observed that the best CV obtained by a correction will provide the best Dice coefficient. It is curious to look at the relation between the best methods when improving CNR and the results obtained for Dice coefficient for these corrections. For 3% noise images it seems to exist a concordance between them. It can be stated that the improvement of CNR could be more crucial than the CV, when looking to improve the segmentation. For 9% noise images that relation is not so notorious. As expected the CV is reduced by almost all correction methods and its parameters. In this work no major differences were found between the CV in GM and CV in WM as stated by Chua Z. *et al.*[55].

Another feature that is curious to observe is that for almost all the images the better values for Dice coefficient match with the best relation between sensitivity and specificity found in the ROC space.

When looking at the RMS it can be said that, for FSL and SPM8, higher FWHM gives better results when the IIH is very smooth (rf20), and lower FWHM when the bias is more pronounced (rf100), These results are independent of the image type, in agreement with Ashburner J. and Friston K.[16] and Guillemaud R. and Brady M. [49]. However, this fact can become a problem, especially for SPM8, that is most affected by this parameter, because in a real image the IIH is unknown, and in some cases the smoothness of the IIH is also unknown, that could be a problem if a inadequate FWHM was chosen. To solve this problem it could be found a relation between the smoothness of the bias and the MRI sequences used.

The RMS is considered an accuracy measure, i.e., evaluates if the values of the extracted bias field are close to the true field, but does not evaluate the distribution is the intended one. The linearity of this distribution will define the precision of the results. A bigger spread of the points in the scatter plot will give a worse precision. The Pearson correlation seems to help to combine accuracy and precision.

The algorithms integrated in a segmentation framework, SPM8 and FSL, demonstrate bigger Pearson coefficients, meaning that the distribution is somehow linear and it is not too disperse.

The SPM8 is more difficult to use because its performance improving RMS is much influenced by the choice of the FWHM.

The generalization of these results for images from other body parts, can be performed but with some reservations. With the exception of the SPM8 and the FSL, the other algorithms have the conditions to be applied to images besides brain images. The SPM8, since it is highly dedicated to brain image, will need more readjustments, namely the probability maps used. The FSL demands adjustments namely in the brain extraction proceding with the BET software. As examples the PABIC was shown to successfully correct IIH in breast [42] and the N3 was tested to correct lungs image [61].

Rui Lavrador

Chapter 7

Conclusion

The initial objective of this work was to find the best IIH correction algorithm for an image corrupted by this kind of distortions.

Consulting the related literature, soon it was acknowledged that, until now, there was not found an algorithm that overcomes all the others in all aspects.

This work is one of the most complete assessment related to IIH correction and incorporates some new algorithms, such as the FSL and SPM8, that were not included in former evaluations.

There were chosen four popular algorithms, already implemented in widely used tools for image processing, and they were tested using simulated images with known features.

It was found that the performance of the algorithms does not depend much on the shape of the bias field, but it is clearly dependent, in some cases, on the image that is being corrected.

The corrections show significant results in the performance of the segmentation, particularly for higher levels of inhomogeneities, that is, the results are significantly better if one corrects the images before segmentation.

As expected, there was not found an algorithm clearly superior to the other. Still, some similarities and stabilities that allows to build a table, Table 7.1 and 7.2. These findings will allow suggesting an algorithm and its parameters accordingly to the nature and parameters of the imaged to be corrected.

These tables could be used in order to support the decision about the algorithms that should be incorporated in magnetic resonance (MR) scanners or incorporated on Syngo®. Besides the improvement in some subsequent analysis, such as segmentation, this correction also improve SNR and CNR, and this upgrade has market value, since the improvement of this parameters generally ask for an investment in the scanner machine or in detriment of other image features.

This fits the Siemens objectives to provide the best solution to its customers, helping physicians and technicians to provide the best health care possible.

Table 7.1: Best correction methods for 3% noise images, taking into account the image and image quality parameter that want to be improved.

	SNR_GM	SNR_WM	CNR	CV_GM	CV_WM	RMS	DICE_GM	DICE_WM
				Quality parameters				
rf20								
T2_EPI_no3_rf20	SPM_90	FSL_3_10	SPM_90	FSL_3_10	FSL_3_10	N3_03_2_4	SPM_90	SPM_90
PD_SE_no3_rf20	FSL_3_20	FSL_3_10	SPM_90	FSL_3_10	FSL_3_10	N3_01_2_4	SPM_90	SPM_90
T1_fl_no3_rf20	FSL_3_20	FSL_4_20	FSL_3_30	FSL_3_10	FSL_3_10	N3_01_2_4	FSL_3_30	FSL_3_30
T1_IR_no3_rf20	FSL_3_10	FSL_4_20	FSL_3_30	FSL_3_10	FSL_3_10	N3_01_2_4	FSL_3_30	SPM_90/FSL_3_30
T2_fl_no3_rf20	FSL_2_20	FSL_3_20	uncorrected	N3_015_2_6	FSL_3_10	SPM_90	N/A	N/A
T2_SE_no3_rf20	N3_015_2_2	FSL_3_10	SPM_90	FSL_3_10	FSL_3_10	SPM_90	SPM_90	SPM_90
rf40								
T2_EPI_no3_rf40	FSL_3_10	FSL_3_10	SPM_90	FSL_3_10	FSL_3_10	N3_03_2_4	SPM_90	SPM_90
PD_SE_no3_rf40	FSL_3_20	FSL_3_10	SPM_90	FSL_3_10	FSL_3_10	N3_01_2_4	SPM_90	SPM_90
T1_fl_no3_rf40	FSL_3_10	FSL_3_30	FSL_3_30	FSL_3_10	FSL_3_10	SPM_60	FSL_3_30	SPM_90/FSL_3_30
T1_IR_no3_rf40	FSL_3_20	FSL_4_20	FSL_3_30	FSL_3_10	FSL_3_10	SPM_60	FSL_3_30	SPM_90/FSL_3_30
T2_fl_no3_rf40	FSL_3_10	FSL_3_20	uncorrected	FSL_3_10	FSL_3_10	SPM_60	N/A	N/A
T2_SE_no3_rf40	PABIC_2cl	FSL_3_10	SPM_90	FSL_3_10	FSL_3_10	SPM_60	SPM_90	SPM_90
rf100								
T2_EPI_no3_rf100	FSL_3_10	FSL_3_10	SPM_90	FSL_3_10	FSL_3_10	N3_015_2_6	SPM_90	SPM_90
PD_SE_no3_rf100	FSL_3_10	FSL_3_20	SPM_90	FSL_3_10	FSL_3_10	N3_015_2_6	SPM_90	SPM_90
T1_fl_no3_rf100	FSL_3_10	FSL_3_30	FSL_4_20	FSL_3_10	FSL_3_10	N3_015_2_6	SPM_90	SPM_90
T1_IR_no3_rf100	FSL_3_20	FSL_3_30	FSL_3_30	FSL_3_10	FSL_3_10	SPM_30	FSL_3_20	SPM_90
T2_fl_no3_rf100	FSL_3_10	FSL_3_10	uncorrected	N3_015_2_6	N3_015_2_6	SPM_30	N/A	N/A
T2_SE_no3_rf100	SPM_90	FSL_3_10	SPM_90	FSL_3_10	FSL_3_10	PABIC_2cl	SPM_90	SPM_90

Table 7.2: Best correction methods for 9% noise images, taking into account the image and image quality parameter that want to be improved.

	SNR_GM	SNR_WM	CNR	CV_GM	CV_WM	RMS	DICE_GM	DICE_WM
				Quality parameters				
rf20								
T2_EPI_no9_rf20	FSL_03_10	FSL_03_10	SPM_90	FSL_03_10	FSL_03_10	N3_03_2_4	N/A	N/A
PD_SE_no9_rf20	FSL_03_30	FSL_4_20	N3_01_2_4	FSL_03_10	FSL_03_10	N3_03_2_4	N/A	N/A
T1_fl_no9_rf20	FSL_03_10	FSL_4_20	FSL_03_30	FSL_03_10	FSL_03_10	N3_015_4_4	N3_015_2_2	N3_015_2_2
T1_IR_no9_rf20	FSL_03_10	FSL_4_20	FSL_03_30	FSL_03_10	FSL_03_10	N3_015_4_4	N3_015_2_2	N3_015_2_2
T2_fl_no9_rf20	FSL_4_20	FSL_4_20	uncorrected	FSL_03_10	FSL_03_10	N3_015_4_4	N/A	N/A
T2_SE_no9_rf20	FSL_03_10	FSL_03_10	SPM_90	FSL_03_10	FSL_03_10	N3_015_4_4	N/A	N/A
rf40								
T2_EPI_no9_rf40	FSL_03_10	FSL_03_10	SPM_90	FSL_03_10	FSL_03_10	N3_03_2_4	N/A	N/A
PD_SE_no9_rf40	FSL_4_20	FSL_03_20	N3_01_2_4	FSL_03_10	FSL_03_10	N3_03_2_4	N/A	N/A
T1_fl_no9_rf40	FSL_03_10	FSL_4_20	FSL_4_20	FSL_03_10	FSL_03_10	N3_015_2_6	N3_015_2_2	N3_015_2_2
T1_IR_no9_rf40	FSL_03_10	FSL_03_10	FSL_03_30	FSL_03_10	FSL_03_10	N3_015_4_4	N3_01_2_4	N3_01_2_4
T2_fl_no9_rf40	FSL_03_10	FSL_4_20	uncorrected	FSL_03_10	FSL_03_10	N3_01_2_4	N/A	N/A
T2_SE_no9_rf40	FSL_4_20	FSL_03_10	SPM_90	FSL_03_10	FSL_03_10	FSL_03_30	N/A	N/A
rf100								
T2_EPI_no9_rf100	FSL_03_20	FSL_03_10	SPM_90	FSL_03_10	FSL_03_10	FSL_2_20	N/A	N/A
PD_SE_no9_rf100	FSL_4_20	FSL_4_20	N3_01_2_4	FSL_03_10	FSL_03_10	FSL_2_20	N/A	N/A
T1_fl_no9_rf100	FSL_4_20	FSL_4_20	FSL_4_20	FSL_03_10	FSL_03_10	FSL_2_20	SPM_90	SPM_90
T1_IR_no9_rf100	FSL_03_10	FSL_4_20	FSL_4_20	FSL_03_10	FSL_03_10	FSL_2_20	SPM_90	N3_015_4_4/SPM_90
T2_fl_no9_rf100	FSL_4_20	FSL_4_20	uncorrected	FSL_03_10	FSL_03_10	PABIC_3cl	N/A	N/A
T2_SE_no9_rf100	FSL_03_10	FSL_03_10	SPM_90	FSL_03_10	FSL_03_10	FSL_03_30	N/A	N/A

N/A: not applicable

7.1 Limitations and future work

This work is based on simulated images. They facilitate the evaluation of some parameters and give a solid base to predict the behaviour of the algorithms when they are applied to real images.

The tool used to simulate the MRI images has some limitations. For some sequences the parameter range, such as TR or TE, is limited and there are some acquisition protocols that are widely used in today clinical practice, that are not available for simulated images using the BrainWeb. As examples it can be mentioned the MPRAGE, GE sequences, EPI and other sequences use in for functional MRI. The EPI images, for example, are often used for diffusion MRI, the presence of IIH probably will affect its analysis.

The next step that should be followed is to run tests on real images and confirm the obtained results are also valid for real images.

Parallel coil transmission/acquisition is now commonly used for clinical MR imaging and the resulting intensity inhomogeneity variations become more complex. The used of higher magnetic fields and its affects in IIH should be carefully analysed.

Taking into account the complete and intensive analysis already made, still it was considered that there were some important parameters in the images that were not properly evaluated and the type of images evaluated was restricted.

Some preliminary tests were performed on real images, and in a qualitative observation of the images it was possible some improvements, namely when looking at the results of the segmentation. For a quantitative evaluation it will be necessary to have the participation of physicians.

If we run tests in a larger number of images in the future it could became possible to use a tool that reads the DICOM header, and depending on the information about the image, it performs a determined correction, depending on the aim of the image.

Even with all the assessments in IIH correction algorithm done in this work, this area still is an open problem that requires more investigation and development.

7.2 Final work assessment

This project allowed the increase of the knowledge about MRI technology, problems in image acquisition, image processing and also about diverse tools available to perform them.

The familiarization with several software, from Siemens and also other general tools used in image processing, other programming languages and operative systems, has taken much time, but it was a challenging task, this knowledge probably will become very useful in the future.

The project allowed me to enlarge my network, and the fact that the project takes place in a company environment provided me contact with the problems that the Siemens professionals face every day.

Beside the specific work on the thesis theme, the integration in this company provide me some online formations, a visit to the Hospital da Luz and also participation in solidarity activities with children.

This project was integrated on a group of research, GID group, in which several PhD and other MSc students are included. Their knowledge and experience helped in the development of my project.

I had the opportunity to propose some papers to conferences, a paper named *Intensity inhomogeneity corrections in MRI simulated images for segmentation* was accepted in the "6th International Conference on Technology and Medical Sciences", Appendix C. We also intend to publish the final results of the present project in a reference journal in the area of MRI and image processing.

The obtained results show the behaviour of some IIH correction algorithms and demonstrate that evaluation of the correction performance of an algorithm is not a straightforward matter and it should be performed always having in mind the purpose of the images.

This project, which seemed to be simple in the beginning, grew up to be an exhaustive evaluation of IIH correction methods that I hope will help Siemens upgrade their MRI scans.

Bibliography

[1] W. Hendee, *Medical imaging physics*, 4th ed., New York ;Wiley-Liss, 2002.

[2] J. Duncan and N. Ayache, "Medical image analysis: progress over two decades and the challenges ahead," *IEEE Transactions on Pattern Analysis and Machine Intelligence*, vol. 22, no. 1, pp. 85–106, 2000.

[3] B. Belaroussi, J. Milles, S. Carme, Y. M. Zhu, and H. Benoit-Cattin, "Intensity non-uniformity correction in MRI: existing methods and their validation," *Medical Image Analysis*, vol. 10, no. 2, pp. 234–246, Apr. 2006.

[4] C. Westbrook, *Handbook of MRI technique*, 2nd ed. Malden MA.: Blackwell Science, 1999.

[5] E. Haacke, *Magnetic resonance imaging : physical principles and sequence design*. New York: Wiley, 1999.

[6] M. Brown, *MRI : basic principles and applications*, 3rd ed. Hoboken N.J.: Wiley-Liss, 2003.

[7] U. Vovk, F. Pernus, and B. Likar, "A review of methods for correction of intensity inhomogeneity in MRI." *IEEE Trans Med Imaging*, vol. 26, no. 3, pp. 421, 405, Mar. 2007.

[8] Z. Hou, "A review on MR image intensity inhomogeneity correction," *International Journal of Biomedical Imaging*, vol. 2006, 2006.

[9] J. B. Arnold, J. Liow, K. A. Schaper, J. J. Stern, J. G. Sled, D. W. Shattuck, A. J. Worth, M. S. Cohen, R. M. Leahy, J. C. Mazziotta, and D. A. Rottenberg, "Qualitative and quantitative evaluation of six algorithms for correcting intensity nonuniformity effects," *NeuroImage*, vol. 13, no. 5, pp. 931–943, May 2001.

[10] A. Hendrix, *Magnets, Spins, and Resonances – An Introduction to the basics of Magnetic Resonance*. Erlangen, Alemanha: Siemens AG Medical Solutions, 2003.

[11] R. Y. Kwong, *Cardiovascular Magnetic Resonance Imaging*. Springer, 2007.

[12] D. Weishaupt, V. D. Köchli, and B. Marincek, *How does MRI work?* Springer, Oct. 2006.

[13] I. Bankman, *Handbook of medical imaging : processing and analysis*. San Diego CA: Academic Press, 2000.

[14] P. Jezzard, *Functional MRI : an introduction to methods.* Oxford ;;New York: Oxford University Press, 2001.

[15] A. Hendrix, *Magnets, Flows, and Artifacts – Basics, Techniques, and Applications of Magnetic Resonance Tomography.* Erlangen, Alemanha: Siemens AG Medical Solutions, 2005.

[16] J. Ashburner and K. J. Friston, "Unified segmentation," *NeuroImage*, vol. 26, no. 3, pp. 839–851, Jul. 2005.

[17] Y. Zhang, M. Brady, and S. Smith, "Segmentation of brain MR images through a hidden markov random field model and the expectation-maximization algorithm," *IEEE Transactions on Medical Imaging*, vol. 20, no. 1, pp. 45–57, 2001.

[18] L. Zhou, "A method of radio-frequency inhomogeneity correction for brain tissue segmentation in MRI," *Computerized Medical Imaging and Graphics*, vol. 25, no. 5, pp. 379–389, 2001.

[19] V. Positano, K. Cusi, M. F. Santarelli, A. Sironi, R. Petz, R. DeFronzo, L. Landini, and A. Gastaldelli, "Automatic correction of intensity inhomogeneities improves unsupervised assessment of abdominal fat by MRI," *Journal of Magnetic Resonance Imaging*, vol. 28, no. 2, pp. 403–410, 2008.

[20] J. C. Rajapakse and F. Kruggel, "Segmentation of MR images with intensity inhomogeneities," *Image and Vision Computing*, vol. 16, no. 3, pp. 165–180, Mar. 1998.

[21] D. Pham, C. Xu, and J. Prince, "A survey of current methods in medical image segmentation," in *Annual Review of Biomedical Engineering*, 2000, vol. 2, pp. 338, 315.

[22] J. Haselgrove and M. Prammer, "An algorithm for compensation of surface-coil images for sensitivity of the surface coil," *Magnetic Resonance Imaging*, vol. 4, no. 6, pp. 469–472, 1986.

[23] E. R. McVeigh, M. J. Bronskill, and R. M. Henkelman, "Phase and sensitivity of receiver coils in magnetic resonance imaging," *Medical Physics*, vol. 13, no. 6, pp. 806–814, Dec. 1986.

[24] L. Axel, J. Costantini, and J. Listerud, "Intensity correction in surface-coil MR imaging," *American Journal of Roentgenology*, vol. 148, no. 2, pp. 418–420, Feb. 1987.

[25] N. Gelber, R. Ragland, and J. Knorr, "Surface coil MR imaging: utility of image intensity correction filter," *American Journal of Roentgenology*, vol. 162, no. 3, pp. 695–697, Mar. 1994.

[26] C. M. Collins, S. Li, Q. X. Yang, and M. B. Smith, "A method for accurate calculation ofB1Fields in three dimensions. effects of shield geometry on field strength and homogeneity in the birdcage coil," *Journal of Magnetic Resonance*, vol. 125, no. 2, pp. 233–241, Apr. 1997.

[27] C. M. Collins and M. B. Smith, "Calculations of b(1) distribution, SNR, and SAR for a surface coil adjacent to an anatomically-accurate human body model," *Magnetic Resonance in Medicine: Official Journal of the Society of Magnetic Resonance in Medicine / Society of Magnetic Resonance in Medicine*, vol. 45, no. 4, pp. 692–699, Apr. 2001.

[28] A. Simmons, P. S. Tofts, G. J. Barker, and S. R. Arridge, "Sources of intensity nonuniformity in spin echo images at 1.5 t," *Magnetic Resonance in Medicine*, vol. 32, no. 1, pp. 121–128, 1994.

[29] G. Barker, A. Simmons, S. Arridge, and P. Tofts, "A simple method for investigating the effects of non-uniformity of radiofrequency transmission and radiofrequency reception in MRI," *Br J Radiol*, vol. 71, no. 841, pp. 59–67, Jan. 1998.

[30] J. G. Sled and G. B. Pike, "Standing-wave and RF penetration artifacts caused by elliptic geometry: an electrodynamic analysis of MRI," *IEEE Transactions on Medical Imaging*, vol. 17, no. 4, pp. 653–662, Aug. 1998.

[31] B. R. Condon, J. Patterson, D. Wyper, A. Jenkins, and D. M. Hadley, "Image non-uniformity in magnetic resonance imaging: its magnitude and methods for its correction," *The British Journal of Radiology*, vol. 60, no. 709, pp. 83–87, Jan. 1987.

[32] J. Sled, A. Zijdenbos, and A. Evans, "A nonparametric method for automatic correction of intensity nonuniformity in MRI data," *IEEE Transactions on Medical Imaging*, vol. 17, no. 1, pp. 87–97, Feb. 1998.

[33] D. L. Pham and J. L. Prince, "Adaptive fuzzy segmentation of magnetic resonance images," *IEEE Transactions on Medical Imaging*, vol. 18, no. 9, pp. 737–752, Sep. 1999.

[34] D. W. Shattuck, S. R. Sandor-Leahy, K. A. Schaper, D. A. Rottenberg, and R. M. Leahy, "Magnetic resonance image tissue classification using a partial volume model," *NeuroImage*, vol. 13, no. 5, pp. 856–876, May 2001.

[35] G. Collewet, A. Davenel, C. Toussaint, and S. Akoka, "Correction of intensity nonuniformity in spin-echo t(1)-weighted images," *Magnetic Resonance Imaging*, vol. 20, no. 4, pp. 365–373, May 2002.

[36] P. A. Narayana, W. W. Brey, M. V. Kulkarni, and C. L. Sievenpiper, "Compensation for surface coil sensitivity variation in magnetic resonance imaging," *Magnetic Resonance Imaging*, vol. 6, no. 3, pp. 271–274, Jun. 1988.

[37] J. W. Murakami, C. E. Hayes, and E. Weinberger, "Intensity correction of phased-array surface coil images," *Magnetic Resonance in Medicine: Official Journal of the Society of Magnetic Resonance in Medicine / Society of Magnetic Resonance in Medicine*, vol. 35, no. 4, pp. 585–590, Apr. 1996.

[38] A. Fan, W. M. Wells, J. W. Fisher, M. Cetin, S. Haker, R. Mulkern, C. Tempany, and A. S. Willsky, "A unified variational approach to denoising and bias correction in MR,"

Information Processing in Medical Imaging: Proceedings of the ... Conference, vol. 18, pp. 148–159, Jul. 2003.

[39] H. Mihara, N. Iriguchi, and S. Ueno, "A method of RF inhomogeneity correction in MR imaging," *Magma (New York, N.Y.)*, vol. 7, no. 2, pp. 115–120, Dec. 1998.

[40] B. Johnston, M. S. Atkins, B. Mackiewich, and M. Anderson, "Segmentation of multiple sclerosis lesions in intensity corrected multispectral MRI," *IEEE Transactions on Medical Imaging*, vol. 15, no. 2, pp. 154–169, 1996.

[41] C. Meyer, P. Bland, and J. Pipe, "Retrospective correction of intensity inhomogeneities in MRI," *Medical Imaging, IEEE Transactions on*, vol. 14, no. 1, pp. 36–41, 1995.

[42] M. Styner, C. Brechbuhler, G. Szckely, and G. Gerig, "Parametric estimate of intensity inhomogeneities applied to MRI," *Medical Imaging, IEEE Transactions on*, vol. 19, no. 3, pp. 153–165, 2000.

[43] M. A. Balafar, A. R. Ramli, M. I. Saripan, and S. Mashohor, "Review of brain MRI image segmentation methods," *Artificial Intelligence Review*, vol. 33, no. 3, pp. 261–274, 2010.

[44] J. Ashburner and K. Friston, "MRI sensitivity correction and tissue classification," *NeuroImage*, vol. 7, p. S706, 1998.

[45] M. N. Ahmed, S. M. Yamany, A. A. Farag, and T. Moriarty, "Bias field estimation and adaptive segmentation of mri data using a modified fuzzy c-means algorithm," *Computer Vision and Pattern Recognition, IEEE Computer Society Conference on*, vol. 1, p. 1250, 1999.

[46] J. Sled, A. Zijdenbos, and A. Evans, "A comparison of retrospective intensity non-uniformity correction methods for MRI," in *Information Processing in Medical Imaging*, 1997, pp. 459–464.

[47] W. M. Wells, W. L. Grimson, R. Kikinis, and F. A. Jolesz, "Adaptive segmentation of MRI data," *IEEE Transactions on Medical Imaging*, vol. 15, no. 4, pp. 429–442, 1996.

[48] B. Dawant, A. Zijdenbos, and R. Margolin, "Correction of intensity variations in MR images for computer-aided tissue classification," *IEEE Transactions on Medical Imaging*, vol. 12, no. 4, pp. 770–781, Dec. 1993.

[49] R. Guillemaud and M. Brady, "Estimating the bias field of MR images," *IEEE Transactions on Medical Imaging*, vol. 16, no. 3, pp. 238–251, 1997.

[50] R. P. Velthuizen, J. J. Heine, A. B. Cantor, H. Lin, L. M. Fletcher, and L. P. Clarke, "Review and evaluation of MRI nonuniformity corrections for brain tumor response measurements," *Medical Physics*, vol. 25, no. 9, p. 1655, 1998.

[51] D. A. Wicks, G. J. Barker, and P. S. Tofts, "Correction of intensity nonuniformity in MR images of any orientation," *Magnetic Resonance Imaging*, vol. 11, no. 2, pp. 183–196, 1993.

[52] P. A. Narayana and A. Borthakur, "Effect of radio frequency inhomogeneity correction on the reproducibility of intra-cranial volumes using MR image data," *Magnetic Resonance in Medicine: Official Journal of the Society of Magnetic Resonance in Medicine / Society of Magnetic Resonance in Medicine*, vol. 33, no. 3, pp. 396–400, Mar. 1995.

[53] B. Brinkmann, A. Manduca, and R. Robb, "Optimized homomorphic unsharp masking for MR grayscale inhomogeneity correction," *IEEE Transactions on Medical Imaging*, vol. 17, no. 2, pp. 161–171, 1998.

[54] M. S. Cohen, R. M. DuBois, and M. M. Zeineh, "Rapid and effective correction of RF inhomogeneity for high field magnetic resonance imaging," *Human Brain Mapping*, vol. 10, no. 4, pp. 204–211, Aug. 2000.

[55] Z. Y. Chua, W. Zheng, M. W. L. Chee, and V. Zagorodnov, "Evaluation of performance metrics for bias field correction in MR brain images," *Journal of Magnetic Resonance Imaging: JMRI*, vol. 29, no. 6, pp. 1271–1279, Jun. 2009.

[56] C. Cocosco, V. Kollokian, R. Kwan, B. Pike, and A. Evans, "BrainWeb: online interface to a 3D MRI simulated brain database," *NeuroImage*, vol. 5, 1997.

[57] M. García-Sebastin, A. I. González, and M. Graña, "An adaptive field rule for nonparametric MRI intensity inhomogeneity estimation algorithm," *Neurocomputing*, vol. 72, no. 16-18, pp. 3556–3569, 2009.

[58] Y. Zhou and J. Bai, "Atlas-based fuzzy connectedness segmentation and intensity nonuniformity correction applied to brain MRI," *IEEE Transactions on Bio-Medical Engineering*, vol. 54, no. 1, pp. 122–129, Jan. 2007.

[59] Z. Hou, S. Huang, Q. Hu, and W. Nowinski, "A fast and automatic method to correct intensity inhomogeneity in MR brain images," in *Medical Image Computing and Computer-Assisted Intervention MICCAI 2006*, 2006, pp. 324–331.

[60] Y. Zhuge, J. Udupa, J. Liu, and P. Saha, "Image background inhomogeneity correction in MRI via intensity standardization," *Computerized Medical Imaging and Graphics*, vol. 33, no. 1, pp. 7–16, 2009.

[61] "Insight journal - N4ITK: nick's n3 ITK implementation for MRI bias field correction," http://www.midasjournal.org/browse/publication/640, Mar. 2010. [Online]. Available: http://www.midasjournal.org/browse/publication/640

[62] M. Styner and G. Gerig, "Evaluation of 2d/3d bias correction with 1+1es-optimization," Tech. Rep. 179, Image Science Lab, ETH Zurich, 1997.

[63] "FAST DOCS," http://www.fmrib.ox.ac.uk/fsl/fast4/index.html, Dec. 2009. [Online]. Available: http://www.fmrib.ox.ac.uk/fsl/fast4/index.html

[64] E. D'Agostino, F. Maes, D. Vandermeulen, and P. Suetens, "Atlas-to-image non-rigid registration by minimization of conditional local entropy," *Information Processing in Medical Imaging: Proceedings of the ... Conference*, vol. 20, pp. 320–332, 2007.

[65] R. Boyes, J. Gunter, C. Frost, A. Janke, T. Yeatman, D. Hill, M. Bernstein, P. Thompson, M. Weiner, and N. Schuff, "Intensity non-uniformity correction using n3 on 3-T scanners with multichannel phased array coils," *NeuroImage*, vol. 39, no. 4, pp. 1752–1762, 2008.

[66] B. Likar, M. Viergever, and F. Pernus, "Retrospective correction of MR intensity inhomogeneity by information minimization," in *Medical Image Computing and Computer-Assisted Intervention MICCAI 2000*, 2000, pp. 177–201.

Appendix A

Correction evaluation

A.1   Tables of evaluating parameters

A.1.1 SNR grey mater

Table A.1: SNR values for GM, 3% noise and A field images.

	Uncorrected	N3_01_2_4	N3_03_2_4	N3_015_2_2	N3_015_2_4	N3_015_2_6	N3_015_4_4	FSL_2_20	FSL_3_10	FSL_3_20	FSL_3_30	FSL_4_20	SPM_30	SPM_60	SPM_90	PABIC_2cl	PABIC_3cl
rf20																	
T2_EPI_no3_rf20_A	8.1531	7.4538	7.5262	**8.2718**	7.699	6.0212	7.699	7.9736	_**8.4207**_	8.1963	8.2826	8.3104	4.3296	8.0205	**8.4067**	7.391	6.9663
PD_SE_no3_rf20_A	9.4268	9.3812	9.3268	**9.6794**	9.377	9.2748	9.377	10.5916	10.5181	_**10.6691**_	10.6634	10.6543	7.9833	**9.8106**	9.7217	9.3589	9.0476
T1_fl_no3_rf20_A	13.0112	12.4113	12.5837	**13.0518**	12.7327	11.3916	12.7327	19.1863	_**19.6365**_	19.4432	19.2673	19.1376	5.8282	10.0401	**13.0358**	12.7024	**13.4801**
T1_IR_no3_rf20_A	17.2015	16.7346	16.8578	**17.2879**	17.0695	16.1982	17.0695	24.352	_**25.4927**_	25.1391	25.206	25.1268	12.8519	14.6061	16.5361	16.9651	**17.8937**
T2_fl_no3_rf20_A	10.7109	8.807	9.2173	**10.7773**	9.126	9.3725	9.126	_**14.1139**_	14.0191	14.0735	14.0683	13.9819	7.7431	9.6682	10.6241	10.2401	10.5256
T2_SE_no3_rf20_A	5.0918	5.136	5.1297	5.1014	**5.2021**	3.655	**5.2021**	4.5997	4.5635	4.7643	4.9043	4.9766	3.0344	4.8571	4.9615	_**5.4078**_	5.1005
rf40																	
T2_EPI_no3_rf40_A	8.0268	7.7417	8.0037	**8.3053**	8.0075	6.5796	8.0551	8.5595	8.5667	8.6294	**8.713**	8.7043	4.8829	_**8.8351**_	8.5253	6.931	7.9874
PD_SE_no3_rf40_A	9.2317	**9.9317**	9.8752	9.7884	9.8907	9.8014	9.931	_**10.9943**_	10.9141	10.983	10.8903	10.8016	7.8655	**10.2841**	10.1978	8.2297	8.3794
T1_fl_no3_rf40_A	12.7345	11.7457	12.4879	12.8132	11.9649	**13.1594**	9.803	19.8825	_**20.6214**_	20.3131	20.0851	19.9104	5.6057	11.3557	**13.4931**	12.1156	**13.2268**
T1_IR_no3_rf40_A	17.0235	17.5838	17.8696	17.1471	**17.9537**	15.6717	13.4775	25.922	27.3023	_**27.3142**_	26.8721	27.0382	12.8272	15.3938	**17.8345**	16.9515	17.2342
T2_fl_no3_rf40_A	10.5099	9.3625	9.7041	**10.8468**	9.6109	9.5476	9.4659	14.5568	_**14.6421**_	14.3827	14.1837	14.0783	8.979	9.5731	10.9716	10.1576	9.7743
T2_SE_no3_rf40_A	5.0254	5.0987	**5.2646**	5.0426	5.2051	3.2855	5.1994	5.0764	5.0454	5.2027	**5.3389**	5.2308	3.5674	4.4303	**5.2499**	_**5.482**_	5.1089
rf100																	
T2_EPI_no3_rf100_A	7.5624	8.1084	**9.4208**	7.8283	9.0936	7.7404	9.1485	9.7064	9.7213	**9.7233**	9.6459	9.5729	4.8516	9.4831	_**9.9753**_	6.8049	**7.9919**
PD_SE_no3_rf100_A	8.5709	10.3523	10.4961	8.9639	10.4644	10.4095	**10.632**	12.1125	_**12.1763**_	12.0302	11.593	11.6196	3.335	**10.8171**	10.7643	**8.7101**	8.6319
T1_fl_no3_rf100_A	11.8031	10.6725	10.2027	11.8971	9.8182	**12.2453**	8.3029	21.0031	_**22.2493**_	21.7248	21.2311	20.9873	7.8931	13.9502	**14.7661**	12.104	**12.7093**
T1_IR_no3_rf100_A	16.5697	19.2582	20.2828	16.6514	19.2615	**21.0365**	16.6194	26.7304	29.7826	29.2689	_**30.1182**_	29.4809	15.9206	18.0611	**20.7005**	14.5505	**17.4783**
T2_fl_no3_rf100_A	9.7885	10.7547	10.7007	9.9958	10.6081	10.6745	**10.8257**	15.8517	_**16.0629**_	15.9937	15.294	15.1668	9.3128	11.0279	**12.2453**	**10.3685**	10.0626
T2_SE_no3_rf100_A	4.7557	5.3062	5.2691	4.7615	**5.3563**	4.3727	5.2891	5.8278	5.6952	5.8364	_**5.8795**_	5.8309	2.9766	3.7293	**5.1022**	3.8745	1.5531

No background = worse than the uncorrected, background = better than the uncorrected, bold = best parameters for the algorithm, underline = best correction for the image.

Table A.2: SNR values for GM, 3% noise and B field images.

	Uncorrected	N3_01_2_4	N3_03_2_4	N3_015_2_2	N3_015_2_4	N3_015_2_6	N3_015_4_4	FSL_2_20	FSL_3_10	FSL_3_20	FSL_3_30	FSL_4_20	SPM_30	SPM_60	SPM_90	PABIC_2cl	PABIC_3cl
rf20																	
T2_EPI_no3_rf20_B	8.1981	7.3655	7.5995	**8.2128**	7.5564	6.1407	7.5947	8.0931	**8.2483**	8.1276	8.1792	8.209	5.7199	<u>**8.3077**</u>	8.2482	7.0201	7.9697
PD_SE_no3_rf20_B	9.4642	9.302	9.2287	**10.0257**	9.2742	9.1089	9.2846	10.607	<u>**10.6642**</u>	10.6185	10.605	10.5686	7.4742	9.1519	9.2632	9.4057	8.9699
T1_fl_no3_rf20_B	13.0273	11.5534	11.9794	**13.1115**	12.18	10.4785	10.89	18.2814	18.03	18.2467	18.0643	<u>**18.3213**</u>	7.7266	11.3494	12.8013	10.3842	12.2568
T1_IR_no3_rf20_B	17.0301	16.7408	16.5106	**17.1296**	16.8843	16.066	16.108	23.419	<u>**25.2398**</u>	24.6565	24.4184	24.6788	13.8327	14.975	15.9812	16.4943	16.4249
T2_fl_no3_rf20_B	10.7473	9.068	9.2354	**11.0113**	9.2233	9.2773	9.2058	<u>**14.0629**</u>	14.0031	13.9939	13.882	13.839	8.7654	10.4129	10.4136	10.3709	10.519
T2_SE_no3_rf20_B	5.1181	5.1783	5.1423	5.1274	<u>**5.1945**</u>	4.0128	5.1543	4.871	4.9632	5.0137	5.1162	5.0339	2.7732	5.1608	5.1889	5.1435	**5.158**
rf40																	
T2_EPI_no3_rf40_B	8.0894	7.9405	**8.4417**	8.3625	8.1287	6.9825	8.2049	8.7744	8.8007	8.7953	8.7752	**8.8121**	5.36	<u>**9.0692**</u>	9.0666	7.0413	**8.3749**
PD_SE_no3_rf40_B	9.2768	9.7032	9.7284	**10.1403**	9.7163	9.6014	9.7848	10.8142	<u>**10.9207**</u>	10.8094	10.7672	10.6916	7.7807	9.5187	**9.765**	9.2563	9.5304
T1_fl_no3_rf40_B	12.7146	11.2741	11.9374	**12.8554**	11.193	11.956	8.6546	18.9905	<u>**20.0556**</u>	19.3229	19.141	19.3619	8.4515	12.2735	**13.2564**	11.0022	12.9452
T1_IR_no3_rf40_B	17.6189	18.0062	17.8203	17.6937	18.229	17.2014	**18.4296**	27.3353	<u>**27.3631**</u>	26.5103	26.913	27.3521	13.2537	17.4703	18.5931	17.6606	17.9354
T2_fl_no3_rf40_B	10.5525	9.5547	9.5736	**10.9334**	9.6479	9.7051	9.5832	14.6459	<u>**14.7614**</u>	14.6754	14.3813	14.3864	8.7439	10.7066	**11.1768**	10.4114	10.1727
T2_SE_no3_rf40_B	5.0657	5.1153	**5.1727**	5.0729	5.1627	3.861	5.1533	5.2113	5.2233	5.2923	**5.3066**	5.2632	3.6738	4.82	<u>**5.7225**</u>	5.3126	4.6698
rf100																	
T2_EPI_no3_rf100_B	7.5116	8.8785	**10.0369**	7.716	9.6264	8.6008	9.2895	9.9963	**10.082**	10.0187	9.8856	9.7126	7.9913	10.1141	<u>**10.2031**</u>	7.9659	**8.0803**
PD_SE_no3_rf100_B	8.4915	11.1624	11.2094	8.793	11.2828	10.1707	**11.2728**	<u>**11.9891**</u>	11.737	11.5784	11.2163	11.0665	7.6408	11.1154	**11.1596**	8.9798	**9.181**
T1_fl_no3_rf100_B	11.5743	9.9503	10.4127	11.6835	8.7813	**12.1855**	8.2311	20.6769	<u>**21.9287**</u>	20.9185	20.4192	20.5083	8.3847	13.803	**14.9126**	**13.0463**	9.9333
T1_IR_no3_rf100_B	16.0552	17.5365	**19.7639**	16.1729	18.3852	17.7231	13.6035	26.5897	28.0426	<u>**28.2887**</u>	28.0069	28.1489	19.4749	19.881	20.9369	**16.994**	16.768
T2_fl_no3_rf100_B	9.7003	10.9421	11.2534	9.8776	**11.2547**	10.7961	11.2482	**15.8205**	15.6049	15.1662	14.5637	14.3365	9.7624	11.8493	12.3583	10.5158	**10.8355**
T2_SE_no3_rf100_B	4.7228	5.2315	5.2647	4.7531	**5.3302**	4.6214	5.3282	5.8857	5.876	5.9127	**5.9583**	5.8432	5.135	6.1876	<u>**6.3949**</u>	4.4482	2.2237

No background = worse than the uncorrected, background = better than the uncorrected, bold = best parameters for the algorithm, underline = best correction for the image.

Table A.3: SNR values for GM, 3% noise and C field images.

	Uncorrected	N3_01_2_4	N3_03_2_4	N3_015_2_2	N3_015_2_4	N3_015_2_6	N3_015_4_4	FSL_2_20	FSL_3_10	FSL_3_20	FSL_3_30	FSL_4_20	SPM_30	SPM_60	SPM_90	PABIC_2cl	PABIC_3cl
rf20																	
T2_EPI_no3_rf20_C	8.2133	7.3854	7.3977	**8.2725**	7.6702	6.16	7.6817	8.1521	8.0385	8.2502	8.3733	**8.3819**	6.1305	7.0977	<u>8.4562</u>	7.2731	7.2146
PD_SE_no3_rf20_C	9.5078	9.3762	9.3335	**9.526**	9.3714	9.4399	9.4363	10.3866	10.3372	<u>**10.3909**</u>	10.363	10.3777	7.7693	**9.7554**	9.6079	9.3147	9.131
T1_fl_no3_rf20_C	13.1737	12.5273	12.1183	**13.2351**	12.5548	11.8649	12.3846	19.3094	<u>**20.1176**</u>	19.5713	19.3762	19.5423	6.7552	10.6384	13.0037	12.4902	12.8199
T1_IR_no3_rf20_C	17.4512	17.5037	17.142	17.526	17.7113	17.3386	**17.7637**	25.9392	<u>**27.1848**</u>	26.4131	26.5588	26.809	12.3863	15.4787	16.5521	17.0021	**18.0144**
T2_fl_no3_rf20_C	10.7954	9.1281	9.427	**10.9364**	9.4769	9.5785	9.3843	14.2301	14.2928	14.2834	14.2187	<u>**14.3082**</u>	8.6232	9.7071	10.7671	10.5179	10.725
T2_SE_no3_rf20_C	5.122	5.1065	5.0995	5.1199	5.1171	4.3272	<u>**5.1406**</u>	4.8469	4.8596	5.0175	5.0994	5.0233	1.8879	4.6177	4.9264	4.9859	5.0342
rf40																	
T2_EPI_no3_rf40_C	8.1503	7.4391	7.8037	**8.2241**	7.8458	6.162	7.8706	8.4117	8.4896	8.4797	8.529	**8.5411**	7.0527	8.653	<u>**8.7744**</u>	7.0659	8.0908
PD_SE_no3_rf40_C	9.4028	9.5786	9.5321	**9.829**	9.5863	9.7426	9.6225	10.7986	10.8348	10.8651	<u>**10.8848**</u>	10.8077	8.0282	**9.9774**	9.8338	**9.4426**	8.9981
T1_fl_no3_rf40_C	13.0354	12.4043	12.744	**13.1096**	12.7349	9.4363	11.0711	19.6709	<u>**20.2055**</u>	19.7198	19.4809	19.4867	5.8855	12.0974	**13.6273**	7.9725	**13.5856**
T1_IR_no3_rf40_C	16.8082	17.5381	17.553	16.9721	17.4573	**18.2477**	13.0467	25.4888	25.614	24.8675	25.1914	<u>**25.6217**</u>	14.9176	15.9255	**17.4828**	16.6447	16.748
T2_fl_no3_rf40_C	10.7035	9.3398	9.3866	**10.8931**	9.4271	9.6153	9.4953	14.7408	<u>**14.8297**</u>	14.6737	14.4523	14.5179	8.4003	10.0665	**11.1706**	10.5448	9.9682
T2_SE_no3_rf40_C	5.0905	5.1191	5.0636	5.0792	5.1554	3.9393	**5.1593**	4.9947	4.9961	5.0956	**5.1834**	5.0943	3.0041	5.0297	<u>**5.3801**</u>	5.131	**5.3011**
rf100																	
T2_EPI_no3_rf100_C	7.901	8.2582	**8.8457**	7.9965	8.639	7.3641	8.6353	9.218	**9.4666**	9.236	9.085	9.1643	7.6832	9.5789	<u>9.6285</u>	6.592	**7.9592**
PD_SE_no3_rf100_C	9.0301	10.345	**10.4427**	9.3508	10.385	10.3359	10.3453	11.4189	<u>**11.5725**</u>	11.4458	11.1515	11.2346	7.6747	9.9659	**10.6481**	8.9718	**9.5376**
T1_fl_no3_rf100_C	12.5854	12.8089	**13.128**	12.6375	12.3356	11.0702	12.6083	21.8351	21.9522	<u>**22.2352**</u>	21.4638	21.1679	5.8937	13.8625	**14.8571**	11.7371	11.4066
T1_IR_no3_rf100_C	18.0217	19.5451	19.7102	18.0827	19.9747	**21.0337**	18.665	28.7718	<u>**30.51**</u>	30.3655	30.0693	29.6908	13.143	19.782	**20.944**	18.5146	**19.3323**
T2_fl_no3_rf100_C	10.3208	9.9376	10.4822	**10.5073**	10.2392	10.2042	10.0615	15.6462	<u>**15.8861**</u>	15.52	14.91	15.0678	8.963	10.9904	**11.9405**	10.5023	**10.8405**
T2_SE_no3_rf100_C	4.9528	5.3479	5.2501	4.94	**5.3526**	4.197	5.3408	5.4956	**5.5534**	5.4921	5.5193	5.4833	3.7552	5.5172	<u>**5.9889**</u>	4.4025	4.1687

No background = worse than the uncorrected, background = better than the uncorrected, bold = best parameters for the algorithm, underline = best correction for the image.

Table A.4: SNR values for GM, 9% noise and A field images.

		Correction methods															
	Uncorrected	N3_01_2_4	N3_03_2_4	N3_015_2_2	N3_015_2_4	N3_015_2_6	N3_015_4_4	FSL_2_20	FSL_3_10	FSL_3_20	FSL_3_30	FSL_4_20	SPM_30	SPM_60	SPM_90	PABIC_2cl	PABIC_3cl
rf20																	
T2_EPI_no9_rf20_A	7.8299	7.4097	7.8257	**7.9107**	7.7563	7.1695	7.724	7.9655	**8.3228**	8.0131	8.0566	8.0673	3.4724	8.0186	**8.2002**	7.1602	7.3251
PD_SE_no9_rf20_A	8.8625	8.5016	8.5731	**8.8671**	8.5852	8.4263	8.5202	8.9248	8.8642	8.9877	**9.0119**	8.9822	5.1175	8.789	**8.9097**	8.309	8.4138
T1_fl_no9_rf20_A	7.7427	7.5471	7.6545	7.7454	7.6283	**7.9965**	6.8662	10.2582	**10.5475**	10.1937	10.0537	10.1634	4.3209	5.8447	7.5922	5.2239	5.1878
T1_IR_no9_rf20_A	6.6662	7.0681	7.0372	6.6253	**7.1611**	6.4567	5.9961	8.8489	**9.4047**	8.6807	8.4134	8.6422	4.8969	5.394	6.4201	0.6954	2.7107
T2_fl_no9_rf20_A	8.8725	7.5743	8.0774	8.8198	7.9264	8.0629	8.0775	10.2817	10.3063	10.3483	10.3398	**10.3796**	5.9715	7.4919	8.2588	7.5691	8.5002
T2_SE_no9_rf20_A	4.8684	4.8719	4.869	4.8568	4.8505	4.6288	**4.8992**	4.79	**4.9926**	4.7832	4.7957	4.8374	2.9449	4.5274	4.6665	2.3829	2.1216
rf40																	
T2_EPI_no9_rf40_A	7.7464	7.5857	**8.2714**	7.9086	8.0142	7.4159	7.9594	8.7117	**9.0376**	8.718	8.604	8.5785	5.5682	**8.6206**	8.457	7.1159	7.2201
PD_SE_no9_rf40_A	8.7291	8.8737	**9.1888**	9.1687	9.1177	8.2515	9.079	9.578	9.5636	9.6086	9.6335	**9.6351**	7.598	**9.2649**	9.1976	8.1149	8.4687
T1_fl_no9_rf40_A	7.7716	8.1085	8.1539	7.7934	8.1431	**8.3458**	8.1033	10.2248	**10.7243**	10.204	9.9683	10.3683	5.1573	6.593	**8.083**	**7.7753**	6.8828
T1_IR_no9_rf40_A	6.7248	7.1365	**7.3628**	6.7225	7.1798	6.3497	5.9597	9.1443	**9.4419**	9.1256	8.9855	9.1654	4.5631	6.0451	6.2482	0.71	2.4479
T2_fl_no9_rf40_A	8.81	7.8498	8.5386	**8.9787**	8.2968	8.7052	8.5767	10.8665	**10.9895**	10.854	10.8106	10.8711	7.5291	7.8449	**9.1974**	7.7863	8.7491
T2_SE_no9_rf40_A	4.8245	4.8515	**5.1473**	4.8339	4.9935	4.4526	4.9596	5.1991	5.3943	5.3883	5.4675	**5.5017**	3.0576	4.5931	**5.0846**	0.7585	1.8049
rf100																	
T2_EPI_no9_rf100_A	7.3923	7.3966	**8.3247**	7.5894	8.2236	7.3861	8.2543	9.2593	9.1806	**9.2785**	9.2138	9.2605	4.0555	7.2927	**8.8793**	6.0496	5.7326
PD_SE_no9_rf100_A	8.2696	9.0376	9.4813	8.5853	9.4083	9.3825	**9.4834**	10.285	10.2407	10.5565	10.6561	**10.6874**	6.3871	**10.1278**	9.8719	8.4337	8.3493
T1_fl_no9_rf100_A	7.7541	7.5439	8.0616	7.8058	7.6578	**8.5056**	6.7185	10.9329	11.2807	11.1826	11.2942	**11.7561**	4.0876	7.9309	**9.2482**	3.3513	5.4428
T1_IR_no9_rf100_A	6.9113	7.7479	**8.2078**	6.9194	8.1991	6.9357	6.1445	10.1205	**10.8228**	10.3751	10.3969	10.5878	5.6182	5.3962	**7.4589**	1.8741	2.737
T2_fl_no9_rf100_A	8.5342	8.7645	9.8325	8.6921	9.4346	**9.9283**	9.5727	11.8365	11.5205	11.9844	11.964	**12.2742**	3.2615	6.6669	**9.5867**	**8.7956**	7.5131
T2_SE_no9_rf100_A	4.6369	4.7309	**5.1853**	4.6405	4.9471	3.3362	4.9539	5.4407	**5.8337**	5.4272	5.5187	5.4688	3.9348	5.1733	**5.4803**	2.7721	2.2781

No background = worse than the uncorrected, background = better than the uncorrected, bold = best parameters for the algorithm, underline = best correction for the image.

A.1.2 SNR white matter

Table A.5: SNR values for WM, 3% noise and A field images.

	Uncorrected	N3_01_2_4	N3_03_2_4	N3_015_2_2	N3_015_2_4	N3_015_2_6	N3_015_4_4	FSL_2_20	FSL_3_10	FSL_3_20	FSL_3_30	FSL_4_20	SPM_30	SPM_60	SPM_90	PABIC_2cl	PABIC_3cl
rf20																	
T2_EPI_no3_rf20_A	7,1795	6,4280	6,5533	**7,2539**	6,6612	5,7371	6,6612	7,1701	**7,7552**	7,3109	7,3035	7,3426	3,9177	7,0204	**7,2961**	6,3511	5,9192
PD_SE_no3_rf20_A	8,9020	8,7457	8,6900	**9,0476**	8,7504	8,9719	8,7504	9,9895	10,0233	**10,0248**	9,9814	10,0067	7,6285	**9,1887**	9,0578	8,7424	8,4448
T1_fl_no3_rf20_A	16,4491	15,0767	15,0372	**16,4790**	15,4533	12,3899	15,4533	22,5900	22,6711	23,3445	**23,5136**	23,3903	6,8325	12,2297	16,0553	15,7589	**16,8931**
T1_IR_no3_rf20_A	26,4576	25,0886	25,0831	**26,5737**	25,6258	20,6522	25,6258	33,5289	36,6827	37,1233	**37,6115**	37,2706	18,1160	21,6365	24,7856	25,9493	**27,2867**
T2_fl_no3_rf20_A	11,3173	8,8530	9,2790	11,3122	9,1981	9,4226	9,1981	14,5342	14,3513	14,5319	**14,5957**	14,5061	7,9143	9,9568	10,9678	10,7398	11,0413
T2_SE_no3_rf20_A	3,7159	3,7457	3,7594	3,7161	**3,7944**	2,8800	**3,7944**	3,5420	3,6965	3,6485	3,6708	**3,7162**	2,3047	3,4895	3,5365	**3,9251**	3,6802
rf40																	
T2_EPI_no3_rf40_A	7,2073	6,6864	6,9677	**7,4069**	6,9206	6,2792	6,9724	7,6935	**7,9049**	7,7283	7,7280	7,7617	4,4759	7,7879	**7,4153**	6,0175	7,0286
PD_SE_no3_rf40_A	8,8858	9,2617	9,2070	9,2752	9,2349	**9,4882**	9,2876	10,3856	**10,4190**	10,3629	10,2607	10,2188	7,5981	**9,7208**	9,5322	7,8518	7,8980
T1_fl_no3_rf40_A	16,4097	14,3055	14,9440	**16,4787**	14,4951	14,3140	11,8780	23,5296	24,4080	24,8258	**24,8721**	24,6249	6,5893	13,8685	16,6483	15,3849	**16,7796**
T1_IR_no3_rf40_A	26,6950	26,4433	26,6961	26,8830	**26,9936**	20,5284	20,2371	35,7917	39,3285	**40,4886**	40,3449	40,3932	18,1991	22,8383	26,8421	26,1734	**26,9090**
T2_fl_no3_rf40_A	11,3204	9,4289	9,7725	**11,6034**	9,6918	9,6043	9,5785	15,0271	**15,0315**	14,9238	14,8238	14,7208	9,2963	9,9249	**11,3911**	10,8206	10,4876
T2_SE_no3_rf40_A	3,7448	3,7950	**3,9295**	3,7457	3,8763	2,6937	3,8713	3,8945	**4,0160**	3,9338	3,9745	3,9434	2,7109	3,2262	**3,7778**	4,0237	3,7193
rf100																	
T2_EPI_no3_rf100_A	7,1655	7,0259	**8,2728**	7,3773	7,9068	7,4035	7,9875	8,7779	**9,0281**	8,7869	8,6735	8,6843	4,3805	8,3410	**8,6933**	5,8685	**7,1937**
PD_SE_no3_rf100_A	8,7040	9,6822	9,8153	9,0392	9,7923	**10,2959**	9,9910	11,5687	**11,6947**	11,5144	11,2047	11,2226	3,2760	**10,3496**	10,1424	8,5950	8,5225
T1_fl_no3_rf100_A	16,0337	13,4466	12,3597	**16,1468**	11,9833	13,4233	10,1311	25,1222	26,2028	26,7456	**26,7723**	26,5603	9,6498	17,3672	**18,4697**	15,6776	**16,3267**
T1_IR_no3_rf100_A	27,3290	30,1755	**31,1124**	27,4911	29,8373	29,5270	25,7335	37,1919	42,1797	43,5735	**45,8725**	45,0420	22,7788	27,0679	31,4148	22,8363	27,8558
T2_fl_no3_rf100_A	11,1196	10,9763	10,8583	**11,3169**	10,7658	10,7851	11,0354	16,5925	16,6976	**16,9273**	16,4478	16,2648	9,9106	11,6145	12,8569	**11,2976**	10,9574
T2_SE_no3_rf100_A	3,7466	4,1768	4,1603	3,7469	**4,2073**	3,7031	4,1606	4,5074	**4,6328**	4,5010	4,4609	4,4909	2,3283	2,7897	3,7411	2,8520	1,0597

No background = worse than the uncorrected, background = better than the uncorrected, bold = best parameters for the algorithm, underline = best correction for the image.

Table A.6: SNR values for WM, 3% noise and B field images.

	Uncorrected	N3_01_2_4	N3_03_2_4	N3_015_2_2	N3_015_2_4	N3_015_2_6	N3_015_4_4	FSL_2_20	FSL_3_10	FSL_3_20	FSL_3_30	FSL_4_20	SPM_30	SPM_60	SPM_90	PABIC_2cl	PABIC_3cl
rf20																	
T2_EPI_no3_rf20_B	7,2495	6,3467	6,6162	7,2283	6,5357	5,8569	6,5823	7,2686	7,6149	7,2751	7,2407	7,2808	5,1606	7,2790	7,1611	6,0462	6,9872
PD_SE_no3_rf20_B	8,9713	8,6687	8,5971	9,3896	8,6525	8,8110	8,6787	10,0077	10,1595	9,9953	9,9581	9,9537	7,1485	8,5432	8,6025	8,7810	8,3434
T1_fl_no3_rf20_B	16,5414	14,0437	14,3362	16,6154	14,8081	11,4159	13,2754	21,6173	21,4492	22,2991	22,3156	22,5305	9,1285	13,8662	15,8049	12,9641	15,4929
T1_IR_no3_rf20_B	26,3234	25,1478	24,6176	26,4554	25,3914	20,7096	24,2400	32,3143	36,3696	36,5046	36,5637	36,7182	19,3862	22,2005	23,9946	25,3685	25,1253
T2_fl_no3_rf20_B	11,4008	9,1100	9,2961	11,6023	9,2965	9,3258	9,3056	14,5006	14,3483	14,4779	14,4418	14,3923	8,9456	10,7159	10,7554	10,9800	10,9985
T2_SE_no3_rf20_B	3,7532	3,7941	3,7946	3,7535	3,8084	3,2232	3,7877	3,7336	3,9158	3,7650	3,7846	3,7691	2,0878	3,7271	3,7162	3,7296	3,6956
rf40																	
T2_EPI_no3_rf40_B	7,3229	6,8417	7,3461	7,5154	7,0100	6,6631	7,1014	7,9070	8,1477	7,9107	7,8216	7,8972	4,9169	8,0146	7,8804	6,0790	7,3689
PD_SE_no3_rf40_B	9,0032	9,0450	9,0699	9,6886	9,0703	9,2990	9,1578	10,2430	10,4413	10,2375	10,2001	10,1717	7,4475	8,8864	9,0771	8,8654	9,0060
T1_fl_no3_rf40_B	16,5157	13,7911	14,2967	16,6628	13,5549	12,9996	10,5009	22,5328	23,7037	23,6652	23,8046	24,0745	10,0333	15,0605	16,4275	13,9264	16,3744
T1_IR_no3_rf40_B	27,6610	27,1382	26,6641	27,7754	27,4496	22,7826	27,7084	37,7994	39,5254	39,4043	40,5236	40,9617	18,8760	26,0570	28,0625	27,2702	27,6992
T2_fl_no3_rf40_B	11,4592	9,6229	9,6393	11,7936	9,7246	9,7639	9,7001	15,1608	15,1960	15,3022	15,1274	15,1403	9,0177	11,0496	11,5648	11,1274	10,8410
T2_SE_no3_rf40_B	3,8058	3,8408	3,8923	3,8061	3,8763	3,2011	3,8715	4,0089	4,1804	4,0241	3,9744	3,9910	2,7784	3,5139	4,1247	3,8768	3,3635
rf100																	
T2_EPI_no3_rf100_B	7,2703	7,6954	8,8813	7,4360	8,4344	8,2420	8,1582	9,1033	9,3900	9,1219	8,9870	8,9192	7,2735	8,9465	8,9443	7,1042	7,2542
PD_SE_no3_rf100_B	8,8065	10,4035	10,4899	9,0775	10,5566	10,3486	10,5925	11,5628	11,4208	11,2538	11,0159	10,9343	7,3422	10,4379	10,4653	8,8919	9,0147
T1_fl_no3_rf100_B	16,0437	12,5732	12,6710	16,1804	10,7140	13,3031	10,0131	24,8977	26,0519	26,0493	26,1219	26,3890	10,1086	17,0657	18,6575	16,7480	12,6899
T1_IR_no3_rf100_B	26,9961	27,8995	30,4862	27,1982	28,7489	24,5475	21,2870	37,2803	39,5271	42,3236	43,1081	43,7445	27,8506	29,9448	31,8569	26,7440	26,5866
T2_fl_no3_rf100_B	11,2516	11,1629	11,5121	11,4304	11,5366	10,9394	11,5638	16,7221	16,4333	16,2882	15,9201	15,6894	10,3155	12,3493	12,9122	11,4772	11,8907
T2_SE_no3_rf100_B	3,8059	4,1879	4,2270	3,8099	4,2566	3,9523	4,2577	4,5904	4,7938	4,5942	4,5783	4,5566	3,9271	4,5238	4,6278	3,3250	1,5059

Correction methods

No background = worse than the uncorrected, background = better than the uncorrected, bold = best parameters for the algorithm, underline = best correction for the image.

Table A.7: SNR values for WM, 3% noise and C field images.

	Uncorrected	N3_01_2_4	N3_03_2_4	N3_015_2_2	N3_015_2_4	N3_015_2_6	N3_015_4_4	FSL_2_20	FSL_3_10	FSL_3_20	FSL_3_30	FSL_4_20	SPM_30	SPM_60	SPM_90	PABIC_2cl	PABIC_3cl
rf20																	
T2_EPI_no3_rf20_C	7,2373	6,3575	6,4426	**7,2653**	6,6333	5,8771	6,6637	7,3171	7,4053	7,3706	7,3998	**7,4202**	5,5228	6,1836	**7,3203**	6,2590	6,1117
PD_SE_no3_rf20_C	8,9834	8,7422	8,6980	8,9146	8,7471	**9,1375**	8,8200	9,7947	**9,8360**	9,7720	9,7201	9,7610	7,4330	**9,1236**	8,9452	8,6935	8,5106
T1_fl_no3_rf20_C	16,6659	15,2082	14,4857	**16,7206**	15,2546	12,9272	15,0563	22,8098	23,9583	23,9097	23,9078	**24,0066**	7,9022	12,9629	16,0289	15,5997	16,0626
T1_IR_no3_rf20_C	26,8959	26,2820	25,5410	**27,0011**	26,6206	22,2583	26,7176	35,7697	39,2000	39,0977	39,7358	**39,8671**	17,4981	22,9400	24,8476	26,2772	**27,4608**
T2_fl_no3_rf20_C	11,4162	9,1705	9,4924	**11,4940**	9,5537	9,6279	9,4872	14,6684	14,6414	14,7668	14,7745	**14,8639**	8,8814	10,0411	11,1510	11,0049	11,2096
T2_SE_no3_rf20_C	3,7415	3,7278	3,7434	3,7398	3,7355	3,4249	**3,7549**	3,7128	**3,8208**	3,7589	3,7637	3,7532	1,4189	3,3200	3,5153	3,6318	3,6271
rf40																	
T2_EPI_no3_rf40_C	7,3207	6,3972	6,7916	7,3468	6,7693	5,8792	6,8090	**7,5701**	**7,8336**	7,6037	7,5804	7,6274	6,3542	7,6025	**7,6266**	6,0507	7,1495
PD_SE_no3_rf40_C	9,0568	8,9313	8,8868	9,3507	8,9495	9,4327	9,0032	**10,2151**	**10,3460**	10,2664	10,2787	10,2395	7,6948	**9,3298**	9,1617	8,8962	8,4505
T1_fl_no3_rf40_C	16,8123	15,0999	15,2555	16,8830	15,3973	10,2741	13,5050	**23,3130**	23,9834	24,1697	**24,1956**	24,1715	7,0416	14,9271	**16,9174**	10,0115	**17,1963**
T1_IR_no3_rf40_C	26,5506	26,4874	26,2555	26,7997	26,2758	24,1279	19,6276	**35,2809**	36,8802	36,9461	37,9745	**38,3899**	21,0194	23,7035	26,2947	25,8398	26,2411
T2_fl_no3_rf40_C	11,5376	9,3874	9,4550	11,6749	9,5036	9,6742	9,6064	**15,2460**	15,2497	**15,2654**	15,1531	15,2097	8,7158	10,4343	**11,5838**	11,1949	10,6950
T2_SE_no3_rf40_C	3,7930	3,8024	3,7833	3,7764	3,8362	3,2085	**3,8397**	3,8361	**3,9727**	3,8556	3,8653	3,8451	2,2600	3,6248	**3,8516**	3,7350	**3,8403**
rf100																	
T2_EPI_no3_rf100_C	7,4640	7,0938	7,7674	7,5221	7,4859	7,0466	7,5130	**8,3585**	**8,8008**	8,3760	8,2191	8,3263	7,0003	**8,4168**	8,3990	5,6793	7,0171
PD_SE_no3_rf100_C	9,1479	9,6505	9,7659	9,4168	9,7180	10,0446	9,7116	**10,9695**	**11,1378**	11,0117	10,8448	10,8740	7,5759	9,4688	**10,0328**	8,6826	**9,3584**
T1_fl_no3_rf100_C	17,0633	15,9484	15,9115	17,1271	15,0118	12,1632	15,3376	**26,2409**	26,0169	**27,5700**	27,2529	26,9668	7,2238	17,3506	**18,6656**	15,0167	14,5549
T1_IR_no3_rf100_C	29,7023	30,5930	30,1707	29,8467	30,8103	29,4343	28,6267	**40,1746**	43,6581	45,5359	**46,1038**	45,6688	19,0091	29,8146	**31,8384**	29,2544	30,6024
T2_fl_no3_rf100_C	11,6966	10,0510	10,6397	11,8742	10,3848	10,3035	10,2437	**16,4911**	**16,5646**	16,5128	16,1434	16,1859	9,5413	11,6433	**12,6146**	11,3075	**11,8486**
T2_SE_no3_rf100_C	3,8847	4,1573	4,1069	3,8666	4,1627	3,5882	4,1556	4,2595	**4,5207**	4,2473	4,2029	4,2317	2,9323	4,1132	**4,4122**	3,2291	2,9775

No background = worse than the uncorrected, background = better than the uncorrected, bold = best parameters for the algorithm, underline = best correction for the image.

Table A.8: SNR values for WM, 9% noise and A field images.

	Uncorrected	N3_01_2_4	N3_03_2_4	N3_015_2_2	N3_015_2_4	N3_015_2_6	N3_015_4_4	FSL_2_20	FSL_3_10	FSL_3_20	FSL_3_30	FSL_4_20	SPM_30	SPM_60	SPM_90	PABIC_2cl	PABIC_3cl
rf20																	
T2_EPI_no9_rf20_A	6,9038	6,4006	6,8316	**6,9484**	6,7271	6,8291	6,7038	7,1258	<u>7,6357</u>	7,1273	7,0902	7,1444	3,1837	7,0607	**7,1221**	6,2104	6,3468
PD_SE_no9_rf20_A	8,3749	7,8915	7,9859	8,3320	7,9817	8,1013	7,9340	8,3943	8,4231	<u>8,4481</u>	8,4475	8,4462	4,9185	8,2859	8,3463	7,7748	7,8441
T1_fl_no9_rf20_A	9,7354	9,1993	9,2371	**9,7381**	9,2695	8,6154	8,3277	12,1051	12,1125	12,1763	12,2089	<u>12,2910</u>	5,0393	7,0645	9,3091	6,5427	6,3913
T1_IR_no9_rf20_A	10,0777	10,4611	10,2902	10,0239	**10,5270**	8,0670	8,7508	12,1361	<u>12,5195</u>	12,2563	12,1575	12,3843	6,6058	7,7680	9,4325	0,9943	4,0292
T2_fl_no9_rf20_A	9,3723	7,6060	8,1692	9,2890	7,9970	8,0797	8,1793	10,5587	10,5252	10,6758	10,7242	<u>10,7676</u>	6,0744	7,6560	8,4979	7,8907	8,9622
T2_SE_no9_rf20_A	3,6076	3,6061	3,6046	3,5900	3,5819	**3,6232**	3,6229	3,7962	<u>4,1417</u>	3,6927	3,6134	3,6714	2,2847	3,2964	3,3616	1,6576	1,4654
rf40																	
T2_EPI_no9_rf40_A	6,9645	6,5637	**7,2241**	7,0693	6,9526	7,0720	6,9231	7,8158	<u>8,3189</u>	7,7886	7,6169	7,6537	5,1369	**7,6609**	7,3776	6,1578	6,2343
PD_SE_no9_rf40_A	8,4011	8,2357	8,5611	**8,7418**	8,4836	7,9482	8,4616	9,0267	9,1088	9,0650	9,0806	<u>9,1207</u>	7,2946	**8,7139**	8,6037	7,6337	8,0016
T1_fl_no9_rf40_A	9,9556	**9,9923**	9,8994	9,9762	9,9521	9,0427	9,9196	12,1071	12,3540	12,2504	12,1917	<u>12,6405</u>	6,0346	8,0060	**9,9650**	9,7978	8,5832
T1_IR_no9_rf40_A	10,3564	10,7474	**10,8845**	10,3594	10,7114	8,0454	8,8122	12,5844	12,6379	12,9675	13,0883	<u>13,2541</u>	6,1403	8,7619	9,2414	1,0256	3,6543
T2_fl_no9_rf40_A	9,4827	7,9117	8,6445	**9,6206**	8,3858	8,7390	8,6892	11,1913	11,2522	11,2462	11,2849	<u>11,3589</u>	7,7520	8,1054	**9,5322**	8,2096	9,2726
T2_SE_no9_rf40_A	3,6411	3,6487	**3,8782**	3,6417	3,7554	3,5918	3,7385	4,1124	<u>4,4861</u>	4,1741	4,1401	4,2067	2,3852	3,3657	**3,6848**	0,5279	1,2481
rf100																	
T2_EPI_no9_rf100_A	7,0109	6,5019	**7,3913**	7,1618	7,2350	7,1112	7,2784	8,3718	<u>8,5151</u>	8,3875	8,3008	8,4265	3,8813	6,6651	**7,7884**	5,3401	5,0257
PD_SE_no9_rf100_A	8,3965	8,4547	8,9323	8,6626	8,8414	**9,1379**	8,9426	9,8075	9,8520	10,1194	10,2820	<u>10,3416</u>	6,3385	**9,8187**	9,4372	8,1691	8,0406
T1_fl_no9_rf100_A	10,4564	9,5767	10,0091	10,5194	9,5064	9,5122	8,3486	13,0987	13,1645	13,6620	14,1414	<u>14,6966</u>	4,9782	9,8405	11,6396	4,1854	6,9413
T1_IR_no9_rf100_A	11,1839	12,1297	12,4449	11,2097	**12,5775**	9,1062	9,3905	14,0863	14,7011	15,0232	15,5131	<u>15,7402</u>	7,7691	7,9158	11,1858	2,7949	4,1161
T2_fl_no9_rf100_A	9,6810	9,0040	10,1349	9,8281	9,7026	**10,1376**	9,8683	12,3482	11,9295	12,6334	12,7968	<u>13,1215</u>	3,3576	6,8791	**9,9191**	9,5682	8,1120
T2_SE_no9_rf100_A	3,6822	3,7506	**4,1181**	3,6819	3,9224	2,8352	3,9316	4,3293	<u>4,9107</u>	4,2574	4,2438	4,2728	3,1389	3,9139	**4,1050**	1,9897	1,6395

No background = worse than the uncorrected, background = better than the uncorrected, bold = best parameters for the algorithm, underline = best correction for the image.

A.1.3 CNR between grey matter and white matter

Table A.9: CNR between GM and WM, 3% noise and A field images.

	Uncorrected	N3_01_2_4	N3_03_2_4	N3_015_2_2	N3_015_2_4	N3_015_2_6	N3_015_4_4	FSL_2_20	FSL_3_10	FSL_3_20	FSL_3_30	FSL_4_20	SPM_30	SPM_60	SPM_90	PABIC_2cl	PABIC_3cl
rf20																	
T2_EPI_no3_rf20_A	0,9736	1,0258	0,9730	1,0179	1,0378	0,2841	**1,0505**	0,8035	0,6655	0,8854	**0,9791**	0,9678	0,4070	1,0473	**1,1100**	1,0399	**1,0471**
PD_SE_no3_rf20_A	0,5249	0,6355	**0,6368**	0,6319	0,6266	0,3029	0,6182	0,6022	0,4948	0,6443	<u>0,6820</u>	0,6477	0,2674	0,5633	0,6655	**0,6165**	0,6027
T1_fl_no3_rf20_A	3,4378	2,6654	2,4535	3,4272	2,7205	0,9984	2,6042	3,4037	3,0347	3,9013	4,2464	<u>4,2528</u>	0,9836	2,5127	3,1552	3,0565	3,4129
T1_IR_no3_rf20_A	9,2561	8,3541	8,2253	**9,2858**	8,5562	4,4540	7,6879	9,1769	11,1900	11,9842	<u>12,4054</u>	12,1438	5,3719	7,4445	9,0076	8,9842	**9,3930**
T2_fl_no3_rf20_A	0,6064	0,0460	0,0617	0,5349	0,0721	0,0501	0,0953	0,4203	0,3322	0,4584	0,5273	0,5241	0,3172	0,3519	0,4196	0,4997	0,5156
T2_SE_no3_rf20_A	1,3760	1,3903	1,3702	1,3853	**1,4077**	0,7750	1,3830	1,0577	0,8669	1,1158	1,2335	1,2604	0,8565	1,2041	**1,4721**	<u>1,4827</u>	1,4203
rf40																	
T2_EPI_no3_rf40_A	0,8195	1,0553	1,0359	0,8984	**1,0869**	0,3004	1,0826	0,8661	0,6618	0,9011	**0,9850**	0,9426	0,4070	1,0473	**1,1100**	0,9135	**0,9588**
PD_SE_no3_rf40_A	0,3459	<u>0,6700</u>	0,6682	0,5131	0,6558	0,3132	0,6434	0,6088	0,4952	0,6201	**0,6297**	0,5828	0,2674	0,5633	**0,6655**	0,3779	**0,4814**
T1_fl_no3_rf40_A	3,6751	2,5599	2,4561	3,6654	2,5302	1,1547	2,0750	3,6471	3,7866	4,5127	<u>4,7870</u>	4,7145	0,9836	2,5127	3,1552	3,2693	3,5528
T1_IR_no3_rf40_A	9,6715	8,8595	8,8265	**9,7359**	9,0399	4,8566	6,7596	9,8697	12,0262	13,1744	13,4727	<u>13,3550</u>	5,3719	7,4445	9,0076	9,2219	**9,6747**
T2_fl_no3_rf40_A	0,8105	0,0664	0,0684	0,7565	0,0809	0,0567	0,1126	0,4703	0,3894	0,5411	0,6401	0,6425	0,3172	0,3519	0,4196	0,6630	0,7133
T2_SE_no3_rf40_A	1,2807	1,3037	**1,3351**	1,2969	1,3288	0,5917	1,3282	1,1819	1,0294	1,2689	**1,3644**	1,2874	0,8565	1,2041	<u>1,4721</u>	1,4582	1,3896
rf100																	
T2_EPI_no3_rf100_A	0,3969	1,0824	1,1481	0,4510	**1,1868**	0,3369	1,1611	0,9286	0,6932	0,9364	**0,9724**	0,8886	0,4711	1,1421	**1,2820**	**0,9363**	0,7982
PD_SE_no3_rf100_A	0,1331	0,6701	<u>0,6808</u>	0,0753	0,6721	0,1136	0,6410	**0,5438**	0,4816	0,5157	0,3882	0,3970	0,0590	0,4675	**0,6219**	0,1151	0,1094
T1_fl_no3_rf100_A	4,2307	2,7741	2,1570	**4,2497**	2,1651	1,1781	1,8282	4,1191	3,9535	5,0208	5,5412	<u>5,5730</u>	1,7567	3,4169	3,7036	3,5735	3,6174
T1_IR_no3_rf100_A	10,7594	**10,9173**	10,8296	10,8397	10,5758	8,4905	9,1142	10,4614	12,3971	14,3046	<u>15,7543</u>	15,5611	6,8581	9,0068	10,7143	8,2857	10,3775
T2_fl_no3_rf100_A	1,3311	0,2216	0,1576	1,3211	0,1577	0,1106	0,2097	0,7407	0,6347	0,9336	1,1538	1,0980	0,5978	0,5866	0,6116	0,9290	0,8948
T2_SE_no3_rf100_A	1,0090	1,1295	1,1088	1,0146	**1,1490**	0,6696	1,1285	1,3205	1,0624	1,3355	<u>1,4186</u>	1,3400	0,6483	0,9396	**1,3611**	1,0225	0,4934

No background = worse than the uncorrected, background = better than the uncorrected, bold = best parameters for the algorithm, underline = best correction for the image.

Table A.10: CNR between GM and WM, 3% noise and B field images.

	Uncorrected	N3_01_2_4	N3_03_2_4	N3_015_2_2	N3_015_2_4	N3_015_2_6	N3_015_4_4	FSL_2_20	FSL_3_10	FSL_3_20	FSL_3_30	FSL_4_20	SPM_30	SPM_60	SPM_90	PABIC_2cl	PABIC_3cl
rf20																	
T2_EPI_no3_rf20_B	0,9486	1,0188	0,9832	0,9845	**1,0208**	0,2838	1,0124	0,8245	0,6333	0,8525	0,9385	0,9282	0,5594	1,0287	<u>**1,0871**</u>	0,9738	**0,9825**
PD_SE_no3_rf20_B	0,4930	0,6332	0,6316	**0,6361**	0,6217	0,2979	0,6060	0,5994	0,5047	0,6231	**0,6469**	0,6149	0,3257	0,6087	<u>**0,6607**</u>	0,6246	**0,6265**
T1_fl_no3_rf20_B	3,5141	2,4904	2,3568	3,5039	2,6282	0,9374	2,3854	3,3360	3,4193	4,0524	<u>**4,2514**</u>	4,2092	1,4019	2,5168	3,0036	2,5799	3,2361
T1_IR_no3_rf20_B	9,2933	8,4070	8,1070	**9,3258**	8,5071	4,6436	8,1320	8,8953	11,1298	11,8480	<u>**12,1453**</u>	12,0393	5,5535	7,2254	8,0134	8,8742	8,7004
T2_fl_no3_rf20_B	0,6535	0,0420	0,0607	0,5910	0,0732	0,0485	0,0998	0,4377	0,3452	0,4839	0,5598	0,5533	0,1801	0,3030	0,3418	0,6092	0,4795
T2_SE_no3_rf20_B	1,3649	1,3842	1,3477	1,3739	**1,3860**	0,7897	1,3666	1,1374	1,0473	1,2488	1,3316	1,2649	0,6854	1,4337	<u>**1,4727**</u>	1,4140	**1,4624**
rf40																	
T2_EPI_no3_rf40_B	0,7665	1,0989	1,0956	0,8471	**1,1187**	0,3194	1,1036	0,8674	0,6530	0,8846	**0,9536**	0,9149	0,4431	1,0546	<u>**1,1863**</u>	0,9623	**1,0061**
PD_SE_no3_rf40_B	0,2736	0,6582	**0,6585**	0,4517	0,6461	0,3024	0,6270	0,5712	0,4794	**0,5719**	0,5671	0,5199	0,3332	0,6323	<u>**0,6879**</u>	0,3909	**0,5244**
T1_fl_no3_rf40_B	3,8011	2,5170	2,3593	**3,8073**	2,3619	1,0436	1,8463	3,5424	3,6482	4,3423	4,6636	<u>**4,7126**</u>	1,5817	2,7871	3,1711	2,9242	3,4292
T1_IR_no3_rf40_B	10,0421	9,1320	8,8438	**10,0816**	9,2206	5,5812	9,2788	10,4641	12,1623	12,8940	<u>**13,6107**</u>	13,6097	5,6224	8,5867	9,4693	9,6096	9,7638
T2_fl_no3_rf40_B	0,9067	0,0682	0,0657	0,8602	0,0767	0,0588	0,1169	0,5149	0,4346	0,6268	0,7461	0,7540	0,2738	0,3430	0,3879	0,7160	0,6683
T2_SE_no3_rf40_B	1,2599	1,2745	1,2804	1,2668	**1,2864**	0,6599	1,2818	1,2024	1,0428	1,2682	**1,3322**	1,2723	0,8954	1,3061	<u>**1,5978**</u>	**1,4357**	1,3063
rf100																	
T2_EPI_no3_rf100_B	0,2413	1,1831	1,1556	0,2799	**1,1920**	0,3588	1,1313	0,8930	0,6920	0,8968	**0,8986**	0,7934	0,7177	1,1676	<u>**1,2588**</u>	**0,8616**	0,8261
PD_SE_no3_rf100_B	0,3150	<u>**0,7589**</u>	0,7194	0,2845	0,7262	0,1779	0,6802	**0,4263**	0,3163	0,3247	0,2004	0,1321	0,2985	0,6776	**0,6943**	0,0879	0,1662
T1_fl_no3_rf100_B	4,4694	2,6229	2,2583	**4,4969**	1,9326	1,1175	1,7820	4,2208	4,1232	5,1309	5,7027	<u>**5,8807**</u>	1,7239	3,2627	3,7449	3,7017	2,7567
T1_IR_no3_rf100_B	10,9409	10,3629	10,7222	**11,0253**	10,3637	6,8244	7,6835	10,6906	11,4845	14,0348	15,1012	<u>**15,5956**</u>	8,3757	10,0639	10,9200	9,7500	9,8186
T2_fl_no3_rf100_B	1,5512	0,2208	0,2586	<u>**1,5528**</u>	0,2819	0,1433	0,3156	0,9015	0,8284	1,1220	1,3564	1,3529	0,5531	0,5001	0,5540	0,9614	1,0552
T2_SE_no3_rf100_B	0,9169	1,0436	1,0376	0,9432	**1,0736**	0,6690	1,0705	1,2953	1,0822	1,3185	**1,3800**	1,2866	1,2079	1,6637	<u>**1,7670**</u>	**1,1233**	0,7178

No background = worse than the uncorrected, background = better than the uncorrected, bold = best parameters for the algorithm, underline = best correction for the image.

Table A.11: CNR between GM and WM, 3% noise and C field images.

	Uncorrected	N3_01_2_4	N3_03_2_4	N3_015_2_2	N3_015_2_4	N3_015_2_6	N3_015_4_4	FSL_2_20	FSL_3_10	FSL_3_20	FSL_3_30	FSL_4_20	SPM_30	SPM_60	SPM_90	PABIC_2cl	PABIC_3cl
rf20																	
T2_EPI_no3_rf20_C	0,9760	1,0279	0,9551	1,0072	**1,0369**	0,2830	1,0180	0,8349	0,6332	0,8796	0,9735	0,9617	0,6078	0,9141	_1,1359_	**1,0141**	1,1030
PD_SE_no3_rf20_C	0,5244	0,6340	**0,6355**	0,6114	0,6243	0,3024	0,6162	0,5919	0,5012	0,6189	**0,6429**	0,6167	0,3362	0,6319	_0,6627_	0,6212	0,6204
T1_fl_no3_rf20_C	3,4921	2,6809	2,3674	3,4855	2,6998	1,0623	2,6717	3,5004	3,8407	4,3385	_4,5316_	4,4642	1,1471	2,3246	3,0252	3,1094	3,2427
T1_IR_no3_rf20_C	9,4448	8,7783	8,3990	**9,4751**	8,9093	4,9198	8,9539	9,8305	12,0152	12,6846	_13,1770_	13,0581	5,1118	7,4613	8,2955	9,2750	**9,4464**
T2_fl_no3_rf20_C	0,6208	0,0424	0,0654	0,5576	0,0768	0,0495	0,1029	0,4383	0,3486	0,4833	0,5558	0,5557	0,2582	0,3340	0,3839	0,4870	0,4846
T2_SE_no3_rf20_C	1,3805	1,3788	1,3561	1,3801	1,3816	0,9023	**1,3858**	1,1342	1,0388	1,2586	1,3357	1,2701	0,4690	1,2977	_1,4111_	1,3541	**1,4071**
rf40																	
T2_EPI_no3_rf40_C	0,8296	1,0418	1,0120	0,8773	**1,0765**	0,2828	1,0616	0,8416	0,6560	0,8760	**0,9486**	0,9137	0,6985	1,0505	_1,1478_	**1,0152**	0,9413
PD_SE_no3_rf40_C	0,3459	**0,6474**	0,6453	0,4783	0,6368	0,3099	0,6193	0,5835	0,4888	0,5988	**0,6062**	0,5681	0,3334	0,6476	_0,6720_	0,5463	**0,5477**
T1_fl_no3_rf40_C	3,7768	2,6955	2,5115	3,7734	2,6624	0,8377	2,4340	3,6421	3,7779	4,4499	_4,7148_	4,6848	1,1561	2,8296	3,2900	2,0390	3,6107
T1_IR_no3_rf40_C	9,7424	8,9493	8,7025	**9,8276**	8,8184	5,8802	6,5809	9,7921	11,2662	12,0786	_12,7832_	12,7682	6,1017	7,7780	8,8119	9,1951	9,4931
T2_fl_no3_rf40_C	0,8341	0,0476	0,0684	0,7818	0,0765	0,0589	0,1111	0,5052	0,4200	0,5917	0,7008	0,6918	0,3155	0,3678	0,4133	0,6501	0,7269
T2_SE_no3_rf40_C	1,2975	1,3168	1,2803	1,3027	1,3192	0,7308	**1,3196**	1,1586	1,0234	1,2400	**1,3180**	1,2491	0,7441	1,4049	_1,5284_	1,3961	**1,4607**
rf100																	
T2_EPI_no3_rf100_C	0,4370	**1,1644**	1,0783	0,4744	1,1531	0,3175	1,1223	0,8594	0,6658	0,8600	**0,8659**	0,8380	0,6829	1,1621	_1,2295_	0,9127	**0,9421**
PD_SE_no3_rf100_C	0,1178	_0,6945_	0,6768	0,0659	0,6670	0,2913	0,6338	**0,4494**	0,4347	0,4341	0,3067	0,3606	0,0988	0,4971	**0,6153**	0,2892	0,1792
T1_fl_no3_rf100_C	4,4779	3,1395	2,7835	**4,4896**	2,6762	1,0931	2,7293	4,4059	4,0647	5,3348	5,7890	_5,7990_	1,3300	3,4881	3,8085	3,2796	3,1483
T1_IR_no3_rf100_C	11,6806	11,0479	10,4604	**11,7641**	10,8356	8,4006	9,9617	11,4028	13,1481	15,1704	_16,0345_	15,9781	5,8661	10,0326	10,8945	10,7398	11,2701
T2_fl_no3_rf100_C	1,3758	0,1134	0,1575	1,3669	0,1457	0,0993	0,1822	0,8449	0,6785	0,9928	1,2334	1,1181	0,5782	0,6529	0,6740	0,8053	1,0081
T2_SE_no3_rf100_C	1,0681	**1,1906**	1,1432	1,0734	1,1899	0,6088	1,1852	1,2360	1,0327	1,2448	**1,3164**	1,2516	0,8229	1,4040	_1,5767_	1,1734	**1,1912**

No background = worse than the uncorrected, background = better than the uncorrected, bold = best parameters for the algorithm, underline = best correction for the image.

Table A.12: CNR between GM and WM, 9% noise and A field.

	Uncorrected	N3_01_2_4	N3_03_2_4	N3_015_2_2	N3_015_2_4	N3_015_2_6	N3_015_4_4	FSL_2_20	FSL_3_10	FSL_3_20	FSL_3_30	FSL_4_20	SPM_30	SPM_60	SPM_90	PABIC_2cl	PABIC_3cl
rf20																	
T2_EPI_no9_rf20_A	0,9261	1,0091	0,9941	0,9623	**1,0292**	0,3403	1,0201	0,8397	0,6871	0,8858	**0,9663**	0,9228	0,2887	0,9579	_**1,0780**_	0,9497	**0,9783**
PD_SE_no9_rf20_A	0,4876	_**0,6101**_	0,5872	0,5351	0,6035	0,3249	0,5862	0,5305	0,4410	0,5396	**0,5643**	0,5359	0,1990	0,5030	**0,5634**	0,5343	**0,5696**
T1_fl_no9_rf20_A	1,9927	1,6522	1,5826	1,9926	1,6411	0,6189	1,4615	1,8469	1,5650	1,9826	_**2,1552**_	2,1276	0,7184	1,2199	1,7169	1,3188	1,2035
T1_IR_no9_rf20_A	3,4114	3,3930	3,2529	3,3987	3,3660	1,6103	2,7547	3,2873	3,1148	3,5756	_**3,7441**_	3,7421	1,7089	2,3740	3,0124	0,2989	1,3185
T2_fl_no9_rf20_A	0,4998	0,0317	0,0918	0,4692	0,0707	0,0168	0,1017	0,2769	0,2189	0,3275	0,3844	0,3880	0,1029	0,1641	0,2391	0,3216	0,4620
T2_SE_no9_rf20_A	1,2609	1,2658	1,2644	1,2668	1,2686	1,0056	**1,2763**	0,9938	0,8509	1,0905	1,1823	1,1660	0,6601	1,2310	_**1,3049**_	0,7253	0,6562
rf40																	
T2_EPI_no9_rf40_A	0,7819	1,0219	1,0473	0,8393	**1,0616**	0,3438	1,0363	0,8959	0,7187	0,9294	**0,9871**	0,9248	0,4314	0,9597	_**1,0794**_	0,9581	**0,9858**
PD_SE_no9_rf40_A	0,3280	_**0,6380**_	0,6277	0,4269	0,6341	0,3032	0,6174	0,5513	0,4548	0,5436	**0,5529**	0,5144	0,3034	0,5511	**0,5940**	**0,4812**	0,4671
T1_fl_no9_rf40_A	2,1840	1,8838	1,7455	2,1828	1,8090	0,6969	1,8163	1,8823	1,6297	2,0464	2,2235	_**2,2722**_	0,8773	1,4130	1,8820	2,0225	1,7004
T1_IR_no9_rf40_A	3,6316	3,6110	3,5217	**3,6369**	3,5316	1,6957	2,8525	3,4401	3,1959	3,8418	_**4,1027**_	4,0887	1,5772	2,7168	2,9932	0,3156	1,2065
T2_fl_no9_rf40_A	0,6727	0,0619	0,1059	0,6419	0,0889	0,0338	0,1125	0,3248	0,2628	0,3922	0,4743	0,4878	0,2229	0,2605	0,3348	0,4233	0,5235
T2_SE_no9_rf40_A	1,1833	1,2028	**1,2691**	1,1923	1,2381	0,8608	1,2211	1,0867	0,9082	1,2141	**1,3274**	1,2950	0,6724	1,2274	_**1,3999**_	0,2305	0,5568
rf100																	
T2_EPI_no9_rf100_A	0,3814	0,8947	0,9334	0,4276	**0,9886**	0,2749	0,9759	0,8874	0,6655	0,8909	**0,9130**	0,8340	0,1743	0,6277	_**1,0909**_	**0,7095**	0,6277
PD_SE_no9_rf100_A	0,1269	_**0,5829**_	0,5490	0,0774	0,5669	0,2446	0,5407	**0,4775**	0,3887	0,4371	0,3742	0,3457	0,0486	0,3091	**0,4347**	0,2646	**0,3091**
T1_fl_no9_rf100_A	2,7023	2,0328	1,9474	**2,7136**	1,8486	1,0066	1,6301	2,1658	1,8838	2,4794	2,8471	_**2,9405**_	0,8905	1,9096	2,3914	0,8341	1,9096
T1_IR_no9_rf100_A	4,2726	**4,3818**	4,2371	4,2902	4,3784	2,1705	3,2460	3,9657	3,8783	4,6480	5,1162	_**5,1524**_	2,1509	2,5196	3,7270	0,9208	2,5196
T2_fl_no9_rf100_A	1,1468	0,2396	0,3024	1,1360	0,2680	0,2093	0,2956	0,5116	0,4091	0,6490	0,8329	0,8473	0,0961	0,2123	0,3324	0,7725	0,2123
T2_SE_no9_rf100_A	0,9547	0,9803	**1,0672**	0,9586	1,0247	0,5010	1,0223	1,1115	0,9230	1,1698	**1,2749**	1,1960	0,7960	1,2594	_**1,3753**_	0,7824	**1,2594**

No background = worse than the uncorrected, background = better than the uncorrected, bold = best parameters for the algorithm, underline = best correction for the image.

A.1.4 CV grey matter

Table A.13: CV values for GM, 3% noise and A field images.

	Uncorrected	N3_01_2_4	N3_03_2_4	N3_015_2_2	N3_015_2_4	N3_015_2_6	N3_015_4_4	FSL_2_20	FSL_3_10	FSL_3_20	FSL_3_30	FSL_4_20	SPM_30	SPM_60	SPM_90	PABIC_2cl	PABIC_3cl
rf20																	
T2_EPI_no3_rf20_A	0,0865	0,1103	0,0888	**0,0834**	0,0948	0,0854	0,0932	0,0774	**0,0753**	0,0782	0,0794	0,0777	0,0893	0,0814	**0,0793**	**0,0833**	0,1069
PD_SE_no3_rf20_A	0,0668	0,0513	0,0515	0,0547	0,0512	**0,0511**	0,0518	0,0502	**0,0489**	0,0501	0,0513	0,0513	0,0532	0,0512	**0,0508**	0,0567	0,0579
T1_fl_no3_rf20_A	0,1495	0,1387	0,1381	0,1479	0,1380	0,1451	**0,1377**	0,1317	**0,1286**	0,1327	0,1337	0,1334	0,1427	0,1401	**0,1374**	0,1391	0,1449
T1_IR_no3_rf20_A	0,2740	0,2658	**0,2645**	0,2736	0,2658	0,2714	0,2662	0,2563	**0,2523**	0,2583	0,2598	0,2585	**0,2614**	0,2648	0,2661	0,2710	**0,2697**
T2_fl_no3_rf20_A	0,0805	0,0795	0,0698	0,0717	0,0710	**0,0625**	0,0693	0,0606	**0,0596**	0,0613	0,0625	0,0631	0,0640	0,0638	**0,0627**	0,0712	**0,0709**
T2_SE_no3_rf20_A	0,2415	0,2423	0,2420	0,2433	0,2424	**0,2379**	0,2427	0,2350	**0,2274**	0,2367	0,2393	0,2373	0,2423	0,2420	0,2424	0,2438	0,2456
rf40																	
T2_EPI_no3_rf40_A	0,1130	0,1205	0,0899	0,1028	0,1023	**0,0856**	0,1015	0,0780	**0,0758**	0,0797	0,0829	0,0820	0,0842	0,0834	**0,0809**	0,0943	**0,0882**
PD_SE_no3_rf40_A	0,1011	0,0524	0,0523	0,0721	0,0520	**0,0513**	0,0528	0,0516	**0,0499**	0,0529	0,0573	0,0589	0,0669	0,0601	**0,0534**	0,0942	**0,0757**
T1_fl_no3_rf40_A	0,1724	0,1397	**0,1384**	0,1687	0,1395	0,1471	0,1388	0,1330	**0,1289**	0,1346	0,1373	0,1377	0,1421	0,1400	**0,1381**	0,1645	**0,1572**
T1_IR_no3_rf40_A	0,2893	0,2669	**0,2655**	0,2884	0,2662	0,2682	0,2666	0,2561	**0,2523**	0,2591	0,2613	0,2601	**0,2635**	0,2657	0,2667	**0,2761**	0,2860
T2_fl_no3_rf40_A	0,1133	0,0822	0,0709	0,0998	0,0727	**0,0626**	0,0714	0,0619	**0,0607**	0,0641	0,0682	0,0699	0,0816	0,0715	**0,0659**	0,0930	0,1148
T2_SE_no3_rf40_A	0,2475	0,2479	0,2444	0,2485	0,2467	**0,2440**	0,2473	0,2362	**0,2291**	0,2369	0,2393	0,2384	0,2486	0,2492	**0,2458**	0,2468	**0,2452**
rf100																	
T2_EPI_no3_rf100_A	0,2233	0,1367	0,0913	0,2113	0,1040	**0,0862**	0,1058	0,0815	**0,0764**	0,0844	0,0971	0,0999	0,0921	0,0885	**0,0832**	0,1213	0,1362
PD_SE_no3_rf100_A	0,2204	0,0631	0,0579	0,2030	**0,0576**	0,0950	0,0606	0,0645	**0,0561**	0,0715	0,0984	0,0908	0,1083	0,0792	**0,0670**	0,1512	**0,1480**
T1_fl_no3_rf100_A	0,2681	0,1629	**0,1446**	0,2644	0,1462	0,1671	0,1462	0,1373	**0,1322**	0,1436	0,1548	0,1618	0,1946	0,1568	**0,1476**	0,1935	**0,1879**
T1_IR_no3_rf100_A	0,3611	0,2948	**0,2819**	0,3601	0,2848	0,2966	0,2853	0,2582	**0,2532**	0,2644	0,2708	0,2752	0,2723	**0,2700**	0,2715	0,2986	0,3174
T2_fl_no3_rf100_A	0,2292	0,0847	0,0767	0,2204	0,0786	**0,0675**	0,0780	0,0770	**0,0716**	0,0882	0,1106	0,1090	0,1496	0,0988	**0,0812**	0,1380	0,1452
T2_SE_no3_rf100_A	0,3043	0,2991	0,2917	0,3053	0,2950	**0,2753**	0,2956	0,2353	**0,2251**	0,2354	0,2412	0,2422	0,2766	0,2700	**0,2546**	**0,2704**	0,4465

No background = worse than the uncorrected, background = better than the uncorrected, bold = best parameters for the algorithm, underline = best correction for the image.

Table A.14: CV values for GM, 3% noise and B field images.

	Uncorrected	N3_01_2_4	N3_03_2_4	N3_015_2_2	N3_015_2_4	N3_015_2_6	N3_015_4_4	FSL_2_20	FSL_3_10	FSL_3_20	FSL_3_30	FSL_4_20	SPM_30	SPM_60	SPM_90	PABIC_2cl	PABIC_3cl
rf20																	
T2_EPI_no3_rf20_B	0,0884	0,1194	0,0899	**0,0844**	0,1005	0,0857	0,0989	0,0778	_0,0757_	0,0786	0,0801	0,0786	0,0895	0,0814	**0,0793**	0,0828	**0,0817**
PD_SE_no3_rf20_B	0,0694	0,0517	0,0518	0,0557	0,0515	**0,0511**	0,0523	0,0507	_0,0497_	0,0515	0,0536	0,0538	0,0517	0,0510	**0,0507**	0,0590	**0,0582**
T1_fl_no3_rf20_B	0,1521	0,1393	0,1387	0,1501	0,1388	0,1450	**0,1382**	0,1331	_0,1293_	0,1341	0,1359	0,1350	0,1505	0,1457	**0,1388**	0,1430	0,1507
T1_IR_no3_rf20_B	0,2761	0,2666	**0,2653**	0,2756	0,2666	0,2714	0,2669	0,2568	_0,2530_	0,2592	0,2609	0,2595	**0,2617**	0,2650	0,2665	0,2741	**0,2733**
T2_fl_no3_rf20_B	0,0838	0,0825	0,0704	0,0748	0,0718	**0,0627**	0,0698	0,0614	_0,0603_	0,0625	0,0644	0,0649	**0,0625**	0,0629	0,0629	0,0774	**0,0740**
T2_SE_no3_rf20_B	0,2412	0,2421	0,2416	0,2430	0,2416	**0,2370**	0,2416	0,2368	_0,2297_	0,2371	0,2391	0,2377	0,2489	0,2453	0,2454	0,2456	0,2466
rf40																	
T2_EPI_no3_rf40_B	0,1190	0,1348	0,0917	0,1074	0,1113	**0,0859**	0,1097	0,0788	_0,0758_	0,0800	0,0840	0,0830	0,0843	0,0841	**0,0803**	0,0926	**0,0902**
PD_SE_no3_rf40_B	0,1084	0,0539	0,0534	0,0793	0,0531	**0,0519**	0,0546	0,0532	**0,0513**	0,0557	0,0621	0,0641	0,0521	0,0514	_0,0512_	0,0886	0,0706
T1_fl_no3_rf40_B	0,1787	0,1413	**0,1394**	0,1748	0,1408	0,1504	0,1400	0,1340	_0,1301_	0,1366	0,1405	0,1413	0,1577	0,1468	**0,1403**	0,1628	**0,1553**
T1_IR_no3_rf40_B	0,2871	0,2676	**0,2653**	0,2862	0,2664	0,2676	0,2662	0,2557	_0,2525_	0,2592	0,2615	0,2600	**0,2646**	0,2669	0,2674	**0,2764**	0,2806
T2_fl_no3_rf40_B	0,1211	0,0875	0,0723	0,1080	0,0754	**0,0633**	0,0734	0,0641	_0,0628_	0,0683	0,0747	0,0764	0,0764	0,0648	**0,0644**	0,0932	0,1097
T2_SE_no3_rf40_B	0,2479	0,2480	0,2432	0,2495	0,2457	**0,2426**	0,2460	0,2360	_0,2282_	0,2364	0,2393	0,2379	0,2489	0,2493	**0,2454**	0,2445	0,2500
rf100																	
T2_EPI_no3_rf100_B	0,2458	0,1247	0,0925	0,2357	0,1040	**0,0872**	0,1059	0,0852	_0,0780_	0,0892	0,1066	0,1089	0,0923	0,0844	**0,0841**	0,1317	0,1658
PD_SE_no3_rf100_B	0,2435	0,0686	**0,0624**	0,2312	0,0625	0,1483	0,0650	0,0754	**0,0726**	0,0911	0,1201	0,1279	0,0590	_0,0546_	0,0569	0,1715	0,1746
T1_fl_no3_rf100_B	0,2909	0,1725	**0,1513**	0,2870	0,1535	0,1891	0,1529	0,1429	_0,1388_	0,1558	0,1731	0,1825	0,1862	0,1533	**0,1479**	0,1972	0,2103
T1_IR_no3_rf100_B	0,3794	0,3087	**0,2877**	0,3777	0,2924	0,3043	0,2936	0,2613	_0,2570_	0,2709	0,2812	0,2892	0,2734	**0,2729**	0,2731	**0,3015**	0,3150
T2_fl_no3_rf100_B	0,2531	0,0917	0,0828	0,2460	0,0831	_0,0722_	0,0837	0,0891	**0,0866**	0,1075	0,1350	0,1390	0,1334	0,0777	**0,0747**	0,1769	**0,1733**
T2_SE_no3_rf100_B	0,3185	0,3023	0,2942	0,3180	0,2969	**0,2715**	0,2979	0,2359	_0,2249_	0,2366	0,2455	0,2440	0,2476	0,2463	**0,2452**	0,2703	0,4572

No background = worse than the uncorrected, background = better than the uncorrected, bold = best parameters for the algorithm, underline = best correction for the image.

Table A.15: CV values for GM, 3% noise and C field images.

	Uncorrected	N3_01_2_4	N3_03_2_4	N3_015_2_2	N3_015_2_4	N3_015_2_6	N3_015_4_4	FSL_2_20	FSL_3_10	FSL_3_20	FSL_3_30	FSL_4_20	SPM_30	SPM_60	SPM_90	PABIC_2cl	PABIC_3cl
rf20																	
T2_EPI_no3_rf20_C	0,0876	0,1140	0,0891	**0,0849**	0,0964	0,0851	0,0958	0,0773	**_0,0755_**	0,0785	0,0798	0,0785	0,0898	0,0827	**0,0788**	**0,0826**	0,1071
PD_SE_no3_rf20_C	0,0663	0,0509	0,0512	0,0543	0,0509	**0,0507**	0,0515	0,0499	**_0,0491_**	0,0507	0,0522	0,0526	0,0552	0,0507	**0,0503**	0,0543	0,0568
T1_fl_no3_rf20_C	0,1482	0,1380	0,1377	0,1468	0,1373	0,1435	**0,1372**	0,1322	**_0,1283_**	0,1329	0,1344	0,1335	0,1416	0,1392	**0,1374**	**0,1435**	0,1465
T1_IR_no3_rf20_C	0,2733	0,2659	**0,2644**	0,2730	0,2657	0,2710	0,2659	0,2561	**_0,2525_**	0,2584	0,2599	0,2586	**0,2614**	0,2648	0,2661	0,2776	**0,2716**
T2_fl_no3_rf20_C	0,0796	0,0802	0,0693	0,0710	0,0705	**0,0618**	0,0690	0,0601	**_0,0591_**	0,0609	0,0623	0,0628	0,0718	0,0673	**0,0633**	0,0689	**0,0676**
T2_SE_no3_rf20_C	0,2440	0,2442	0,2428	0,2440	0,2438	**0,2370**	0,2439	0,2367	**_0,2300_**	0,2373	0,2394	0,2382	0,2482	0,2457	0,2452	0,2458	0,2484
rf40																	
T2_EPI_no3_rf40_C	0,1140	0,1265	0,0906	0,1054	0,1054	**0,0848**	0,1066	0,0775	**_0,0755_**	0,0795	0,0827	0,0814	0,0909	0,0841	**0,0791**	0,0967	**0,0937**
PD_SE_no3_rf40_C	0,1000	0,0517	0,0517	0,0754	0,0513	**0,0506**	0,0525	0,0511	**_0,0493_**	0,0527	0,0574	0,0590	0,0542	0,0503	**0,0502**	0,0684	**0,0674**
T1_fl_no3_rf40_C	0,1691	0,1383	0,1372	0,1662	0,1386	0,1451	**0,1370**	0,1317	**_0,1278_**	0,1337	0,1366	0,1369	0,1580	0,1452	**0,1394**	0,1518	**0,1490**
T1_IR_no3_rf40_C	0,2941	0,2694	**0,2672**	0,2930	0,2677	0,2704	0,2680	0,2570	**_0,2536_**	0,2608	0,2636	0,2618	**0,2637**	0,2661	0,2669	0,2777	0,2897
T2_fl_no3_rf40_C	0,1112	0,0843	0,0699	0,0993	0,0721	**0,0617**	0,0703	0,0613	**_0,0601_**	0,0642	0,0690	0,0698	0,0859	0,0702	**0,0634**	**0,0859**	0,1095
T2_SE_no3_rf40_C	0,2522	0,2527	0,2466	0,2522	0,2502	**0,2417**	0,2498	0,2366	**_0,2295_**	0,2377	0,2406	0,2396	**0,2441**	0,2446	0,2444	0,2519	**0,2470**
rf100																	
T2_EPI_no3_rf100_C	0,2154	0,1309	0,0909	0,2064	0,1051	**0,0847**	0,1054	0,0805	**_0,0756_**	0,0847	0,0998	0,0962	0,0919	0,0841	**0,0810**	0,1178	**0,1115**
PD_SE_no3_rf100_C	0,2093	0,0569	0,0559	0,1946	0,0554	**_0,0529_**	0,0577	0,0691	**0,0552**	0,0750	0,1049	0,0900	0,1146	0,0735	**0,0665**	0,1408	**0,1349**
T1_fl_no3_rf100_C	0,2546	0,1519	**0,1434**	0,2521	0,1449	0,1579	0,1437	0,1357	**_0,1307_**	0,1437	0,1566	0,1640	0,1902	0,1593	**0,1490**	0,1751	**0,1747**
T1_IR_no3_rf100_C	0,3493	0,2930	0,2803	0,3491	0,2814	0,2922	**0,2792**	0,2569	**_0,2530_**	0,2649	0,2720	0,2764	0,2736	0,2713	**0,2706**	0,2989	0,3011
T2_fl_no3_rf100_C	0,2168	0,0852	0,0751	0,2095	0,0773	**_0,0644_**	0,0763	0,0809	**0,0709**	0,0913	0,1180	0,1067	0,1453	0,1086	**0,0894**	0,1210	0,1406
T2_SE_no3_rf100_C	0,3074	0,2941	0,2887	0,3066	0,2924	**0,2708**	0,2927	0,2361	**_0,2247_**	0,2361	0,2428	0,2467	0,2833	0,2638	**0,2561**	0,2650	**0,2599**

No background = worse than the uncorrected, background = better than the uncorrected, bold = best parameters for the algorithm, underline = best correction for the image.

Table A.16: CV values for GM, 9% noise and A field images.

	Uncorrected	N3_01_2_4	N3_03_2_4	N3_015_2_2	N3_015_2_4	N3_015_2_6	N3_015_4_4	FSL_2_20	FSL_3_10	FSL_3_20	FSL_3_30	FSL_4_20	SPM_30	SPM_60	SPM_90	PABIC_2cl	PABIC_3cl
rf20																	
T2_EPI_no9_rf20_A	0,1356	0,1509	0,1356	**0,1342**	0,1393	0,1393	0,1396	0,1304	**_0,1287_**	0,1304	0,1309	0,1307	0,1380	0,1332	**0,1320**	**0,1355**	0,1381
PD_SE_no9_rf20_A	0,1182	0,1123	**0,1111**	0,1145	0,1114	0,1117	0,1118	0,1101	**_0,1097_**	0,1106	0,1113	0,1115	0,1163	0,1123	**0,1121**	**0,1133**	0,1139
T1_fl_no9_rf20_A	0,2222	0,2170	**0,2161**	0,2225	0,2166	0,2337	0,2170	0,2123	**_0,2095_**	0,2124	0,2132	0,2128	0,2229	0,2203	**0,2174**	0,2335	0,2289
T1_IR_no9_rf20_A	0,3282	0,3250	**0,3235**	0,3293	0,3247	0,3391	0,3259	0,3168	**_0,3108_**	0,3165	0,3180	0,3168	0,3249	0,3249	**0,3248**	0,5470	0,3643
T2_fl_no9_rf20_A	0,1458	0,1520	**0,1405**	0,1440	0,1444	0,1410	0,1432	0,1362	**_0,1357_**	0,1367	0,1373	0,1376	0,1387	0,1386	**0,1380**	**0,1447**	0,1529
T2_SE_no9_rf20_A	0,2937	0,2951	0,2942	0,2946	0,2949	**0,2925**	0,2948	0,2888	**_0,2799_**	0,2896	0,2918	0,2908	0,3034	0,3000	0,2996	0,3875	0,3938
rf40																	
T2_EPI_no9_rf40_A	0,1530	0,1591	**0,1364**	0,1473	0,1431	0,1394	0,1441	0,1307	**_0,1289_**	0,1309	0,1323	0,1328	0,1406	0,1367	**0,1328**	**0,1403**	**0,1403**
PD_SE_no9_rf40_A	0,1395	0,1160	**0,1115**	0,1275	0,1124	0,1118	0,1126	0,1105	**_0,1100_**	0,1117	0,1138	0,1149	0,1156	0,1120	**0,1118**	0,1196	**0,1186**
T1_fl_no9_rf40_A	0,2360	0,2185	**0,2165**	0,2353	0,2172	0,2354	0,2172	0,2124	**_0,2095_**	0,2127	0,2140	0,2143	0,2236	0,2208	**0,2183**	**0,2292**	0,2346
T1_IR_no9_rf40_A	0,3378	0,3272	**0,3232**	0,3379	0,3248	0,3398	0,3243	0,3159	**_0,3098_**	0,3157	0,3175	0,3166	0,3255	0,3243	**0,3241**	0,5129	0,3742
T2_fl_no9_rf40_A	0,1645	0,1555	**0,1410**	0,1591	0,1460	0,1415	0,1443	0,1366	**_0,1360_**	0,1376	0,1392	0,1403	0,1433	0,1401	**0,1386**	**0,1528**	0,1556
T2_SE_no9_rf40_A	0,2975	0,2995	**0,2964**	0,2990	0,2978	0,2991	0,2982	0,2877	**_0,2793_**	0,2889	0,2913	0,2906	0,3026	0,2978	0,2978	0,3922	0,3990
rf100																	
T2_EPI_no9_rf100_A	0,2431	0,1754	0,1470	0,2336	0,1542	**0,1454**	0,1553	0,1353	**_0,1327_**	0,1372	0,1450	0,1473	0,1784	0,1593	**0,1383**	0,1691	**0,1670**
PD_SE_no9_rf100_A	0,2378	0,1337	0,1211	0,2241	0,1228	**0,1202**	0,1252	0,1187	**_0,1166_**	0,1240	0,1366	0,1363	0,1647	0,1438	**0,1319**	0,1624	0,1504
T1_fl_no9_rf100_A	0,3058	0,2412	0,2322	0,3037	**0,2294**	0,2599	0,2297	0,2185	**_0,2155_**	0,2211	0,2266	0,2294	0,2592	0,2349	**0,2319**	0,2635	0,2708
T1_IR_no9_rf100_A	0,3905	0,3518	**0,3350**	0,3904	0,3375	0,3620	0,3365	0,3187	**_0,3126_**	0,3204	0,3247	0,3260	0,3419	0,3297	**0,3295**	0,5058	**0,3669**
T2_fl_no9_rf100_A	0,2542	0,1670	0,1523	0,2470	0,1550	**0,1520**	0,1553	0,1445	**_0,1431_**	0,1497	0,1597	0,1609	0,1562	0,1480	**0,1476**	**0,1877**	0,1992
T2_SE_no9_rf100_A	0,3406	0,3403	**0,3311**	0,3414	0,3370	0,3351	0,3378	0,2894	**_0,2799_**	0,2896	0,2941	0,2954	0,3242	0,3128	**0,3092**	0,3720	0,3844

No background = worse than the uncorrected, background = better than the uncorrected, bold = best parameters for the algorithm, underline = best correction for the image.

A.1.5 CV white matter

Table A.17: CV values for WM, 3% noise and A field images.

	Uncorrected	N3_01_2_4	N3_03_2_4	N3_015_2_2	N3_015_2_4	N3_015_2_6	N3_015_4_4	FSL_2_20	FSL_3_10	FSL_3_20	FSL_3_30	FSL_4_20	SPM_30	SPM_60	SPM_90	PABIC_2cl	PABIC_3cl
rf20																	
T2_EPI_no3_rf20_A	0,0730	0,0940	0,0741	**0,0715**	0,0799	0,0763	0,0781	0,0673	**0,0629**	0,0661	0,0678	0,0663	0,0716	**0,0694**	0,0696	0,0767	0,1035
PD_SE_no3_rf20_A	0,0551	0,0476	0,0478	0,0491	0,0474	**0,0469**	0,0475	0,0462	**0,0453**	0,0463	0,0471	0,0467	0,0471	**0,0469**	0,0473	**0,0500**	0,0529
T1_fl_no3_rf20_A	0,0924	0,0827	0,0841	0,0907	0,0814	0,0942	**0,0805**	0,0790	**0,0745**	0,0769	0,0783	0,0781	0,0819	**0,0790**	0,0795	**0,0837**	0,0888
T1_IR_no3_rf20_A	0,1334	0,1217	**0,1204**	0,1319	0,1216	0,1401	0,1216	0,1207	**0,1146**	0,1185	0,1204	0,1197	**0,1181**	0,1191	0,1211	0,1287	**0,1280**
T2_fl_no3_rf20_A	0,0566	0,0695	0,0560	0,0497	0,0578	**0,0455**	0,0551	**0,0430**	**0,0430**	0,0432	0,0437	0,0442	0,0450	0,0441	**0,0437**	0,0504	**0,0489**
T2_SE_no3_rf20_A	0,1683	0,1687	0,1673	0,1687	0,1674	**0,1572**	0,1682	0,1661	**0,1546**	0,1636	0,1673	0,1637	**0,1611**	0,1655	0,1671	0,1717	0,1721
rf40																	
T2_EPI_no3_rf40_A	0,0897	0,1036	**0,0743**	0,0831	0,0862	0,0761	0,0845	0,0667	**0,0633**	0,0665	0,0690	0,0673	0,0694	**0,0692**	0,0696	0,0850	**0,0747**
PD_SE_no3_rf40_A	0,0773	0,0476	0,0475	0,0582	0,0472	**0,0461**	0,0473	0,0461	**0,0449**	0,0464	0,0486	0,0494	0,0482	0,0477	**0,0468**	0,0812	**0,0664**
T1_fl_no3_rf40_A	0,1125	0,0842	0,0840	0,1089	0,0832	0,0956	**0,0827**	0,0773	**0,0745**	0,0777	0,0803	0,0817	0,0811	**0,0781**	0,0788	0,1086	**0,0992**
T1_IR_no3_rf40_A	0,1500	0,1222	**0,1209**	0,1477	0,1218	0,1319	0,1218	0,1205	**0,1150**	0,1192	0,1218	0,1218	**0,1190**	**0,1190**	0,1214	**0,1353**	0,1443
T2_fl_no3_rf40_A	0,0818	0,0726	0,0566	0,0710	0,0592	**0,0445**	0,0561	**0,0423**	0,0424	0,0434	0,0461	0,0480	0,0461	0,0441	**0,0431**	0,0693	0,0882
T2_SE_no3_rf40_A	0,1750	0,1745	0,1709	0,1757	0,1729	**0,1703**	0,1729	0,1614	**0,1540**	0,1623	0,1662	0,1639	**0,1619**	0,1657	0,1653	0,1762	**0,1733**
rf100																	
T2_EPI_no3_rf100_A	0,1634	0,1189	**0,0716**	0,1543	0,0856	0,0720	0,0846	0,0669	**0,0633**	0,0672	0,0741	0,0764	0,0708	**0,0680**	0,0680	0,1107	**0,0987**
PD_SE_no3_rf100_A	0,1585	0,0520	0,0482	0,1449	**0,0481**	0,0562	0,0491	0,0481	**0,0456**	0,0518	0,0683	0,0677	0,0545	0,0486	**0,0472**	0,1081	0,1073
T1_fl_no3_rf100_A	0,1859	0,0938	**0,0843**	0,1829	0,0884	0,1042	0,0878	0,0768	**0,0755**	0,0814	0,0908	0,1026	0,0907	0,0803	**0,0801**	0,1233	0,1192
T1_IR_no3_rf100_A	0,2137	0,1383	**0,1264**	0,2113	0,1297	0,1613	0,1297	0,1196	**0,1155**	0,1211	0,1276	0,1378	**0,1191**	0,1191	0,1218	0,1522	0,1713
T2_fl_no3_rf100_A	0,1646	0,0713	0,0576	0,1573	0,0624	**0,0436**	0,0585	**0,0453**	0,0483	0,0575	0,0747	0,0797	0,0619	0,0470	**0,0441**	0,0936	0,0993
T2_SE_no3_rf100_A	0,2199	0,2122	0,2078	0,2203	0,2075	**0,1960**	0,2096	0,1596	**0,1495**	0,1600	0,1669	0,1661	0,1674	0,1694	**0,1655**	0,1890	0,3879

No background = worse than the uncorrected, background = better than the uncorrected, bold = best parameters for the algorithm, underline = best correction for the image.

Table A.18: CV values for WM, 3% noise and B field images.

					Correction methods												
	Uncorrected	N3_01_2_4	N3_03_2_4	N3_015_2_2	N3_015_2_4	N3_015_2_6	N3_015_4_4	FSL_2_20	FSL_3_10	FSL_3_20	FSL_3_30	FSL_4_20	SPM_30	SPM_60	SPM_90	PABIC_2cl	PABIC_3cl
rf20																	
T2_EPI_no3_rf20_B	0,0748	0,1010	0,0749	**0,0722**	0,0843	0,0771	0,0824	0,0672	<u>**0,0642**</u>	0,0668	0,0684	0,0668	0,0717	**0,0692**	0,0695	0,0760	**0,0711**
PD_SE_no3_rf20_B	0,0579	0,0479	0,0481	0,0494	0,0477	**0,0469**	0,0479	0,0468	<u>**0,0456**</u>	0,0468	0,0480	0,0479	0,0483	**0,0476**	0,0481	0,0533	0,0525
T1_fl_no3_rf20_B	0,0955	0,0833	0,0842	0,0932	0,0818	0,0947	**0,0809**	0,0781	<u>**0,0749**</u>	0,0780	0,0801	0,0794	0,0838	0,0806	**0,0800**	0,0851	0,0938
T1_IR_no3_rf20_B	0,1359	0,1224	**0,1209**	0,1342	0,1222	0,1357	0,1223	0,1210	<u>**0,1148**</u>	0,1190	0,1213	0,1204	**0,1186**	0,1195	0,1216	0,1331	**0,1305**
T2_fl_no3_rf20_B	0,0604	0,0722	0,0564	0,0524	0,0583	**0,0456**	0,0553	0,0433	<u>**0,0432**</u>	0,0437	0,0448	0,0452	0,0449	0,0438	**0,0437**	0,0539	**0,0534**
T2_SE_no3_rf20_B	0,1694	0,1690	0,1684	0,1698	0,1682	**0,1581**	0,1692	0,1629	<u>**0,1562**</u>	0,1638	0,1669	0,1646	**0,1653**	0,1659	0,1671	0,1731	0,1740
rf40																	
T2_EPI_no3_rf40_B	0,0969	0,1140	**0,0756**	0,0879	0,0931	0,0762	0,0905	0,0672	<u>**0,0639**</u>	0,0670	0,0697	0,0683	0,0695	0,0694	**0,0693**	0,0852	**0,0773**
PD_SE_no3_rf40_B	0,0860	0,0484	0,0481	0,0634	0,0477	**0,0465**	0,0483	0,0465	<u>**0,0455**</u>	0,0474	0,0509	0,0525	0,0478	**0,0471**	0,0477	0,0697	0,0579
T1_fl_no3_rf40_B	0,1206	0,0844	0,0850	0,1166	0,0851	0,0988	**0,0837**	0,0777	<u>**0,0747**</u>	0,0789	0,0830	0,0842	0,0843	0,0807	**0,0803**	0,1079	0,0982
T1_IR_no3_rf40_B	0,1464	0,1215	**0,1202**	0,1444	0,1215	0,1268	0,1209	0,1196	<u>**0,1142**</u>	0,1187	0,1215	0,1208	**0,1185**	0,1186	0,1209	0,1352	0,1356
T2_fl_no3_rf40_B	0,0913	0,0764	0,0574	0,0798	0,0613	**0,0450**	0,0577	**0,0431**	0,0433	0,0458	0,0508	0,0530	0,0452	0,0432	<u>**0,0430**</u>	0,0667	0,0840
T2_SE_no3_rf40_B	0,1791	0,1782	**0,1733**	0,1795	0,1756	0,1802	0,1760	0,1622	<u>**0,1543**</u>	0,1631	0,1677	0,1654	**0,1647**	0,1659	0,1653	0,1763	0,1785
rf100																	
T2_EPI_no3_rf100_B	0,1880	0,1041	0,0703	0,1797	0,0803	**0,0698**	0,0809	0,0684	<u>**0,0640**</u>	0,0690	0,0785	0,0826	0,0689	**0,0677**	0,0682	**0,1080**	0,1357
PD_SE_no3_rf100_B	0,1839	0,0553	**0,0488**	0,1735	0,0490	0,0959	0,0494	**0,0529**	0,0608	0,0682	0,0888	0,1003	0,0465	<u>**0,0457**</u>	0,0461	0,1291	0,1353
T1_fl_no3_rf100_B	0,2102	0,1008	**0,0867**	0,2070	0,0924	0,1260	0,0935	0,0793	<u>**0,0792**</u>	0,0894	0,1052	0,1183	0,0927	**0,0813**	0,0822	0,1336	0,1441
T1_IR_no3_rf100_B	0,2359	0,1532	**0,1315**	0,2333	0,1374	0,1767	0,1383	0,1205	<u>**0,1151**</u>	0,1250	0,1364	0,1487	**0,1194**	0,1210	0,1237	0,1628	0,1736
T2_fl_no3_rf100_B	0,1903	0,0746	0,0566	0,1839	0,0583	**0,0447**	0,0568	**0,0517**	0,0651	0,0750	0,0961	0,1063	0,0619	<u>**0,0435**</u>	<u>**0,0435**</u>	0,1359	**0,1293**
T2_SE_no3_rf100_B	0,2403	0,2226	0,2169	0,2414	0,2168	**0,2006**	0,2175	0,1624	<u>**0,1518**</u>	0,1635	0,1732	0,1718	**0,1607**	0,1632	0,1640	**0,1993**	0,3991

No background = worse than the uncorrected, background = better than the uncorrected, bold = best parameters for the algorithm, underline = best correction for the image.

Table A.19: CV values for WM, 3% noise and C field images.

	Uncorrected	N3_01_2_4	N3_03_2_4	N3_015_2_2	N3_015_2_4	N3_015_2_6	N3_015_4_4	FSL_2_20	FSL_3_10	FSL_3_20	FSL_3_30	FSL_4_20	SPM_30	SPM_60	SPM_90	PABIC_2cl	PABIC_3cl
rf20																	
T2_EPI_no3_rf20_C	0,0728	0,0961	0,0742	**0,0715**	0,0808	0,0763	0,0797	0,0667	<u>**0,0635**</u>	0,0663	0,0677	0,0663	0,0719	**0,0688**	0,0695	0,0753	0,1024
PD_SE_no3_rf20_C	0,0542	0,0470	0,0473	0,0484	0,0470	**0,0464**	0,0470	0,0461	<u>**0,0450**</u>	0,0462	0,0470	0,0469	0,0467	**0,0466**	0,0469	**0,0495**	0,0511
T1_fl_no3_rf20_C	0,0908	0,0822	0,0837	0,0892	0,0806	0,0921	**0,0805**	0,0776	<u>**0,0743**</u>	0,0773	0,0790	0,0784	0,0810	**0,0784**	0,0792	**0,0875**	0,0905
T1_IR_no3_rf20_C	0,1321	0,1215	**0,1201**	0,1308	0,1213	0,1364	0,1213	0,1205	<u>**0,1144**</u>	0,1184	0,1204	0,1195	**0,1185**	0,1188	0,1211	0,1366	**0,1264**
T2_fl_no3_rf20_C	0,0548	0,0691	0,0551	0,0481	0,0567	**0,0445**	0,0541	0,0422	<u>**0,0421**</u>	0,0425	0,0431	0,0435	0,0450	0,0439	**0,0429**	0,0473	**0,0467**
T2_SE_no3_rf20_C	0,1692	0,1687	0,1672	0,1693	0,1676	<u>**0,1553**</u>	0,1679	0,1620	**0,1554**	0,1631	0,1660	0,1637	**0,1641**	0,1648	0,1664	0,1722	0,1718
rf40																	
T2_EPI_no3_rf40_C	0,0879	0,1064	**0,0744**	0,0823	0,0876	0,0748	0,0876	0,0661	<u>**0,0626**</u>	0,0658	0,0680	0,0662	0,0709	**0,0674**	0,0682	0,0899	**0,0762**
PD_SE_no3_rf40_C	0,0741	0,0466	0,0467	0,0579	0,0463	**0,0454**	0,0466	0,0454	<u>**0,0443**</u>	0,0457	0,0477	0,0487	0,0459	**0,0457**	0,0459	**0,0569**	0,0577
T1_fl_no3_rf40_C	0,1082	0,0829	0,0831	0,1053	0,0831	0,0928	**0,0799**	0,0764	<u>**0,0733**</u>	0,0770	0,0799	0,0811	0,0830	**0,0788**	0,0788	0,0955	**0,0907**
T1_IR_no3_rf40_C	0,1568	0,1232	**0,1221**	0,1543	0,1226	0,1292	0,1226	0,1204	<u>**0,1150**</u>	0,1200	0,1237	0,1228	**0,1190**	0,1198	0,1217	**0,1373**	0,1529
T2_fl_no3_rf40_C	0,0775	0,0725	0,0547	0,0679	0,0573	**0,0431**	0,0545	<u>**0,0410**</u>	0,0412	0,0427	0,0459	0,0471	0,0457	0,0427	**0,0414**	**0,0583**	0,0814
T2_SE_no3_rf40_C	0,1757	0,1765	0,1703	0,1755	0,1723	**0,1635**	0,1722	0,1605	<u>**0,1531**</u>	0,1617	0,1657	0,1633	**0,1614**	0,1625	0,1642	0,1785	**0,1752**
rf100																	
T2_EPI_no3_rf100_C	0,1507	0,1121	0,0703	0,1437	0,0856	**0,0702**	0,0838	0,0651	<u>**0,0615**</u>	0,0655	0,0720	0,0709	0,0662	**0,0656**	**0,0656**	0,1112	0,0892
PD_SE_no3_rf100_C	0,1439	0,0464	0,0450	0,1321	0,0446	<u>**0,0429**</u>	0,0453	0,0496	**0,0436**	0,0508	0,0685	0,0647	0,0514	0,0452	**0,0451**	0,1115	0,0899
T1_fl_no3_rf100_C	0,1703	0,0845	**0,0826**	0,1674	0,0858	0,0965	0,0848	0,0750	<u>**0,0732**</u>	0,0808	0,0907	0,1056	0,0888	**0,0792**	0,0792	0,1092	0,1078
T1_IR_no3_rf100_C	0,1992	0,1360	**0,1239**	0,1971	0,1259	0,1652	0,1245	0,1180	<u>**0,1132**</u>	0,1206	0,1275	0,1385	**0,1173**	0,1182	0,1206	0,1548	**0,1547**
T2_fl_no3_rf100_C	0,1488	0,0739	0,0548	0,1427	0,0594	<u>**0,0407**</u>	0,0555	0,0469	**0,0465**	0,0583	0,0777	0,0742	0,0626	0,0485	**0,0444**	0,0814	0,0905
T2_SE_no3_rf100_C	0,2141	0,1967	0,1949	0,2128	0,1955	**0,1900**	0,1958	0,1580	<u>**0,1472**</u>	0,1583	0,1652	0,1661	0,1691	0,1642	**0,1629**	0,1869	**0,1824**

No background = worse than the uncorrected, background = better than the uncorrected, bold = best parameters for the algorithm, underline = best correction for the image.

Table A.20: CV values for WM, 9% noise and A field images.

								Correction methods									
	Uncorrected	N3_01_2_4	N3_03_2_4	N3_015_2_2	N3_015_2_4	N3_015_2_6	N3_015_4_4	FSL_2_20	FSL_3_10	FSL_3_20	FSL_3_30	FSL_4_20	SPM_30	SPM_60	SPM_90	PABIC_2cl	PABIC_3cl
rf20																	
T2_EPI_no9_rf20_A	0,1394	0,1515	0,1398	**0,1392**	0,1427	0,1493	0,1427	0,1371	**0,1362**	0,1369	0,1374	0,1369	0,1421	**0,1386**	**0,1386**	0,1430	0,1456
PD_SE_no9_rf20_A	0,1172	0,1157	**0,1145**	0,1157	0,1148	0,1150	0,1150	0,1139	**0,1135**	0,1140	0,1143	0,1143	0,1158	**0,1144**	**0,1144**	**0,1157**	0,1158
T1_fl_no9_rf20_A	0,1627	0,1583	**0,1576**	0,1628	0,1579	0,1899	0,1581	0,1560	**0,1550**	0,1556	0,1561	0,1559	0,1619	0,1582	**0,1575**	0,1748	0,1680
T1_IR_no9_rf20_A	0,1914	0,1864	**0,1845**	0,1916	0,1858	0,2258	0,1871	0,1831	**0,1791**	0,1816	0,1830	0,1820	0,1880	**0,1844**	0,1851	0,4180	0,2248
T2_fl_no9_rf20_A	0,1287	0,1422	0,1286	0,1277	0,1336	**0,1276**	0,1316	**0,1241**	**0,1241**	**0,1241**	0,1242	0,1244	0,1263	0,1253	**0,1249**	0,1293	0,1348
T2_SE_no9_rf20_A	0,2852	0,2852	0,2856	0,2864	0,2859	0,3016	0,2864	0,2837	**0,2786**	0,2829	0,2850	0,2833	0,2906	0,2873	0,2872	0,3665	0,3731
rf40																	
T2_EPI_no9_rf40_A	0,1460	0,1556	**0,1372**	0,1432	0,1426	0,1459	0,1427	0,1343	**0,1333**	0,1341	0,1350	0,1348	0,1382	0,1361	**0,1358**	**0,1445**	0,1456
PD_SE_no9_rf40_A	0,1269	0,1167	**0,1127**	0,1202	0,1134	0,1130	0,1132	0,1118	**0,1115**	0,1121	0,1130	0,1134	0,1126	**0,1121**	0,1123	0,1175	**0,1155**
T1_fl_no9_rf40_A	0,1719	0,1573	**0,1552**	0,1710	0,1562	0,1874	0,1555	0,1533	**0,1522**	0,1531	0,1540	0,1544	0,1590	0,1556	**0,1552**	0,1675	0,1706
T1_IR_no9_rf40_A	0,2003	0,1871	**0,1827**	0,2001	0,1845	0,2217	0,1837	0,1805	**0,1767**	0,1793	0,1810	0,1805	0,1859	**0,1821**	0,1830	0,3758	0,2314
T2_fl_no9_rf40_A	0,1383	0,1444	0,1262	0,1347	0,1330	**0,1247**	0,1305	**0,1210**	**0,1210**	0,1213	0,1220	0,1227	0,1230	0,1220	**0,1216**	**0,1315**	0,1334
T2_SE_no9_rf40_A	0,2852	0,2870	**0,2845**	0,2854	0,2857	0,3150	0,2867	0,2799	**0,2747**	0,2792	0,2817	0,2800	0,2882	**0,2836**	0,2836	0,3694	0,3726
rf100																	
T2_EPI_no9_rf100_A	0,1939	0,1587	**0,1328**	0,1874	0,1404	0,1389	0,1400	0,1293	**0,1283**	0,1297	0,1330	0,1344	0,1435	0,1352	**0,1309**	**0,1544**	0,1575
PD_SE_no9_rf100_A	0,1826	0,1238	0,1091	0,1728	0,1114	**0,1086**	0,1120	0,1081	**0,1077**	0,1101	0,1162	0,1173	0,1181	0,1119	**0,1098**	0,1317	**0,1284**
T1_fl_no9_rf100_A	0,2191	0,1635	**0,1547**	0,2167	0,1561	0,1844	0,1559	0,1478	**0,1474**	0,1496	0,1539	0,1573	0,1594	0,1519	0,1522	**0,1881**	0,1925
T1_IR_no9_rf100_A	0,2445	0,2017	**0,1859**	0,2430	0,1883	0,2209	0,1869	0,1759	**0,1732**	0,1769	0,1814	0,1840	0,1836	**0,1782**	0,1802	0,3460	**0,2178**
T2_fl_no9_rf100_A	0,1926	0,1454	**0,1217**	0,1871	0,1293	0,1193	0,1278	**0,1166**	0,1168	0,1193	0,1252	0,1272	0,1202	**0,1182**	0,1195	**0,1406**	0,1548
T2_SE_no9_rf100_A	0,3000	0,3008	**0,2952**	0,3000	0,2988	0,3232	0,3002	0,2697	**0,2638**	0,2691	0,2727	0,2717	0,2777	**0,2745**	0,2752	0,3382	0,3387

No background = worse than the uncorrected, background = better than the uncorrected, bold = best parameters for the algorithm, underline = best correction for the image.

Table A.21: RMS values, 3% noise and B field images.

					Correction methods											
	N3_01_2_4	N3_03_2_4	N3_015_2_2	N3_015_2_4	N3_015_2_6	N3_015_4_4	FSL_2_20	FSL_3_10	FSL_3_20	FSL_3_30	FSL_4_20	SPM_30	SPM_60	SPM_90	PABIC_2cl	PABIC_3cl
rf20																
T2_EPI_no3_rf20_B	0,0528	0,0267	0,0390	0,0460	0,0372	0,0426	0,0503	0,0645	0,0486	0,0440	0,0437	0,4049	0,0539	0,0419	0,1540	0,0213
PD_SE_no3_rf20_B	0,0096	0,0111	0,0097	0,0212	0,0111	0,0451	0,0409	0,0428	0,0400	0,0399	0,0403	0,2287	0,0198	0,0188	0,0353	0,0386
T1_fl_no3_rf20_B	0,0165	0,0403	0,0187	0,0568	0,0172	0,0323	0,0670	0,0565	0,0454	0,0420	0,0422	0,7118	0,1420	0,0269	0,2300	0,0439
T1_IR_no3_rf20_B	0,0144	0,0563	0,0533	0,0854	0,0272	0,0383	0,1032	0,0628	0,0493	0,0448	0,0463	0,2825	0,1453	0,0793	0,0484	0,0883
T2_fl_no3_rf20_B	0,0298	0,0200	0,0206	0,0351	0,0191	0,0436	0,0413	0,0425	0,0401	0,0394	0,0392	0,2083	0,0231	0,0214	0,0272	0,0278
T2_SE_no3_rf20_B	0,0837	0,0680	0,0816	0,0990	0,0862	0,0428	0,0697	0,0815	0,0550	0,0492	0,0537	0,8245	0,0521	0,0511	0,0516	0,0535
rf40																
T2_EPI_no3_rf40_B	0,0949	0,0371	0,0671	0,0971	0,0628	0,0947	0,0829	0,0929	0,0818	0,0793	0,0800	0,4567	0,1753	0,1696	0,1391	0,1048
PD_SE_no3_rf40_B	0,0157	0,0178	0,0153	0,0329	0,0159	0,1008	0,0781	0,0791	0,0774	0,0777	0,0782	0,1338	0,0905	0,1121	0,0828	0,0972
T1_fl_no3_rf40_B	0,0492	0,0644	0,0476	0,1352	0,0350	0,0720	0,0958	0,0918	0,0816	0,0789	0,0778	0,5059	0,0589	0,1045	0,1109	0,0936
T1_IR_no3_rf40_B	0,0500	0,1123	0,0847	0,1524	0,0771	0,0869	0,1265	0,1018	0,0953	0,0932	0,0928	0,3517	0,0954	0,1325	0,1120	0,1620
T2_fl_no3_rf40_B	0,0559	0,0339	0,0367	0,0487	0,0312	0,0865	0,0790	0,0789	0,0772	0,0774	0,0775	0,1640	0,0778	0,1172	0,0681	0,0656
T2_SE_no3_rf40_B	0,1555	0,1655	0,1801	0,2019	0,1870	0,0950	0,0937	0,1094	0,0880	0,0845	0,0876	0,3301	0,0528	0,1766	0,1172	0,0878
rf100																
T2_EPI_no3_rf100_B	0,3075	0,2237	0,2616	0,3575	0,2552	0,2988	0,1857	0,1908	0,1847	0,1850	0,1861	0,2314	0,4183	0,4233	0,2394	0,2509
PD_SE_no3_rf100_B	0,2236	0,2116	0,2107	0,2769	0,2037	0,3305	0,1827	0,1828	0,1842	0,1907	0,1944	0,1016	0,3959	0,3986	0,2542	0,2712
T1_fl_no3_rf100_B	0,2660	0,2640	0,2725	0,3567	0,2588	0,2593	0,1889	0,1884	0,1841	0,1867	0,1898	0,3372	0,3204	0,3876	0,2905	0,1402
T1_IR_no3_rf100_B	0,2067	0,2611	0,2160	0,4475	0,2581	0,2837	0,2039	0,1965	0,1861	0,1861	0,1883	0,3246	0,3542	0,3979	0,2672	0,2501
T2_fl_no3_rf100_B	0,2939	0,2505	0,2582	0,2510	0,2444	0,3040	0,1825	0,1821	0,1845	0,1916	0,1942	0,1827	0,3407	0,3754	0,2699	0,2953
T2_SE_no3_rf100_B	0,4861	0,5053	0,5130	0,5119	0,5225	0,2824	0,1899	0,2017	0,1887	0,1890	0,1914	0,2539	0,3927	0,4156	0,1527	1,7829

Background = best parameters for the algorithm, darker background = best RMS for the image.

Table A.22: RMS values, 3% noise and C field images.

	Correction methods															
	N3_01_2_4	N3_03_2_4	N3_015_2_2	N3_015_2_4	N3_015_2_6	N3_015_4_4	FSL_2_20	FSL_3_10	FSL_3_20	FSL_3_30	FSL_4_20	SPM_30	SPM_60	SPM_90	PABIC_2cl	PABIC_3cl
rf20																
T2_EPI_no3_rf20_C	0,0644	0,0358	0,0488	0,0562	0,0468	0,0443	0,0666	0,0768	0,0648	0,0618	0,0616	0,2930	0,1155	0,0812	0,0906	0,1519
PD_SE_no3_rf20_C	0,0126	0,0157	0,0137	0,0374	0,0142	0,0379	0,0597	0,0607	0,0591	0,0590	0,0593	0,1658	0,0794	0,0627	0,0359	0,0281
T1_fl_no3_rf20_C	0,0204	0,0627	0,0270	0,0773	0,0247	0,0347	0,0782	0,0694	0,0620	0,0601	0,0602	0,9668	0,2053	0,0426	0,0300	0,0457
T1_IR_no3_rf20_C	0,0180	0,0776	0,0572	0,0980	0,0302	0,0435	0,1092	0,0746	0,0649	0,0621	0,0630	0,4379	0,1210	0,0688	0,0671	0,1169
T2_fl_no3_rf20_C	0,0452	0,0254	0,0272	0,0618	0,0237	0,0456	0,0595	0,0603	0,0589	0,0586	0,0585	0,2077	0,0681	0,0493	0,0359	0,0505
T2_SE_no3_rf20_C	0,0906	0,0782	0,0763	0,1102	0,0836	0,0517	0,0822	0,0905	0,0695	0,0651	0,0687	1,6739	0,0773	0,0334	0,0466	0,0455
rf40																
T2_EPI_no3_rf40_C	0,1193	0,0581	0,0885	0,1195	0,0861	0,0982	0,1199	0,1254	0,1188	0,1177	0,1180	0,0860	0,1659	0,1750	0,1074	0,1070
PD_SE_no3_rf40_C	0,0249	0,0281	0,0252	0,0525	0,0252	0,1003	0,1163	0,1169	0,1161	0,1163	0,1166	0,0714	0,1623	0,1473	0,1156	0,0714
T1_fl_no3_rf40_C	0,0626	0,0987	0,0709	0,1441	0,0542	0,0737	0,1260	0,1226	0,1174	0,1165	0,1161	1,1864	0,0531	0,1475	0,5389	0,1532
T1_IR_no3_rf40_C	0,0891	0,1099	0,0797	0,2069	0,0818	0,1304	0,1608	0,1380	0,1303	0,1268	0,1275	0,1646	0,1031	0,1548	0,1149	0,1190
T2_fl_no3_rf40_C	0,0862	0,0462	0,0517	0,0961	0,0444	0,0978	0,1162	0,1163	0,1157	0,1160	0,1161	0,1832	0,0489	0,1446	0,1016	0,0853
T2_SE_no3_rf40_C	0,1401	0,1560	0,1671	0,2061	0,1895	0,1145	0,1279	0,1371	0,1230	0,1210	0,1231	0,6137	0,0969	0,1555	0,1203	0,1478
rf100																
T2_EPI_no3_rf100_C	0,3545	0,2346	0,2980	0,3671	0,2868	0,3344	0,2815	0,2837	0,2821	0,2844	0,2843	0,2488	0,4398	0,4420	0,1688	0,2756
PD_SE_no3_rf100_C	0,1946	0,1896	0,1858	0,2172	0,1763	0,3539	0,2818	0,2800	0,2826	0,2885	0,2861	0,1248	0,3626	0,4188	0,2860	0,3470
T1_fl_no3_rf100_C	0,2915	0,2807	0,2791	0,4295	0,2764	0,2808	0,2797	0,2805	0,2807	0,2841	0,2876	0,9755	0,3601	0,4216	0,2093	0,1804
T1_IR_no3_rf100_C	0,2429	0,2908	0,2329	0,5018	0,2902	0,3137	0,2844	0,2810	0,2802	0,2826	0,2858	0,2568	0,3518	0,4041	0,3111	0,3519
T2_fl_no3_rf100_C	0,3239	0,2400	0,2594	0,2151	0,2448	0,3333	0,2810	0,2798	0,2835	0,2897	0,2874	0,1462	0,3332	0,4061	0,2996	0,3373
T2_SE_no3_rf100_C	0,4321	0,4837	0,4875	0,5792	0,4988	0,2987	0,2871	0,2932	0,2866	0,2870	0,2906	0,1511	0,3796	0,4460	0,1635	0,1428

Background = best parameters for the algorithm, darker background = best RMS for the image.

Table A.23: RMS values, 9% noise and A field images.

	N3_01_2_4	N3_03_2_4	N3_015_2_2	N3_015_2_4	N3_015_2_6	N3_015_4_4	FSL_2_20	FSL_3_10	FSL_3_20	FSL_3_30	FSL_4_20	SPM_30	SPM_60	SPM_90	PABIC_2cl	PABIC_3cl
rf20																
T2_EPI_no9_rf20_A	0,0531	0,0307	0,0387	0,0489	0,0373	0,0342	0,0477	0,0612	0,0438	0,0390	0,0410	1,2255	0,0611	0,0737	0,0835	0,0708
PD_SE_no9_rf20_A	0,0190	0,0125	0,0138	0,0255	0,0165	0,0240	0,0356	0,0379	0,0356	0,0358	0,0368	0,6937	0,0299	0,0374	0,0423	0,0342
T1_fl_no9_rf20_A	0,0310	0,0346	0,0403	0,0612	0,0246	0,0177	0,0560	0,0701	0,0474	0,0395	0,0398	0,8269	0,3216	0,0317	0,4648	0,4820
T1_IR_no9_rf20_A	0,0234	0,0320	0,0233	0,0696	0,0350	0,0230	0,0851	0,0971	0,0614	0,0484	0,0495	0,4263	0,2445	0,0563	11,4805	1,5349
T2_fl_no9_rf20_A	0,0365	0,0281	0,0250	0,0343	0,0250	0,0169	0,0358	0,0383	0,0344	0,0338	0,0343	0,4728	0,1688	0,0583	0,1486	0,0572
T2_SE_no9_rf20_A	0,0972	0,0942	0,0966	0,0715	0,0963	0,0284	0,0936	0,1239	0,0682	0,0531	0,0547	0,6566	0,0777	0,0459	1,2719	1,5579
rf40																
T2_EPI_no9_rf40_A	0,0905	0,0391	0,0584	0,1001	0,0562	0,0745	0,0741	0,0839	0,0722	0,0702	0,0722	0,3433	0,1636	0,1394	0,0788	0,0767
PD_SE_no9_rf40_A	0,0351	0,0158	0,0203	0,0343	0,0204	0,0634	0,0669	0,0682	0,0674	0,0688	0,0701	0,0939	0,1159	0,1072	0,0388	0,0409
T1_fl_no9_rf40_A	0,0368	0,0332	0,0315	0,1202	0,0307	0,0343	0,0780	0,0887	0,0720	0,0676	0,0686	0,5116	0,1533	0,0949	0,0823	0,1083
T1_IR_no9_rf40_A	0,0538	0,0750	0,0616	0,1392	0,0509	0,0497	0,0995	0,1086	0,0796	0,0707	0,0718	0,5329	0,1088	0,0636	10,8578	1,8365
T2_fl_no9_rf40_A	0,0741	0,0402	0,0598	0,0499	0,0575	0,0511	0,0666	0,0679	0,0662	0,0669	0,0679	0,1304	0,0807	0,0956	0,0874	0,0784
T2_SE_no9_rf40_A	0,1766	0,1874	0,1927	0,1616	0,2299	0,0745	0,1032	0,1368	0,0898	0,0805	0,0833	0,5614	0,0533	0,1055	6,0615	1,9887
rf100																
T2_EPI_no9_rf100_A	0,2091	0,1972	0,1684	0,3104	0,1684	0,2387	0,1588	0,1637	0,1595	0,1630	0,1660	0,7016	0,1493	0,3085	0,1651	0,2466
PD_SE_no9_rf100_A	0,1449	0,1470	0,1321	0,1607	0,1325	0,2461	0,1563	0,1563	0,1593	0,1663	0,1671	0,1710	0,3436	0,3152	0,1895	0,1725
T1_fl_no9_rf100_A	0,1800	0,2018	0,1809	0,3500	0,1766	0,1540	0,1568	0,1624	0,1576	0,1612	0,1654	0,8421	0,1708	0,3136	1,2973	0,3299
T1_IR_no9_rf100_A	0,1592	0,1002	0,1743	0,3781	0,1984	0,1774	0,1645	0,1710	0,1586	0,1600	0,1640	0,2311	0,1956	0,2197	3,3084	1,5266
T2_fl_no9_rf100_A	0,2197	0,1875	0,1980	0,2170	0,1954	0,2150	0,1548	0,1552	0,1582	0,1651	0,1666	1,5825	0,1804	0,2484	0,2032	0,1124
T2_SE_no9_rf100_A	0,4624	0,4830	0,5015	0,4473	0,4570	0,2058	0,1812	0,2040	0,1727	0,1717	0,1779	0,1522	0,2622	0,3091	0,7706	1,1412

Correction methods

Background = best parameters for the algorithm, darker background = best RMS for the image.

A.2 Scatter plots (extracted bias vs. true bias)
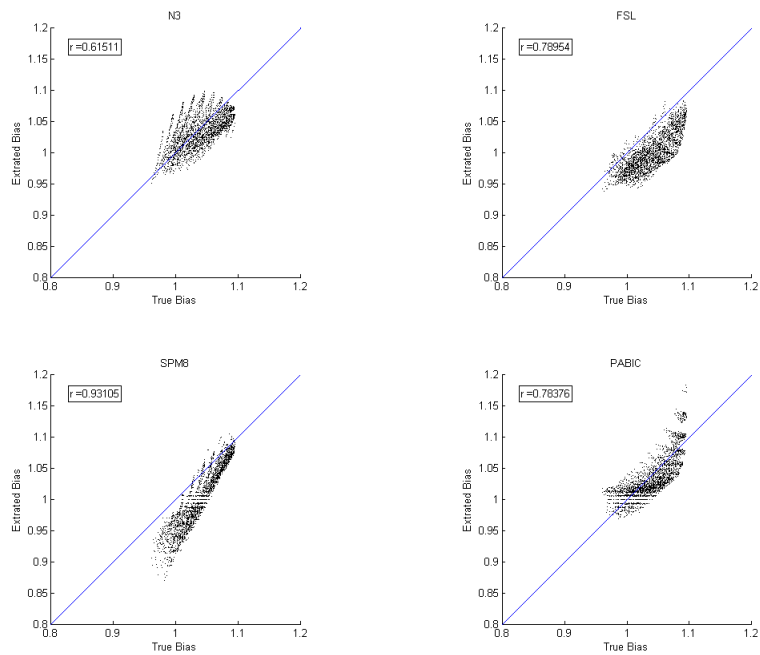
(a) T2_EPI

(b) PD_SE

Figure A.1: Scatter plots relating the extracted bias and the true bias, for the better results obtained with the four IIH correction algorithms, for rf20 images, with 3% noise and B bias field.
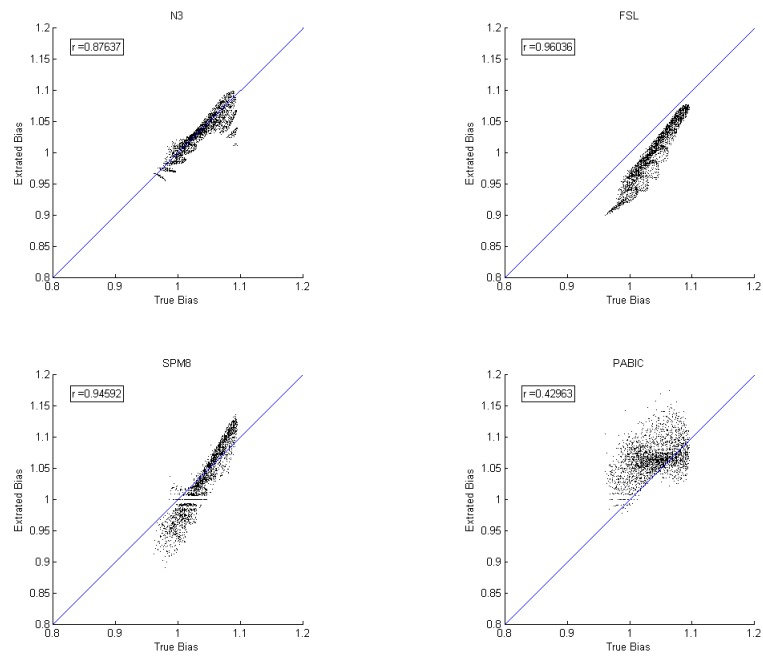
(c) T1_fl
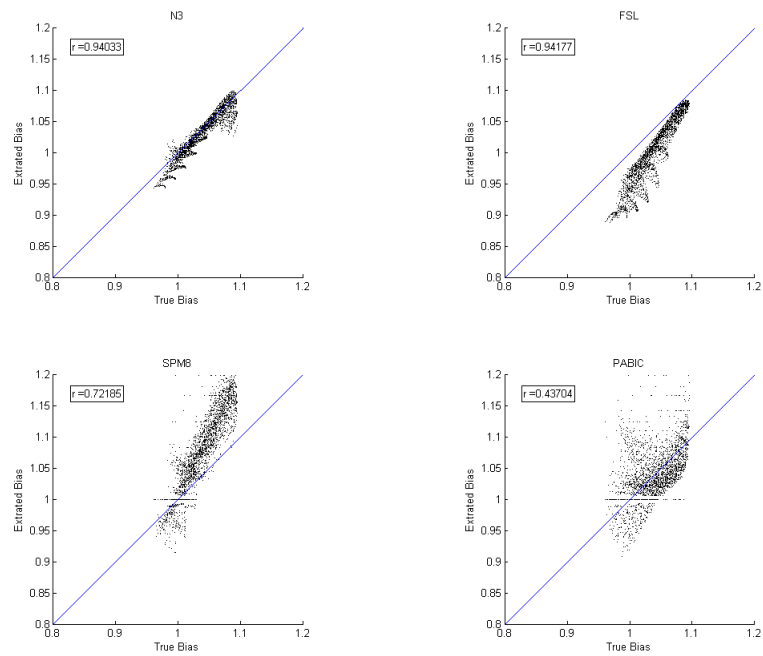
(d) T1_IR

Figure A.1: Scatter plots relating the extracted bias and the true bias, for the better results obtained with the four IIH correction algorithms, for rf20 images, with 3% noise and B bias field.

(e) T2_fl
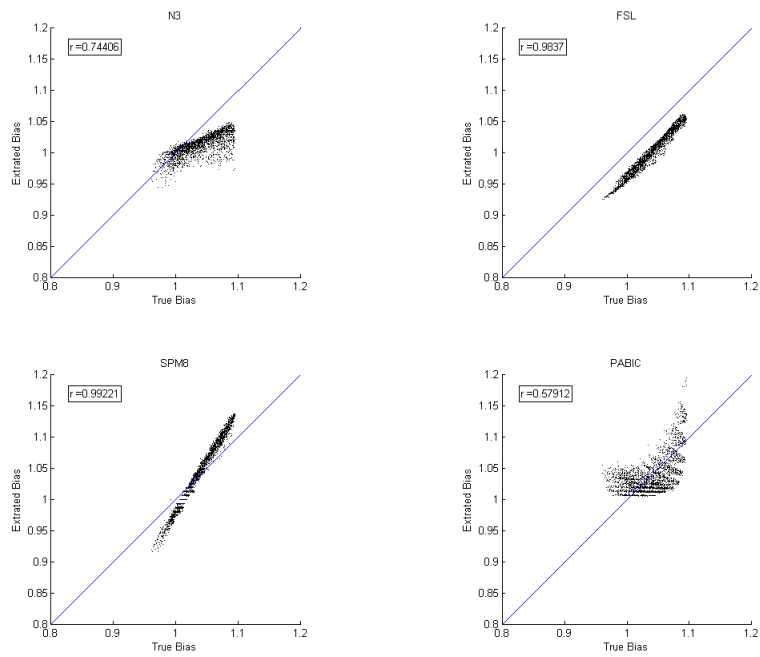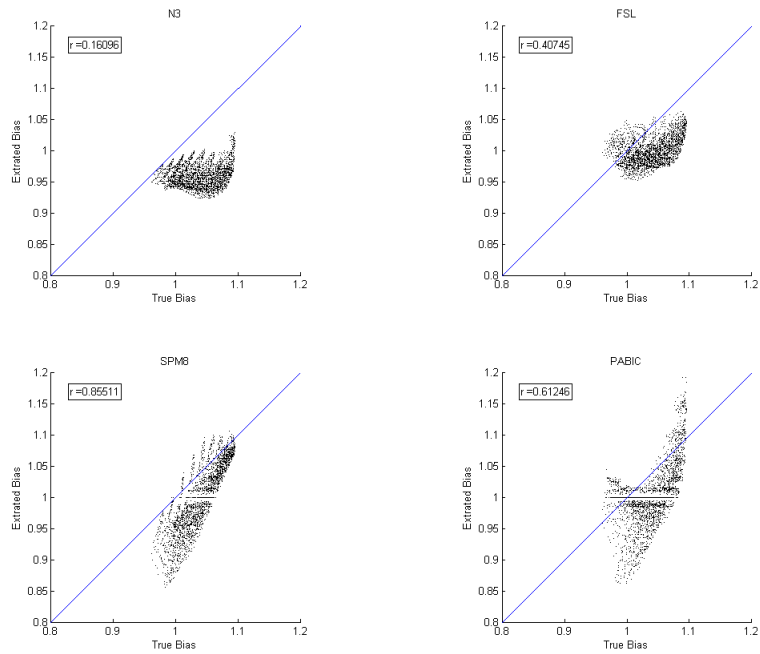
(f) T2_SE

Figure A.1: Scatter plots relating the extracted bias and the true bias, for the better results obtained in with the four IIH correction algorithms, for rf20 images, with 3% noise and B bias field.

Appendix B

Segmentation evaluation

B.1 Tables with the segmentation evaluation parameters

B.1.1 Dice coefficient grey matter

Table B.1: Dice values for GM, 3% noise and B field images.

	Uncorrected	N3_01_2_4	N3_03_2_4	N3_015_2_2	N3_015_2_4	N3_015_2_6	N3_015_4_4	FSL_2_20	FSL_3_10	FSL_3_20	FSL_3_30	FSL_4_20	SPM_30	SPM_60	SPM_90	PABIC_2cl	PABIC_3cl
rf20																	
T2_EPI_no3_rf20_B	0,7050	0,6571	0,6932	0,7028	0,6785	0,5141	0,6786	0,7037	0,6196	0,7061	0,7290	**0,7368**	0,6572	0,7425	<u>**0,7629**</u>	**0,7582**	0,7480
PD_SE_no3_rf20_B	0,6089	**0,7428**	0,7397	0,7151	0,7408	0,6320	0,7333	0,7147	0,6970	**0,7170**	0,7082	0,6977	0,6696	0,7405	<u>**0,7546**</u>	0,7082	**0,7142**
T1_fl_no3_rf20_B	0,7622	0,7554	0,7355	**0,7672**	0,7578	0,5507	0,7635	0,7326	0,7547	0,7741	<u>**0,7789**</u>	0,7768	0,6890	0,7486	**0,7765**	**0,7756**	0,7624
T1_IR_no3_rf20_B	0,7999	0,8047	0,8042	0,8014	<u>**0,8057**</u>	0,6844	0,8055	0,7664	0,8002	0,8037	**0,8055**	0,8050	0,7768	0,8033	**0,8052**	0,8035	0,8018
T2_SE_no3_rf20_B	0,7119	0,7103	0,7021	0,7118	0,7081	0,5159	0,7066	0,6733	0,6502	0,6981	0,7080	0,7005	0,6605	0,7144	<u>**0,7200**</u>	0,7099	**0,7179**
rf40																	
T2_EPI_no3_rf40_B	0,5879	0,6275	**0,7076**	0,6291	0,6700	0,5120	0,6682	0,6971	0,6049	0,6858	0,6988	**0,7056**	0,6216	0,7157	<u>**0,7604**</u>	**0,7301**	0,7147
PD_SE_no3_rf40_B	0,4969	0,7256	0,7254	0,5744	**0,7267**	0,6182	0,7122	**0,6966**	0,6836	0,6871	0,6551	0,6297	0,6665	0,7395	<u>**0,7519**</u>	0,5700	**0,6498**
T1_fl_no3_rf40_B	0,7085	**0,7605**	0,7358	0,7182	0,7476	0,5490	0,7536	0,7385	0,7442	0,7726	**0,7761**	0,7717	0,6846	0,7513	<u>**0,7785**</u>	0,7301	0,7534
T1_IR_no3_rf40_B	0,7937	0,8054	0,8059	0,7957	**0,8064**	0,7246	0,8061	0,7697	0,8021	0,8052	**0,8067**	0,8067	0,7848	0,8052	<u>**0,8073**</u>	0,8023	0,8003
T2_SE_no3_rf40_B	0,6643	0,6674	**0,6743**	0,6682	0,6721	0,5588	0,6717	0,6695	0,6333	0,6880	**0,6971**	0,6844	0,6601	0,6971	<u>**0,7156**</u>	**0,7093**	0,7072
rf100																	
T2_EPI_no3_rf100_B	0,4166	0,6392	**0,7112**	0,4227	0,6835	0,5140	0,6747	**0,6708**	0,5785	0,6344	0,6171	0,6084	0,6551	0,7285	<u>**0,7501**</u>	**0,4205**	0,3985
PD_SE_no3_rf100_B	0,4497	0,6952	0,7072	0,4477	**0,7096**	0,5270	0,6876	**0,6134**	0,5236	0,5306	0,4898	0,4637	0,6643	0,7283	<u>**0,7318**</u>	0,3825	0,3892
T1_fl_no3_rf100_B	0,5588	0,7189	**0,7349**	0,5633	0,7310	0,5383	0,7260	0,7402	0,7290	**0,7442**	0,7197	0,6863	0,6828	0,7478	<u>**0,7697**</u>	0,4106	0,3992
T1_IR_no3_rf100_B	0,6919	0,7668	**0,7920**	0,6956	0,7865	0,6942	0,7852	0,7725	0,7833	**0,7951**	0,7920	0,7821	0,7757	0,8025	<u>**0,8055**</u>	0,4345	0,4323
T2_SE_no3_rf100_B	0,3196	0,3442	0,3444	0,3205	**0,3486**	0,3381	0,3478	0,6580	0,6108	**0,6674**	0,6661	0,6449	0,6531	0,7019	<u>**0,7102**</u>	0,3835	0,3576

No background = worse than the uncorrected, background = better than the uncorrected, bold = best parameters for the algorithm, underline = best correction for the image.

Table B.2: Dice values for GM, 3% noise and C field images.

	Uncorrected	N3_01_2_4	N3_03_2_4	N3_015_2_2	N3_015_2_4	N3_015_2_6	N3_015_4_4	FSL_2_20	FSL_3_10	FSL_3_20	FSL_3_30	FSL_4_20	SPM_30	SPM_60	SPM_90	PABIC_2cl	PABIC_3cl
rf20																	
T2_EPI_no3_rf20_C	0,7182	0,6631	0,7135	**0,7320**	0,6968	0,5136	0,6949	0,7064	0,6307	0,7169	0,7387	**0,7409**	0,6630	0,7476	**_0,7676_**	**0,7572**	0,6974
PD_SE_no3_rf20_C	0,6390	**0,7412**	0,7376	0,7136	0,7388	0,6240	0,7319	0,7195	0,7001	**0,7201**	0,7148	0,7054	0,6778	0,7462	**_0,7540_**	0,7237	0,7131
T1_fl_no3_rf20_C	0,7684	0,7569	0,7361	**0,7727**	0,7609	0,5546	0,7622	0,7346	0,7591	0,7773	**_0,7821_**	0,7796	0,7000	0,7615	**0,7782**	0,7690	0,7670
T1_IR_no3_rf20_C	0,8027	0,8048	0,8045	0,8039	**_0,8059_**	0,6804	0,8058	0,7668	0,8006	0,8040	0,8057	0,8049	0,7829	0,8033	0,8051	0,8006	**0,8042**
T2_SE_no3_rf20_C	0,7134	0,7135	0,7091	**0,7140**	0,7126	0,6237	0,7118	0,6752	0,6564	0,7003	0,7097	0,7020	0,6643	0,7188	**_0,7238_**	0,7110	**0,7156**
rf40																	
T2_EPI_no3_rf40_C	0,6382	0,6423	**0,7130**	0,6655	0,6801	0,5132	0,6738	0,7048	0,6243	0,7051	0,7200	**0,7238**	0,6819	0,7502	**_0,7666_**	**0,7120**	0,7063
PD_SE_no3_rf40_C	0,5527	**0,7356**	0,7335	0,6188	0,7346	0,6250	0,7240	**0,7088**	0,6970	0,7062	0,6837	0,6628	0,6755	0,7474	**_0,7536_**	**0,6545**	0,6532
T1_fl_no3_rf40_C	0,7131	0,7594	0,7400	0,7230	0,7496	0,5537	**0,7664**	0,7422	0,7567	**0,7792**	0,7827	0,7776	0,6948	0,7584	**_0,7799_**	0,7509	0,7695
T1_IR_no3_rf40_C	0,7854	0,8052	0,8030	0,7884	**0,8053**	0,7184	0,8048	0,7678	0,7987	0,8027	0,8039	**0,8043**	0,7785	0,8047	**_0,8061_**	0,8029	0,7898
T2_SE_no3_rf40_C	0,6747	0,6766	**0,6806**	0,6765	0,6794	0,5679	0,6802	0,6719	0,6428	0,6908	**0,6993**	0,6871	0,6702	0,7180	**_0,7225_**	0,7014	0,7118
rf100																	
T2_EPI_no3_rf100_C	0,4638	0,6268	**0,7174**	0,4744	0,6792	0,5110	0,6755	**0,6913**	0,5746	0,6362	0,6215	0,6677	0,6661	0,7575	**_0,7698_**	0,6226	**0,6681**
PD_SE_no3_rf100_C	0,4540	0,7234	0,7222	0,4677	**_0,7246_**	0,6156	0,7060	0,6335	**0,6638**	0,6292	0,5722	0,5536	0,6380	0,7073	0,7203	0,3846	0,3538
T1_fl_no3_rf100_C	0,5806	**0,7491**	0,7432	0,5853	0,7441	0,5688	0,7464	0,7532	0,7473	**_0,7654_**	0,7474	0,7104	0,7037	0,7450	**0,7631**	0,7003	**0,7059**
T1_IR_no3_rf100_C	0,7162	0,7801	0,7963	0,7197	0,7969	0,7267	**0,7985**	0,7772	0,7978	**0,8036**	0,8023	0,7915	0,7807	0,8042	**_0,8082_**	0,7833	0,7800
T2_SE_no3_rf100_C	0,3660	0,3513	0,3490	0,3638	0,3471	0,3574	0,3454	0,6654	0,6076	0,6653	**0,6728**	0,6573	0,5187	0,6778	**0,6876**	0,6607	**_0,6926_**

No background = worse than the uncorrected, background = better than the uncorrected, bold = best parameters for the algorithm, underline = best correction for the image.

Table B.3: Dice values for GM, 9% noise and A field images.

	Uncorrected	N3_01_2_4	N3_03_2_4	N3_015_2_2	N3_015_2_4	N3_015_2_6	N3_015_4_4	FSL_2_20	FSL_3_10	FSL_3_20	FSL_3_30	FSL_4_20	SPM_30	SPM_60	SPM_90	PABIC_2cl	PABIC_3cl
rf20																	
T1_fl_no9_rf20_A	0,6275	0,6102	0,6016	**0,6280**	0,6077	0,4890	0,6062	0,5825	0,5543	0,5949	0,6106	0,6059	0,5635	0,5976	0,6165	0,6162	0,6051
T1_IR_no9_rf20_A	0,7038	0,6980	0,6931	**0,7040**	0,6948	0,5615	0,6895	0,6523	0,6313	0,6733	0,6881	0,6839	0,6351	0,6794	0,6941	0,4891	0,6621
rf40																	
T1_fl_no9_rf40_A	0,6180	0,6170	0,6063	**0,6199**	0,6119	0,4910	0,6132	0,5862	0,5560	0,5991	0,6164	0,6110	0,5629	0,6021	**0,6200**	**0,6253**	0,6065
T1_IR_no9_rf40_A	0,6983	**0,7044**	0,7002	0,6993	0,7029	0,5720	0,6989	0,6580	0,6385	0,6808	0,6952	0,6909	0,6368	0,6879	**0,7003**	0,5103	0,6519
rf100																	
T1_fl_no9_rf100_A	0,5539	0,6074	0,6023	0,5570	0,6092	0,4912	**0,6102**	0,5942	0,5636	0,6061	**0,6190**	0,6089	0,5595	0,6038	**0,6199**	0,5918	0,5814
T1_IR_no9_rf100_A	0,6486	0,6875	0,6977	0,6512	0,6999	0,5763	**0,7003**	0,6684	0,6506	0,6906	**0,7018**	0,6944	0,6372	0,6888	**0,7026**	0,5771	**0,6572**

No background = worse than the uncorrected, background = better than the uncorrected, bold = best parameters for the algorithm, underline = best correction for the image.

B.1.2 Dice coefficient white matter

Table B.4: Dice values for WM, 3% noise and B field images.

	Uncorrected	N3_01_2_4	N3_03_2_4	N3_015_2_2	N3_015_2_4	N3_015_2_6	N3_015_4_4	FSL_2_20	FSL_3_10	FSL_3_20	FSL_3_30	FSL_4_20	SPM_30	SPM_60	SPM_90	PABIC_2cl	PABIC_3cl
rf20																	
T2_EPI_no3_rf20_B	0,7390	0,6808	0,7533	**0,7649**	0,7245	0,5565	0,7276	0,7410	0,6733	0,7458	0,7646	**0,7708**	0,7049	0,7804	_**0,7990**_	**0,7916**	0,7814
PD_SE_no3_rf20_B	0,5864	0,7225	_0,7226_	0,7000	0,7200	0,5740	0,7112	0,6619	0,6329	0,6746	**0,6754**	0,6626	0,5922	0,6936	0,7075	0,6570	**0,6719**
T1_fl_no3_rf20_B	0,8297	0,8215	0,8027	**0,8341**	0,8239	0,6088	0,8298	0,8016	0,8203	0,8396	_0,8443_	0,8424	0,7692	0,8250	**0,8430**	**0,8419**	0,8306
T1_IR_no3_rf20_B	0,8532	0,8573	0,8574	0,8543	_0,8579_	0,7492	0,8574	0,8306	0,8544	0,8565	**0,8578**	0,8565	0,8290	0,8566	**0,8577**	0,8546	**0,8547**
T2_SE_no3_rf20_B	0,8142	0,8127	0,8049	0,8141	0,8112	0,6957	0,8091	0,7768	0,7488	0,8018	0,8116	0,8038	0,7686	0,8202	_0,8259_	0,8147	**0,8219**
rf40																	
T2_EPI_no3_rf40_B	0,6225	0,6291	**0,7438**	0,6625	0,6906	0,5328	0,6921	0,7339	0,6640	0,7305	0,7382	**0,7389**	0,6647	0,7530	_0,7960_	**0,7419**	0,7397
PD_SE_no3_rf40_B	0,4641	0,6873	**0,6903**	0,5491	0,6889	0,5533	0,6734	0,6492	0,6222	**0,6527**	0,6345	0,6062	0,5921	0,6960	_0,7067_	0,5350	**0,6062**
T1_fl_no3_rf40_B	0,7847	**0,8266**	0,8028	0,7931	0,8128	0,6056	0,8196	0,8067	0,8087	0,8363	**0,8402**	0,8373	0,7703	0,8276	_0,8440_	0,7995	**0,8203**
T1_IR_no3_rf40_B	0,8456	0,8569	**0,8575**	0,8476	0,8574	0,7844	0,8570	0,8340	0,8546	0,8566	_0,8579_	0,8564	0,8357	0,8568	0,8575	0,8547	0,8521
T2_SE_no3_rf40_B	0,7636	0,7678	**0,7769**	0,7679	0,7741	0,6267	0,7732	0,7749	0,7324	0,7914	**0,7995**	0,7886	0,7621	0,8030	_0,8221_	0,8101	**0,8116**
rf100																	
T2_EPI_no3_rf100_B	0,4557	0,6496	**0,7442**	0,4630	0,7198	0,5589	0,7120	**0,7113**	0,6488	0,6973	0,6818	0,6559	0,7056	0,7652	_0,7837_	**0,6315**	0,5725
PD_SE_no3_rf100_B	0,4045	0,6675	0,6878	0,4041	**0,6881**	0,5677	0,6692	**0,6012**	0,4951	0,5040	0,4498	0,4162	0,6051	0,6874	_0,6926_	0,4204	**0,4397**
T1_fl_no3_rf100_B	0,6772	0,8077	**0,8120**	0,6808	0,8022	0,6268	0,7968	0,8128	0,7928	**0,8157**	0,8009	0,7734	0,7662	0,8302	_0,8423_	0,7578	0,7360
T1_IR_no3_rf100_B	0,7617	0,8233	**0,8486**	0,7650	0,8417	0,7288	0,8398	0,8352	0,8392	**0,8498**	0,8479	0,8304	0,8300	_0,8553_	_0,8553_	0,8315	0,8154
T2_SE_no3_rf100_B	0,4317	0,4663	0,4681	0,4293	0,4694	**0,4904**	0,4700	0,7603	0,7166	**0,7733**	0,7688	0,7438	0,7531	0,8094	_0,8176_	0,7343	0,6133

No background = worse than the uncorrected, background = better than the uncorrected, bold = best parameters for the algorithm, underline = best correction for the image.

Table B.5: Dice values for WM, 3% noise and C field images.

	Uncorrected	N3_01_2_4	N3_03_2_4	N3_015_2_2	N3_015_2_4	N3_015_2_6	N3_015_4_4	FSL_2_20	FSL_3_10	FSL_3_20	FSL_3_30	FSL_4_20	SPM_30	SPM_60	SPM_90	PABIC_2cl	PABIC_3cl
															Correction methods		
rf20																	
T2_EPI_no3_rf20_C	0,7491	0,6835	0,7529	**0,7650**	0,7320	0,5329	0,7300	0,7437	0,6807	0,7540	0,7716	**0,7749**	0,7123	0,7891	_0,8038_	**0,7975**	0,6795
PD_SE_no3_rf20_C	0,6187	**0,7012**	0,7001	0,6831	0,6981	0,5526	0,6909	0,6670	0,6388	0,6785	**0,6818**	0,6710	0,6149	0,6929	_0,7100_	0,6829	0,6747
T1_fl_no3_rf20_C	0,8358	0,8228	0,8027	**0,8393**	0,8266	0,6175	0,8279	0,8025	0,8238	0,8415	_0,8458_	0,8439	0,7661	0,8304	**0,8432**	0,8368	0,8316
T1_IR_no3_rf20_C	0,8551	0,8574	0,8578	0,8560	_0,8582_	0,7450	_0,8582_	0,8312	0,8545	0,8567	**0,8581**	0,8570	0,8345	0,8566	**0,8576**	0,8535	**0,8581**
T2_SE_no3_rf20_C	0,8167	0,8172	0,8144	0,8174	**0,8176**	0,7157	0,8169	0,7792	0,7572	0,8047	0,8143	0,8062	0,7735	0,8253	_0,8307_	0,8147	0,8211
rf40																	
T2_EPI_no3_rf40_C	0,6719	0,6536	**0,7502**	0,6933	0,7081	0,5361	0,7019	0,7429	0,6797	0,7457	0,7556	**0,7570**	0,7307	0,7857	_0,7999_	0,7323	**0,7395**
PD_SE_no3_rf40_C	0,5325	0,6996	**0,7000**	0,6076	0,6979	0,5595	0,6863	0,6605	0,6347	**0,6697**	0,6608	0,6389	0,6105	0,6995	_0,7132_	0,6263	0,6100
T1_fl_no3_rf40_C	0,8036	0,8260	0,8065	0,8105	0,8153	0,6165	**0,8321**	0,8097	0,8202	0,8426	**0,8464**	0,8429	0,7840	0,8379	_0,8466_	0,8190	0,8356
T1_IR_no3_rf40_C	0,8413	_0,8573_	0,8562	0,8442	0,8571	0,7795	0,8566	0,8324	0,8533	0,8561	**0,8571**	0,8548	0,8294	0,8565	**0,8572**	0,8562	0,8439
T2_SE_no3_rf40_C	0,7776	0,7799	**0,7862**	0,7795	0,7840	0,6482	0,7849	0,7783	0,7450	0,7955	**0,8032**	0,7933	0,7788	0,8255	_0,8300_	0,8035	0,8118
rf100																	
T2_EPI_no3_rf100_C	0,5828	0,6326	**0,7532**	0,5921	0,7088	0,5483	0,7067	**0,7318**	0,6497	0,7061	0,7020	0,7100	0,7169	0,7928	_0,8019_	0,3274	0,0802
PD_SE_no3_rf100_C	0,3747	0,6980	0,7011	0,3645	**0,7020**	0,5610	0,6841	0,6177	0,6184	**0,6316**	0,5912	0,5316	0,6299	0,7061	_0,7141_	0,4632	**0,5307**
T1_fl_no3_rf100_C	0,7123	**0,8333**	0,8191	0,7166	0,8157	0,6442	0,8177	0,8239	0,8104	**0,8360**	0,8315	0,7971	0,7945	0,8400	_0,8470_	0,7947	0,7975
T1_IR_no3_rf100_C	0,7968	0,8379	**0,8517**	0,7997	0,8504	0,7645	0,8516	0,8390	0,8490	**0,8544**	0,8544	0,8339	0,8393	_0,8559_	0,8556	**0,8356**	0,8317
T2_SE_no3_rf100_C	0,4712	0,4424	0,4347	0,4651	0,4287	**0,4858**	0,4257	0,7735	0,7217	0,7880	**0,7909**	0,7635	0,3363	0,7817	**0,7917**	0,7645	_0,7978_

No background = worse than the uncorrected, background = better than the uncorrected, bold = best parameters for the algorithm, underline = best correction for the image.

Table B.6: Dice values for GM, 9% noise and A field images.

	Uncorrected	N3_01_2_4	N3_03_2_4	N3_015_2_2	N3_015_2_4	N3_015_2_6	N3_015_4_4	FSL_2_20	FSL_3_10	FSL_3_20	FSL_3_30	FSL_4_20	SPM_30	SPM_60	SPM_90	PABIC_2cl	PABIC_3cl
rf20																	
T1_fl_no9_rf20_A	0,7125	0,6903	0,6804	**0,7126**	0,6877	0,5078	0,6857	0,6577	0,6229	0,6728	0,6914	0,6862	0,6341	0,6792	0,6979	0,6922	0,6847
T1_IR_no9_rf20_A	0,7928	0,7875	0,7825	**0,7930**	0,7842	0,6262	0,7787	0,7447	0,7240	0,7645	0,7780	0,7741	0,7253	0,7716	0,7842	0,5605	0,7480
rf40																	
T1_fl_no9_rf40_A	0,7107	0,7015	0,6892	**0,7121**	0,6949	0,5142	0,6974	0,6651	0,6300	0,6815	0,7009	0,6958	0,6396	0,6874	0,7058	0,7082	0,6912
T1_IR_no9_rf40_A	0,7884	**0,7935**	0,7895	0,7893	0,7919	0,6418	0,7880	0,7498	0,7304	0,7707	0,7840	0,7801	0,7268	0,7784	0,7893	0,5899	0,7385
rf100																	
T1_fl_no9_rf100_A	0,6751	**0,7104**	0,7042	0,6777	0,7048	0,5437	0,7062	0,6844	0,6518	0,7005	**0,7168**	0,7077	0,6708	0,7073	**0,7227**	**0,6773**	0,6755
T1_IR_no9_rf100_A	0,7541	0,7881	0,7934	0,7562	**0,7965**	0,6654	**0,7965**	0,7615	0,7439	0,7815	**0,7928**	0,7871	0,7413	0,7852	**0,7955**	0,6548	0,7499

No background = worse than the uncorrected, background = better than the uncorrected, bold = best parameters for the algorithm, underline = best correction for the image.

B.1.3 Sensitivity for grey matter

Table B.7: Sensitivity values for GM, 3% noise and a field images.

	Uncorrected	N3_01_2_4	N3_03_2_4	N3_015_2_2	N3_015_2_4	N3_015_2_6	N3_015_4_4	FSL_2_20	FSL_3_10	FSL_3_20	FSL_3_30	FSL_4_20	SPM_30	SPM_60	SPM_90	PABIC_2cl	PABIC_3cl
rf20																	
T2_EPI_no3_rf20_A	0,6756	0,6393	0,6858	**0,6978**	0,6732	0,4777	0,6744	0,6148	0,5467	0,6348	0,6620	0,6681	0,6167	0,7151	<u>**0,7437**</u>	**0,7274**	0,7116
PD_SE_no3_rf20_A	0,6159	**0,7431**	0,7394	0,7144	0,7406	0,6144	0,7330	0,7613	0,7475	<u>**0,7733**</u>	0,7698	0,7569	0,6706	0,7430	**0,7584**	0,7175	**0,7198**
T1_fl_no3_rf20_A	0,7119	0,6882	0,6591	**0,7163**	0,6904	0,4742	0,6988	0,6338	0,6228	0,7258	0,7644	<u>**0,7833**</u>	0,6241	0,6921	**0,7190**	**0,7281**	0,7151
T1_IR_no3_rf20_A	0,7654	0,7694	0,7654	0,7674	<u>**0,7708**</u>	0,5800	0,7706	0,6905	0,7605	0,7665	**0,7694**	0,7694	0,7302	0,7654	**0,7691**	**0,7669**	0,7593
T2_SE_no3_rf20_A	0,6243	**0,6245**	0,6190	0,6234	0,6222	0,5475	0,6193	0,4089	0,3874	0,4230	0,4412	0,4267	0,5734	0,6288	<u>**0,6342**</u>	0,6276	**0,6316**
rf40																	
T2_EPI_no3_rf40_A	0,5767	0,6147	**0,6833**	0,6123	0,6541	0,4737	0,6531	0,6564	0,5640	0,6538	0,6715	**0,6751**	0,5828	0,6967	<u>**0,7382**</u>	0,6672	**0,6832**
PD_SE_no3_rf40_A	0,5142	**0,7315**	0,7299	0,6004	0,7309	0,6105	0,7193	0,7028	0,6924	**0,7036**	0,6769	0,6477	0,6324	0,6979	<u>**0,7355**</u>	0,4768	**0,5591**
T1_fl_no3_rf40_A	0,6512	**0,6889**	0,6619	0,6629	0,6811	0,4778	0,6838	0,6594	0,6820	0,7174	**0,7261**	0,7223	0,6312	0,6978	<u>**0,7733**</u>	0,6689	0,6978
T1_IR_no3_rf40_A	0,7526	**0,7686**	0,7671	0,7557	0,7712	0,6240	0,7696	0,6942	0,7611	0,7674	0,7705	<u>**0,7736**</u>	0,7355	**0,7672**	0,7216	**0,7683**	0,7646
T2_SE_no3_rf40_A	0,5799	0,5817	**0,5876**	0,5834	0,5834	0,4879	0,5822	0,5783	0,5506	0,5968	**0,6061**	0,5925	0,5673	0,6077	<u>**0,6280**</u>	0,6018	**0,6172**
rf100																	
T2_EPI_no3_rf100_A	0,3729	0,5761	**0,6754**	0,3839	0,6467	0,4694	0,6359	**0,6432**	0,5139	0,5863	0,5775	0,5911	0,6547	0,7279	<u>**0,7420**</u>	**0,6113**	0,5583
PD_SE_no3_rf100_A	0,3614	0,6712	0,6943	0,3579	**0,6946**	0,5526	0,6619	0,6379	**0,6475**	0,6074	0,5336	0,5257	0,6035	0,6655	<u>**0,7055**</u>	0,4773	**0,4692**
T1_fl_no3_rf100_A	0,5106	0,6615	0,6673	0,5146	0,6723	0,4799	**0,6726**	0,6720	0,6652	**0,7065**	0,6985	0,6711	0,6159	0,6794	<u>**0,7088**</u>	0,6215	**0,6270**
T1_IR_no3_rf100_A	0,6439	0,7508	**0,7660**	0,6490	0,7651	0,6780	0,7637	0,7031	0,7472	0,7639	0,7647	**0,7716**	0,7283	0,7733	<u>**0,7794**</u>	**0,7493**	0,7285
T2_SE_no3_rf100_A	0,2818	0,2938	0,2937	0,2806	0,2952	**0,2988**	0,2907	0,5706	0,5227	0,5700	**0,5764**	0,5613	0,5661	0,5820	<u>**0,5953**</u>	0,5552	0,4795

No background = worse than the uncorrected, background = better than the uncorrected, bold = best parameters for the algorithm, underline = best correction for the image.

Table B.8: Sensitivity values for GM, 3% noise and B field images.

	Uncorrected	N3_01_2_4	N3_03_2_4	N3_015_2_2	N3_015_2_4	N3_015_2_6	N3_015_4_4	FSL_2_20	FSL_3_10	FSL_3_20	FSL_3_30	FSL_4_20	SPM_30	SPM_60	SPM_90	PABIC_2cl	PABIC_3cl
rf20																	
T2_EPI_no3_rf20_B	0,6528	0,6259	**0,6735**	0,6700	0,6535	0,4874	0,6533	0,6560	0,5606	0,6600	0,6879	**0,6971**	0,6241	0,7176	_0,7443_	**0,7409**	0,7156
PD_SE_no3_rf20_B	0,5857	**0,7550**	0,7514	0,7202	0,7525	0,6307	0,7413	0,7113	0,6931	**0,7156**	0,7042	0,6899	0,6628	0,7437	_0,7624_	0,6989	**0,7073**
T1_fl_no3_rf20_B	0,7088	0,6870	0,6596	**0,7139**	0,6903	0,4782	0,6987	0,6537	0,6877	0,7142	_0,7222_	0,7201	0,6101	0,6807	0,7187	**0,7181**	0,7076
T1_IR_no3_rf20_B	0,7622	0,7687	0,7656	0,7645	0,7703	0,5967	_0,7707_	0,6920	0,7592	0,7661	0,7696	**0,7706**	0,7230	0,7648	0,7695	**0,7687**	0,7651
T2_SE_no3_rf20_B	0,6230	0,6191	0,6095	0,6211	0,6162	0,3925	0,6147	0,5820	0,5628	0,6067	0,6171	0,6091	0,5707	0,6265	_0,6322_	0,6198	**0,6316**
rf40																	
T2_EPI_no3_rf40_B	0,5295	0,5962	0,6772	0,5677	**0,6399**	0,4738	0,6370	0,6461	0,5409	0,6325	0,6481	**0,6549**	0,5780	0,6867	_0,7418_	**0,7030**	0,6755
PD_SE_no3_rf40_B	0,4807	0,7213	0,7224	0,5539	**0,7236**	0,6057	0,7026	**0,6869**	0,6777	0,6759	0,6362	0,6083	0,6581	0,7418	_0,7580_	0,5517	0,6267
T1_fl_no3_rf40_B	0,6523	**0,6945**	0,6610	0,6621	0,6767	0,4764	0,6841	0,6614	0,6737	0,7134	**0,7211**	0,7197	0,6048	0,6861	_0,7235_	0,6699	**0,6987**
T1_IR_no3_rf40_B	0,7592	0,7725	0,7712	0,7617	0,7736	0,6440	**0,7738**	0,6967	0,7649	0,7712	0,7736	_0,7767_	0,7387	0,7719	_0,7767_	0,7651	0,7633
T2_SE_no3_rf40_B	0,5745	0,5762	**0,5818**	0,5779	0,5785	0,4855	0,5784	0,5763	0,5443	0,5939	**0,6029**	0,5898	0,5720	0,6051	_0,6263_	**0,6240**	0,6222
rf100																	
T2_EPI_no3_rf100_B	0,3768	0,6034	**0,6759**	0,3830	0,6492	0,4717	0,6380	**0,6181**	0,5107	0,5707	0,5534	0,5432	0,6219	0,7009	_0,7271_	**0,5740**	0,5046
PD_SE_no3_rf100_B	0,3619	0,6837	0,6972	0,3703	**0,7004**	0,4686	0,6685	**0,5877**	0,4980	0,5110	0,4754	0,4526	0,6526	0,7232	_0,7266_	0,3399	0,3114
T1_fl_no3_rf100_B	0,5049	0,6530	**0,6597**	0,5089	0,6574	0,4473	0,6531	0,6678	0,6614	**0,6853**	0,6605	0,6325	0,6085	0,6841	_0,7175_	0,6038	0,5744
T1_IR_no3_rf100_B	0,6358	0,7440	**0,7614**	0,6397	0,7611	0,6569	0,7612	0,7045	0,7317	0,7533	0,7510	**0,7575**	0,7275	0,7718	_0,7786_	0,7378	0,7190
T2_SE_no3_rf100_B	0,2441	0,2676	0,2680	0,2450	**0,2721**	0,2645	0,2712	0,5628	0,5171	**0,5673**	0,5671	0,5506	0,5653	0,6113	_0,6206_	0,5524	0,4215

Correction methods

No background = worse than the uncorrected, background = better than the uncorrected, bold = best parameters for the algorithm, underline = best correction for the image.

Table B.9: Sensitivity values for GM, 3% noise and C field images.

	Uncorrected	N3_01_2_4	N3_03_2_4	N3_015_2_2	N3_015_2_4	N3_015_2_6	N3_015_4_4	FSL_2_20	FSL_3_10	FSL_3_20	FSL_3_30	FSL_4_20	SPM_30	SPM_60	SPM_90	PABIC_2cl	PABIC_3cl
rf20																	
T2_EPI_no3_rf20_C	0,6710	0,6331	0,6843	**0,6891**	0,6677	0,4755	0,6647	0,6595	0,5740	0,6735	0,6999	**0,7032**	0,6296	0,7260	_0,7529_	**0,7409**	0,6703
PD_SE_no3_rf20_C	0,6180	**0,7453**	0,7406	0,7109	0,7418	0,6126	0,7319	0,7174	0,6952	**0,7182**	0,7116	0,6988	0,6702	0,7480	_0,7629_	0,7224	0,7065
T1_fl_no3_rf20_C	0,7168	0,6884	0,6598	**0,7210**	0,6936	0,4794	0,6959	0,6559	0,6937	0,7187	_0,7263_	0,7233	0,6237	0,6966	**0,7204**	0,7073	0,7087
T1_IR_no3_rf20_C	0,7679	0,7693	0,7659	0,7696	_0,7708_	0,5921	0,7706	0,6923	0,7611	0,7674	**0,7704**	0,7704	0,7332	0,7658	**0,7700**	0,7630	0,7650
T2_SE_no3_rf20_C	0,6235	0,6233	0,6178	**0,6241**	0,6218	0,5457	0,6209	0,5837	0,5675	0,6089	0,6187	0,6104	0,5732	0,6299	_0,6353_	0,6225	**0,6245**
rf40																	
T2_EPI_no3_rf40_C	0,5813	0,6119	**0,6838**	0,6103	0,6501	0,4733	0,6426	0,6560	0,5653	0,6579	0,6762	**0,6789**	0,6514	0,7262	_0,7477_	**0,6861**	0,6631
PD_SE_no3_rf40_C	0,5359	**0,7360**	0,7343	0,5952	0,7352	0,6140	0,7194	**0,7025**	0,6938	0,6996	0,6702	0,6442	0,6686	0,7512	_0,7623_	0,6340	0,6295
T1_fl_no3_rf40_C	0,6561	0,6933	0,6654	0,6670	0,6794	0,4782	**0,7036**	0,6657	0,6911	0,7235	_0,7305_	0,7269	0,6152	0,6957	**0,7257**	0,6947	**0,7206**
T1_IR_no3_rf40_C	0,7411	0,7703	0,7656	0,7451	**0,7713**	0,6375	0,7705	0,6947	0,7571	0,7648	0,7669	**0,7729**	0,7277	0,7700	_0,7734_	0,7638	0,7479
T2_SE_no3_rf40_C	0,5791	0,5807	**0,5849**	0,5810	0,5829	0,4954	0,5838	0,5780	0,5512	0,5962	**0,6048**	0,5916	0,5790	0,6294	_0,6345_	0,6155	0,6243
rf100																	
T2_EPI_no3_rf100_C	0,3870	0,5943	**0,6843**	0,3981	0,6465	0,4684	0,6412	**0,6415**	0,5044	0,5761	0,5651	0,6081	0,6321	0,7367	_0,7495_	0,5801	**0,6270**
PD_SE_no3_rf100_C	0,4243	0,7166	0,7160	0,4399	_0,7191_	0,6031	0,6918	0,6094	**0,6518**	0,5973	0,5314	0,5345	0,6144	0,6958	**0,7137**	0,3434	0,3189
T1_fl_no3_rf100_C	0,5144	**0,6838**	0,6685	0,5188	0,6721	0,4830	0,6757	0,6823	0,6825	_0,7119_	0,6920	0,6622	0,6305	0,6817	**0,7077**	0,6436	**0,6438**
T1_IR_no3_rf100_C	0,6650	0,7558	**0,7684**	0,6698	0,7727	0,6937	0,7728	0,7093	0,7594	0,7710	0,7698	**0,7742**	0,7370	0,7772	_0,7852_	**0,7502**	0,7499
T2_SE_no3_rf100_C	0,2893	0,2758	0,2737	0,2872	0,2718	0,2881	0,2700	**0,5679**	0,5164	0,5594	0,5672	0,5568	0,5389	0,5819	**0,5921**	0,5728	_0,6062_

No background = worse than the uncorrected, background = better than the uncorrected, bold = best parameters for the algorithm, underline = best correction for the image.

Table B.10: Sensitivity values for GM, 9% noise and A field images.

	Uncorrected	N3_01_2_4	N3_03_2_4	N3_015_2_2	N3_015_2_4	N3_015_2_6	N3_015_4_4	FSL_2_20	FSL_3_10	FSL_3_20	FSL_3_30	FSL_4_20	SPM_30	SPM_60	SPM_90	PABIC_2cl	PABIC_3cl
rf20																	
T1_fl_no9_rf20_A	0,5626	0,5426	0,5340	**0,5630**	0,5401	0,4455	0,5385	0,5163	0,4918	0,5275	0,5423	0,5384	0,5008	0,5300	0,5485	0,5554	0,5420
T1_IR_no9_rf20_A	0,6292	0,6188	0,6122	**0,6294**	0,6146	0,4931	0,6081	0,5661	0,5459	0,5900	0,6070	0,6023	0,5512	0,5968	0,6139	0,4350	0,5895
rf40																	
T1_fl_no9_rf40_A	0,5554	0,5498	0,5384	**0,5568**	0,5443	0,4466	0,5450	0,5185	0,4911	0,5299	0,5472	0,5428	0,4983	0,5332	0,5509	**0,5642**	0,5435
T1_IR_no9_rf40_A	0,6269	**0,6289**	0,6212	0,6276	0,6258	0,5011	0,6201	0,5717	0,5530	0,5984	0,6156	0,6111	0,5514	0,6062	0,6214	0,4532	0,5814
rf100																	
T1_fl_no9_rf100_A	0,4942	0,5393	0,5308	0,4968	0,5396	0,4417	**0,5404**	0,5220	0,4930	0,5335	**0,5481**	0,5401	0,4861	0,5303	**0,5471**	**0,5263**	0,5217
T1_IR_no9_rf100_A	0,5794	0,6163	0,6226	0,5820	**0,6262**	0,4998	0,6259	0,5825	0,5654	0,6113	**0,6267**	0,6197	0,5492	0,6075	**0,6258**	0,5197	**0,5843**

No background = worse than the uncorrected, background = better than the uncorrected, bold = best parameters for the algorithm, underline = best correction for the image.

B.1.4 Sensitivity for white matter

Table B.11: Sensitivity values for WM, 3% noise and a field images.

	Uncorrected	N3_01_2_4	N3_03_2_4	N3_015_2_2	N3_015_2_4	N3_015_2_6	N3_015_4_4	FSL_2_20	FSL_3_10	FSL_3_20	FSL_3_30	FSL_4_20	SPM_30	SPM_60	SPM_90	PABIC_2cl	PABIC_3cl
rf20																	
T2_EPI_no3_rf20_A	0,8720	0,7961	0,8704	**0,8868**	0,8520	0,6295	0,8579	0,9328	0,9149	0,9353	0,9368	_0,9377_	0,8218	0,8904	**0,9032**	**0,8952**	0,8803
PD_SE_no3_rf20_A	0,7222	**0,8071**	**0,8071**	0,7912	0,8043	0,6506	0,7991	0,8116	0,7659	0,8247	_0,8350_	0,8269	0,7123	0,7950	**0,8114**	0,7756	**0,7959**
T1_fl_no3_rf20_A	0,8482	**0,8661**	0,8637	0,8510	0,8660	0,6845	0,8658	_0,9360_	0,9168	0,9151	0,9110	0,8965	0,8326	**0,8648**	0,8646	0,8586	**0,8628**
T1_IR_no3_rf20_A	0,8406	0,8411	**0,8463**	0,8403	0,8410	0,8308	0,8409	_0,8853_	0,8452	0,8422	0,8408	0,8385	**0,8505**	0,8453	0,8421	0,8398	**0,8486**
T2_SE_no3_rf20_A	0,8365	**0,8370**	0,8346	0,8369	0,8369	0,7257	0,8345	0,9637	0,9516	0,9637	0,9671	_0,9707_	0,7890	0,8399	**0,8432**	0,8429	0,8400
rf40																	
T2_EPI_no3_rf40_A	0,7882	0,7603	**0,8669**	0,8136	0,8234	0,6241	0,8267	0,8706	0,8248	0,8776	**0,8785**	0,8696	0,7944	0,8707	_0,8930_	0,8445	**0,8634**
PD_SE_no3_rf40_A	0,5719	0,8059	**0,8078**	0,6963	0,8047	0,6528	0,7982	0,7701	0,7357	**0,7845**	0,7791	0,7528	0,6914	0,7753	_0,8082_	0,0630	**0,6605**
T1_fl_no3_rf40_A	0,8128	_0,8673_	0,8638	0,8190	0,8645	0,6835	0,8663	**0,8657**	0,8588	0,8639	0,8611	0,8510	0,8341	**0,8643**	0,8388	0,8165	**0,8317**
T1_IR_no3_rf40_A	0,8382	0,8443	**0,8444**	0,8387	0,8407	0,8433	0,8418	_0,8840_	0,8436	0,8420	0,8405	0,8314	0,8448	0,8433	**0,8632**	0,8360	0,8243
T2_SE_no3_rf40_A	0,8125	0,8162	0,8193	0,8162	**0,8202**	0,6462	0,8196	0,8084	0,7716	0,8270	**0,8344**	0,8261	0,7884	0,8279	_0,8367_	0,8252	**0,8311**
rf100																	
T2_EPI_no3_rf100_A	0,5725	0,7276	**0,8658**	0,5953	0,8227	0,6496	0,8136	0,8527	0,8119	**0,8651**	0,8445	0,8125	0,8340	0,8784	_0,8889_	0,7232	**0,7568**
PD_SE_no3_rf100_A	0,4047	0,7798	**0,8007**	0,4012	0,7978	0,6387	0,7814	**0,7413**	0,7160	0,7318	0,6425	0,5804	0,6808	0,7741	_0,8047_	0,4642	0,4786
T1_fl_no3_rf100_A	0,7250	0,8469	_0,8730_	0,7286	0,8711	0,7210	0,8725	**0,8658**	0,8564	0,8561	0,8421	0,7880	0,8223	0,8450	**0,8487**	0,7799	**0,7912**
T1_IR_no3_rf100_A	0,7995	0,7946	**0,8219**	0,8008	0,8155	0,7501	0,8146	_0,8793_	0,8449	0,8439	0,8424	0,7924	**0,8348**	0,8332	0,8287	**0,8134**	0,8100
T2_SE_no3_rf100_A	0,4897	0,5567	0,5576	0,4840	0,5590	**0,6079**	0,5450	0,8123	0,7393	0,8309	_0,8369_	0,8140	0,4865	0,8108	**0,8258**	**0,7850**	0,6970

No background = worse than the uncorrected, background = better than the uncorrected, bold = best parameters for the algorithm, underline = best correction for the image.

Table B.12: Sensitivity values for WM, 3% noise and B field images.

	Uncorrected	N3_01_2_4	N3_03_2_4	N3_015_2_2	N3_015_2_4	N3_015_2_6	N3_015_4_4	FSL_2_20	FSL_3_10	FSL_3_20	FSL_3_30	FSL_4_20	SPM_30	SPM_60	SPM_90	PABIC_2cl	PABIC_3cl
rf20																	
T2_EPI_no3_rf20_B	0,8671	0,7801	0,8754	**0,9026**	0,8378	0,6677	0,8441	0,8709	0,8188	0,8783	0,8889	**0,8901**	0,8274	0,8908	**<u>0,9046</u>**	**0,8949**	0,8937
PD_SE_no3_rf20_B	0,6962	0,8347	**<u>0,8358</u>**	0,8150	0,8324	0,6747	0,8263	0,7676	0,7351	0,7828	**0,7864**	0,7739	0,6865	0,8001	**0,8124**	0,7664	**0,7830**
T1_fl_no3_rf20_B	0,8517	0,8655	0,8640	0,8538	**<u>0,8659</u>**	0,6834	0,8656	**0,8648**	0,8615	0,8644	0,8628	0,8606	0,8324	0,8591	0,8626	**0,8632**	0,8500
T1_IR_no3_rf20_B	0,8467	0,8424	0,8466	0,8455	0,8422	0,8402	0,8415	**<u>0,8849</u>**	0,8482	0,8445	0,8428	0,8393	**0,8498**	0,8463	0,8426	0,8416	0,8427
T2_SE_no3_rf20_B	0,8316	0,8361	0,8327	0,8364	**0,8359**	0,8096	0,8349	0,8043	0,7718	0,8256	**0,8335**	0,8275	0,7912	0,8337	**<u>0,8381</u>**	0,8358	0,8350
rf40																	
T2_EPI_no3_rf40_B	0,7426	0,7266	**0,8596**	0,7879	0,7974	0,6245	0,8007	0,8639	0,8155	0,8723	**0,8731**	0,8626	0,7919	0,8656	**<u>0,8975</u>**	0,8411	**0,8481**
PD_SE_no3_rf40_B	0,5370	0,8011	**0,8033**	0,6446	0,8016	0,6492	0,7894	0,7595	0,7254	**0,7679**	0,7524	0,7189	0,6882	0,8041	**<u>0,8136</u>**	0,6101	**0,7101**
T1_fl_no3_rf40_B	0,8189	0,8678	0,8660	0,8256	0,8658	0,6802	**<u>0,8688</u>**	0,8675	0,8637	0,8662	0,8622	0,8507	0,8299	0,8560	**0,8606**	0,8365	**0,8398**
T1_IR_no3_rf40_B	0,8389	0,8381	0,8415	0,8392	0,8374	**0,8552**	0,8368	**<u>0,8839</u>**	0,8426	0,8396	0,8397	0,8332	**0,8430**	0,8401	0,8363	**0,8476**	0,8475
T2_SE_no3_rf40_B	0,7945	0,8013	0,8096	0,7991	**0,8113**	0,6324	0,8102	0,8063	0,7634	0,8252	**0,8337**	0,8222	0,7860	0,8283	**<u>0,8374</u>**	0,8244	0,8226
rf100																	
T2_EPI_no3_rf100_B	0,4953	0,7525	**0,8534**	0,5047	0,8337	0,6648	0,8277	0,8387	0,8074	**0,8537**	0,8245	0,7807	0,8213	0,8692	**<u>0,8795</u>**	0,7256	0,6457
PD_SE_no3_rf100_B	0,4383	0,7795	**<u>0,8046</u>**	0,4411	0,8035	0,5900	0,7900	**0,6933**	0,5921	0,5804	0,4964	0,4747	0,7006	0,7983	**<u>0,8046</u>**	0,4241	**0,4396**
T1_fl_no3_rf100_B	0,7108	0,8341	**<u>0,8704</u>**	0,7148	0,8591	0,7298	0,8548	**0,8622**	0,8535	0,8521	0,8343	0,7828	0,8086	**0,8464**	0,8445	0,7696	0,7392
T1_IR_no3_rf100_B	0,7929	0,7770	**0,8224**	0,7955	0,8039	0,7201	0,7999	**<u>0,8763</u>**	0,8585	0,8504	0,8481	0,8012	**0,8379**	0,8327	0,8283	**0,8207**	0,8065
T2_SE_no3_rf100_B	0,4689	0,5210	0,5273	0,4664	0,5277	**0,5730**	0,5275	0,8033	0,7611	**0,8264**	0,8247	0,7926	0,7786	0,8286	**<u>0,8331</u>**	0,7727	0,6255

No background = worse than the uncorrected, background = better than the uncorrected, bold = best parameters for the algorithm, underline = best correction for the image.

Table B.13: Sensitivity values for WM, 3% noise and C field images.

	Uncorrected	N3_01_2_4	N3_03_2_4	N3_015_2_2	N3_015_2_4	N3_015_2_6	N3_015_4_4	FSL_2_20	FSL_3_10	FSL_3_20	FSL_3_30	FSL_4_20	SPM_30	SPM_60	SPM_90	PABIC_2cl	PABIC_3cl
rf20																	
T2_EPI_no3_rf20_C	0,8684	0,7916	0,8704	**0,8829**	0,8483	0,6248	0,8468	0,8730	0,8228	0,8797	0,8876	**0,8905**	0,8302	0,8946	_0,9055_	**0,9052**	0,7731
PD_SE_no3_rf20_C	0,7316	**0,8093**	0,8092	0,7936	0,8065	0,6474	0,8010	0,7730	0,7430	0,7881	**0,7936**	0,7838	0,7127	0,8017	_0,8151_	**0,7917**	0,7870
T1_fl_no3_rf20_C	0,8503	0,8657	0,8641	0,8535	**0,8665**	0,6971	0,8662	**0,8657**	0,8612	0,8642	0,8631	0,8620	0,8338	**0,8657**	0,8644	_0,8693_	0,8657
T1_IR_no3_rf20_C	0,8435	0,8414	**0,8465**	0,8426	0,8413	0,8362	0,8421	_0,8852_	0,8452	0,8425	0,8418	0,8394	**0,8476**	0,8454	0,8417	0,8480	**0,8509**
T2_SE_no3_rf20_C	0,8355	0,8360	0,8346	0,8359	**0,8368**	0,7231	0,8365	0,8062	0,7806	0,8272	0,8347	0,8293	0,7985	0,8410	_0,8434_	0,8317	**0,8426**
rf40																	
T2_EPI_no3_rf40_C	0,7938	0,7598	**0,8649**	0,8119	0,8197	0,6302	0,8142	0,8717	0,8270	0,8779	**0,8792**	0,8725	0,8379	0,8848	_0,8993_	0,8405	**0,8531**
PD_SE_no3_rf40_C	0,5926	0,8124	**0,8125**	0,7104	0,8098	0,6563	0,8014	0,7704	0,7389	**0,7852**	0,7804	0,7561	0,7085	0,8083	_0,8203_	**0,7277**	0,7262
T1_fl_no3_rf40_C	0,8135	**0,8663**	0,8660	0,8189	0,8647	0,6961	0,8646	_0,8678_	0,8615	0,8625	0,8594	0,8514	0,8355	0,8568	**0,8603**	0,8456	0,8449
T1_IR_no3_rf40_C	0,8525	0,8415	0,8449	0,8524	0,8397	0,8522	0,8397	_0,8831_	0,8486	0,8450	0,8448	0,8336	0,8453	0,8411	0,8381	0,8494	0,8482
T2_SE_no3_rf40_C	0,8200	0,8221	0,8234	0,8214	0,8257	0,6549	**0,8259**	0,8100	0,7787	0,8287	**0,8357**	0,8276	0,8040	0,8397	_0,8410_	0,8183	**0,8332**
rf100																	
T2_EPI_no3_rf100_C	0,6402	0,7375	**0,8621**	0,6547	0,0581	0,6510	0,8186	0,8605	0,8155	**0,8730**	0,8567	0,8337	0,8292	0,8834	_0,8902_	0,6967	0,0527
PD_SE_no3_rf100_C	0,4091	0,1411	0,1388	**0,4100**	0,1393	0,3006	0,1439	0,2237	0,7214	_0,7330_	0,6531	0,3241	0,2490	0,1576	0,1482	0,4897	**0,5675**
T1_fl_no3_rf100_C	0,7286	0,8572	_0,8740_	0,7312	0,8678	0,7382	0,8673	**0,8679**	0,8562	0,8502	0,8374	0,7790	0,8200	0,8394	**0,8422**	0,7918	**0,8094**
T1_IR_no3_rf100_C	0,7997	0,7957	**0,8218**	0,8000	0,8146	0,7427	0,8196	_0,8796_	0,8428	0,8388	0,8391	0,7951	**0,8323**	0,8272	0,8234	**0,8248**	0,8150
T2_SE_no3_rf100_C	0,5281	0,5012	0,4903	0,5205	0,4821	**0,5627**	0,4772	0,1705	0,7445	0,8360	_0,8430_	0,8186	0,2395	0,8224	**0,8292**	0,7890	**0,8134**

No background = worse than the uncorrected, background = better than the uncorrected, bold = best parameters for the algorithm, underline = best correction for the image.

Table B.14: Sensitivity values for WM, 9% noise and A field images.

	Uncorrected	N3_01_2_4	N3_03_2_4	N3_015_2_2	N3_015_2_4	N3_015_2_6	N3_015_4_4	FSL_2_20	FSL_3_10	FSL_3_20	FSL_3_30	FSL_4_20	SPM_30	SPM_60	SPM_90	PABIC_2cl	PABIC_3cl
rf20																	
T1_fl_no9_rf20_A	0,7799	0,7627	0,7534	**0,7800**	0,7603	0,5614	0,7582	0,7304	0,6947	0,7468	0,7649	0,7587	0,7052	0,7529	0,7707	0,7601	0,7520
T1_IR_no9_rf20_A	0,8373	**0,8407**	0,8398	0,8375	0,8401	0,6835	0,8379	0,8199	0,7992	0,8294	0,8364	0,8352	0,8016	0,8359	**0,8417**	0,5534	0,8002
rf40																	
T1_fl_no9_rf40_A	0,7733	0,7728	0,7624	**0,7750**	0,7673	0,5686	0,7702	0,7394	0,7057	0,7585	**0,7756**	0,7681	0,7122	0,7620	**0,7799**	0,7715	0,7588
T1_IR_no9_rf40_A	0,8262	0,8389	**0,8425**	0,8275	0,8408	0,7015	0,8413	0,8249	0,8058	0,8339	**0,8397**	0,8372	0,8063	0,8405	**0,8442**	0,5907	0,7842
rf100																	
T1_fl_no9_rf100_A	0,7286	0,8572	**0,8740**	0,7312	0,8678	0,7382	0,8673	**0,8679**	0,8562	0,8502	0,8374	0,7790	0,8200	0,8394	**0,8422**	0,7918	**0,8094**
T1_IR_no9_rf100_A	0,7997	0,7957	**0,8218**	0,8000	0,8146	0,7427	0,8196	**0,8796**	0,8428	0,8388	0,8391	0,7951	**0,8323**	0,8272	0,8234	**0,8248**	0,8150

No background = worse than the uncorrected, background = better than the uncorrected, bold = best parameters for the algorithm, underline = best correction for the image.

B.1.5 Specificity for grey matter

Table B.15: Specificity values for GM, 3% noise and a field images.

	Uncorrected	N3_01_2_4	N3_03_2_4	N3_015_2_2	N3_015_2_4	N3_015_2_6	N3_015_4_4	FSL_2_20	FSL_3_10	FSL_3_20	FSL_3_30	FSL_4_20	SPM_30	SPM_60	SPM_90	PABIC_2cl	PABIC_3cl
rf20																	
T2_EPI_no3_rf20_A	0,8057	0,7391	0,7741	**0,8091**	0,7637	0,6389	0,7666	0,7106	0,7036	0,7088	0,7075	0,7080	0,7305	0,7878	0,7976	0,7948	0,7878
PD_SE_no3_rf20_A	0,6930	**0,7396**	0,7379	0,7347	0,7388	0,6592	0,7389	0,7354	0,7138	0,7357	**0,7362**	0,7348	0,7013	**0,7465**	0,7448	**0,7357**	0,7300
T1_fl_no3_rf20_A	0,8526	0,8715	0,8690	0,8562	**0,8720**	0,7487	0,8719	0,8341	0,8300	0,8397	0,8412	0,8428	0,8443	0,8688	**0,8720**	0,8673	0,8637
T1_IR_no3_rf20_A	0,8566	0,8605	**0,8647**	0,8570	0,8605	0,8512	0,8603	**0,8895**	0,8634	0,8620	0,8611	0,8595	**0,8655**	0,8628	0,8612	0,8568	0,8639
T2_SE_no3_rf20_A	0,8795	0,8797	0,8782	**0,8799**	0,8798	0,8031	0,8781	0,7095	0,7070	0,7081	0,7085	0,7097	0,8447	0,8800	**0,8828**	**0,8836**	0,8819
rf40																	
T2_EPI_no3_rf40_A	0,7549	0,7262	0,7747	**0,7767**	0,7531	0,6346	0,7548	0,7959	0,7571	0,7908	0,7957	**0,8040**	0,7265	0,7770	**0,7933**	0,7660	**0,7952**
PD_SE_no3_rf40_A	0,6033	**0,7394**	0,7385	0,6871	0,7390	0,6584	0,7379	**0,7303**	0,7097	0,7283	0,7227	0,7136	0,6858	0,7375	**0,7399**	0,6205	**0,6712**
T1_fl_no3_rf40_A	0,8181	**0,8710**	0,8681	0,8244	0,8696	0,7487	0,8708	**0,8730**	0,8648	0,8702	0,8683	0,8608	0,8473	**0,8687**	0,8585	0,8277	0,8393
T1_IR_no3_rf40_A	0,8492	0,8623	**0,8627**	0,8505	0,8605	0,8609	0,8610	**0,8892**	0,8622	0,8615	0,8604	0,8539	0,8616	0,8605	**0,8709**	0,8540	0,8414
T2_SE_no3_rf40_A	0,8607	0,8634	0,8664	0,8633	**0,8665**	0,7556	0,8660	0,8600	0,8355	0,8723	**0,8770**	0,8720	0,8449	0,8721	**0,8786**	0,8675	0,8731
rf100																	
T2_EPI_no3_rf100_A	0,6695	0,7012	0,7555	0,6805	0,7543	0,6438	**0,7556**	**0,7833**	0,7520	0,7658	0,7513	0,7751	0,7445	0,7899	**0,8003**	0,7193	0,7183
PD_SE_no3_rf100_A	0,5988	0,7269	0,7339	0,5925	**0,7340**	0,6723	0,7321	**0,7155**	0,6978	0,7091	0,6749	0,6106	0,6927	0,7366	**0,7359**	0,5844	**0,6149**
T1_fl_no3_rf100_A	0,7391	0,8524	0,8707	0,7430	**0,8715**	0,7793	0,8705	**0,8718**	0,8574	0,8581	0,8460	0,8090	0,8409	0,8573	**0,8598**	0,7983	**0,8091**
T1_IR_no3_rf100_A	0,8104	0,8228	**0,8428**	0,8118	0,8385	0,7944	0,8378	**0,8866**	0,8604	0,8600	0,8578	0,8223	**0,8530**	0,8519	0,8498	**0,8333**	0,8248
T2_SE_no3_rf100_A	0,7174	0,7152	0,7141	0,7171	0,7141	0,6945	0,7147	0,8628	0,8162	0,8764	**0,8793**	0,8632	0,6411	0,8636	**0,8722**	0,8389	0,7960

No background = worse than the uncorrected, background = better than the uncorrected, bold = best parameters for the algorithm, underline = best correction for the image.

Table B.16: Specificity values for GM, 3% noise and B field images.

	Uncorrected	N3_01_2_4	N3_03_2_4	N3_015_2_2	N3_015_2_4	N3_015_2_6	N3_015_4_4	FSL_2_20	FSL_3_10	FSL_3_20	FSL_3_30	FSL_4_20	SPM_30	SPM_60	SPM_90	PABIC_2cl	PABIC_3cl
rf20																	
T2_EPI_no3_rf20_B	0,8062	0,7337	0,7428	0,7744	0,7398	0,6101	0,7405	0,7972	0,7577	0,7963	0,8060	_0,8101_	0,7321	0,7905	0,7987	0,7923	**0,8075**
PD_SE_no3_rf20_B	0,6709	**0,7350**	0,7327	0,7195	0,7338	0,6519	0,7326	**0,7281**	0,7122	0,7269	0,7231	0,7201	0,6915	0,7422	_0,7487_	0,7324	**0,7339**
T1_fl_no3_rf20_B	0,8530	0,8716	0,8696	0,8568	**0,8721**	0,7484	0,8719	_0,8726_	0,8689	0,8724	0,8714	0,8697	0,8433	0,8659	**0,8711**	**0,8699**	0,8554
T1_IR_no3_rf20_B	0,8602	0,8618	**0,8652**	0,8603	0,8619	0,8570	0,8609	_0,8892_	0,8654	0,8634	0,8624	0,8598	**0,8651**	0,8640	0,8618	0,8591	0,8601
T2_SE_no3_rf20_B	0,8762	0,8816	0,8791	_0,8817_	0,8814	0,8770	0,8806	0,8571	0,8361	0,8720	**0,8774**	0,8734	0,8468	0,8761	**0,8795**	**0,8771**	0,8755
rf40																	
T2_EPI_no3_rf40_B	0,7354	0,7042	**0,7696**	0,7694	0,7370	0,6333	0,7377	0,7979	0,7593	0,7938	0,7987	_0,8039_	0,7257	0,7739	**0,7963**	0,7833	**0,7910**
PD_SE_no3_rf40_B	0,5582	**0,7402**	0,7379	0,6353	0,7394	0,6556	0,7369	**0,7225**	0,7033	0,7162	0,7022	0,6849	0,6919	0,7428	_0,7487_	0,6263	**0,7058**
T1_fl_no3_rf40_B	0,8160	0,8716	0,8681	0,8233	0,8698	0,7478	**0,8720**	_0,8738_	0,8668	0,8701	0,8666	0,8584	0,8424	0,8634	**0,8684**	0,8391	**0,8481**
T1_IR_no3_rf40_B	0,8501	0,8582	0,8610	0,8511	0,8586	**0,8700**	0,8579	_0,8893_	0,8614	0,8596	0,8595	0,8549	**0,8597**	0,8582	0,8563	**0,8615**	0,8592
T2_SE_no3_rf40_B	0,8489	0,8536	0,8600	0,8521	**0,8608**	0,7545	0,8600	0,8586	0,8299	0,8710	**0,8767**	0,8697	0,8434	0,8726	_0,8793_	0,8682	0,8661
rf100																	
T2_EPI_no3_rf100_B	0,5793	0,7231	**0,7813**	0,5823	0,7562	0,6461	0,7537	**0,7814**	0,7519	0,7776	0,7663	0,7640	0,7308	0,7828	_0,7941_	**0,7480**	0,6809
PD_SE_no3_rf100_B	0,5517	0,7243	0,7327	0,5491	**0,7337**	0,6986	0,7313	**0,6803**	0,6068	0,5958	0,5467	0,5138	0,6960	0,7441	_0,7477_	**0,6325**	0,6175
T1_fl_no3_rf100_B	0,7060	0,8407	_0,8680_	0,7101	0,8624	0,7911	0,8578	**0,8672**	0,8508	0,8478	0,8299	0,7950	0,8308	**0,8584**	0,8572	**0,8046**	0,7793
T1_IR_no3_rf100_B	0,8034	0,8087	**0,8429**	0,8056	0,8302	0,7707	0,8270	_0,8837_	0,8672	0,8621	0,8584	0,8252	**0,8557**	0,8520	0,8495	**0,8409**	0,8267
T2_SE_no3_rf100_B	0,7241	0,7201	0,7193	0,7236	0,7190	0,7078	0,7191	0,8562	0,8287	**0,8710**	0,8681	0,8474	0,8387	0,8730	_0,8762_	0,8267	0,7126

No background = worse than the uncorrected, background = better than the uncorrected, bold = best parameters for the algorithm, underline = best correction for the image.

Table B.17: Specificity values for GM, 3% noise and C field images.

	Uncorrected	N3_01_2_4	N3_03_2_4	N3_015_2_2	N3_015_2_4	N3_015_2_6	N3_015_4_4	FSL_2_20	FSL_3_10	FSL_3_20	FSL_3_30	FSL_4_20	SPM_30	SPM_60	SPM_90	PABIC_2cl	PABIC_3cl
rf20																	
T2_EPI_no3_rf20_C	0,8078	0,7311	0,7725	0,8115	0,7578	0,6338	0,7583	0,7980	0,7604	0,8001	0,8101	0,8101	0,7377	0,7896	0,7969	0,7898	0,7547
PD_SE_no3_rf20_C	0,6923	0,7415	0,7396	0,7261	0,7407	0,6584	0,7391	0,7308	0,7171	0,7309	0,7281	0,7251	0,7010	0,7500	0,7462	0,7334	0,7324
T1_fl_no3_rf20_C	0,8550	0,8728	0,8707	0,8587	0,8740	0,7573	0,8734	0,8735	0,8697	0,8730	0,8725	0,8713	0,8461	0,8705	0,8725	0,8713	0,8644
T1_IR_no3_rf20_C	0,8586	0,8614	0,8655	0,8589	0,8616	0,8558	0,8617	0,8898	0,8636	0,8621	0,8618	0,8600	0,8637	0,8626	0,8609	0,8607	0,8657
T2_SE_no3_rf20_C	0,8789	0,8794	0,8785	0,8792	0,8799	0,8014	0,8797	0,8588	0,8425	0,8734	0,8785	0,8748	0,8515	0,8804	0,8831	0,8750	0,8822
rf40																	
T2_EPI_no3_rf40_C	0,7661	0,7144	0,7720	0,7823	0,7453	0,6385	0,7423	0,8001	0,7608	0,7972	0,8033	0,8081	0,7479	0,7957	0,8025	0,7653	0,7911
PD_SE_no3_rf40_C	0,6076	0,7420	0,7393	0,6804	0,7408	0,6585	0,7393	0,7277	0,7109	0,7258	0,7175	0,7082	0,6974	0,7480	0,7462	0,7047	0,7099
T1_fl_no3_rf40_C	0,8211	0,8711	0,8706	0,8266	0,8703	0,7577	0,8711	0,8753	0,8681	0,8700	0,8675	0,8611	0,8485	0,8648	0,8683	0,8485	0,8518
T1_IR_no3_rf40_C	0,8578	0,8607	0,8625	0,8588	0,8597	0,8663	0,8595	0,8882	0,8650	0,8630	0,8626	0,8549	0,8618	0,8598	0,8582	0,8649	0,8578
T2_SE_no3_rf40_C	0,8661	0,8677	0,8696	0,8671	0,8706	0,7574	0,8710	0,8613	0,8405	0,8737	0,8783	0,8731	0,8552	0,8796	0,8816	0,8641	0,8737
rf100																	
T2_EPI_no3_rf100_C	0,7257	0,7061	0,7827	0,7274	0,7498	0,6447	0,7498	0,7914	0,7554	0,7714	0,7534	0,7924	0,7414	0,7972	0,8074	0,7244	0,7567
PD_SE_no3_rf100_C	0,5673	0,7426	0,7402	0,5708	0,7415	0,6534	0,7391	0,6939	0,6965	0,7067	0,6827	0,6142	0,6968	0,7357	0,7392	0,5695	0,5292
T1_fl_no3_rf100_C	0,7493	0,8620	0,8729	0,7529	0,8693	0,7905	0,8688	0,8741	0,8598	0,8557	0,8445	0,8034	0,8428	0,8556	0,8569	0,8109	0,8245
T1_IR_no3_rf100_C	0,8129	0,8229	0,8427	0,8137	0,8379	0,7904	0,8416	0,8872	0,8596	0,8561	0,8548	0,8227	0,8526	0,8483	0,8461	0,8390	0,8318
T2_SE_no3_rf100_C	0,7162	0,7139	0,7131	0,7161	0,7138	0,6844	0,7143	0,8647	0,8215	0,8809	0,8843	0,8663	0,4756	0,8687	0,8733	0,8433	0,8595

Correction methods

No background = worse than the uncorrected, background = better than the uncorrected, bold = best parameters for the algorithm, underline = best correction for the image.

Table B.18: Specificity values for GM, 9% noise and A field images.

	Uncorrected	N3_01_2_4	N3_03_2_4	N3_015_2_2	N3_015_2_4	N3_015_2_6	N3_015_4_4	FSL_2_20	FSL_3_10	FSL_3_20	FSL_3_30	FSL_4_20	SPM_30	SPM_60	SPM_90	PABIC_2cl	PABIC_3cl
rf20																	
T1_fl_no9_rf20_A	0,7756	0,7704	0,7652	**0,7761**	0,7691	0,6335	0,7682	0,7504	0,7251	0,7606	0,7725	0,7677	0,7307	0,7627	0,7753	0,7593	0,7573
T1_IR_no9_rf20_A	0,8453	**0,8498**	**0,8498**	0,8456	0,8497	0,7438	0,8484	0,8350	0,8214	0,8419	**0,8468**	0,8453	0,8201	0,8442	**0,8491**	0,6543	0,8136
rf40																	
T1_fl_no9_rf40_A	0,7647	**0,7740**	0,7689	0,7669	0,7715	0,6375	0,7736	0,7561	0,7322	0,7672	**0,7779**	0,7723	0,7351	0,7684	**0,7799**	**0,7661**	0,7578
T1_IR_no9_rf40_A	0,8361	0,8475	**0,8510**	0,8372	0,8493	0,7558	0,8498	0,8385	0,8258	0,8447	**0,8487**	0,8464	0,8245	0,8479	**0,8509**	0,6759	0,8024
rf100																	
T1_fl_no9_rf100_A	0,7175	0,7698	0,7743	0,7205	0,7745	0,6526	**0,7755**	0,7715	0,7502	0,7792	**0,7834**	0,7723	0,7552	0,7798	**0,7876**	**0,7544**	0,7344
T1_IR_no9_rf100_A	0,7984	0,8282	0,8422	0,8002	0,8412	0,7717	**0,8426**	0,8439	0,8318	0,8452	**0,8452**	0,8391	0,8299	0,8478	**0,8485**	0,7232	**0,8110**

No background = worse than the uncorrected, background = better than the uncorrected, bold = best parameters for the algorithm, underline = best correction for the image.

B.1.6 Specificity for white matter

Table B.19: Specificity values for WM, 3% noise and a field images.

	Uncorrected	N3_01_2_4	N3_03_2_4	N3_015_2_2	N3_015_2_4	N3_015_2_6	N3_015_4_4	FSL_2_20	FSL_3_10	FSL_3_20	FSL_3_30	FSL_4_20	SPM_30	SPM_60	SPM_90	PABIC_2cl	PABIC_3cl
rf20																	
T2_EPI_no3_rf20_A	0,7593	0,7256	0,7652	**0,7754**	0,7534	0,6190	0,7544	0,7033	0,6518	0,7191	0,7396	0,7440	0,7172	0,7886	_0,8076_	**0,7961**	0,7837
PD_SE_no3_rf20_A	0,6545	**0,7340**	0,7329	0,7132	0,7317	0,6314	0,7250	0,7382	0,7225	0,7524	_0,7543_	0,7427	0,6739	0,7239	**0,7406**	0,7088	**0,7208**
T1_fl_no3_rf20_A	0,8984	0,8712	0,8447	**0,9014**	0,8735	0,6979	0,8814	0,7480	0,7417	0,8244	0,8555	0,8767	0,8198	0,8805	**0,8999**	_0,9081_	0,8934
T1_IR_no3_rf20_A	0,9301	0,9353	0,9321	0,9320	**0,9361**	0,7715	0,9360	0,8686	0,9290	0,9336	0,9361	_0,9362_	0,8999	0,9316	**0,9352**	0,9316	0,9279
T2_SE_no3_rf20_A	0,8883	**0,8885**	0,8859	0,8881	0,8881	0,8437	0,8852	0,5660	0,5498	0,5761	0,5893	0,5788	0,8511	0,8944	_0,8988_	0,8870	**0,8957**
rf40																	
T2_EPI_no3_rf40_A	0,6875	0,7058	**0,7645**	0,7133	0,7392	0,6158	0,7390	0,7446	0,6746	0,7395	0,7531	**0,7624**	0,6887	0,7771	_0,8075_	0,7461	**0,7662**
PD_SE_no3_rf40_A	0,6266	**0,7263**	0,7262	0,6423	0,7255	0,6300	0,7163	0,6988	0,6837	**0,7015**	0,6882	0,6698	0,6808	0,7107	0,7273	_0,8953_	0,6254
T1_fl_no3_rf40_A	0,8745	0,8706	0,8478	**0,8801**	0,8643	0,6995	0,8672	0,8482	0,8653	0,8964	0,9052	**0,9064**	0,8258	0,8866	_0,9372_	0,8788	0,8916
T1_IR_no3_rf40_A	0,9178	0,9338	0,9328	0,9205	**0,9361**	0,8106	0,9347	0,8720	0,9290	0,9337	0,9360	_0,9389_	0,9047	0,9323	0,9022	0,9319	0,9280
T2_SE_no3_rf40_A	0,8488	0,8500	**0,8578**	0,8515	0,8517	0,7984	0,8507	0,8550	0,8331	0,8643	**0,8698**	0,8621	0,8469	0,8767	_0,8948_	0,8673	0,8826
rf100																	
T2_EPI_no3_rf100_A	0,6665	0,6741	**0,7669**	0,6674	0,7401	0,6157	0,7326	**0,7370**	0,6365	0,6864	0,6871	0,7070	0,7570	0,8099	_0,8144_	0,7091	**0,7170**
PD_SE_no3_rf100_A	0,6028	0,6943	0,7083	0,5924	**0,7085**	0,6804	0,6848	**0,6799**	0,6641	0,6649	0,6679	0,6167	0,7040	0,7233	_0,7425_	**0,6488**	0,6343
T1_fl_no3_rf100_A	0,8146	**0,8871**	0,8572	0,8173	0,8558	0,7032	0,8569	0,8629	0,8454	0,8906	0,8985	**0,9023**	0,8560	0,9048	_0,9132_	0,8794	0,8776
T1_IR_no3_rf100_A	0,8675	_0,9441_	0,9405	0,8710	0,9431	0,8865	0,9428	0,8801	0,9151	0,9290	0,9305	**0,9404**	0,9079	0,9386	**0,9420**	0,9254	0,9094
T2_SE_no3_rf100_A	0,6184	0,6122	0,6052	0,6166	0,6075	0,5951	0,6081	0,8440	0,8279	**0,8503**	0,8485	0,8299	_0,8853_	0,8523	0,8614	**0,8426**	0,8164

No background = worse than the uncorrected, background = better than the uncorrected, bold = best parameters for the algorithm, underline = best correction for the image.

Table B.20: Specificity values for WM, 3% noise and B field images.

	Uncorrected	N3_01_2_4	N3_03_2_4	N3_015_2_2	N3_015_2_4	N3_015_2_6	N3_015_4_4	FSL_2_20	FSL_3_10	FSL_3_20	FSL_3_30	FSL_4_20	SPM_30	SPM_60	SPM_90	PABIC_2cl	PABIC_3cl
rf20																	
T2_EPI_no3_rf20_B	0,7443	0,7276	**0,7611**	0,7565	0,7471	0,6103	0,7464	0,7444	0,6730	0,7458	0,7675	**0,7765**	0,7228	0,7910	**0,8082**	**0,8050**	0,7901
PD_SE_no3_rf20_B	0,6385	**0,7466**	0,7457	0,7265	0,7446	0,6399	0,7352	0,7058	0,6867	**0,7134**	0,7110	0,7004	0,6631	0,7298	**0,7419**	0,6980	**0,7082**
T1_fl_no3_rf20_B	0,8927	0,8712	0,8461	**0,8969**	0,8743	0,7007	0,8823	0,8439	0,8727	0,8963	**0,9035**	0,9027	0,8231	0,8809	**0,9019**	**0,9002**	0,8952
T1_IR_no3_rf20_B	0,9264	0,9345	0,9316	0,9286	**0,9354**	0,7853	**0,9354**	0,8689	0,9268	0,9321	0,9348	**0,9358**	0,8930	0,9308	**0,9348**	**0,9318**	0,9310
T2_SE_no3_rf20_B	0,8875	0,8820	0,8742	0,8836	0,8802	0,7243	0,8782	0,8580	0,8457	0,8754	0,8826	0,8766	0,8574	0,8939	**0,8979**	0,8849	**0,8951**
rf40																	
T2_EPI_no3_rf40_B	0,6571	0,6892	**0,7592**	0,6851	0,7272	0,6164	0,7266	0,7386	0,6584	0,7250	0,7376	**0,7484**	0,6851	0,7689	**0,8095**	**0,7728**	0,7628
PD_SE_no3_rf40_B	0,5858	0,7175	**0,7208**	0,6251	0,7198	0,6283	0,7041	**0,6907**	0,6769	0,6881	0,6698	0,6520	0,6608	0,7301	**0,7394**	0,6426	0,6627
T1_fl_no3_rf40_B	0,8570	**0,8764**	0,8446	0,8634	0,8590	0,6983	0,8661	0,8490	0,8549	0,8906	0,8987	**0,9034**	0,8269	0,8867	**0,9047**	0,8635	**0,8892**
T1_IR_no3_rf40_B	0,9226	0,9371	0,9354	0,9249	**0,9382**	0,8266	0,9381	0,8743	0,9311	0,9357	0,9372	**0,9400**	0,9068	0,9354	**0,9390**	0,9276	0,9242
T2_SE_no3_rf40_B	0,8473	0,8476	**0,8536**	0,8497	0,8483	0,7943	0,8479	0,8536	0,8289	0,8613	**0,8658**	0,8598	0,8526	0,8749	**0,8935**	0,8876	**0,8911**
rf100																	
T2_EPI_no3_rf100_B	0,6386	0,6993	**0,7655**	0,6399	0,7427	0,6193	0,7351	**0,7232**	0,6367	0,6828	0,6833	0,6803	0,7300	0,7853	**0,8054**	**0,6949**	0,6747
PD_SE_no3_rf100_B	0,6117	0,7037	0,7148	0,6047	0,7165	**0,7396**	0,6956	**0,6731**	0,5737	0,6148	0,6212	0,5703	0,6721	0,7204	**0,7236**	0,6835	**0,7017**
T1_fl_no3_rf100_B	0,7929	**0,8767**	0,8543	0,7948	0,8492	0,6809	0,8451	0,8618	0,8403	**0,8736**	0,8673	0,8713	0,8390	0,8974	**0,9143**	0,8606	0,8564
T1_IR_no3_rf100_B	0,8460	0,9411	0,9383	0,8485	0,9433	0,8635	**0,9439**	0,8816	0,9001	0,9195	0,9187	**0,9315**	0,9034	0,9390	**0,9422**	0,9180	0,9083
T2_SE_no3_rf100_B	0,6251	0,6196	0,6133	0,6236	0,6159	0,5929	0,6177	**0,8349**	0,8064	0,8343	0,8290	0,8196	0,8458	0,8834	**0,8908**	**0,8231**	0,7793

Correction methods

No background = worse than the uncorrected, background = better than the uncorrected, bold = best parameters for the algorithm, underline = best correction for the image.

Table B.21: Specificity values for WM, 3% noise and C field images.

	Uncorrected	N3_01_2_4	N3_03_2_4	N3_015_2_2	N3_015_2_4	N3_015_2_6	N3_015_4_4	FSL_2_20	FSL_3_10	FSL_3_20	FSL_3_30	FSL_4_20	SPM_30	SPM_60	SPM_90	PABIC_2cl	PABIC_3cl
rf20																	
T2_EPI_no3_rf20_C	0,7600	0,7203	0,7646	**0,7734**	0,7498	0,6163	0,7477	0,7470	0,6830	0,7582	0,7799	**0,7826**	0,7330	0,8012	_0,8148_	**0,8056**	0,7322
PD_SE_no3_rf20_C	0,6624	**0,7341**	0,7323	0,7176	0,7314	0,6292	0,7240	0,7095	0,6891	0,7148	**0,7152**	0,7056	0,6773	0,7269	_0,7437_	**0,7191**	0,7091
T1_fl_no3_rf20_C	0,9017	0,8729	0,8461	**0,9039**	0,8775	0,7012	0,8795	0,8445	0,8777	0,8988	_0,9052_	0,9036	0,8172	0,8831	0,9009	0,8889	0,8847
T1_IR_no3_rf20_C	0,9311	0,9353	0,9323	0,9328	_0,9363_	0,7822	0,9359	0,8695	0,9291	0,9337	0,9359	_0,9363_	0,9018	0,9314	**0,9353**	0,9259	0,9293
T2_SE_no3_rf20_C	0,8878	0,8880	0,8854	**0,8885**	0,8880	0,8414	0,8873	0,8597	0,8502	0,8781	0,8852	0,8785	0,8582	0,8949	_0,9003_	0,8881	**0,8882**
rf40																	
T2_EPI_no3_rf40_C	0,6966	0,6988	**0,7651**	0,7175	0,7359	0,6159	0,7305	0,7467	0,6768	0,7460	0,7613	**0,7693**	0,7572	0,8041	_0,8138_	0,7576	**0,7579**
PD_SE_no3_rf40_C	0,6627	0,7282	**0,7287**	0,6653	0,7277	0,6324	0,7154	0,7002	0,6858	**0,7018**	0,6900	0,6745	0,6736	0,7320	_0,7441_	0,6823	0,6510
T1_fl_no3_rf40_C	0,8874	0,8767	0,8499	**0,8924**	0,8634	0,7004	0,8863	0,8530	0,8726	0,9016	0,9087	_0,9100_	0,8424	0,8996	**0,9083**	0,8831	0,9055
T1_IR_no3_rf40_C	0,9072	0,9351	0,9313	0,9109	**0,9362**	0,8218	0,9356	0,8727	0,9252	0,9311	0,9325	_0,9378_	0,8969	0,9344	**0,9375**	0,9281	0,9137
T2_SE_no3_rf40_C	0,8460	0,8475	**0,8554**	0,8476	0,8505	0,8050	0,8514	0,8553	0,8338	0,8642	**0,8693**	0,8621	0,8611	0,8963	_0,9011_	**0,8835**	0,8830
rf100																	
T2_EPI_no3_rf100_C	0,7032	0,6833	**0,7724**	0,7033	0,7372	0,6143	0,7345	**0,7382**	0,6297	0,6804	0,6886	0,7257	0,7420	0,8161	**0,8241**	_0,9234_	0,8606
PD_SE_no3_rf100_C	0,5660	0,7190	0,7219	0,5525	**0,7237**	0,6354	0,7048	0,6809	0,6740	0,6866	**0,7034**	0,6467	0,7211	0,7461	_0,7486_	0,6669	**0,6956**
T1_fl_no3_rf100_C	0,8310	**0,8933**	0,8614	0,8351	0,8615	0,7049	0,8645	0,8728	0,8631	0,9021	0,9058	**0,9064**	0,8698	0,9151	_0,9219_	0,8929	0,8825
T1_IR_no3_rf100_C	0,8893	0,9448	0,9424	0,8930	_0,9460_	0,8932	0,9439	0,8842	0,9239	0,9336	0,9333	**0,9404**	0,9194	0,9436	**0,9459**	0,9204	0,9228
T2_SE_no3_rf100_C	0,6196	0,5925	0,5920	0,6173	0,5911	0,5982	0,5925	0,8445	0,8302	**0,8477**	0,8460	0,8265	_0,9016_	0,8498	0,8585	0,8534	**0,8797**

No background = worse than the uncorrected, background = better than the uncorrected, bold = best parameters for the algorithm, underline = best correction for the image.

Table B.22: Specificity values for WM, 9% noise and A field images.

	Uncorrected	N3_01_2_4	N3_03_2_4	N3_015_2_2	N3_015_2_4	N3_015_2_6	N3_015_4_4	FSL_2_20	FSL_3_10	FSL_3_20	FSL_3_30	FSL_4_20	SPM_30	SPM_60	SPM_90	PABIC_2cl	PABIC_3cl
rf20																	
T1_fl_no9_rf20_A	0,7819	0,7618	0,7542	<u>**0,7819**</u>	0,7597	0,6537	0,7583	0,7384	0,7144	0,7478	0,7614	0,7587	0,7235	0,7526	0,7665	0,7675	0,7630
T1_IR_no9_rf20_A	0,8535	0,8430	0,8365	0,8535	0,8388	0,7337	0,8325	0,7964	0,7822	0,8185	0,8327	0,8280	0,7820	0,8236	0,8375	0,7686	0,8189
rf40																	
T1_fl_no9_rf40_A	0,7853	0,7705	0,7601	<u>**0,7860**</u>	0,7650	0,6574	0,7663	0,7420	0,7152	0,7508	0,7668	0,7656	0,7257	0,7575	0,7708	0,7829	0,7672
T1_IR_no9_rf40_A	0,8563	0,8531	0,8445	<u>**0,8565**</u>	0,8493	0,7417	0,8433	0,8000	0,7865	0,8240	0,8389	0,8353	0,7801	0,8298	0,8428	0,7744	0,8185
rf100																	
T1_fl_no9_rf100_A	0,7807	**0,7826**	0,7706	0,7813	0,7724	0,6754	0,7731	0,7529	0,7241	0,7627	0,7804	0,7799	0,7463	0,7721	<u>**0,7851**</u>	0,7577	0,7657
T1_IR_no9_rf100_A	0,8520	<u>**0,8678**</u>	0,8596	0,8531	0,8652	0,7558	0,8632	0,8097	0,7978	0,8380	**0,8547**	0,8539	0,7941	0,8389	**0,8536**	0,7934	0,8272

No background = worse than the uncorrected, background = better than the uncorrected, bold = best parameters for the algorithm, underline = best correction for the image.

Appendix C

Paper for the 6th International Conference on Technology and Medical Sciences

Intensity inhomogeneity corrections in MRI simulated images for segmentation

R. Lavrador
Siemens S. A. Healthcare Sector, Matosinhos, Portugal and FCT University of Coimbra, Coimbra, Portugal

L.Caldeira
Siemens S. A. Healthcare Sector, Matosinhos, Portugal and Instituto de Biofísica e Engenharia Biomédica, Faculty of Sciences of University of Lisbon, Lisbon, Portugal

N.F. Lori
Faculty of Medicine of the University of Coimbra, Coimbra, Portugal and Brain Imaging Network, Portugal

F. Janela
Siemens S. A. Healthcare Sector, Matosinhos, Portugal

ABSTRACT: In this work four known algorithms were used to correct intensity inhomogeneities in order to find an optimal method and parameters that improve automatic segmentation in T1-weighted MRI simulated images, generated with similar sequence parameters of real acquisitions. The resulting segmentation was measured by several features and the results are similar for both gray matter and white matter and for different applied bias fields. The intensity inhomogeneity correction algorithm that shows to be more stable was the one present in SPM8, but it was not found an algorithm that overcomes all the others in all aspects. With higher noise levels (9%) the correcting algorithms fail to improve segmentation. It was also found that the segmentation with a better relationship between sensitivity and specificity in the majority of the cases corresponds to a higher Dice coefficient.

1 INTRODUCTION

Magnetic resonance imaging (MRI) is a powerful non invasive technique that allows great contrast on soft tissues, high spatial resolution and has both anatomical and functional information. The automatic extraction of clinical relevant information has become mandatory to efficiently deal with the large amount of data generated using this modality.

The vast amounts of image data presently used in many studies leads to an increased interest in computer-aided image analysis methods. The segmentation of clinical images helps physicians to differentiate between tissues, providing a unique insight into morphometric changes in the brain; they are particularly useful in monitoring neurodegenerative diseases such as Alzheimer's disease, or the effect of possible treatments (Boyes et al. 2008; de Boer et al. 2010). If these procedures were assisted by an automatic segmentation algorithm, it could simplify and reduce the cost of image analysis (Duncan & Ayache 2000; Kaus et al. 2001). However, several artifacts can degrade the quality of acquired data, namely the intensity inhomogeneity (IIH) (Duncan & Ayache 2000; Hendee 2002; Vovk, Pernus & Likar 2007).

The IIH is mainly caused by unwanted local flip angle variations and that happen due to inhomogeneous radio-frequency (RF) excitation, non-uniform reception sensitivity and electrodynamic interactions with the object often described as RF penetration, and standing wave effects. This results in a smooth undesirable variation of intensity levels of a tissue across the image. Thus the same tissue has different intensities according to its location. This distortion, in many cases, is hardly noticeable to a human observer but can influence many medical image analysis methods such as segmentation and registration (Zhang, M Brady & Smith 2001; Vovk, Pernus & Likar 2007; Ashburner & Friston 2005).

In the literature the most common model assumes that the IIH is multiplicative, that means that the inhomogeneity field (b) is multiplied to the image (u). This model is frequently used due to its consistency with the inhomogeneous sensibility of the reception coil. In addition a high-frequency noise (n), typically with a Rician distribution, should be incorporated to the MR image formation model (v), Equation 1.

$$v = ub + n \qquad (1)$$

IIH correction is often a necessary preprocessing step to enable a better segmentation, yet it is unknown which are the IIH correction algorithms that improve segmentation and if it stands for several acquisition protocols, levels of noise and of IIH.

T1-weighted images are commonly used for segmentation, because they have good contrast between white matter and gray matter and high resolution in the usual neuroimaging protocols.

This work is intended to segment T1-weighted images that were corrected with four known IIH correction algorithms and find the IIH correction algorithm and parameters that improve segmentation of T1-weighted the most. It is also important to observe

if the results for the two sequence protocols are identical.
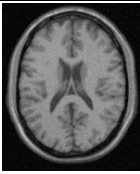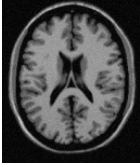
2 METHODS

2.1 *Images*

In order to have ground truth images, in this work we used MRI simulated images of the brain obtained using BrainWeb (Cocosco et al. 1997), with parameters, for FLASH (fl) and Inversion Recovery (IR) pulse sequences, identical to the parameters usually used to perform scans on patients (Table 1). The image size was maintained constant and equal to 217x181x60. We used two levels of noise (no), 3% and 9%. For the 3% noise level we simulated an image with no inhomogeneities (control image) and images with 3 different bias fields, A, B and C, provided by the simulator. The 3 bias fields were applied with also 3 levels of inhomogeneities (rf), 20%, 40% and 100%, which means that, as an example for 20%, the multiplicative field has a range of values of 0.90 to 1.10 over the brain area.

For the 9% noise level it was simulated an image with no inhomogeneities and three more images, one for each inhomomogeneity level of field A.

The images with no inhomogeneity applied and 3% noise are shown on Table 1.

Table 1. Simulated images, 3% noise and no bias field applied.

Custom Designation	Sequence Parameters	Simulated Images
T1_fl_no3_rf0	FLASH TR: 250ms TE: 2,46ms Flip angle: 70º	
T1_IR_no3_rf0	INVERSION RECOVERY TR: 2300ms TE: 2.28ms Flip angle: 90º IR: 900ms	

2.2 *IIH correction algorithms*

The IIH in the simulated images was corrected by four well known algorithms: the N3 developed by Sled et al.(Sled, Zijdenbos & AC Evans 2002) with minor changes (http://hdl.handle.net/10380/3053) and the parametric bias field correction (PABIC) developed by Styner et al. (Styner et al. 2000), both algorithms are implemented on Insight Segmentation and Registration Toolkit (ITK) (Ibanez et al. 2003); the algorithm developed by Guillemaud and Brady (R Guillemaud & M Brady 1997) that is integrated on a segmentation framework developed by Zhang et al. (Zhang, M Brady & Smith 2001) and implemented on FMRIB Software Library (FSL) soft-

ware; and the last algorithm was developed by Ashburner and Friston (Ashburner & Friston 2005) and implemented on Statistical Parametric Mapping (SPM8) [site SPM].

N3 is described as a non-uniform intensity normalization method that finds the smooth, slowly varying, multiplicative field that maximizes the frequency content of the intensity distribution of the uncorrected image. The N3 proceeds by estimating a Gaussian distribution of an ideal uncorrupted image by deconvolution, and then uses this distribution and the distribution of the original corrupted image to estimate the non-uniform field. This field is smoothed by a B-spline curve. The resulting bias field is then removed from the original image and this process iterates until reaching a convergence threshold (Sled, Zijdenbos & AC Evans 2002).

The second algorithm is called PABIC. It assumes that each pixel of the image is associated to a small number of categories with a prior known statistics and that the bias field can be modeled by smooth functions, which in this case are Legendre polynomials. The estimation of the bias is formulated as a nonlinear energy minimization problem using an evolution strategy (Styner, Brechbuhler, Szckely & Gerig 2000). The starting mean values for each class were obtained with k-means classifier using MATLAB.

The algorithm proposed by (R. Guillemaud & M. Brady 1997) is a modification of Wells et al. algorithm for IIH correction (Wells et al. 1996), introducing a new class "others" with a non-Gaussian probability distribution. On the FSL software the method is integrated in a hidden Markov random field model that uses an estimation-maximization algorithm (HMRF-EM), so as to use the information about spatial connectedness of neighboring pixels of the same class (Zhang, M Brady & Smith 2001).

In the algorithm proposed in SPM8 it is used an iterative framework that interleaves segmentation, registration and IIH correction. The model is based in a finite Gaussians mixture and is extended to incorporate a smooth intensity variation and nonlinear registration with tissue probability maps. For optimization of the objective function it is used an iterated conditional modes approach, using the EM to find the mixture-classification parameters and Levenberg-Marquardt optimization for inhomogeneity field and registration step.

The algorithms were used as automatically as possible and for each algorithm several parameters were chosen, considering those with greater potential impact on the algorithm performance.

In N3 we chose to vary the full width at half maximum (FWHM), the shrink factor, and the number of fitting levels. For the FSL algorithm it was changed the number of classes and the FWHM. The FWHM was the only parameter changed on the IIH correc-

tion algorithm present in SPM8. In PABIC it was changed the number of classes.

2.3 *Segmentation*

After correcting the images for inhomogeneities, the segmentation was performed using the segmentation framework developed by Zhang et al. (Zhang, M Brady & Smith 2001) and implemented on FSL software, using 3 classes, the default parameters and with no additional IIH correction.

As said before the segmentation algorithm implemented on FSL incorporates a hidden Markov random field and in this method the segmentation is treated as a statistical model-based problem with 3 steps: model selection, model fitting and classification. The HMRF-EM enables an adaptive and reliable automatic segmentation (Zhang, M Brady & Smith 2001).

2.4 *Evaluation parameters*

The effects in the performance of the segmentation were quantitatively evaluated calculating the dice coefficient, the specificity and sensitivity of each segmented image.

Dice coefficient, Equation 2, is used to compare the similarity between sample sets, in this case, between the obtained segmentation and the gold standard segmentation. In this work it has been used a discrete anatomical model, available on BrainWeb as gold standard segmentation.

$$Dice(S_1, S_2) = \frac{2\,|\,S_1 \cap S_2\,|}{|\,S_1\,| + |\,S_2\,|} \qquad (2)$$

Where the S_1 and S_2 sets are, respectively, the obtained and the gold standard segmentations.

Sensitivity, Equation 3, is intended to evaluate the ability of the segmentation to correctly classify the tissues, and it gives the probability of deciding if a tissue was well classified, when it belongs to that class.

$$sensitivity = \frac{TP}{TP + FN} \qquad (3)$$

Where TP is true positives and FN is false negatives.

The sensitivity, by itself, does not give us if the other tissues were well classified, for that it is necessary to calculate the specificity. The specificity, Equation 4, intends to evaluate the ability of the segmentation to correctly exclude the tissues that do not belong to a given class. So it gives the probability of deciding if the tissue in question was excluded of a class, when it actually does not belong to it.

$$specificity = \frac{TN}{TN + FP} \qquad (4)$$

Where TN is true negatives and FN is false negatives.

After obtaining the specificity and the sensitivity, a receiver operator characteristic (ROC) space was built for each image with the four correcting algorithms.

All evaluation parameters were calculated for grey matter (GM) and white matter (WM).

In order to evaluate the significance of changes in the Dice coefficients in relation to the IIH correction method an ANOVA of repeated measures was performed. The multiple comparisons were made using contrasts and having the uncorrected image as reference. All analysis was performed on SPSS software.

3 RESULTS

The Dice coefficient for each image, with different bias field and noise was obtained. The values of the Dice coefficient, for GM and WM, could be considered similar for all bias fields and noise levels, except in few situations. The identical results for GM and WM, show that the IIH correction acts equally in all tissues. Some representative results are shown in Table 2-5.

The sigma values resulting of a test from the ANOVA analysis are shown in Table 7.

Table 2. Dice coefficient for T1_fl images with 3% noise, bias field A, 3 different rf levels and for GM.

Parameters				Images		
				rf20	rf40	rf100
Uncorrected				0.7641	0.7086	0.5742
N3	a	b	c			
	0.1	2	4	0.7561	0.7564	0.7297
	0.3	2	4	0.7349	0.7365	0.7414
	0.15	2	2	0.7579	0.7192	0.5786
	0.15	2	4	0.7688	0.7505	0.7451
FSL algorithm		d	c			
		2	20	0.6980	0.7368	0.7451
		3	10	0.6883	0.7491	0.7343
		3	20	0.7632	0.7753	0.7629
		3	30	0.7884	0.7801	0.7524
		4	20	**0.8009**	0.7745	0.7188
SPM algorithm			c			
			60	0.7577	0.7615	0.7441
			90	0.7771	**0.8061**	**0.8061**
PABIC			c			
			2	0.7811	0.7247	0.6797
			3	0.7709	0.7492	0.6878

Backgrounds: no background = worse than the uncorrected image, ░ = better than the uncorrected image, ▓ = best value for this algorithm, bold = best value
Parameters: a = shrink factor; b = number of fitting levels, c = full width at half maximum, d = number of classes

Table 3. Dice coefficient for T1_IR images with 3% noise, bias field A, 3 different rf levels and for GM.

	Parameters			Images		
				rf20	rf40	rf100
Uncorrected				0.8003	0.7891	0.7004
N3	a	b	c			
	0.1	2	4	0.8046	0.8048	0.7769
	0.3	2	4	0.8039	0.8041	0.7948
	0.15	2	2	**0.8055**	0.7916	0.7046
	0.15	2	4	0.8022	**0.8056**	0.7925
FSL algorithm		d	c			
		2	20	0.7655	0.7679	0.7728
		3	10	0.8002	0.8001	0.7905
		3	20	0.8033	0.8037	0.8009
		3	30	0.8048	0.8051	0.8004
		4	20	0.8040	0.8043	0.7897
SPM algorithm			c			
			60	0.8031	0.8033	**0.8033**
			90	0.8047	0.7784	0.7651
PABIC			c			
			2	0.8013	0.8010	0.7806
			3	0.7998	0.7934	0.7637

Backgrounds: no background = worse than the uncorrected image, ▫ = better than the uncorrected image, ▪ = best value for this algorithm, bold = best value

Parameters: a = shrink factor; b = number of fitting levels, c = full width at half maximum, d = number of classes

Table 5. Dice coefficient for T1_IR images with 3% noise, bias field B, 3 different rf levels and for WM

	Parameters			Images		
				rf20	rf40	rf100
Uncorrected				0.8532	0.8456	0.7617
N3	a	b	c			
	0.1	2	4	0.8573	0.8569	0.8233
	0.3	2	4	0.8574	0.8575	0.8486
	0.15	2	2	0.8543	0.8476	0.7650
	0.15	2	4	**0.8579**	0.8574	0.8417
FSL algorithm		d	c			
		2	20	0.8306	0.8340	0.8352
		3	10	0.8544	0.8546	0.8392
		3	20	0.8565	0.8566	0.8498
		3	30	0.8578	**0.8579**	0.8479
		4	20	0.8565	0.8564	0.8304
SPM algorithm			c			
			60	0.8566	0.8568	**0.8553**
			90	0.8430	0.8440	0.8423
PABIC			c			
			2	0.8546	0.8547	0.8315
			3	0.8547	0.8521	0.8154

Backgrounds: no background = worse than the uncorrected image, ▫ = better than the uncorrected image, ▪ = best value for this algorithm, bold = best value

Parameters: a = shrink factor; b = number of fitting levels, c = full width at half maximum, d = number of classes

Table 4. Dice coefficient for T1_fl images with 3% noise, bias field B, 3 different rf levels and for WM

	Parameters			Images		
				rf20	rf40	rf100
Uncorrected				0.8297	0.7847	0.6772
N3	a	b	c			
	0.1	2	4	0.8215	0.8266	0.8077
	0.3	2	4	0.8027	0.8028	0.8120
	0.15	2	2	0.8341	0.7931	0.6808
	0.15	2	4	0.8239	0.8128	0.8022
FSL algorithm		d	c			
		2	20	0.8016	0.8067	0.8128
		3	10	0.8203	0.8087	0.7928
		3	20	0.8396	0.8363	0.8157
		3	30	0.8443	0.8402	0.8009
		4	20	0.8424	0.8373	0.7734
SPM algorithm			c			
			60	0.8250	0.8276	0.8302
			90	**0.8577**	**0.8575**	**0.8553**
PABIC			c			
			2	0.8419	0.7995	0.7578
			3	0.8306	0.8203	0.7360

Backgrounds: no background = worse than the uncorrected image, ▫ = better than the uncorrected image, ▪ = best value for this algorithm, bold = best value

Parameters: a = shrink factor; b = number of fitting levels, c = full width at half maximum, d = number of classes

Table 6. Dice coefficient for T1_fl images with 9% noise, bias field A, 3 different rf levels and for GM

	Parameters			Images		
				rf20	rf40	rf100
Uncorrected				0.6275	0.6180	0.5539
N3	a	b	c			
	0.1	2	4	0.6102	0.6170	0.6074
	0.3	2	4	0.6016	0.6063	0.6023
	0.15	2	2	0.6280	0.6199	0.5570
	0.15	2	4	0.6077	0.6119	0.6092
FSL algorithm		d	c			
		2	20	0.5825	0.5862	0.5942
		3	10	0.5543	0.5560	0.5636
		3	20	0.5949	0.5991	0.6061
		3	30	0.6106	0.6164	0.6190
		4	20	0.6059	0.6110	0.6089
SPM algorithm			c			
			60	0.5976	0.6021	0.6038
			90	**0.6941**	**0.7003**	**0.7026**
PABIC			c			
			2	0.6162	0.6253	0.5918
			3	0.6051	0.6065	0.5814

Backgrounds: no background = worse than the uncorrected image, ▫ = better than the uncorrected image, ▪ = best value for this algorithm, bold = best value

Parameters: a = shrink factor; b = number of fitting levels, c = full width at half maximum, d = number of classes

Table 7. Sigma values of the tests of within-subjects contrasts (ANOVA test) of the Dice Coefficients.

	Parameters			Images			
				T1 fl		T1 IR	
				GM	WM	GM	WM
N3	a	b	c				
	0.1	2	4	0.024	0.048	0.012	0.008
	0.3	2	4	0.095	0.229	0.021	0.018
	0.15	2	2	0.007	0.03	7E-05	2E-04
	0.15	2	4	0.027	0.633	0.016	0.341
FSL algorithm	d	c					
	2	20		0.18	0.453	0.883	0.96
	3	10		0.227	0.746	0.386	0.558
	3	20		0.018	0.048	0.055	0.066
	3	30		0.005	0.012	0.023	0.023
	4	20		0.004	0.012	0.029	0.036
SPM algorithm	c						
	60			0.038	0.048	0.044	0.044
	90			4E-04	3E-04	0.656	0.887
PABIC	c						
	2			0.012	0.043	0.326	0.34
	3			0.019	0.060	0.012	0.683

Parameters: a = shrink factor; b = number of fitting levels, c = full width at half maximum, d = number of classes
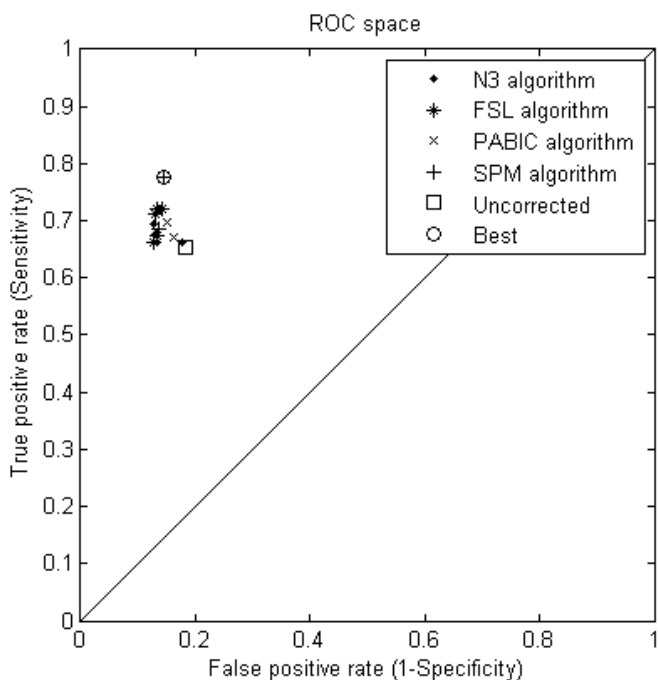

Figure 1. ROC space considering the sensitivity and specificity of the segmentation of the GM in the T1_IR image, with 3% noise, B bias field and 40% inhomogeneity.

Table 6 shows the influence of a higher noise level in the correction and segmentation of GM in a T1_fl image.

In each figure1 we represent the ROC points for the four algorithms and the best relation between the sensitivity and specificity (point closer to the coordinates (0,1) is marked with a circle). An example of a Roc space is shown in Figure 1.

4 DISCUSSION

It can be observed that the IIH corrections improve the subsequent segmentation of most images.

In the N3 algorithm, it is unclear what are the parameters which allow for higher Dice coefficients, and it works well for higher rf's. N3 is the algorithm that appears to deal better with images that have high noise levels and/or high rf. For the IR image the best parameters seem to be a FWHM of 0.15, with shrink factor of 2 and fitting levels of 4. For the T1_fl image the parameters are not so clear. Some other experiences showed that a higher fitting level gives a worse segmentation and it was also observed that using a greater shrink factor, e.g. 4, the results do not vary much and the time necessary for correction decreases.

In FSL the parameters that allow a greater Dice coefficient, are number of classes equal to 3, and for a rf20 and rf40 a FWHM of 30mm, whereas for a rf100 a 20mm FWHM is better. This occurs because the variation is more abrupt for higher rf values and a smaller FWHM fits those cases better.

The IIH correction algorithm present on SPM is considered to be the most regular of the algorithms. The best parameter for T1_fl images is to use a FWHM of 90mm, and for the T1_IR images is to use a FWHM of 60mm. A FWHM of 30mm was also used, but the results of the segmentations show it is worse than for the uncorrected image.

The analysis of the PABIC and SPM is quite limited, since we only have change two parameters. However, it can be observed that for rf20 the use of 2 classes is adequate for T1_fl images, while the use of 3 classes is adequate for T1_IR images. For higher rf's, the opposite happens

It can be seen that the algorithm used for the segmentation does not perform as well in 9% noise images. However, the correction algorithms still fail to improve segmentation. An analysis of the coefficient of variation is likely to provide better answers.

With the analysis of the Table 7 it is possible to say that the increase of the Dice coefficients with the corrections is statistically significant for most of the correction methods, sigma lower than 0.05.

A typical problem of segmentation methods was observed: a higher sensitivity corresponds normally to a lower specificity and vice versa. However, observing the ROC space it is possible to find the best relationship, and often this relationship corresponds to a higher Dice coefficient.

5 CONCLUSION

It is unquestionable that the IIH corrections improve the segmentation of MRI brain images, especially for higher rf, as long as the noise level is not too high. However it was not found an IIH correction algorithm or set of parameters that performs well for all analyzed images. Besides that, it can be said that the algorithm that shows to be the most stable and offers the best evaluation parameters for the majority of images is the one present on SPM8 software.

With these results we reinforce the utility and the need of using a preprocessing method for IIH correction, before applying a segmentation algorithm.

6 REFERENCES

Ashburner, J & Friston, KJ 2005, "Unified segmentation." *NeuroImage*, vol. 26, no. 3, pp. 839-851.

de Boer, R, Vrooman, HA, Ikram, MA, Vernooij, MW et al. 2010, "Accuracy and reproducibility study of automatic MRI brain tissue segmentation methods." *NeuroImage*, vol. 51, no. 3, pp. 1047-1056.

Boyes, R, Gunter, J, Frost, C, Janke, A et al. 2008, "Intensity non-uniformity correction using N3 on 3-T scanners with multichannel phased array coils." *NeuroImage*, vol. 39, no. 4, pp. 1752-1762.

Cocosco, C, Kollokian, V, Kwan, R, Pike, B & Evans, A 1997, "BrainWeb: Online Interface to a 3D MRI Simulated Brain Database." *NeuroImage*, vol. 5.

Duncan, J & Ayache, N 2000, "Medical image analysis: progress over two decades and the challenges ahead." *IEEE Transactions on Pattern Analysis and Machine Intelligence*, vol. 22, no. 1, pp. 85-106.

Guillemaud, R & Brady, M 1997, "Estimating the bias field of MR images." *IEEE Transactions on Medical Imaging*, vol. 16, no. 3, pp. 238-251.

Guillemaud, R & Brady, M 1997, "Estimating the bias field of MR images." *IEEE Transactions on Medical Imaging*, vol. 16, no. 3, pp. 238-251.

Hendee, W 2002, *Medical imaging physics* 4th ed., New York ;Wiley-Liss.

Ibanez, L, Schroeder, W, Ng, L & Cates, J 2003, *The ITK Software Guide: The Insight Segmentation and Registration Toolkit*, Kitware Inc.

Kaus, MR, Warfield, SK, Nabavi, A, Black, PM et al. 2001, "Automated Segmentation of MR Images of Brain Tumors1." *Radiology*, vol. 218, no. 2, pp. 586-591.

Sled, J, Zijdenbos, A & Evans, A 2002, "A nonparametric method for automatic correction of intensity nonuniformity in MRI data." *Medical Imaging, IEEE Transactions on*, vol. 17, no. 1, pp. 97, 87.

Styner, M, Brechbuhler, C, Szckely, G & Gerig, G 2000, "Parametric estimate of intensity inhomogeneities applied to MRI." *Medical Imaging, IEEE Transactions on*, vol. 19, no. 3, pp. 153-165.

Vovk, U, Pernus, F & Likar, B 2007, "A review of methods for correction of intensity inhomogeneity in MRI.." *IEEE Trans Med Imaging*, vol. 26, no. 3, pp. 421, 405.

Wells, WM, Grimson, WL, Kikinis, R & Jolesz, FA 1996, "Adaptive segmentation of MRI data." *IEEE Transactions on Medical Imaging*, vol. 15, no. 4, pp. 429-442.

Zhang, Y, Brady, M & Smith, S 2001, "Segmentation of brain MR images through a hidden Markov random field model and the expectation-maximization algorithm." *IEEE Transactions on Medical Imaging*, vol. 20, no. 1, pp. 45-57.